POLYMER COLLOIDAL CRYSTALS:

SYNTHESIS AND TEMPLATE-ASSISTED FABRICATION WITH CONTROLLED STRUCTURE AND ORIENTATION

Nina Dziomkina

Polymer colloidal crystals: synthesis and template-assisted fabrication with controlled structure and orientation
Nina Dziomkina

Ph.D. Thesis, University of Twente, MESA$^+$ Institute for Nanotechnology,
Enschede, The Netherlands
ISBN 90-365-2335-4

This research was financially supported by the MESA$^+$ Institute for Nanotechnology of the University of Twente in the Strategic Research Orientation "Advanced Photonic Structures" and by NanoImpuls, a nanotechnology program of the Ministry of Economic Affairs.

Printed by PrintPartners Ipskamp, Enschede, The Netherlands
http://www.ppi.nl

POLYMER COLLOIDAL CRYSTALS:

SYNTHESIS AND TEMPLATE-ASSISTED FABRICATION WITH CONTROLLED STRUCTURE AND ORIENTATION

PROEFSCHRIFT

ter verkrijging van
de graad van doctor aan de Universiteit Twente,
op gezag van de rector magnificus,
prof.dr. W.H.M. Zijm,
volgens besluit van het College voor Promoties
in het openbaar te verdedigen
op donderdag 6 April 2006 om 15.00 uur

door

Nina Dziomkina

geboren op 8 Augustus 1978
te Gomel, Belarus

Dit proefschrift is goedgekeurd door:

Promotor:	prof. dr. G. J. Vancso
Assistent-Promotor:	dr. M. A. Hempenius

In memory of my grandfather
Andrei Lysenko

Table of Contents

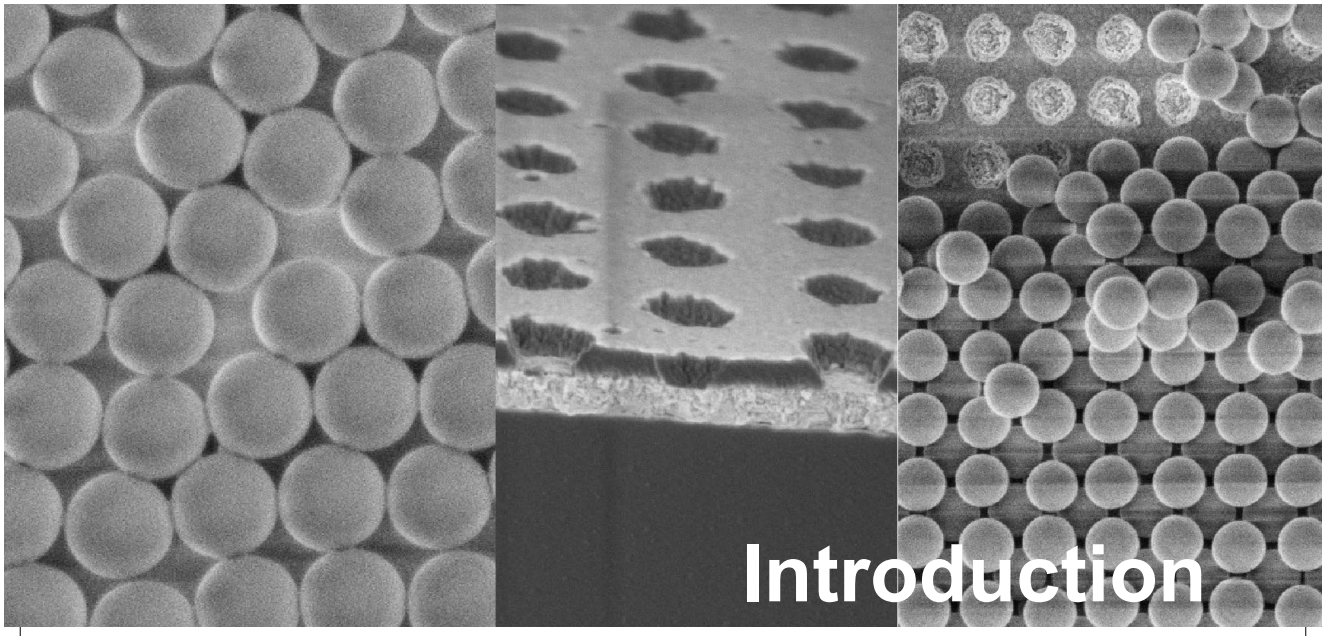

Introduction

The topic of this thesis is the development of a deposition technique for placing charged polymer colloidal particles on patterned electrodes by electrophoresis to achieve directed colloidal crystal growth. The ultimate objective is to realize an independent control of colloidal crystal structure, orientation and thickness. Polystyrene colloidal particles with controlled surface charge densities are synthesized and employed as building blocks of colloidal crystals. Lithographically patterned electrode surfaces are demonstrated to predetermine the colloidal crystal growth. The method of electrophoretic colloidal deposition on patterned surfaces is successfully applied to grow colloidal monolayers, colloidal crystals with face-centered cubic (FCC) crystal structures and (111), (100) and (110) planes oriented parallel to the electrode surface, body-centered cubic (BCC) colloidal crystals grown from a (100) crystal plane, colloidal non-close-packed crystals with a hexagonal close-packed (HCP) crystal sequence and various binary colloidal crystal structures.

General introduction

Colloidal dispersions exhibit a continuous liquid phase in which a colloidal solid is dispersed. If the solid phase is built up of highly monodisperse spheres of dielectric materials, including particles made of soft matter such as polymers, these can under proper conditions form regular, periodic arrays. Such arrays that exhibit translational symmetry are called colloidal crystals.[1] Monodisperse in this context refers to size, shape and interaction for the dielectric microparticles. Colloidal crystals have been of tremendous interest in relation to a wide range of scientific phenomena. Colloidal particles suspended in solution provide fascinating models for studying basic physics problems including phase transitions,[2] fundamental problems of kinetics of crystallization,[3,4] and the physics of nucleation and growth.[5,6]

Organized colloidal structures have intriguing properties, which make them useful in a wide range of applications in optics,[7] as chemical sensors,[8] in data storage devices,[9] etc. Due to a great scientific interest and wide range of applications, the fabrication of colloidal structures has been reviewed by several authors.[10,11,12,13]

Among all possible optical applications of colloidal crystals, their use in photonics has attracted the most current interest. Photonic devices have important potential applications in optical communication systems, optical chips, and all optical computers.[14,15] Particularly important are photonic band gap (PBG) crystals, which are periodic structures that are able to block the propagation of light through the crystal in one, or more, directions. The works of E. Yablonovitch[16] and S. John,[17] describing the inhibition of spontaneous emission and light localization caused by the presence of a "photonic band gap", respectively, gave a powerful incentive to the field of photonic crystals. Photons behave in PBG crystals analogous to the propagation of Bloch electron waves in semiconductors.[18] When the wavelength of light is of the order of the period of a photonic crystal, photons can be Bragg-diffracted by the crystal lattice planes resulting in a forbidden range of frequencies, which are referred to as "stop gaps". Light with frequencies within the stop band is thus not allowed to propagate through the material along certain directions. Periodic photonic structures that are built up such that light cannot propagate in any direction within a given frequency range, are referred to as crystals exhibiting a photonic band gap. The existence of a photonic band gap in a photonic material and its properties are dependent on the photonic strength, which is determined by the crystal symmetry and refractive-index contrast.[19] The most vivid examples of photonic-crystal materials can be found in nature in opals, iridescent butterfly wings, and in spins and treads of

the sea mouse.[20,21] The opal itself consists of closely packed silica spheres that are often used, in addition to polymeric microspheres, for making artificial colloidal crystals. Photonic band structures were calculated for various crystal symmetries and dielectrics.[22,23,24,25] It was found that an FCC structure (see Figure 1) – a close-packed structure that is favourable in spontaneous colloid self-assembly[26] has a PBG only in the second Brillouin zone, second-order Bragg diffraction, and not in the first Brillouin zone. Therefore, the refractive-index contrast between the building blocks of the FCC crystal (colloidal particles and the interparticle space) should exceed 2.8 to obtain a photonic band gap. Optical properties of photonic crystals are very sensitive to unavoidable structural disorder such as size dispersion, displacement and roughness of the crystal building blocks.[27] The higher-order diffraction as seen in FCC crystals can be destroyed. A PBG due to the lowest-order Bragg diffraction was predicted for structures with diamond-like symmetries,[23,24,25] for a minimum refractive-index contrast of 1.9. This low-frequency PBG is less sensitive to structural disorder. Furthermore, the lower required refractive-index contrast allows a broader choice of dielectric materials. Although the diamond structure with tetrahedral packing is very well suited to fabricate PBG crystals, its formation is not favoured by spontaneous colloidal self-assembly. The packing density of this structure is very low; the packing fraction for the diamond structure is 0.34 as compared with the favoured FCC that has a packing efficiency of 0.74.

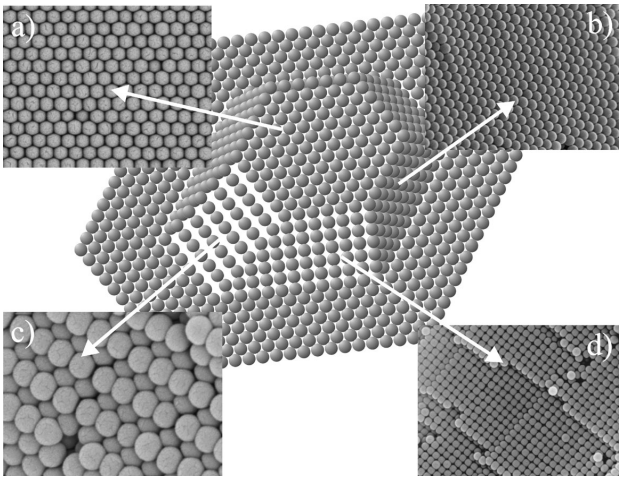

Figure 1. Scanning electron microscopy (SEM) images of four facets of a face-centered cubic (FCC) structure compared with a model crystal (center): (a) outer (111), (b) inner (111), (c) inner (110), (d) inner (100).[13]

In order to fabricate colloidal crystals with a diamond structure, one can think of mimicking the packing of ionic crystal lattices based on scaling up the ions with the corresponding ionic radii and charges to colloidal dimensions. For example, the zinc blende type of packing has a diamond lattice structure but consists of oppositely charged ions (Zn^{2+} and S^{2-}) of different sizes. Calculation of a band gap structure of an inverse zinc blend colloidal crystal showed a complete PBG in the first Brillouin zone.* A complete PBG of 2.1 % (for a colloid size ratio of 0.225) and 3.0 % (for slightly overlapping colloidal spheres with a colloid size ratio of 0.233)[28] was obtained for a dielectric constant ratio of 11.56, taken for air spheres in a silicon matrix, Figure 2.[29] Possessing a complete PBG in the first Brillouin zone, these structures could be promising candidates for photonic crystal applications. If colloidal crystals with a zinc blende structure are stable, then prerequisite for successful fabrication of such structures is a full control over size and surface charge of the polymer microparticles. In addition, if PBG structures of practical relevance were to be built using colloidal particles as building blocks, one must find a colloidal assembly approach that would allow controlling packing symmetry, packing order and packing efficiency of such colloidal crystals.

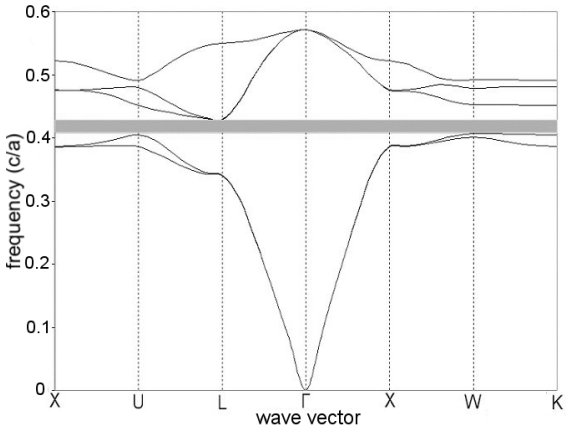

Figure 2. Photonic dispersion relation for a crystal of air spheres possessing a zinc blende structure embedded in a silicon matrix (ε = 11.56). The photonic dispersion relation is plotted for the wave vectors in the irreducible Brillouin zone.[19] A complete PBG of 3 % between the second and the third band was obtained for slightly overlapping air spheres (sphere size ratio = 0.233).

* The calculation of the PBG of the zinc blende structure was performed using MIT Photonic-Bands software.

Colloidal crystals made of polymer or silica spheres possess a low refractive-index contrast that is insufficient to open a PBG. Nevertheless, these colloidal crystals can be used as templates to fabricate inverse structures with high refractive-index contrast. The inverse structure, where the low refractive-index dielectric occupies the major part of the unit-cell volume, accompanied by high dielectric contrast are favourable for wide "stop gaps" and, therefore, for opening a PBG.[22-25] For this purpose, colloidal crystals are first infiltrated with a material with a high refractive index, and then colloidal spheres are selectively removed by chemical etching, or calcination, leaving inverse structures with high refractive-index contrast.[30,31,32,33]

Emerging micro- and nanofabrication technologies, including template structuring and controlled assembly of colloidal particles, have a tremendous potential for use in colloidal crystal engineering. Such directed assembly approaches will eventually allow one to fabricate crystals exhibiting the desired packing characteristics (symmetry, packing density, etc…). For example, template-directed crystallization and growth allow one to a certain degree to tailor the packing structure, lattice orientation, and the size of the colloidal crystals. Van Blaaderen *et al*.[34] have shown in 1997 that slow sedimentation of colloidal particles into the "holes" of topologically patterned templates direct the formation of FCC colloidal crystals with crystal orientation of (100) planes parallel to the patterned surface that is different from the usual (111) plane orientation with respect to the surface. These authors succeeded with the fabrication of large, regular, oriented crystals and tailored their defect structure by the mentioned surface graphoepitaxy approach. The basic idea of this approach was successfully borrowed from semiconductor technology. In semiconductor structure manufacturing, controlled growth of inorganic thin films with a certain orientation on topologically patterned surfaces, known as graphoepitaxy or "artificial epitaxy"[35] has been used with success. Growth of crystals by graphoepitaxy, as its name states, is controlled by substrate topology as opposed to atomic (lattice) epitaxy in which a material is crystallized onto an existing crystal of another material such that the crystal supergrowth results in a continuation of the crystal structure of the substrate.[36]

The example of a graphoepitaxial approach underlines the power of using topological templates, or other patterns such as chemical[37] or optical,[38] in directed colloidal crystal assembly to remedy the shortcomings of spontaneous colloidal self-assembly for the manufacturing of tailored colloidal crystals for realistic photonics applications. Therefore, the development of directed, robust methods is essential for obtaining high quality, uniform, and

mechanically stable structures with a controlled packing symmetry and with a predetermined crystal structure orientation with respect to the substrates (templates) used.

Concept of this thesis

The goal of this study is to establish a fabrication technique that allows control of colloidal crystal growth. The method of colloidal crystallization on patterned surfaces under an applied electric field is proposed. In this method, patterned surfaces predetermine the location of colloids on the surface and an electric field act as a driving force in the colloidal crystallization process. In this content, the research described in this thesis comprises synthesis, characterization and crystallization of colloidal particles as well as patterning approaches of electrode surfaces.

Chapter 1 is a literature-based introduction to the topic of colloidal crystallization. Various colloidal crystallization methods, such as colloidal crystallization on flat, chemically and lithographically modified substrates as well as under applied external fields are briefly discussed. Special emphasis is placed on reviewing the current status in the area of colloidal crystallization on topologically patterned substrates.

Computer simulations of colloidal crystallization processes are discussed in **Chapter 2**. Molecular Dynamic simulations are performed. The stability of binary colloidal crystals formed from oppositely charged colloidal particles is examined. Colloidal radii ratios are varied between 0.2 and 1. In addition, a theory on colloidal particle interactions is presented.

Synthesis and characterization of negatively and positively charged colloidal particles are presented in **Chapter 3** and **Chapter 4**, respectively. Colloidal particles are synthesised by seeded (core-shell) emulsifier-free emulsion polymerization. The influence of monomer type, initiator and polymerization conditions on colloid size, size monodispersity and surface charge density are discussed.

In **Chapter 5**, a lithographic approach for electrode surface patterning, referred to as "lift-off" method is presented. Hexagonal, square and rectangular types of periodic patterns in photoresist layers are generated at the surface of conducting ITO electrodes by laser interference lithography. Pattern periodicities are varied between 300 nm and 900 nm. The influence of various process parameters on pattern structure is discussed.

The method of electrophoretic deposition of colloidal particles onto patterned electrode substrates is presented in **Chapter 6**. Deposition on flat and patterned electrode surfaces is compared. Deposition parameters such as electric field strength, colloid

concentration, surface charge density, withdrawal speed of electrodes etc. are shown to play an important role in colloidal crystal growth. Specifically, the formation of colloidal monolayers (two-dimensional crystals) is discussed in depth in this chapter.

The growth of colloidal crystals with FCC and BCC structures is discussed in **Chapter 7**. Colloidal crystals are deposited on patterned electrode surfaces with various symmetries in order to induce colloidal crystal growth from different crystal planes. Colloidal crystals with FCC crystal structure grown in [111], [100] and [110] crystal directions and BCC structure in the [100] direction are presented. The influence of topologically patterned electrode surfaces on colloidal crystal growth is a main topic of this chapter. Optimization of deposition parameters for these self-assembled structures is also discussed.

The layer-by-layer deposition method of colloidal particles on patterned electrode surfaces is presented in **Chapter 8**. We show that by applying this method, non-close-packed colloidal multilayers with a colloidal particle size to electrode pattern periodicity ratio of 0.75 and a layer sequence as in the HCP crystal structure can be grown. Thick FCC colloidal crystal growth in the direction perpendicular to the (110) crystal plane can be realized. Plane defects in the form of a colloidal layer of different colloidal particle size can be introduced in a colloidal crystal. Finally, growth of bimodal colloidal monolayers and crystals fabricated by sequential deposition of colloidal particles either of identical or opposite charge signs is presented in this chapter, as well.

References

[1] R. J. Hunter, *Foundations of Colloid Science*, Oxford University Press, **2001**.
[2] A. P. Gast, W. B. Russel, *Physics Today* **1998**, *51*, 24.
[3] S. Auer, D. Frenkel, *Nature* **2001**, *409*, 1020.
[4] A. Yethiraj, A. van Blaaderen, *Nature* **2003**, *421*, 513.
[5] U. Gasser, E. R. Weeks, A. Schofield, P. N. Pusey, D. A. Weitz, *Science* **2001**, *292*, 258.
[6] P. Habdas, E. R. Weeks, *Curr. Opin. Coll. Int. Sci.* **2002**, *7*, 196.
[7] V. L. Colvin, *MRS Bulletin* **2001**, *26*, 637.
[8] J. H. Holtz, S. A. Asher, *Nature* **1997**, *389*, 829.
[9] I. Gourevich, H. Pham, J. E. N. Jonkman, E. Kumacheva, *Chem. Mater.* **2004**, *16*, 1472.
[10] Y. Xia, B. Gates, Y. Yin, Y. Lu, *Adv. Mater.* **2000**, *12*, 693.
[11] D. Wang, H. Möhwald, *J. Mater. Chem.* **2004**, *14*, 459.
[12] D. J. Norris, E. G. Arlinghaus, L. Meng, R. Heiny, L. E. Scriven, *Adv. Mater.* **2004**, *16*, 1393.
[13] C. Lopez, *Adv. Mater.* **2003**, *15*, 1679.
[14] J.-M. Liu, *Photonic Devices*, Cambridge University Press, Cambridge, **2005.**
[15] *Polymers for Photonic Applications*, *Adv. Polym. Sci.* Springer, Berlin/Heidelberg, **2002**, *158*.
[16] E. Yablonovitch, *Phys. Rev. Lett.* **1987**, *58*, 2059.
[17] S. John, *Phys. Rev. Lett.* **1987**, *58*, 2486.
[18] C. Kittel, *Introduction to solid state physics*, 7th ed., Wiley, NJ **1995**.
[19] J. D. Joannopoulos, R. D. Meade, J. N. Winn, *Photonic Crystals, Molding the Flow of Light*, Princeton University Press, Princeton, NJ **1996**.
[20] G. Tayeb. B. Gralak, S. Enoch, *Optics & Photonics News*, **2003**, *2*, 38.
[21] L. P. Biro, Zs. Balint, K. Kertesz, Z. Vertesy, G. I. Mark, Z. E. Horvath, J. Balazs, D. Mehn, I. Kiricsi, V. Lousse, J.-P. Vigneron, *Phys. Rev. E* **2003**, *67*, 21907.
[22] K. Busch, S. John, *Phys. Rev. E* **1998**, *58*, 3896.
[23] K. M. Ho, C. T. Chan, C. M. Soukoulis, *Phys. Rev. Lett.* **1990**, *65*, 3152.
[24] E. Yablonovitch, T. J. Gmitter, K. M. Leung, *Phys. Rev. Lett.* **1991**, *67*, 2295.
[25] K. M. Ho, C. T. Chan, C. M. Soukoulis, R. Biswas, M. Sigalas, *Solid State Commun.* **1994**, *89*, 413.
[26] L. V. Woodcock, *Nature* **1997**, *385*, 141.
[27] A. F. Koenderink, A. Lagendijk, W. L. Vos, *Phys. Rev. B* **2005**, *72*, 153102.
[28] The photonic gap size is normally given as a percentage of the ratio of frequency gap width to the middle gap frequency.
[29] Parameters for the PBG calculations were optimized and taken as: resolution of 32, 4 k-points, mesh-size of 7 (for details see diploma thesis by E. Leenders).
[30] J. E. G. J. Wijnhoven, W. L. Vos, *Science*, **1998**, *281*, 802.
[31] A. Blanco, E. Chomski, S. Grabtchak, M. Ibisate, S. John, S. W. Leonard, C. Lopez, F. Meseguer, H. Miguez, J. P. Mondia, G. A. Ozin, O. Toader, H. M. van Driel, *Nature* **2000**, *405*, 437.
[32] Y. A. Vlasov, X. Z. Bo, J. C. Sturm, D. J. Norris, *Nature* **2001**, *414*, 289;
[33] Review: D. J. Norris, Y. A. Vlasov, *Adv. Mater.* **2001**, *13*, 371.
[34] A. van Bladeren, R. Ruel, P. Wiltzius, *Nature* **1997**, *385*, 321.
[35] H. I. Smith, M. W. Geis, C. V. Thompson, H. A. Atwater, *J. Cryst. Growth* **1983**, *63*, 527.
[36] See for example: L. B. Freund, S. Suresh, *Thin Film Materials: Stress, Defect Formation and Surface Evolution*, Cambridge University Press, Cambridge, **2004**.
[37] I. Lee, H. Zheng, M. F. Rubner, P. T. Hammond, *Adv. Mater.* **2002**, *14*, 572.
[38] R. C. Hayward, D. A. Saville, I. A. Aksay, *Nature* **2000**, *404*, 56.

Chapter 1

Ordering of Colloidal Crystals[*]

A literature review on the topic of colloidal crystallization is presented in this chapter. Various colloidal crystallization methods, such as colloidal crystallization on flat, chemically and lithographically modified substrates, as well as under applied external fields are discussed. Special emphasis is placed on reviewing the current status in the field of colloidal crystallization on topologically patterned substrates. In this context, the various interactions and forces that control growth for a broad range of colloidal crystals are also included. In addition, the synthesis of colloidal particles with different sizes, shapes and surface functionalization is first outlined briefly. As to the composition of the colloidal particles, emphasis is laid on polymer microspheres.

[*] Parts of this chapter have been published in: N. V. Dziomkina, G. J. Vancso, *Soft Matter* **2005**, *1*, 265.

1.1. Colloidal microparticles used in photonic crystal assembly

With the advent of photonics in need of colloidal crystals, inorganic colloidal particles[1,2] and particularly silica[3,4] and polymer[5-17] colloidal microspheres quickly found their place in applications where size monodispersity, colloidal dimensions (of the order of the wavelength of visible and near-infrared light), surface functionality, and the ability to self-assemble in crystalline arrays are essential. Synthesis and structure-property studies of polymer colloidal particles are one of the largest areas of polymer research with a long tradition. It revolves around the preparation and study of finely dispersed polymer colloidal particles in either aqueous or organic systems. The colloidal particles of interest for photonic crystal engineering usually have a spherical shape and are often made of silica[3,4] or polymers[5,6] such as poly(methyl methacrylate) (PMMA)[7,19] or polystyrene (PS).[11-18]

The best-known method for the preparation of spherical silica colloidal particles (see Figure 1.2B) was originally developed by Stöber *et al*. It is based on the hydrolysis of tetraethoxysilane with subsequent polymerisation of Si-O units in ethanol medium. The diameter of colloidal particles can be tuned from a few nanometers to a few micrometers by choosing appropriate synthetic conditions such as concentration of the additives, temperature, and pH.

Preparation strategies, and applications of functional polymer colloidal microspheres including their use in medical, and chemical functions, optical and optoelectronic areas have been extensively reviewed.[8,9,10] Various polymerization methods such as emulsion, dispersion, precipitation and suspension polymerizations are used to synthesize polymer colloidal particles, Figure 1.1. Among the polymerization methods mentioned above,

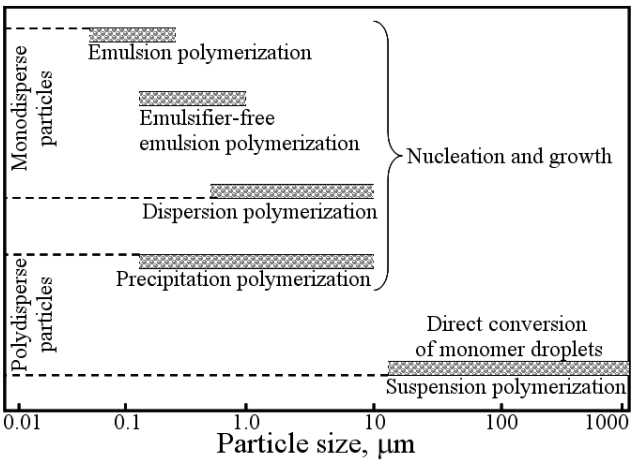

Figure 1.1. Particle size range and particle polydispersity obtained by different polymerization methods.[10]

emulsion, emulsifier-free emulsion and dispersion polymerizations yield monodisperse particles in the range between 0.05 and 10 μm. Monodisperse polymer colloidal particles of sub-micrometer size that possess surface functionalities of choice are usually prepared by emulsion polymerisation.[5-18] In the conventional emulsion polymerization process, surfactant molecules such as sodium dodecyl sulfate are used. Surfactant molecules are amphiphilic and, therefore, can self-assemble into micelles above a critical concentration.[5,6] In these micelles, polymerisation of water-insoluble monomers occurs, resulting in the polymer microparticle of interest. Surfactants in this case also act as stabilizing agents. In addition to conventional emulsion polymerisations, emulsifier-free emulsion polymerisation[11-18] found its wide applicability due to the possibility of colloidal stabilization via ionic initiator residues covalently bound to polymer particles. For an example of a polymer colloidal particle see Figure 1.2A. The emulsifier-free emulsion polymerisation was successfully applied to both the preparation of anionic[11,12,13,14] as well as cationic[15,16,17,18] colloidal particles. This approach allows one to form monodisperse colloidal particles with sizes of up to 1μm. This method is usually used either in combination with copolymerisation of functional co-monomers, or without. Monodispersity in size (the diameter uniformity ratio of colloidal particles) of such colloidal systems can be precisely controlled. The amount of charged groups (or surface charge density) of polymer colloidal particles can be effectively tailored via copolymerisation with functional co-monomers in the second step of polymerisation around pre-formed particles,[12-14,16-18] either by seeded polymerization or by two-stage growth polymerization reactions.[12,16] In seeded emulsion polymerization, the pre-formed polymer colloidal particles are introduced to the reaction mixture at the beginning of the reaction and swelling around colloidal particles occurs during the polymerisation, which is normally utilized for the enlargement of colloidal particle size. In two-stage polymerisation the second portion of reactants is added before the polymerisation is finished, therefore allowing one to incorporate larger amounts of functional co-monomer molecules in comparison to seeded polymerizations. As a result, higher surface charge densities at the colloidal microparticles are achieved. Two-stage polymerisation of styrene with styrene derivatives as co-monomer[12,16] has been reported.

A simple method for preparing sterically stabilized PMMA colloidal particles that is widely used in colloid chemistry is a procedure reported by Antl and coworkers.[19] The colloidal particles are stabilized by poly(12-hydroxystearic acid) in hydrocarbon media. By variation of solvency conditions, it was possible to tune particle size. There is evidence that these particles behave as almost perfect hard spheres,[20] which allows one to study packing

structure and kinetics using colloidal particles as mimics for atoms and molecules. If colloidal particles are labelled with fluorescent molecules,[21] their position within the crystal can be imaged by confocal techniques.[22] This allows one to monitor the packing process and structures formed in three dimensions (3D). In addition to the particles labelled by fluorescent molecules, core-shell systems are also described.[23,24] Examples of the incorporation of gold nanoparticles in polymer and silica colloidal particles are presented in Figure 1.2, C and D.[25,26] Based on this method, nanoparticles of various materials can be incorporated in polymer colloidal particles.

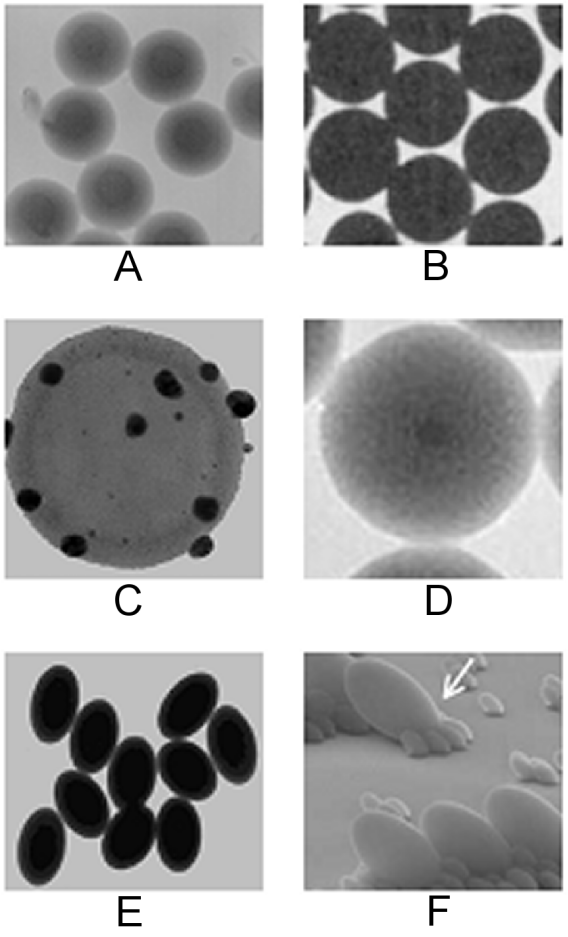

Figure 1.2. Representative examples of colloidal particles as building blocks for crystal assembly. TEM images of A) polymer colloidal particles (particle diameter = 300 nm) and B); silica (particle diameter = 400 nm); C) polymer colloidal particles loaded with gold nanoparticles (particle diameter = 250 nm); D) silica coated gold nanoparticles (particle diameter = 100 nm); E) polymer colloidal particles of ellipsoidal shape (colloidal particle dimensions are 1.08 by 0.78 μm); and F) SEM image of silica colloidal particles modified by ion irradiation (the length of the colloidal particle = 1.2 μm and the aspect ratio = 2).

Colloidal particles, which are assembled from equal-sized colloidal spheres can have other complex shapes.[27] These particles can then pack into complex crystal structures. We note that in a recent review by Polman *et al*.[28] the synthesis and characterization of transparent, non-spherical, monodisperse particles with typical dimensions suitable for PBG fabrication have been summarized. Polymer colloidal particles of ellipsoidal shape can also be prepared by making use of viscoelastic deformation. In this approach, monodisperse spherical polymer colloidal particles [PS or PMMA] are dispersed in an elastic matrix [poly(vinyl alcohol) or poly(dimethylsiloxane)], and by subsequent matrix stretching and heating above the glass transition temperature of the polymer, the microparticles stretch and assume an ellipsoidal shape.[29,30] The particles can be visualized after the matrix with colloidal particles is cooled down and the matrix is removed, Figure 1.2E. Such ellipsoid-shaped particles, when assembled in crystals, can enlarge the optical band gap, hence are of great interest in photonics. In Figure 1.2 we display a few representative examples of colloidal particles that can be used as building blocks in colloidal crystals, including silica as well as polymer microparticles.

1.2. Methods of colloidal crystal assembly

Commonly used methods for assembly of colloidal crystals are based on gravitational, electrostatic, and capillary forces, or on the use of physical confinement in combination with pressure and flow. Representative examples of the related approaches will be briefly described in the following section. The examples include self-assembly by sedimentation and controlled evaporation, electrodeposition, and the use of chemically patterned templates and physical confinement for template fabrication.

The phase transitions from a disordered (liquid) state to an ordered (crystalline) state that suspensions of spherical colloidal particles can exhibit have been intensively studied by means of experiments,[31,32,33,34] as well as computer simulations.[35,36,37,38] As model systems, “hard” spheres or colloidal particles that interact via steep (or short-range) repulsion potential and “soft” spheres, where a long-range repulsion keeps the colloidal particles sufficiently separated, have been considered. In practice, sterically stabilized polymer colloidal particles such as PMMA microspheres that are stabilized by poly(12-hydroxystearic acid),[19] or charged microspheres with fully-screened electrostatic repulsions[39] are used as hard spheres. Thus, the usual independent variables of phase diagrams include the colloidal volume fraction for hard

spheres, and the volume fraction and ionic strength/charge for "soft", or charged, colloidal suspensions.

Hard spheres redistributed in suspension undergo fluid-crystal transitions upon increasing the volume fraction of colloidal microparticles beyond 0.49.[31,32] At volume fractions higher than 0.58 a glass-like order was reported, Figure 1.3A. The crystal structure in the homogeneous region, as determined by light-scattering, was the FCC structure. Formation of crystal structures like AB_2, AB_{13} in colloidal mixtures of bimodal size (atomic analogs are AlB_2 and $NaZn_{13}$) was also reported.[33] Recently, it was shown that crystallization of oppositely charged singular and bimodal hard spheres led to the formation of a variety of crystal structures that mimic ionic crystals, such as CsCl, NaCl, NiAs and various colloidal structures with AB_2, AB_6, AB_8 stoichiometries.[40] As mentioned, in charged-stabilized suspensions, in addition to the volume fraction, salt concentration as well as charge on the particles can be varied.[8-18] Chaikin *et al*. determined the phase diagram, structure factor, and pair distribution function for a charged polymer (polystyrene) colloidal suspension using small-angle, synchrotron x-ray-scattering. The corresponding phase diagram revealed a rich variety of structures such as liquid, FCC, body-centered-cubic (bcc), and glassy phases, remarkably at volume fractions that are rather low compared to those reported for hard spheres, Figure 1.3B.[34,37,38]

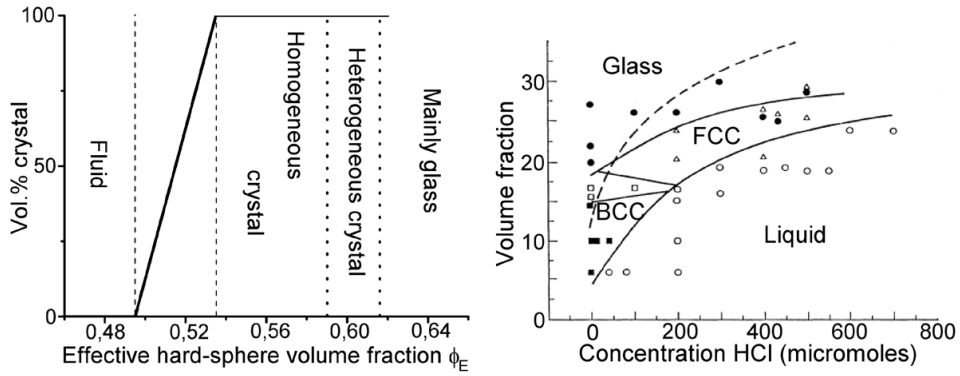

Figure 1.3. Typical "phase-diagram" of a colloidal system of A) hard spheres; and B) "soft", charged colloidal suspensions (volume fraction is specified in %). The region between the bcc and FCC regions, indicated by open squares, represents coexisting packing for these two phases.

Colloidal assembly can be induced by gravitational,[41,42,43,44] electric[45,46,47,48,49] and magnetic[50,51] fields. Although sedimentation in a gravitational field is conceptually straightforward and simple, very precise control of parameters, such as the size and the

density of the colloidal spheres, is essential for successful self-assembly. The colloidal particles will only settle if their size and density are sufficiently high. Controlled sedimentation of colloidal particles in a gravitational field leads to the formation of 3D polycrystalline structures, usually exhibiting an FCC lattice.[43,52,53,54] Silica colloidal particles are commonly used in this type of fabrication due to their high density. Unfortunately, the process of sedimentation is rather slow and successful fabrication of good-quality colloidal crystals can take up to several weeks.[41-44] In order to speed up the sedimentation process, filtration and centrifugation have been applied.[55] Although the use of filtration and centrifugation shorten the time of crystal manufacturing, these techniques do not necessarily yield better quality crystals. The formation of polycrystalline domains with different lattice orientation in colloidal crystals obtained by sedimentation is caused by simultaneous nucleation in different locations of the specimen surface. Subsequent growth of crystalline domains in various directions[56] leads to random orientation of the crystalline grains formed. A significant improvement of ordering of polymer colloidal monolayers under ultrasonic agitation was initially demonstrated by Sasaki *et al*.[57] This method was later applied to improve the fabrication of 3D colloidal structures under physical confinement.[58] Enhanced ordering of colloidal particles during crystal formation can be promoted also by mechanical shear[59] in addition to the above-mentioned sonication. It was also shown that the ordering and crystallinity in the sedimentation process could be enhanced by sedimentation under an oscillatory shear in a confined area.[60]

Another inconvenience of the sedimentation method is that it is difficult to control the number of colloidal layers, while for some applications, such as integration of colloidal crystals into microchips, the crystal thickness plays an essential role. The use of a vertical deposition technique allows one to control the thickness of the crystalline layers formed.[61,62,63,64,65,66,67] In the case of deposition of a 2D particle assembly, the mechanism of colloidal crystallization is represented by two stages and is also known as “convective assembly”. Colloidal crystallization is initiated by attractive capillary immersion forces, mediated in the solvent meniscus between particles at the drying front, Figure 1.4A. These capillary forces induce the colloidal aggregation. Solvent evaporation from the already ordered arrays causes a convective particle flux towards the drying particle layer from the bulk of the colloidal suspension. The formation of a meniscus between particles during the crystallization process is essential for the monotonic formation of 2D colloidal arrays. In the case of 3D colloidal crystals (or multi-layers), the second process of convective transfer of particles from the bulk of the suspension to the thin wetting film prevails, Figure 1.4B.

Colloidal particles, driven to the drying zone of a colloidal film, are pressed towards the crystal front by the solvent influx that percolates through the array's cavities, compensating the evaporation. Evaporating solvent from the colloidal drying film forms capillary bridges between particles that exert strong attractive capillary forces, which can be responsible for the crack formation in the dried colloidal films. The formation of binary colloidal crystals grown by this vertical deposition method was also reported. The authors varied the pattern of the binary crystals formed by the choice of the small to large sphere size ratio as well as their relative amounts in the dispersion. For a full control of ordering, domain size and thickness of colloidal crystals, various parameters must be simultaneously considered including the choice of substrates, tilt angle of the substrate with respect to the free surface of the colloidal suspension (when the substrate is immersed across the suspension-air interface), choice of solvent, evaporation rate, ambient temperature and relative humidity, concentration of colloidal particles,[61-67] etc.

As we will see later, capillary forces can have different effects on colloidal assembly. On the one hand, capillary interactions are advantageous for thickness control, ordering, and domain size definition of colloidal arrays. On the other hand, capillary forces usually lead to the formation of colloidal crystals with close-packed FCC (111) lattices with respect to the substrate surface i.e. limit crystal orientation and type of packing.

In addition to the vertical deposition method, control over the thickness of colloidal crystals can be achieved by Langmuir-Blodgett (LB) deposition, when colloidal 2D arrays of functionalized silica colloidal particles are formed at the water-air interface.[68] By adjusting the speed of downstroke and upstroke of the substrate through the air-water interface, the transfer of a single layer of particles at each cycle can yield 3D colloidal crystals.[69] Park *et al.*[70] reported that the formation of large colloidal crystals with controllable thickness

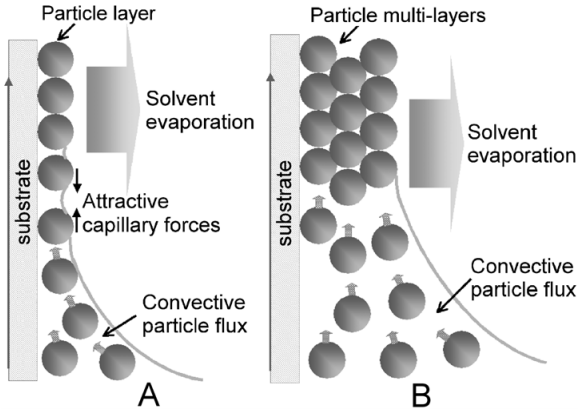

Figure 1.4. Schematic illustration of the mechanism of colloidal self-assembly in the vertical deposition technique in the case of A) 2D colloidal arrays and B) 3D colloidal crystals (multilayers).

obtained by this LB approach can be induced by simply raising the temperature of the solution and by the adjustment of the concentration of the polymer (polystyrene) colloidal particles. Recently, McFarland *et al.*[71] also demonstrated that large-area (wafer-size) colloidal crystals with controllable thickness can be formed by a simple spin-coating process. The thickness of the colloidal crystal-polymer nanocomposite was controlled by the spin-coating speed. Subsequent selective removal either of the polymer matrix or of the silica colloidal crystal led to the formation of colloidal crystals or macroporous polymer, respectively.

Gravitational forces are always present under normal conditions, however other interactions such as electrostatic forces can also be utilized for colloidal crystal engineering. In these approaches, colloidal particles with an electric charge are electrostatically deposited from their aqueous dispersions onto surface domains bearing opposite charges.[72,73,74,75,76,77] The interactions of colloidal particles with direct and alternating electric fields on electrode surfaces were first intensively studied by investigating the formation of 2D colloidal ordering.[47,48,49] In a corresponding study the behaviour of micrometer size colloidal particles on the electrode surface was continuously monitored by optical microscopy. At low electric field strength (2.5 V/mm) colloidal particles approached an electrode surface and deposited on it randomly. When the electric field was increased (from 2.5 V/mm to 7.5 V/mm), colloidal particles started migrating along the electrode surface, forming hexagonal closed packed aggregates. This migration was explained by the electrohydrodynamic flow near the surface arising from the passage of ionic current through the solution. With further increase of the electric field (higher than 10 V/mm) colloidal particles could adhere permanently to the electrode surface. The ordering of colloidal monolayers[78] and crystals[79] could be controlled by applying an electric field in combination with UV irradiation. Specifically, by varying the

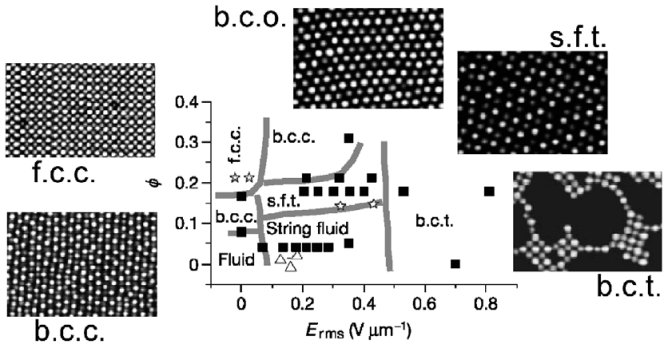

Figure 1.5. Volume fraction – electric field phase diagram, where the phases are labelled as follows: b.c.c. – body-centered cubic, f.c.c. – face-centered cubic, b.c.o. – body-centered orthorhombic, s.f.t. – space-filling tetragonal, and b.c.t. – body-centered tetragonal.

special intensity profile of the applied UV radiation and by using a selective illumination through a photomask, templating of the surface with colloidal particles can be achieved. Recently, it was also shown that the structure of 3D colloidal crystals[45,46] on electrode surfaces can be tuned by the strength of the electric field and by choosing appropriate colloidal volume fractions, Figure 1.5. Colloidal particles with diameters in the submicron length scale were labelled with fluorescent dyes and studied with a confocal microscope. The use of confocal microscopy opens possibilities to determine the depth and position of the labelled colloidal particles within the crystal. Phase diagrams (structures formed as a function of electric field and volume fraction) have been established in great detail in these experiments using PMMA microspheres with fluorescent dye, dispersed in the solvent. The authors tuned the interaction potential including hard sphere repulsion, electrostatic repulsion adjusted by the salt concentration, and an orientation dependent dipolar term (tuneable by the electric field). Details of the structure and phase packing were unveiled by confocal optical imaging. In the absence of an electric field the results found were consistent with earlier obtained results.[31-38] However, with the electric field turned on a rich phase behaviour emerged. Variation of the electric field strength allowed the researchers to tune the structure among the different phases. A drawback of colloidal crystal structure engineering using electrodeposition is the dependence of the structure stability on the presence of the electrostatic field. When the field used for assembly is switched off, the crystals formed can re-disperse back in the suspension or be transformed back to FCC or RHCP structures by capillary forces when the sample is withdrawn from the suspension. Therefore the colloidal crystal must be fixated before its withdrawal, for example, by subsequent polymerization of the dispersion medium.[80,81,82]

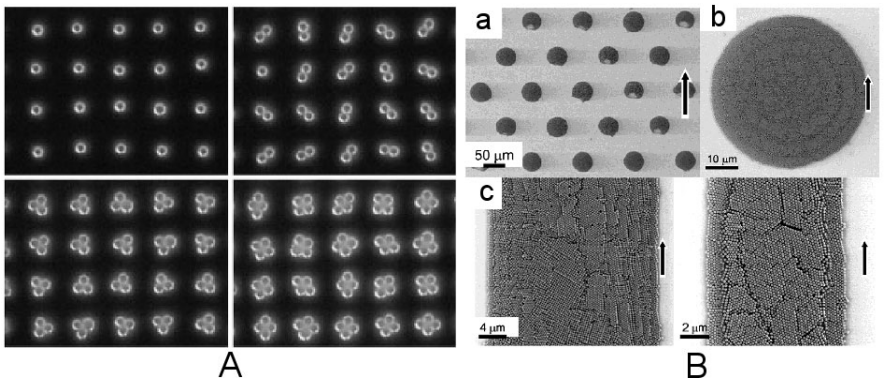

Figure 1.6. Colloidal assembly on chemically patterned substrates: A) colloidal clusters; and B) colloidal crystals assembled on areas of several tens of micrometer size with a given lateral pattern of surface chemistry: (a), (b) circles and (c) stripes, where the arrows show the direction of the sample withdrawal from the suspension.

It is clearly seen from the examples above that it is difficult to control colloidal ordering without the use of adequate templates which direct crystallization. Templates used for "nucleation" of colloidal crystal layers are usually engineered by the modification of their surfaces including physical (lithographically)[83,84,85,86] or chemical[87-91] patterning. Control of surface chemistry and the corresponding patterns of chemical functional units can be achieved by using self-assembling monolayers (SAMs)[87] of organic molecules that have good adhesion to the substrates (for example, thiols to gold,[72-75,87,88,89] silanes to oxide substrates[76,77,87,89]) or polyelectrolytes[73,74,90] in layer-by-layer supramolecular assembly either on homogeneous, or on pre-patterned substrates. The layer-by-layer method allows one to tune the surface charge (positive, negative, or neutral), as well.

Soft lithography and nanoimprint lithography[91] are widely applied techniques for the "printing" of the molecules used for surface modification. The topological pattern of the stamp determines the chemical pattern on the substrate surface. Ordering of colloidal particles on such chemically modified surfaces is governed by the combined effects of electrostatic and capillary forces. Charged microspheres self-assemble on the oppositely charged areas of substrates when the substrate is slowly taken out from the colloidal suspension, Figure 1.6.[72-77] Depending on the ratio between colloidal particle size and the size of the patterned area, colloidal aggregates of very complex forms can be obtained, Figure 1.6A. Colloidal multilayers on chemically modified substrates can be selectively grown by the vertical deposition technique, when a substrate is withdrawn from the suspension with a certain speed, Figure 1.6B. The crystals grown were reported to exhibit mainly non-close-packed hexagonal structures. However, Koumoto *et al*. demonstrated growth of hexagonally close-packed colloidal layers by the vertical deposition technique when a temperature gradient was maintained across the suspension.

1.3. Template directed colloidal assembly

Geometrical confinement has long been known to affect the phase behavior of materials.[92] Crystallization of confined polymer melts in thin films[93,94,95] is an example taken from polymer science describing the influence of geometrical constraints on the physical behavior. Topological patterning of substrates is often used to direct crystallization in semiconductor technology[96] and in block copolymer crystallization.[97] It has been recognized that if one wants to fabricate engineered colloidal crystals, the use of topologically patterned substrates constitutes a very useful approach.[98] We summarize below some representative

achievements in colloidal crystal engineering based on topologically driven, template-assisted growth.

Topological patterns can be manufactured into substrates using standard approaches of micro- and nanofabrication.[99] Relevant fabrication processes include electron beam and photolithography,[83-86] soft lithography, nanoimprint lithography, reactive ion etching,[100] etc.

Leiderer *et al.*[101] in a study aiming at determining the average crystalline radius of polycrystalline colloidal solids realized long ago that the use of colloidal crystals is severely hampered by the lack of controlled approaches to engineer large single crystals with adjustable crystal orientation. Colloidal crystals with a known crystallographic orientation obtained by template-assisted growth were first reported by van Blaaderen *et al*. To tackle the problem of size and orientation of colloidal crystals, silica spheres were deposited in this study onto hole-patterned PMMA layers, which were created by electron beam lithography. Slow sedimentation of the colloidal particles onto the array of holes was shown to direct the formation of crystals. Orientation, size and lattice structure of the resulting crystals was controlled in this pioneering study of a "colloidal epitaxy" process as named by the authors.

In a later experiment Braun *et al.*[102] increased the refractive-index contrast of the colloidal crystals formed with a pre-defined crystal orientation through melt imbibing of selenium and high refractive-index chalcogenide glasses into a graphoepitaxially grown structure obtained under elevated temperature and pressure. This process allowed the researchers to fabricate inverted photonic crystals with known crystallographic orientations. As the colloidal template used possessed a known orientation, photonic crystals could be cut and polished which exposed (001) and (110) facets of the FCC crystal structure, Figure 1.7.

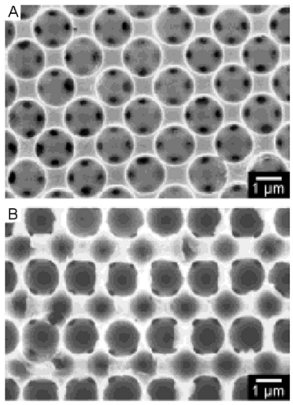

Figure 1.7. Scanning electron micrograph image of an "inverse" selenium photonic crystal, demonstrating A) the polished (001) facet, which was perpendicular to the settling direction and B) the (110) face.

The fabrication of useful photonic devices requires the use of crystals of sufficiently large sizes (exhibiting a volume of mm^3).[41,103] It was shown by Xia *et al.*[103] that when colloidal particles are subjected to a physical confinement, the crystals obtained demonstrate much better ordering and orientation compared with crystals grown on a bare substrate. The authors used dispersions of PS beads, which were injected into the confinement of a rectangular cell (under pressure). This cell constituted a physical confinement possessing typical dimensions of cm in width and length, respectively, and several micrometers in height. By tuning the ratio of the height vs. colloidal particle diameter, the number of layers was easily controlled. Large, defect-free, close-packed crystal layers were observed when the crystals were formed under continuous sonication, Figure 1.8.

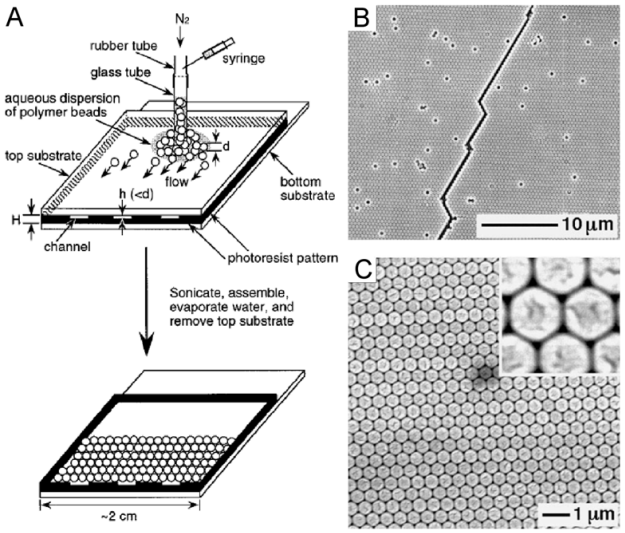

Figure 1.8. Crystallization of colloidal particles under physical confinement: two parallel glass plates separated by walls made of photoresist A) schematics of the fabrication process; B) and C) representative colloidal crystals.

Ordering of latex particles in 3D crystals within a confined cell by oscillatory shear was promoted in a study carried out by Kumacheva *et al.*[60] In this study the ordering was characterized as a function of acceleration ratio that includes an oscillation frequency in the lateral as well as in the vertical directions, respectively. Shear and flow have been used in a subsequent study aiming at flow-driven organization of colloidal spheres in microchannels. One of the simplest topological patterns of possible interest consists of periodic grooves with a rectangular shape. Whitesides *et al.*[104] studied the influence of the width and size of such rectangular grooves (microchannels) on colloidal ordering by coupling laminar flows of colloidal dispersions and topological confinement of the grooves. These authors showed the

formation of close-packed hexagonal, as well as rhombic, or disordered structures, depending on the ratio of the groove width to the particle diameter, Figure 1.9. Similar behaviour was observed when 2D colloidal structures were formed in microchannels in the presence of an electric field.[105,106] The authors used charged PMMA spheres and, in an electrodeposition process between two parallel planar electrodes, assembled colloidal crystals into electroconductive grooves, which were patterned into an ITO anode. Structures on non-patterned electrode surfaces exhibited no packing order, while if the channel width was decreased to below 7.5 μm, ordering was observed to set in. With further decrease of the channel width, oscillatory order-disorder transitions were observed, depending on the commensurability of the colloidal particle row distances with the groove width. Thus packing showed an oscillatory profile in the confinement of the grooves with the variation of channel width. Increasing the mismatch between ideal and experimental ratios of groove width vs. particle diameter to larger than a given threshold value (of ca. 15 %) introduced defects in the crystal structure. In a subsequent study the same group investigated the assembly of crystals on surfaces patterned by narrow grooves into which only parts of one colloidal sphere could (snugly) fit. Thus these narrow profiles provided sites for colloidal deposition in one-bead rows. Depending on the periodicity length of the groove pattern vs. particle diameter, different colloidal ordering was observed.[110] Similar grooves were used by these authors to visualize in-situ the temporal development of template-assisted crystallization by electrodeposition. The electric field served to move the charged colloidal particles toward the electrode with opposite charges and to generate lateral attraction between the colloidal beads.

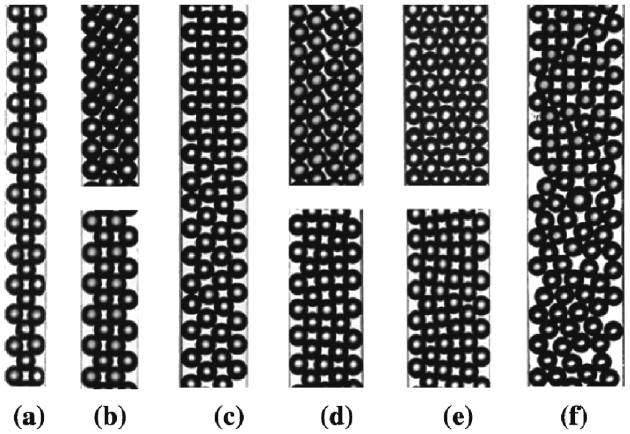

Figure 1.9. Influence of microchannel dimensions on colloidal ordering: fragments of 2D lattices generated from 100-μm beads in microchannels with a relative channel width (L) with respect to particle diameter 2R, *L/(2R)*: (a) 2.20, (b) 2.65, (c) 3.33, (d) 3.71, (e) 4.46; (f) 5.11.

Template-directed self-assembly of colloidal particles with close-packed and non-close-packed structures on 1D and 2D topologically patterned substrates was demonstrated by various groups.[107,108,109,110,111] Crocker *et al*. studying colloidal epitaxy, Natansohn *et al*. using a conventional vertical deposition technique, and Kumacheva *et al*. depositing colloidal particles electrophoretically on 1D patterned surfaces demonstrated that the structure of 2D colloidal monolayers formed on 1D patterned substrates is highly dependent on the ratio between the size of the colloidal particles and the grating periodicity. Introducing 2D gratings of the substrate surface, Kim *et al*.[109] (using a conventional solvent evaporation technique for colloidal deposition when the substrate is tilted under a certain angle to the vertical position) and van Blaaderen *et al*. (using the vertical deposition technique) could realize the fabrication of large, almost defect-free, square-symmetric, close-packed and non-close-packed, 2D structures. Kim, by varying the pattern structure from hexagonal and square to tetragonal types by interference lithography, was able to grow two layers of pseudo – {100} and {110} structures, as well as different hexagonal structures. Van Blaaderen also claimed that on templates consisting of pillars arranged in a square symmetry non-close-packed simple cubic and body centered cubic crystals can be grown by this method.

It is important to emphasize that if the potential of colloidal crystals were to be fully realized in devices, they must be fabricated into planarized microphotonic crystal chips. G. A. Ozin and his group,[112,113] who pioneered the fabrication of planarized microphotonic structures based on colloidal crystals, successfully integrated confinement driven, 2 dimensional templated growth, self-assembly and substrate microfabrication. Such integral strategies are anticipated to play a crucial role to provide simple methods for integration of colloidal crystals into microphotonic components in chips for optical telecommunication applications. The Ozin group used relief structures as templates with tapered dimensions to fabricate colloidal crystals with their (100) planes oriented parallel to the substrate plane. The authors obtained anisotropically etched, V-shaped grooves inside Si (100) wafers using soft lithography patterning. The apex angles of the grooves beneath the Si wafer surface were determined by the Si crystal to 70.6 degrees. The grooves were then partially covered by a piece of flat PDMS and a drop of colloidal dispersion was added at the edge of this PDMS. Capillary action sucked the colloidal microparticles subsequently into the grooves and several layers of silica (100) colloidal single crystals were formed in the channels. This technique is also called micromolding in capillaries (MIMIC). It was initially developed by the Whitesides group for fabrication of polymeric microstructures[114] and was later applied to colloidal microparticle ordering.[115] Subsequently, square-pyramid shaped etch pits were also fabricated

into a Si (100) wafer which were also successfully filled with colloidal particles forming different packing geometries. In subsequent papers, the Ozin group demonstrated ordering of colloidal crystals by the evaporation technique in patterned Si wafers exhibiting rectangular topology.[116,117] It was also shown that the combination of MIMIC[112] with additional colloidal self-assembly by solvent evaporation using vertically placed substrates allows one to fabricate periodic colloidal crystals with modulated lattice dimensions. In these experiments colloid particles of different sizes were used. This work, using rectangular patterned substrates was later extended by different research groups.[118,119,120]

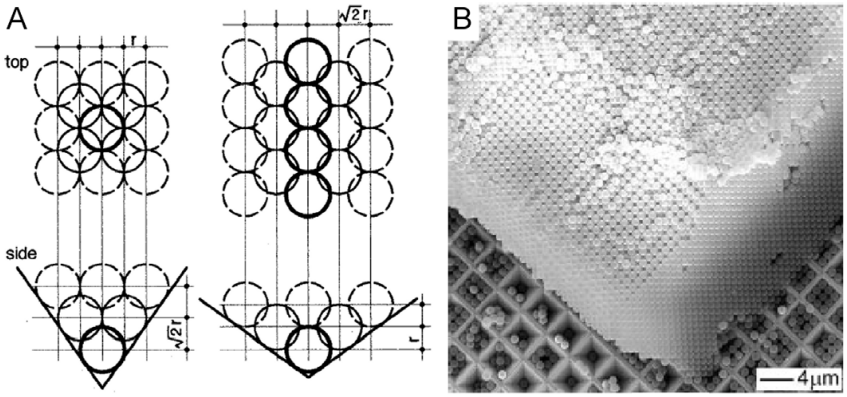

Figure 1.10. A) Scheme of ordering of microspheres in V-shaped grooves made by anisotropic etching of Si (100) and (110) wafer, respectively; B) an example of FCC (100) crystal obtained from a template exhibiting a "negative" pyramide-shape.

Yodh *et al.*[121] showed later the use of square-2D grating templates with a square pattern to drive the growth of 3D-FCC colloidal crystals by convective assembly, where colloidal crystals are formed through the evaporation of the suspension solvent. The (100) planes of the FCC crystals obtained maintained their parallel orientation with respect to the substrate for ca. 50 layers.

A nice continuation of the use of topologically patterned substrates to fabricate large colloidal crystals was done by Xia *et al.*[122,123] These authors etched 2D regular arrays of pyramidal tips into Si wafers in an attempt to grow structures which should be different from the FCC lattices usually grown with their (111) facets oriented parallel to the substrates. Polystyrene beads with different diameters were crystallized into the pits with (100) planes oriented parallel to the substrates, Figure 1.10. The polymer particles were allowed to crystallize into the pits forming long-range ordered lattices over several days. Matsuo *et al.*[124] also demonstrated that the shape of the pyramidal tips and opening angles can be controlled

via silicon wafers possessing (100) and (110) crystallographic orientations, resulting in the formation of colloidal crystals of FCC (100) and (110) lattices, respectively.

Xia *et al.*,[125,126,127] extending the work of the Ozin group, also demonstrated the influence of different surface patterns on colloidal aggregation. Producing patterns of different shapes like triangle, lines or simply round and varied sizes in photoresist, Xia and coworkers could achieve the ordering of colloidal particles into various structures that basically would be impossible to obtain on the bare surface, Figure 1.11.

Colloidal crystals have been considered as an analogue for molecular/atomic crystallization in fundamental physical studies. One could consider – using this analogy – to design and construct colloidal crystal lattices, which mimic inorganic ionic crystals. For example, the zinc blende structure, found for inorganic ZnS crystals, is in packing very similar to the diamond structure, which exhibits a full photonic band gap. However, this structure is stabilized by Coulomb interactions rather than by the covalent bond structure present in diamond. This zinc blende structure could be mimicked, in principle, by using a bimodal distribution of colloidal particles having a given surface charge, which would stabilize colloidal particle packing. Positively and negatively charged colloidal particles with appropriate surface charge densities and particle diameter could then be packed e.g. using layer-by-layer approaches to form useful colloidal crystals. Thus for the formation of these crystals templating as well as layer-by-layer packing are of interest.

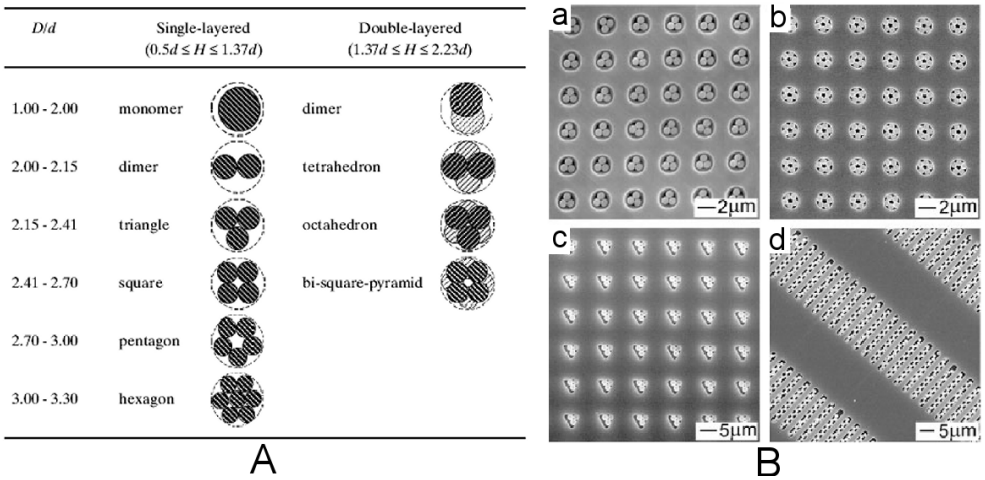

Figure 1.11. 2D Colloidal clusters formed by self-assembly on the patterned surface of different shapes A) schematic drawing of the packing forms as a function of the ratio of colloidal diameter vs. pit diameter; and B) SEM images of colloidal self-assembly in a), b) holes, c) triangles, and d) lines.

Binary colloidal crystals exhibiting building blocks of different sizes were fabricated using a layer-by-layer growth process described by van Blaaderen *et al*.[128] The authors used a layer of hexagonally close-packed colloidal particles previously fabricated on a flat substrate. Crystals with two layers consisting of either silica, or PS colloidal particles were subsequently deposited. The templating colloidal layer acted as a periodically corrugated potential for subsequent growth. Deposition was performed from suspension, using a drying front driven ordering in the successive steps. The authors discussed packing of bilayers (AB, AB_2, AB_3) and claimed to have grown a four-layer crystal of the type AB_2. This approach shows how the possibility to "mimic" inorganic AB_x type crystals can be realized by controlling the size ratio (hard core potential) of the particles.

As layer-by-layer growth fabrication is a time consuming approach, Möhwald *et al*.[129] used a stepwise spin coating strategy and fabricated AB_2 and AB_3 binary colloidal crystals from suspension. The diameter ratio between the two constituents was shown to influence the packing symmetry. Essential for this type of growth (epitaxy on a pre-fabricated colloidal layer or on a periodically corrugated potential) is a tight fit of the particles into the interstitial sites of the templating substrate. Also this statement underlines the long-recognized importance of the existing colloidal crystal layer for the growth of the subsequent overlayer. Thus, if strategies could be devised to grow colloidal monolayers with well-defined symmetry and packing, entire crystals could be built on this as a templating layer (a "sort" of graphoepitaxy, or growth on a corrugated surface potential).

As earlier mentioned, packing of colloidal particles in a diamond structure would be very useful for fabricating full-gap photonic crystals. Attempts to obtain such structures have been described using a one-by-one direct packing approach of colloidal particles in a serial fashion. The idea is based on stacking of two different types of colloidal particles, for example, inorganic and organic in a mixed bcc structure where one type of colloidal particles is removed, leaving a diamond structure of another type of colloidal particles.[130,131] This structure was realized by a nanorobot that places colloidal particles of different kind in certain positions. The result of fabricating a diamond structure out of colloidal particles that do not have a covalent bonding as in diamond itself is very spectacular, but the process itself is time consuming (it takes 7 minutes for a colloidal microsphere to be placed in the correct position). The quest for colloidal crystal engineering continues to devise fast, robust and economical approaches for the fabrication of colloidal crystals under full structural control.

References

[1] E. Matijevic, *Chem. Mater.* **1993**, *5*, 412.
[2] E. Matijevic, *Langmuir* **1994**, *10*, 8.
[3] W. Stöber, A. Fink, E. Bohn, *J. Coll. Int. Sci.* **1968**, *26*, 62.
[4] R. K. Iler, *The Chemistry of Silica*, Wiley, NY, **1979**.
[5] R. M. Fitch, *Polymer Colloids: A Comprehensive Introduction*, Academic Press, San Diego, **1997**.
[6] *Emulsion Polymerization and Emulsion Polymers,* ed. P. A. Lowell, M. S. El-Aasser, Wiley, Chichester, **1997**.
[7] S. Gu, H. Akama, D. Nagao, Y. Kobayashi, M. Konno, *Langmuir* **2004**, *20*, 7948.
[8] J. Hearn, M. C. Wilkinson, A. R. Goodall, *Adv. Coll. Int. Sci.* **1981**, *14*, 173.
[9] H. Kawaguchi, *Prog. Polym. Sci.* **2000**, *25*, 1171.
[10] R. Arshady, *Coll. Polym. Sci.* **1992**, *270*, 717.
[11] J. W. Goodwin, J. Hearn, C. C. Ho, R. H. Ottewill, *Coll. Polym. Sci.* **1974**, *252*, 464.
[12] J. H. Kim, M. Chainey, M. S. El-Aasser, J. W. Vanderhoff, *J. Appl. Polym. Sci. Part A* **1989**, *27*, 3187.
[13] S.-E. Shim, Y.-J. Cha, J.-M. Byun, S. Choe, *J. Appl. Polym. Sci.* **1999**, *71*, 2259.
[14] C. E. Reese, C. D. Guerrero, J. M. Weissman, K. Lee, S. A. Asher, *J. Coll. Int. Sci.* **2000**, *232*, 76.
[15] J. W. Goodwin, R. H. Ottewill, R. Pelton, *Coll. Polym. Sci.* **1979**, *257*, 61.
[16] W. T. Ford, H. Yu, J.-J. Lee, H. El-Hamshary, *Langmuir* **1993**, *9*, 1698.
[17] Y. Deng, Z. Yan, N. Yang, *Coll. Polym. Sci.* **1999**, *277*, 277.
[18] K.-H. van Streun, W. J. Belt, P. Piet, A. L. German, *Eur. Polym. J.* **1991**, *27*, 931.
[19] L. Antl, J. W. Goodwin, R. D. Hill, R. H. Ottewill, S. M. Owens, S. Papworth, J. A. Waters, *Coll. Surf.* **1986**, *17*, 67.
[20] S. M. Underwood, J. R. Taylor, W. van Megen, *Langmuir* **1994**, *10*, 3550.
[21] G. Bosma, C. Pathmamanoharan, E. H. A. de Hoog, W. K. Kegel, A. van Blaaderen, H. N. W. Lekkerkerker, *J. Coll. Int. Sci.* **2002**, *245*, 292.
[22] A. van Blaaderen, P. Wiltzius, *Science*, **1995**, *270*, 1177.
[23] F. Caruso, *Adv. Mater.* **2001**, *13*, 11.
[24] L. M. Liz-Marzán, P. Mulvaney, *J. Phys. Chem. B* **2003,** *107,* 7312.
[25] A. Oláh, M. A. Hempenius, G. J. Vancso, *Eur. Polym. J.* **2004**, *40*, 763.
[26] L. M. Liz-Marzan, M. Giersig, P. Mulvaney, *Langmuir* **1996**, *12*, 4329.
[27] V. N. Manoharan, M. T. Elsesser, D. J. Pine, *Science* **2003**, *301*, 483.
[28] T. van Dillen, A. van Blaaderen, A. Polman, *Materials Today* **2004**, *7*, 40.
[29] M. Nagy, A. Keller, *Polym. Commun.* **1989**, *30*, 130.
[30] Y. Lu, Y. Yin, Y. Xia, *Adv. Mater.* **2001**, *13*, 271.
[31] P. N. Pusey, W. van Megen, *Nature* **1986**, *320*, 340.
[32] Z. Cheng, W. B. Russel, P. M. Chaikin, *Nature* **1999**, *401*, 893.
[33] P. Bartlett, R. H. Ottewill, P. N. Pusey, *Phys. Rev. Lett.* **1992**, *68*, 3801.
[34] E. B. Sirota, H. D. Ou-Yang, S. K. Sinha, P. M. Chaikin, J. D. Axe, Y. Fujii, *Phys. Rev. Lett.* **1989**, *62*, 1524.
[35] A. P. Gast, W. B. Russel, *Physics Today*, **1998**, *51*, 24.
[36] Review: M. Dijkstra, *Curr. Opin. Coll. Int. Sci.* **2001**, *6*, 372.
[37] M. O. Robbins, K. Kremer, G. S. Grest, *J. Chem. Phys.* **1988**, *88*, 3286.
[38] E. J. Meijer, F. E. Azhar, *J. Chem. Phys.* **1997**, *106*, 4678.
[39] Y. Monovoukas, A. P. Gast, *J. Coll. Int. Sci.* **1989**, *128*, 533.
[40] M. E. Leunissen, C. G. Christova, A.-P. Hynninen, C. P. Royall, A. I. Campbell, A. Imhof, M. Dijkstra, R. van Roij, A. van Blaaderen, *Nature* **2005**, *437*, 235.
[41] W. L. Vos, M. Megems, C. M. van Kats, P. Bösecke, *J. Phys.: Condens. Matter* **1996**, *8*, 9503.
[42] R. Mayoral, J. Requena, J. S. Moya, C. Lopez, A. Cintas, H. Miguez, F. Meseguer, L. Vazquez, M. Holgado, A. Blanco, *Adv. Mater.* **1997**, *9*, 257.
[43] H. Miguez, F. Meseguer, C. Lopez, A. Mifsud, J. S. Moya, L. Vazquez, *Langmuir* **1997**, *13*, 6009.
[44] M. A. Bevan, J. A. Lewis, P. V. Braun, P. Wiltzius, *Langmuir* **2004**, *20*, 7045.
[45] A. Yethiraj, A. van Blaaderen, *Nature* **2003**, *421*, 513.
[46] M. Holgado, F. Garcia-Santamaria, A. Blanco, M. Ibisate, A. Cintas, H. Miguiz, C. J. Serna, C. Molpeceres, J. Requena, A. Mifsud, F. Meseguer, C. Lopez, *Langmuir* **1999**, *15*, 4701.
[47] S.-R. Yeh, M. Seul, B. I. Shraiman, *Nature* **1997**, *386*, 57.
[48] M. Trau, D. A. Saville, I. A. Aksay, *Langmuir* **1997**, *13*, 6375.
[49] K.-Q. Zhang, X. Y. Liu, *Nature* **2004**, *429*, 739.
[50] M. Golosovsky, Y. Saado, D. Davidov, *Appl. Phys. Lett.* **1999**, *75*, 4168.
[51] L. E. Helseth, H. Z. Wen, R. W. Hansen, T. H. Johansen, P. Heining, T. M. Fischer, *Langmuir* **2004**, *20*, 7323.
[52] W. L. Vos, M. Megens, C. M. van Kats, P. Bösecke, *Langmuir* **1997**, *13*, 6004.

[53] M. Megens, C. M. van Kats, P. Bösecke, W. L. Vos, *Langmuir* **1997**, *13*, 6120.
[54] L. V. Woodcock, *Nature* **1997**, *385*, 141.
[55] O. D. Velev, A. M. Lenhoff, *Curr. Opin. Coll. Int. Sci.* **2000**, *5*, 56.
[56] P. N. Pusey, W. van Wegen, P. Barlett, B. J. Ackerson, J. G. Rarity, S. M. Underwood, *Phys. Rev. Lett.* **1989**, *63*, 2753.
[57] M. Sasaki, K. Hane, *J. Appl. Phys.* **1996**, *80*, 5427.
[58] S.-H. Park, B. Gates, Y. Xia, *Adv. Mater.* **1999**, *11*, 462.
[59] R. M. Amos, J. G. Rarity, P. R. Tapster, T. J. Shepherd, S. C. Kitson, *Phys. Rev. E* **2000**, *61*, 2929.
[60] O. Vickreva, O. Kalinina, E. Kumacheva, *Adv. Mater.* **2000**, *12*, 110.
[61] A. S. Dimitrov, K. Nagayama, *Langmuir* **1996**, *12*, 1303.
[62] P. Jiang, J. F. Bertone, K. S. Hwang, V. L. Colvin, *Chem. Mater.* **1999**, *11*, 2132.
[63] P. A. Kralchevsky, N. D. Denkov, *Curr. Opin. Coll. Int. Sci.* **2001**, *6*, 383.
[64] S. H. Im, M. H. Kim, O. O. Park, *Chem. Mater.* **2003**, *15*, 1797.
[65] M. A. McLachlan, N. P. Johnson, R. M. De La Rue, D. W. McComb, *J. Mater. Chem.* **2004**, *14*, 144.
[66] V. Kitaev, G. A. Ozin, *Adv. Mater.* **2003**, *15*, 75.
[67] N. D. Denkov, O. D. Velev, P. A. Kralchevsky, I. B. Ivanov, H. Yoshimura, K. Nagayama, *Langmuir* **1992**, *8*, 3183.
[68] B. van Duffel, R. H. A. Ras, F. C. de Schryver, R. A. Schoonheydt, *J. Mater. Chem.* **2001**, *11*, 3333.
[69] S. Reculusa, S. Ravaine, *Chem. Mater.* **2003**, *15*, 598.
[70] S. H. Im, Y. T. Lim, D. J. Suh, O. O. Park, *Adv. Mater.* **2002**, *14*, 1367.
[71] P. Jiang, M. J. McFarland, *J. Am. Chem. Soc.* **2004**, *126*, 13778.
[72] J. Tien, A. Terfort, G. M. Whitesides, *Langmuir* **1997**, *13*, 5349.
[73] K. M. Chen, X. Jiang, L. C. Kimerling, P. T. Hammond, *Langmuir* **2000**, *16*, 7825.
[74] I. Lee, H. Zheng, M. F. Rubner, P. T. Hammond, *Adv. Mater.* **2002**, *14*, 572.
[75] J. Aizenberg, P. V. Braun, P. Wiltzius, *Phys. Rev. Lett.* **2000**, *84*, 2997.
[76] C.-A. Fustin, G. Glasser, H. W. Spiess, U. Jonas, *Langmuir* **2004**, *20*, 9114.
[77] Y. Masuda, T. Itoh, M. Itoh, K. Koumoto, *Langmuir* **2004**, *20*, 5588.
[78] R. C. Hayward, D. A. Saville, I. A. Aksay, *Nature* **2000**, *404*, 56.
[79] T. Gong, D. W. M. Marr, *Appl. Phys. Lett.* **2004**, *85*, 3760.
[80] S. A. Johnson, P. J. Ollivier, T. E. Mallouk, *Science* **1999**, *283*, 963.
[81] B. Gates, Y. Yin, Y. Xia, *Chem. Mater.* **1999**, *11*, 2827.
[82] J. F. Bertone, P. Jiang, K. S. Hwang, D. M. Mittleman, V. L. Colvin, *Phys. Rev. Lett.* **1999**, *83*, 300.
[83] *Handbook of Microlithography, Micromachining, and Microfabrication*, ed. P. Rai-Choudhury, vol. 1, Microlithography, SPIE Press, Washington, **1997**.
[84] Laser interference lithography: S. Kuipers, H. A. G. M. Wolferen, C. van Rijn, W. Nijdam, G. Krijnen, M. Elwenspoek, *J. Micromech. Microeng.* **2001**, *11*, 33.
[85] Laser interference lithography: C. J. M. van Rijn, G. J. Veldhuis, S. Kuipers, *Nanotechnology* **1998**, *9*, 343.
[86] Holographic method: V. Berger, O. Gauthier-Lafayer, E. Costard, *Elect. Lett.* **1997**, *33*, 425.
[87] A. Ulman, *Chem. Rev.* **1996**, *96*, 1533.
[88] E. Delamarche, H. Schmid, A. Bietsch, N. B. Larsen, H. Rothuizen, B. Michel, H. Biebuyck, *J. Phys. Chem. B* **1998**, *102*, 3324.
[89] Y. Xia, G. M. Whitesides, *Angew. Chem. Int. Ed.* **1998**, *37*, 550.
[90] P. Bertrand, A. Jonas, A. Laschewsky, R. Legras, *Macromol. Rapid Commun.* **2000**, *21*, 319.
[91] *Alternative Lithography: Unleashing the Potentials of Nanotechnology*, ed. C. M. Sotomayor Torres, Kluwer Academic, NY, **2003**.
[92] J. Israelachvili, *Intermolecular and Surface Forces,* Academic, London, **1992**.
[93] C. W. Frank, V. Rao, M. M. Despotopoulou, R. F. W. Pease, W. D. Hinsberg, R. D. Miller, J. F. Rabolt, *Science* **1996**, *273*, 912.
[94] G. Reiter, J.-U. Sommer, *Phys. Rev. Lett.* **1998**, *80*, 3771.
[95] G. Reiter, *J. Polym. Sci. Part B* **2003**, *41*, 1869.
[96] H. I. Smith, M. W. Geis, C. V. Thompson, H. A. Atwater, *J. Cryst. Growth* **1983**, *63*, 527.
[97] J. Y. Cheng, C. A. Ross, E. L. Thomas, H. I. Smith, G. J. Vancso, *Appl. Phys. Lett.* **2002**, *81*, 3657.
[98] A. van Blaaderen, P. Wiltzius, *Adv. Mater.* **1997**, *9*, 833.
[99] M. J. Madou, *Fundamentals of Microfabrication: The Science of Miniaturization*, CRC Press, 2nd ed., **2002**.
[100] M. Sugawara, *Plasma Etching: Fundamentals and Applications*, Oxford University Press Inc., NY, **1998**.
[101] T. Palberg, W. Mönch, J. Schwarz, P. Leiderer, *J. Chem. Phys.* **1995**, *102*, 5082.
[102] P. V. Braun, R. W. Zehner, C. A. White, M. K. Weldon, C. Kloc, S. S. Patel, P. Wiltzius, *Adv. Mater.* **2001**, *13*, 721.
[103] S. H. Park, D. Qin, Y. Xia, *Adv. Mater.* **1998**, *10*, 1028.

[104] E. Kumacheva, P. Garstecki, H. Wu, G.M. Whitesides, *Phys. Rev. Lett.* **2003**, *91*, 128301.
[105] E. Kumacheva, R. K. Golding, M. Allard, E. H. Sargent, *Adv. Mater.* **2002**, *14*, 221.
[106] R. G. Golding, P. C. Lewis, E. Kumacheva, *Langmuir* **2004**, *20*, 1414.
[107] K.-H. Lin, J. C. Crocker, V. Prasad, A. Schofield, D. A. Weitz, T. C. Lubensky, A. G. Yodh, *Phys. Rev. Lett.* **2000**, *85*, 1770.
[108] Y.-H. Ye, S. Badilescu, Vo-Van Truong, P. Rochon, A. Natansohn, *Appl. Phys. Lett.* **2001**, *79*, 872.
[109] D. K. Yi, E.-M. Seo, D.-Y. Kim, *Appl. Phys. Lett.* **2002**, *80*, 225.
[110] M. Allard, E. H. Sargent, P. C. Lewis, E. Kumacheva, *Adv. Mater.* **2004**, *16*, 1360.
[111] J. P. Hoogenboom, C. Rétif, E. de Bres, M. van de Boer, A. K. van Langen-Suurling, J. Romijn, A. van Blaaderen, *Nano Letters* **2004**, *4*, 205.
[112] S. M. Yang, G. A. Ozin, *Chem. Commun.* **2000**, 2507.
[113] G. A. Ozin, S. M. Yang, *Adv. Funct. Mater.* **2001**, *11*, 95.
[114] E. Kim, Y. Xia, G. M. Whitesides, *Nature* **1995**, *376*, 581.
[115] E. Kim, Y. Xia, G. M. Whitesides, *Adv. Mater.* **1996**, *8*, 245.
[116] S. M. Yang, H. Miguez, G. A. Ozin, *Adv. Funct. Mater.* **2002**, *12*, 425.
[117] H. Miguez, S. M. Yang, N. Tetreault, G. A. Ozin, *Adv. Mater.* **2002**, *14*, 1805.
[118] P. Ferrand, M. Egen, B. Griesebock, J. Ahopelto, M. Müller, R. Zentel, S. G. Romanov, C. M. Sotomayor Torres, *Appl. Phys. Lett.* **2002**, *81*, 2689.
[119] P. Ferrand, M. J. Minty, M. Egen, J. Ahopelto, R. Zentel, S. G. Romanov, C. M. Sotomayor Torres, *Nanotechnology* **2003**, *14*, 323.
[120] R. E. Schaak, R. E. Cable, B. M. Leonard, B. C. Norris, *Langmuir* **2004**, *20*, 7293.
[121] J. Zhang, A. Alsayed, K. H. Lin, S. Sanyal, F. Zhang, W.-J. Pao, V. S. K. Balagurusamy, P. A. Heiney, A. G. Yodh, *Appl. Phys. Lett.* **2002**, *81*, 3176.
[122] Y. Yin, Y. Xia, *Adv. Mater.* **2002**, *14*, 605.
[123] Y. Yin, Z.-Y. Li, Y. Xia, *Langmuir* **2003**, *19*, 622.
[124] S. Matsuo, T. Fujine, K. Fukuda, S. Juodkazis, H. Misawa, *Appl. Phys. Lett.* **2003**, *82*, 4283.
[125] Y. Yin, Y. Xia, *Adv. Mater.* **2001**, *13*, 267.
[126] Y. Yin, Y. Lu, B. Gates, Y. Xia, *J. Am. Chem. Soc.* **2001**, *123*, 8718.
[127] Y. Xia, Y. Yin, Y. Lu, J. McLellan, *Adv. Funct. Mater.* **2003**, *13*, 907.
[128] K. P. Velikov, C. G. Christova, R. P. A. Dullens, A. van Blaaderen, *Science* **2002**, *296*, 106.
[129] D. Wang, H. Möhwald, *Adv. Mater.* **2004**, *16*, 244.
[130] F. Garcia-Santamaria, C. Lopez, F. Meseguer, F. Lopez-Tejeira, J. Sanchez-Dehesa, H. T. Miyazaki, *Appl. Phys. Lett.* **2001**, *79*, 2309.
[131] F. Garcia-Santamaria, H. T. Miyazaki, A. Urquia, M. Ibisate, M. Belmonte, M. Shinya, F. Meseguer, C. Lopez, *Adv. Mater.* **2002**, *14*, 1144.

Chapter 2

Computer Simulations of Colloidal Crystal Packing[*]

Crystallization of oppositely charged colloidal particles was studied by simulations using "Molecular Dynamics" computations. The stability of colloidal crystals with various crystal structures was calculated. It was found that stable colloidal crystal structures can resemble those found among the inorganic materials. A range of sphere size ratios was determined for stable colloidal structures. Colloidal crystals with a zinc blende inorganic analog were found to be stable at a size ratio of 0.2, with a sodium chloride analog – at a size ratio 0.4 and with a cesium chloride analog – at size ratios higher than 0.6. There were no sharp transition boundaries found between these crystal structures. The presence of a surface charge was necessary to keep the structure together, but the magnitude of this charge was not important for obtained stable structures, although high surface charges speed up the breakdown of unstable crystal structures. We also found that charge stabilized colloidal crystals with the zinc blende structure were stable, while the same structure built out of hard spheres was not.

[*] This chapter is based on a Diploma Thesis by E. Leenders and was carried out in the group of Prof. W. J. Briels "Computational Biophysics" and co-supervised by W. K. den Otter and N. V. Dziomkina.

Introduction

Photonic crystals with a diamond structure possess a photonic band gap in the first Brillouin zone.[1] The corresponding diamond structure has a low packing density of 0.34. Until now, all attempts to fabricate this structure by self-assembly of colloidal particles have been unsuccessful. In nature, the diamond structure was found in carbon and silicium where atoms are held together by covalent bonding and, therefore, the reproduction of this structure by self-assembly of colloidal particles is rather difficult. In order to fabricate colloidal crystals with a diamond structure, one can think of mimicking the packing of ionic crystal lattices based on scaling up the ions with the corresponding ionic radii and charges to colloidal dimensions. For example, the zinc blende type packing has a diamond lattice structure but consists of oppositely charged ions (Zn^{2+} and S^{2-}) of different sizes. Each ion type occupies one of the FCC sites (in other words, each ion is surrounded by four ions of the other type at the tetrahedral positions) that are shifted relatively to each other by (¼,¼,¼) of the lattice constant. The zinc blende structure found in inorganic materials is only partially ionic, which does not give a direct encouragement to mimic colloidal crystal assembly of oppositely charged colloidal particles. Therefore, in order to obtain this structure experimentally using oppositely charged colloidal particles, preliminary calculations of the stability of such colloidal zinc blende structures have to be done.

The crystallization process of colloidal particles has been studied extensively experimentally[2,3,4,5,6] as well as theoretically.[7,8,9,10] As a result, most of the theoretically (simulated) colloidal crystal structures have been confirmed experimentally.[4,6]

Various computational methods are used to simulate colloidal crystallization processes. The greater part of the simulation studies applies the Monte Carlo (MC) method for studying equilibrium phases. The phase diagram of the colloidal particles is calculated, where equilibrium phases and colloidal structures are present at a specific composition and temperature/pressure. In the Monte Carlo simulations, colloidal particles are represented by hard spheres, where the potential energy is set to infinity whenever two particles are too close. Crystallization of hard spheres is not driven by the potential energy that is zero by definition, but occurs due to entropic reasons: the empty volume around each particle may be larger and therefore, the translational entropy of the particle compensates for the loss of entropy of being placed in a lattice. Trizac *et al.*[11] translate this into the 'rule of thumb' that a hard sphere binary crystal is only stable when its density is higher than that of either of the two pure solids. Stable AB_2 structures for colloidal radii ratios of $0.48 < R_A/R_B < 0.62$ and a rocksalt

structure for R_A/R_B = 0.41 were found. The AB_{13} superlattice was found by Eldridge *et al.*[12] using the same method, but with different radii ratios.

Charge stabilized colloidal particles reveal several stable phases such as face-centred cubic (FCC), body-centred cubic (BCC) and liquid phases. Kremer *et al.*[13] and El Azhar *et al.*[14] studied the crystallization of colloids as a function of temperature and screening length, where a repulsive Yukawa potential combined with hard sphere repulsion were used to compare different structures on the basis of their free energy difference. A transition was seen between the FCC structure at low temperatures and the BCC structure at higher temperatures. The same transition has often been observed in metals.[15] Louis *et al.*,[16] studying colloidal interactions of binary particles by MD computer simulations showed that repulsion between large and small colloidal particles enhances attraction between the large spheres due to a depletion effect.

Accounts of simulations on oppositely charged colloids in the literature are scarce. Wu *et al.*[17] performed Monte Carlo simulations studying the pair interaction between two spheres with opposite charges in a solution of a symmetric monovalent salt, using the hypernetted chain closure (HNC). The direct interaction was studied through hard-sphere repulsion and Coulomb forces (without screening). They found a slight difference in interaction between oppositely and equally charged colloids (apart from the sign). In both cases, the results could be fitted very well with a Yukawa potential, although with different values for the fitting parameters. This also seems to agree with Löwen's conclusions.[18] However, two aspects should be mentioned:

- HNC theory is more suitable for Lennard-Jones than for hard-core particles, where in the latter case, the Percus-Yevick closure is more common.
- Wu's particles were much smaller than those in colloidal crystals. Their diameter was only 2 nm (which is more on the order of the surrounding ions than on the order of colloidal particles size).

Therefore, in order to estimate the crystal structure built by oppositely charged colloidal particles, computer simulations should be performed to make predictions for parameters of the systems helping experimental research.

In this chapter, MD computer simulations are presented of colloidal crystals formed by oppositely charged colloidal particles. The stability of colloidal crystal structures for binary colloidal radii ratios between 0.2 and 1 is examined. In addition, theoretical background on colloidal particle interactions is presented.

2.1. Interparticle interactions

2.1.1. *Coulomb potential*

Charges q_1 and q_2 interact through Coulomb forces:

$$U(r_{12}) = \frac{-q_1 q_2}{4\pi\varepsilon\varepsilon_0 r_{12}} \tag{2.1}$$

where ε and ε_0 are the relative permittivities or dielectric constants of the medium and vacuum, respectively, and r_{12} is the distance between the two charges. Long range potentials like the Coulomb potential cause extra problems in simulations.

2.1.2 *Lennard-Jones potential*

Van der Waals forces are attractive forces between two atoms, due to dipole-dipole interactions (both induced and permanent dipoles). In atomic simulations, Van der Waals forces are often formalised using the Lennard-Jones potential (2.2). Here, the potential between atom *i* and atom *j* is:

$$U(r_{ij}) = 4\varepsilon\left[\left(\frac{\sigma}{r_{ij}}\right)^{12} - \left(\frac{\sigma}{r_{ij}}\right)^{6}\right] \tag{2.2}$$

where ε is the lowest value of U and σ the distance where $U = 0$, Figure 2.1. The 6th-power term can be deduced from dipole-dipole interactions[19] and is always attractive. The 12th-power term is a repulsive part that is caused mainly by the Pauli principle. This part is not very well defined. The inverse 12th-power dependence with the distance is chosen basically for mathematical convenience, but the value of the power could lie between 9 and 15. Exponential functions are used, as well.

Interactions between spherical non-charged atoms like argon can be described very well using the Lennard-Jones potential. Crystallisation processes of argon have been extensively studied, using this potential.[20]

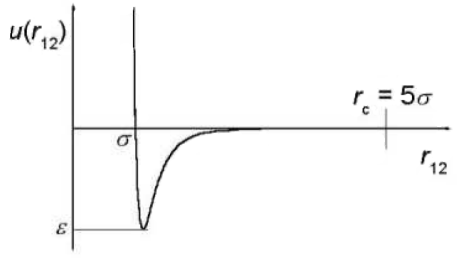

Figure 2.1. Lennard-Jones potential with cut-off distance r_c.

2.1.3 Yukawa potential

In the case of charged colloids, large spheres with a surface charge (the colloids) are surrounded by much smaller counter- and co-ions (the dissolved salt). The distribution of the ions can be described using the electric double layer theory, Figure 2.2.[21] An electric double layer consists of two regions: an inner region with adsorbed counter-ions near the colloidal surface (Stern layer) and a diffuse region with ions distributed according to the influence of electrical forces and random thermal motion. Of course, the whole system must be charge neutral. The electric potential (Yukawa or screened Coulomb potential) around one colloid is given as:[22]

$$\psi(r) = \frac{q}{4\pi\varepsilon(1+\kappa R)r}\exp(-\kappa(r-R)) \tag{2.3}$$

$$\kappa = \left(\frac{2F^2cz^2}{\varepsilon RT}\right)^{1/2} \tag{2.4}$$

$$q = 4\pi\varepsilon R(1+\kappa R)\psi_0 \tag{2.5}$$

where R is the colloid's radius, r is the radial distance from the center of the particle, κ is the inverse Debije-Hückel screening length and q is a total charge in the surroundings of the colloid.

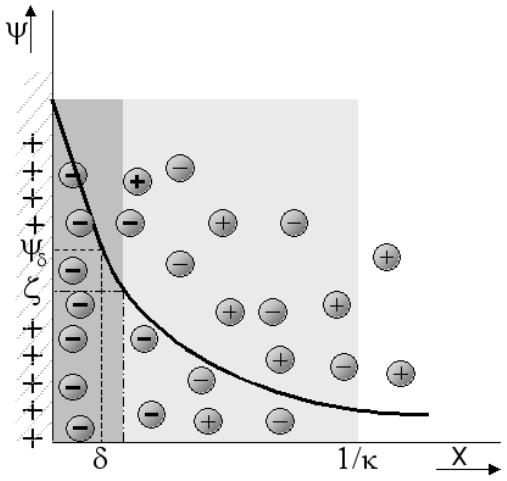

Figure 2.2. Schematic representation of a double electrical layer structure. The first layer is formed by counter ions attracted to the surface by electrostatic and adsorption forces. In this layer with a thickness of δ, a sharp drop of the potential occurs (adsorption or Stern layer). Other counter ions, that compensate the potential determined ions, spread over a certain distance by thermal motion, form the second (or diffusion) layer. In the diffusion layer, the potential decreases nonlinearly, due to a decrease in counter ion concentration towards the bulk of the solution. κ^{-1} is the double layer thickness. ζ is the electrokinetic potential (or ζ - potential) that determines the movement of liquid phase around a particle under an applied electric field. ζ is also an indicator for colloid stability.

In order to obtain the actual interaction with another colloidal particle (below with index 2), (2.3) must be multiplied with the charge of this other colloid. The result is

$$U(r) = \frac{q_1 q_2}{4\pi\varepsilon(1+\kappa R_1)r}\exp(-\kappa(r-R_1)) \tag{2.6}$$

In the case of particles with different radii R_1 and R_2, the force ($F = -\partial U/\partial r$) exerted on sphere 1 by sphere 2 would then differ from the force by sphere 1 on sphere 2, because different sphere radii must be filled in. To solve this problem, one could take the average of both radii instead of just one radius. In this way, the expression becomes symmetric. This results in

$$U(r) = \frac{q_1 q_2}{4\pi\varepsilon(1+1/2\kappa(R_1+R_2))r}\exp(-\kappa(r-1/2(R_1+R_2))) \tag{2.7}$$

Note that this theory is a slight deviation from the well-known DLVO theory (section 2.1.4). The theory gives information about the potential field between two charged colloids. For two equally charged and sized colloids this can give a fairly accurate analytical result. In more difficult cases, no sufficiently simple analytical solutions are available. For this reason, (2.7) was chosen in simulations of binary colloidal crystallizations.

2.1.4 DLVO theory[†]

DLVO theory states that when two particles approach each other as a result of their thermal motion, the colloidal stability is a combination of attractive (Van der Waals) and repulsive (Yukawa/Coulomb) forces. The combination of both the double layer repulsions (U_R) and the van der Waals attractions (U_A), which act over about the same distances, leads to a rather complex set of potential energy curves, Figure 5.8. When these two potentials are added, the result is a potential as shown in (2.8) and depicted in Figure 2.3.

$$U_T = U_R + U_A \tag{2.8}$$

There are two minima: (a) the primary minimum, which results from the combination of the van der Waals attraction (very strong at short distances) and the Born repulsion (where two particles come into "contact"), and (b) a secondary minimum, which is usually quite shallow (often just a fraction of kT). The primary minimum is generally so deep that the energy barrier

[†] The theory of colloidal stability was formulated independently by two groups, Derjaguin and Landau in the USSR and Verweij and Overbeek in The Netherlands and is known as "DLVO theory".

for the reverse process of bringing two particles out of it is considered to be infinite. There are exceptions, however, in which coagulation can be reversed, but these are rare.

The total free energy of interaction of two colloidal particles can be expressed as:[23]

$$U_T = \frac{\varepsilon R \psi_0^2}{2} \ln(1 + \exp(-\kappa H_0)) - \frac{AR}{12 H_0} \tag{2.9}$$

where H_0 is a minimum distance of separation of the spheres and A is the "Hamaker constant", that is characteristic of the material of the particles.

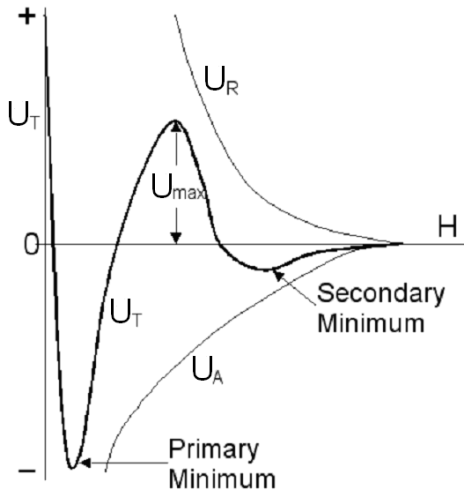

Figure 2.3. Schematic representation of the total free energy U_T of two particles as a function of the interparticle distance H. U_R and U_A are repulsion (caused by electrostatic repulsion of double layers of colloidal particles) and attraction (caused by intermolecular van der Waals attraction between particles) free energies. U_{max} is an energetic barrier, associated with the electrostatic repulsion of the ionic layer around the particles. The height of this barrier is dependent on the ionic strength of the suspension (an increase in ionic strength leads to a pronounced diminution of the barrier, allowing coagulation to occur) and of the surface potential (a higher surface charge density increases the barrier height). The primary minimum is generally so deep that the energy barrier for the reverse process of, i.e. separating the particles, is considered to be infinite (nonreversible coagulation). The second maximum is quite shallow (often just a fraction of kT) and it corresponds to a reverse coagulation.

2.2. Colloidal crystallization

Modeling of binary charged colloidal structures was performed by starting simulation with a perfect colloidal crystal possessing a certain crystal structure and determining whether this structure is still intact after prolonged computational length.[‡] In addition to the zinc blende structure (ZnS) with coordination number 4, other structures such as rocksalt or sodium chloride (NaCl) with coordination number 6 and cesium chloride (CsCl) with coordination number 8 were also investigated. The crystal structure with the lowest potential energy was chosen to be the most stable, as long as its potential energy (Appendix I) was higher than that of the corresponding liquid state.

The molecular dynamics (MD)[§] method was used to study colloidal crystallization (Appendix II). The starting simulation box was prepared by placing bimodally dispersed colloids in a lattice (Figure 2.4A), in which colloidal spheres were just in contact with nearest neighbors (Appendix III). In one cubic simulation box, 125 unit cells were placed. The potential parameters were chosen in such a way that when two neighboring particles approached each other, the repulsive part became dominant and when they were further apart, the Yukawa part dominated. This implies that the minimum of the attractive potential lies at the contact distance. The liquid starting box was prepared by first randomly placing the large particles and after that, randomly placing the smaller ones, Figure 2.4B. A minimum acceptable distance between the sphere centers was used to prevent overlap.

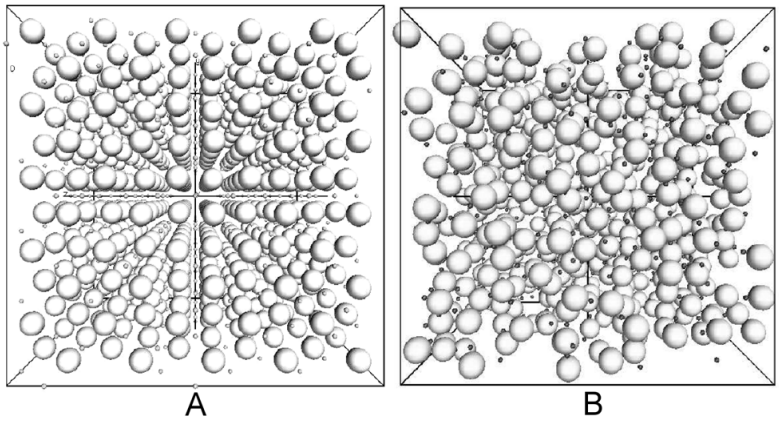

Figure 2.4. A) A *crystal starting box* with the zinc blende structure. The spheres are drawn with a diameter smaller than that used for simulations in order to enhance visibility. B) *Liquid starting box* after equilibration. The spheres are drawn in their original size. It can be seen that the small positive particles stay close to the surface of the large negative particles.

[‡] This approach was chosen after unsuccessful crystallization of colloidal particles from the liquid phase, where the motion of colloidal particles was too slow to study the crystallization process itself.

[§] DL-POLY simulation package by W. Smith and T. R. Forester from Daresbury Laboratory was used for colloidal crystallization modeling.

The sizes and charges of the colloids were chosen within the ranges that are experimentally obtainable, Table 2.1. The absolute charges on the colloids $2.0 \cdot 10^5$ e, $5.5 \cdot 10^5$ e, $1.0 \cdot 10^6$ e or $2.0 \cdot 10^6$ e were used in simulations.[**] Within the range of sizes and surface charges, a selection of simulation boxes was made. Within one crystal, the absolute charge on both types of colloids was the same. In the case of different sizes, the surface charge density was therefore different. To stay within the range of the surface charge density, not all combinations with high charges and small spheres or low charges and large spheres were possible. For example, a colloid with R = 100 nm could not have a charge of $2.0 \cdot 10^6$ e, because the surface charge would need to be too high.

Table 2.1 Range of colloidal parameters

Parameters	**Range**
R	0.1 – 1 μm
σ	1 – 70 μC/cm^2

The maximum time step (Appendix III) was determined using an NVE simulation (Appendix IV) to test how well energy was conserved, both for the solid and for the liquid case, respectively. Every simulation took at least 500,000 time steps. The density of the material of which the colloids consisted, was taken to be 1000 kg/m^3. This parameter only influences the dynamics, not the equilibrium phase. The relative dielectric constant of the solvent was 80. The Debije-Hückel length was of the same order of magnitude as the sphere radius.

NPT simulations were performed with the crystals using the parameters shown in Table 2.2. The simulation box was able to change size if necessary to obtain the correct pressure.[††] The relaxation time for the Berendsen barostat was found by trial and error. It was

Table 2.2. Input parameters for bimodal crystal simulations

Parameter	**Value**	**Description**
C	$6.2 \cdot 10^{22}$ J/mol	parameter in Yukawa potential
κ^{l}	0.017 nm^{-1}	inverse Debije-Hückel screening length
ϕ	10 %	volume fraction spheres in liquid state
Δt	100 ps	time step for simulation
t	50 μs	total time per simulation
T	293 K	temperature
p	1 bar	pressure
τ_T	2	input for Andersen thermostat (Appendix IV)
τ_p	1000 ps	relaxation time for Berendsen barostat (Appendix IV)
N	1000	number of particles in one box

[1] This value corresponds to 0.027 M of a monovalent electrolyte

[**] Absolute charge values were estimated based on the experimentally determined surface charges of synthesized polymer colloidal particles.

[††] Terms as pressure (p) and temperature (T) come from a P-T phase diagram for one- or multi- component systems. Various labeled areas such as, for example, “liquid”, “solid” or “gas” (for one-component system) over which that phase is thermodynamically stable with respect to transformation to another phase can exist.

found that some crystals were stable under NPT conditions and others were not. In the case of non-stability, this could be seen from the temperature, pressure and potential energy during the simulation and of course by determining the radial distribution function (Appendix V) of the final state. Examples of stable and unstable crystal structures are given in Figures 2.5 and 2.6. Zinc blende structures are shown with an absolute charge on all colloids of $2.0 \cdot 10^5$ e. The stable crystal is built of colloids of R = 100 nm (positive) and R = 500 nm (negative), while the unstable one consists of spheres of R = 300 and R = 500 nm, respectively.

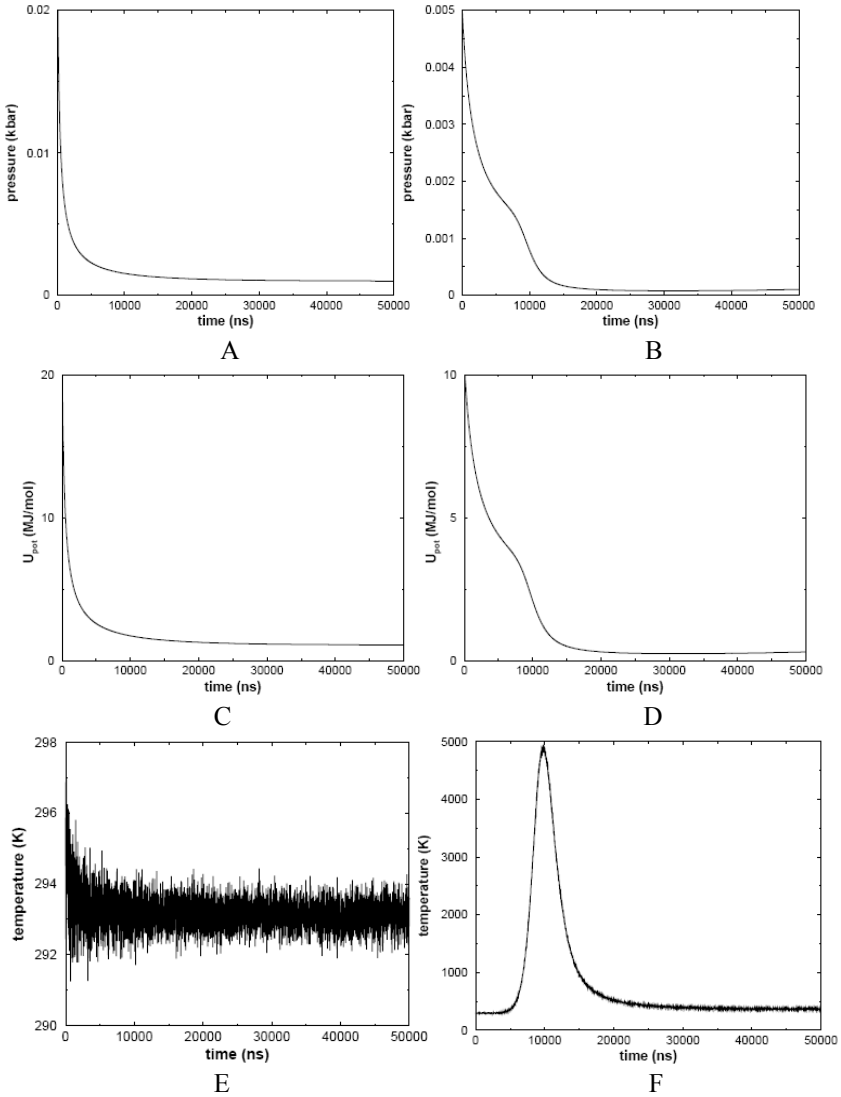

Figure 2.5. *Pressure* in simulations of A) stable and B) unstable colloidal crystals; *Potential energy* in simulations of C) stable and D) unstable colloidal crystals; and *Temperature* in simulations of E) stable and F) unstable colloidal crystals.

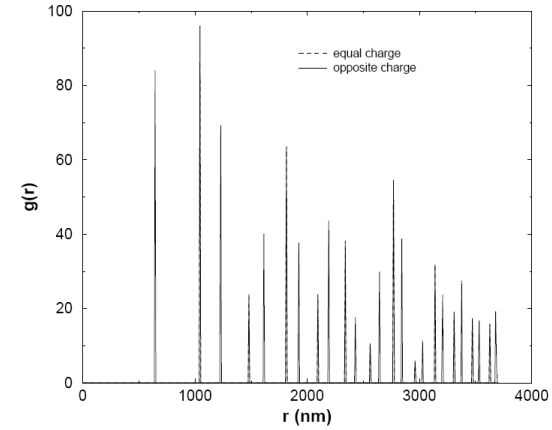

A

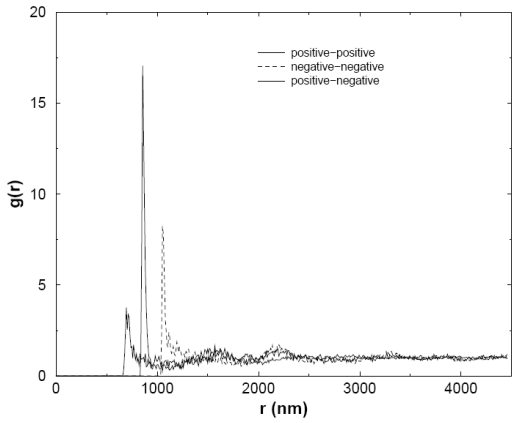

B

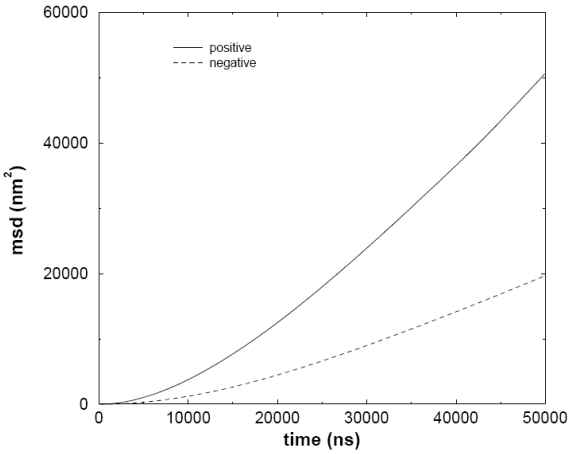

C

Figure 2.6. *Radial distribution function* of A) stable and B) unstable colloidal crystals with the zinc blende structure. An unstable colloidal crystal was formed at the end of the simulations, where it is liquid-like. C) *Mean square displacement* of a "liquid" after NPT simulation of an unstable crystal (zinc blende structure, R_1 = 300 nm, R_2 = 500 nm, $q = 5.5 \cdot 10^5\, e$). The positive particles are smaller and therefore move faster.

The transition to the liquid phase causes a pressure drop beyond the given pressure of 1 bar, Figure 2.5B. It takes a much longer simulation time (about three times as long) to get the pressure back to 1 bar again. The potential energy follows the same path as the pressure. The energy in Figure 2.5D is therefore not the equilibrium potential energy of the liquid. It will rise with the increasing pressure, but the value at 1 bar will probably be lower than the potential energy of the unstable starting configuration. When the phase transition occurs, even the rather "coarse" combinational thermostat cannot keep the temperature at 293 K. The amount of energy that is released is substantial. It takes a very long simulation time to get the temperature back at 293 K after this jump. In Figure 2.5F, the temperature at the end still is around 350 K and it is decreasing only very slowly. The change is visible as well in the radial distribution functions (Figures 2.6, A and B) and in the mean square displacement (Appendix VI), (Figure 2.6C). It is shown that even without being forced, some crystal structures convert into a liquid at standard conditions. This means that they are inherently unstable.

It was observed that at relatively low charges, unstable crystals survived for a longer time than at high charges. It looks like the size of the colloidal spheres is decisive in determining the stability of the crystal, but the charge is decisive in the metastability. In other words, if a crystal is not stable, a higher charge will accelerate the transition into a liquid, i.e. the start of the transition occurs earlier and the process of transition takes less time. This is shown in Table 2.3, were the times are based on the peak in the temperature-time plot (an example of such a temperature-time plot is given in Figure 2.5F).

Table 2.3. Moments of phase transition (in μs from the start of the simulation) as a function of the absolute charge on colloidal particles in a ZnS structure.[1]

Charge (*e*)	**Start peak (μs)[2]**	**Top peak (μs)[2]**
$2.0 \cdot 10^5$	15	75
$5.5 \cdot 10^5$	1.4	5.2
$1.0 \cdot 10^6$	0.5	2.7
$2.0 \cdot 10^6$	0.4	2.8

[1] R_1 = 200 nm and R_2 = 500 nm.
[2] During the phase transition, the temperature shows a peak. The start of this peak, as well as the time at which it was highest, are given.

The structures that were proved to be stable are listed in Table 2.4. Changing the charge on the colloids did not change the (in)stability of a given structure. As shown above, an increased charge only accelerates the breakdown of an unstable crystal. When the size ratio was 0.6, the zinc blende and rocksalt structures both turned into liquid relatively quickly.

Table 2.4. Stable colloidal crystal structures as a function of the size ratio of the two types of colloidal particles.

Size ratio	Stable structure	Coordination number
0.2	Zinc blende	4
0.4	Rocksalt	6
0.6	Cesium chloride (?)	8
0.8	Cesium chloride	8
1	Cesium chloride	8

The cesium chloride structure remained rather crystalline, but not as perfect as at higher size ratios. This is shown in Figure 2.7A. Although the radial distribution function looks more liquid-like, the "peaks" are still where they belong for a cesium chloride structure (Figure 2.7A). Furthermore, the temperature did not show a peak during the simulation. There was only a very small bump, from 293 to 294 K. In this case, a higher charge did not enhance the widening of the peaks.

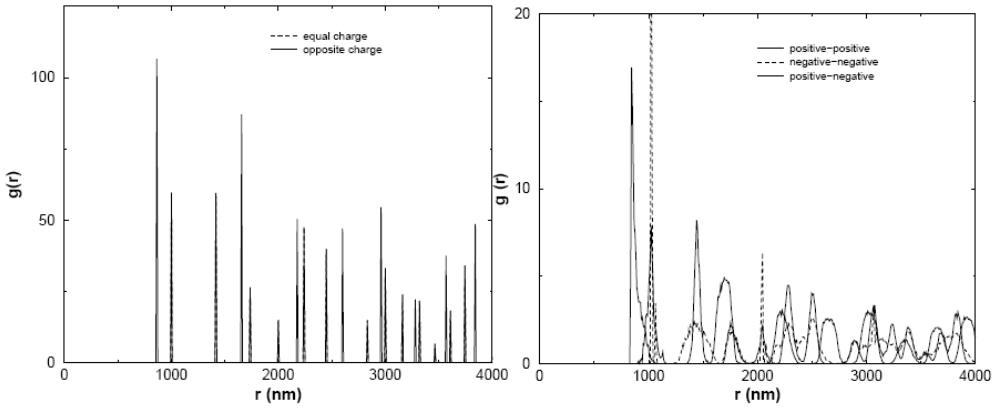

A B

Figure 2.7. A) The radial distribution function for the cesium chloride structure with R_1 = 300 and R_2 = 500 nm ($q = 5.5 \cdot 10^5\ e$) at the start and B) after 110 μs of simulations.

The same phenomenon was observed for the rocksalt structure at a size ratio of 0.2. The zinc blende structure was more stable there (sharp peaks in the *g(r)*), but the rocksalt structure appears to be stable as well. However, the radial distribution function does not nearly look as good as the one of the zinc blende structure (Figure 2.6A). Cooling to 10 K did not sharpen the peaks, which indicates that the spheres are not in their lattice positions. The peaks from the starting configuration were split in smaller peaks around the lattice position.

The results that were obtained for the stability of colloidal crystal structures, as a function of their size ratio, are largely comparable with those from inorganic chemistry.[24] No sharp transition between one crystal structure and another for various size ratios was found.

The relative potential energies of the different crystal structures and liquids give information about the crystal stability as well. When potential energies of the different phases

are compared, some indication can be found for the stability of the different structures: the one with the lowest energy is most likely to be stable. The potential energies of the different phases are given in Figure 2.8. The values were taken from the NPT simulations. However, when a crystal degraded, it was not always possible to obtain a good value of the crystal potential energy at p = 1 bar and T = 293 K. At this point, the system was not in equilibrium. It was shown that after the crystal broke down, for a long time the pressure of the liquid was lower than 1 bar and the temperature higher than 293 K. Therefore, it was not always possible to obtain a value for the potential energy of the liquid under equilibrium conditions. Thus, it must be clear that Figure 2.8 gives only an indication of the energies.

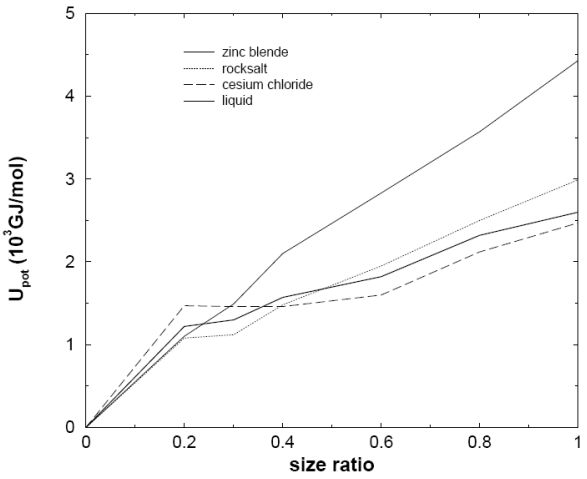

Figure 2.8. The potential energy of the different phases.

Plotting these energies gave results similar to those in Table 2.4, but shifted to lower size ratios. It can be seen that the stable phases shown in Table 2.4 can roughly be detected from the graph as well. For example, in the graph cesium chloride looks stable above size ratio 0.4, while NPT simulations showed that it was hardly stable at size ratio 0.6. The zinc blende and rocksalt structures follow the same path in the beginning, while NPT simulations showed that up to a size ratio of 0.2, the zinc blende was more stable. The error in these results is probably quite large, as some potential energies were taken from non-equilibrium situations and, more importantly, the entropy was completely ignored. An important issue here is that for stability comparison, one should look at the free energy and not at the potential energy alone.

The results of the stability calculations above depend on the potential used. The Yukawa potential has some rigid assumptions that become more problematic the closer the colloids approach each other:

- It was assumed that all charges could be placed in the centre of each colloid. In other words: a colloid feels the same potential from its neighbouring colloid all over its surface, while actually this potential decreases with distance.
- The (counter) ions in between the colloids were depicted as point charges, but their sizes become important when colloids approach each other's Stern layers.
- In this model, the distribution of ions around one colloid, and hence the screening, was determined only by the colloids themselves. An influence of the neighbouring colloids was ignored.

These assumptions make the Yukawa potential less applicable to crystallization simulations. It could be more suitable for research on charge stabilisation of colloidal suspensions. However, as the potential is relatively simple, it is widely used in colloidal crystallisation simulations, as well.[13,14,25]

A second issue about the total potential used is the fact that the attractive Van der Waals forces were not taken into account. This is one of the big differences between the Yukawa (section 2.1.3) and DLVO theory (section 2.1.4). This Van der Waals force works on a much shorter range than the Yukawa potential and can be omitted most of the time. However, it can be an important factor during crystallisation, when colloids approach each other sufficiently close. If the attractive Van der Waals forces would be taken into account, this would increase the stability of an initially stable colloidal crystal. The charges pull the colloids together and only if they are close enough, the Van der Waals forces can make the attraction stronger. This is very hard to simulate using MD simulations: just after the attractive Van der Waals forces prevail over the Yukawa forces, they in turn are dominated by the repulsive “Pauli” potential. This means that the total potential will be very steep (varying between attractive and repulsive within a very short distance) and the simulation time step should be extremely small. In this research, the form of the repulsive potential was chosen more or less for practical reasons.

Conclusions

Crystallisation of charged colloidal spheres (with Yukawa interaction) was simulated using MD simulations. In colloidal crystallisation, the structure stability proved to be comparable to the ionic crystals found in inorganic chemistry. The range of sphere size ratios for stable colloidal structures was determined. The presence of a surface charge was necessary to keep the structure together, but the size of this charge was not important (at least, within the boundaries that were simulated). Unstable structures broke down more easily when the surface charge on the colloids was large. There were no sharp transition boundaries found between different crystal structures as was shown for the CsCl structure at size ratio 0.6 and for the NaCl at size ratio 0.2. At these size ratios, crystals did not fall apart to form liquids, but the colloids did not stay in a perfect lattice either. The radial distribution functions showed some deviation from the lattice positions. We found that a colloidal zinc blende structure with sphere size ratio 0.2 was stable compared to a structure built out of Lennard-Jones (hard) spheres that was not. In stability simulations of bimodal colloidal crystals presented in this chapter, all variables used were taken for real colloidal systems. This gives an indication that with the use of functionalized colloidal particles, for example, the combination of positively and negatively charged colloidal spheres could lead to the formation of a large variety of stable colloidal structures. Specifically, for the first time, stable colloidal crystals with the zinc blende structure made of oppositely charged colloidal particles were demonstrated. It is a grand challenge for the experimentalist to find a method to make such structures.

List of abbreviations

List of parameters and units

β	isothermal compressibility (-)
β	1/kT (J^{-1})
ε	dielectric constant or electric permittivity (F/m)
ε	Lennard-Jones parameter (J/mol)
η	barostat friction coefficient (s^{-1})
κ	inverse Debije-Hückel screening length (m^{-1})
ρ	molar density (mol/m^3)
ρ	volume charge density (C/m^3)
σ	surface charge density (C/m^2)
σ	Lennard-Jones parameter (m)
τ_P	P barostat time constant (s)
τ_T	T thermostat time constant (s)
χ	thermostat friction coefficient (s^{-1})
ϕ	volume fraction (%)
ψ	electric potential (V)
a	a lattice constant (m)
A	electron affinity (eV)
C	parameter in repulsive potential (J/mol)
c	speed of light (m/s)
c	concentration (mol/m^3)
d	diameter (m)
f	force (N)
$g(r)$	radial distribution function (-)
I	ionisation energy (eV)
J	current density (A/m^2)
L	box length (m)
M	molar mass (kg/mol)
m	mass (kg)
N	number of particles (-)
N_f	degrees of freedom (-)
n	number of ions per unit volume (m^{-3})
$\mathbf{P}$	polarisation (C/m^2)
p	pressure (bar)
q	charge (C)
R	particle radius (m)
T	temperature (K)
t	time (s)
U	(potential) energy (J/mol)
V	volume (m^3)
v	volume per particle (m^3)
z	charge number (-)

List of constants

ε_0	dielectric constant of vacuum ($8.8542 \cdot 10^{-12}$ Fm^{-1})
e	elementary charge quantum ($1.6022 \cdot 10^{-19}$ C)
F	Faraday constant ($9.6485 \cdot 10^{4}$ C/mol)
h	Planck's constant ($6.6262 \cdot 10^{-34}$ Js)
k_B	Boltzmann constant ($1.3807 \cdot 10^{-23}$ J/K)
N_A	Avogadro constant ($6.0221 \cdot 10^{23}$ mol^{-1})
R	gas constant (8.3145 J/mol K)

Appendix I

Total potential

In simulations of colloidal crystallization, the total potential between two colloids is determined as a sum of the Yukawa potential (2.7) and a strong repulsive potential of the form:

$$U_{rep} = \frac{C}{(r-a)^6} \tag{I-1}$$

where a is a length slightly smaller than the sum of the radii of the two spheres fitted to make the total potential smooth (which is necessary for MD simulations). C is a large constant, fitted to make the repulsion dominate over the Yukawa potential at the contact distance. Examples of typical potentials are shown in Figure 2-I. The well in the attractive potential is relatively deep compared to the typical kinetic energy, $RT \approx 8.3 \cdot 293 \approx 2.4$ kJ/mol. In Lennard-Jones simulations for example, the limited simulation time implies that only a well depth of up to $10RT$ can be overcome by thermal motion. In other words, the attraction between two oppositely charged colloids is so strong that they are likely never to separate again.

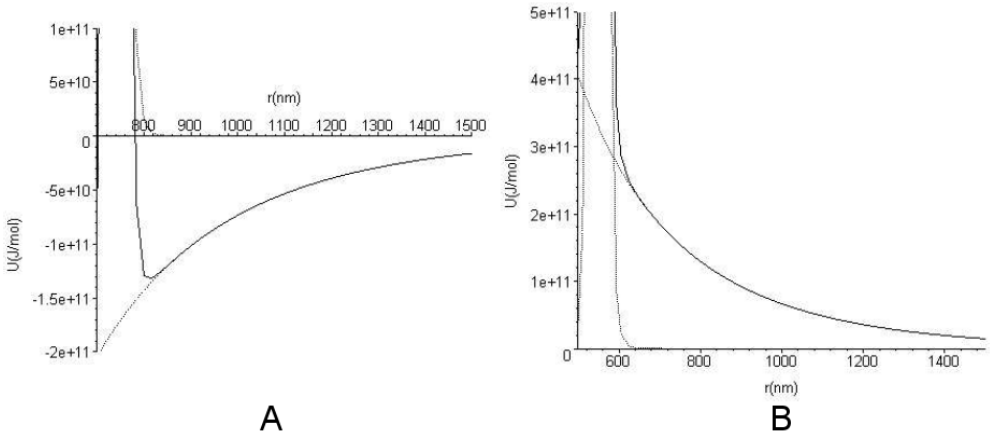

Figure 2-I. A) *Attractive potential* between two oppositely charged particles ($q = 5.5 \cdot 10^5\ e$) of size 300 and 500 nm, where $a = 740$ nm and $C = 6 \cdot 10^{22}$ J/mol; B) *Repulsive potential* between two equally charged particles ($q = 5.5 \cdot 10^5\ e$) of size 300 nm, where $a = 550$ nm and $C = 6 \cdot 10^{22}$ J/mol.

Appendix II

Molecular dynamics

Using molecular dynamics (MD), one can compute both the equilibrium and the transport properties of a system consisting of numerous particles, as long as these particles move according to Newton's laws.[26] With MD, one solves the equations of motion for every particle at every time step.‡‡

The force *f* between two particles can be calculated from the potential (*U*) acting on every particle pair:

$$f^c(r) = -\left(\frac{\partial u(r)}{\partial r}\right) \tag{II-1}$$

The dynamics of the particles is then given by this conservative force alone,

$$m\frac{d^2 r_i}{dt^2} = f_i^c \tag{II-2}$$

The commonly used algorithm for solving the equations of motion is the Verlet algorithm. It can be derived by taking the Taylor expansion of the coordinate of a particle just before and just after time *t* and summing them:

$$r(t+\Delta t) \approx 2r(t) - r(t-\Delta t) + \frac{f(t)}{m}\Delta t^2 \tag{II-3}$$

In the same way velocity can be presented.

The Verlet algorithm is reversible in time and the sum of all forces is zero by definition (conservation of linear momentum). Furthermore, the algorithm conserves energy very well.[27] However, there are some drawbacks of this method. First, two large numbers are subtracted to calculate a much smaller number for $r(t + \Delta t)$ and $v(t)$. A second, less important, drawback is that the calculation of $v(t)$ can only be done if $r(t + \Delta t)$ is known. Therefore, the velocity is always "one step behind". To solve these disadvantages, the "leap-frog" Verlet algorithm was developed. Here, the velocity is calculated at the mid-step, so the new velocities and positions can be calculated without subtraction:

$$v(t+\Delta t) = v(t-\frac{1}{2}\Delta t) + \Delta t r(t)$$

$$r(t+\Delta t) = r(t) + \Delta t v(t+\frac{1}{2}\Delta t) \tag{II-4}$$

‡‡ This section is mainly based on Frenkel and Smit.[26]

Appendix III

Periodic boundary conditions

In practically every molecular simulation, periodic boundary conditions are used. This means that the simulation box is surrounded by other boxes that are exactly equal to the first one (see Figure 2-III). This has the advantage that there are no wall effects: particles close to the border of the box are surrounded by other particles in the neighboring boxes and behave like bulk particles. In this way, the amount of particles seems to be much larger than it really is. But one only needs to calculate the motion of the particles in one box to simulate bulk behavior. Particles in surrounding boxes are called mirror images of the particle in the original box. When a particle leaves the box, it enters the neighboring box. But because this is the same box, it enters at the other side of the original box. In this way, the number of particles is always constant. One must take care though, that interactions between two particles are counted only once. In Figure 2-III for example, the mirror image of particle 2 in box VI is closer to particle 5 than the original particle 2. The force between these two particles should be calculated using the shortest distance.

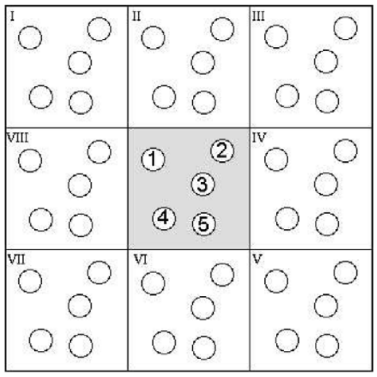

Figure 2-III. Periodic boundary conditions. Box I to VIII are exact copies of the centre box.

Time step definition

Ideally the time step in a simulation should be as large as possible, to minimize the required CPU. However, if the time step taken is too large, the algorithm for solving the equations of motion will not be accurate. In a conservative force field, as used in MD, Newton's equations of motions conserve energy. The simulation should then also conserve energy, providing an easy criterion for establishing the maximum allowable time step. In general, rapidly changing potentials necessitate a small time step, otherwise the errors in (II-3) or (II-4) are too large.

Appendix IV

Thermostats and barostats

In order to keep the temperature constant, as is commonly the case in experiments, one can use a thermostat and do an NVT simulation (with a constant number of particles N, volume V, and temperature T). There are several types of thermostats, algorithms that keep the temperature at (or near) the desired value by changing the velocity (and therefore the kinetic energy) of the particles.

The temperature of a box depends on the kinetic energy of the particles:

$$\left\langle \frac{1}{2} m v_i^2 \right\rangle = \frac{3}{2} k_B T \tag{IV-1}$$

In an MD simulation, the kinetic energy of all particles is used to calculate the temperature, incorporating the number of degrees of freedom $N_f = 3N - 3$, with N the number of particles.

$$T(t) = \frac{1}{2} \sum_{i=1}^{N} \frac{m_i v_i^2(t)}{k_B N_f} \tag{IV-2}$$

The initial velocities can be allocated to the particles by picking random velocities from the Maxwell-Boltzmann distribution, Figure 2-IV:

$$P(p) = \left(\frac{\beta}{2\pi m} \right)^{3/2} \exp\left(\frac{-\beta p^2}{2m} \right) \tag{IV-3}$$

where p is the momentum of the particle and $\beta = 1/kT$.

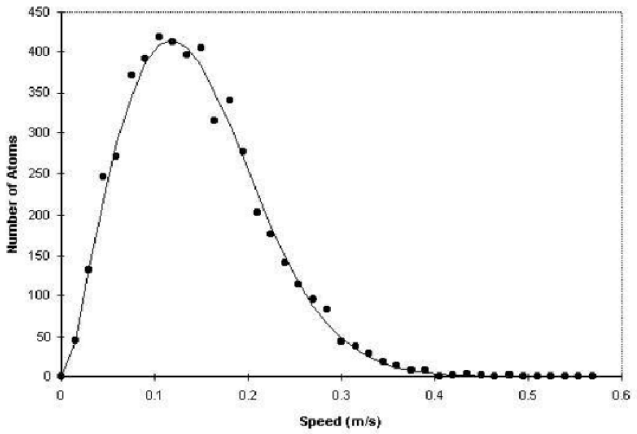

Figure 2-IV. Maxwell-Boltzmann distribution. In this case, the simulation box was very cold (close to 0 K) and, therefore, the velocities were relatively low.

Barostats keep the pressure constant and make NPT simulations possible. They change the box volume and the particle coordinates to adjust the pressure:

$$p = \rho k_B T + \frac{1}{3V}\left\langle f_{ij} \cdot r_{ij} \right\rangle \tag{IV-4}$$

Andersen thermostat

The Andersen thermostat can be used in NVT simulations. Under constant volume, it keeps the temperature at the set value. It does this by giving all particles a new velocity, according to the Maxwell-Boltzmann distribution (IV-3), every time a given number of time steps has passed.[28] One can choose not to change all velocities at the same time, but to pick some particles each time step that get a new velocity. Because the velocities have changed, the dynamics of the system is not correct. However, the Andersen thermostat is one of the best in keeping the temperature constant. Therefore, it is most useful when one is trying to reach an equilibrated configuration from an off-equilibrium starting point. If information on the dynamics is needed, another thermostat like Hoover or Berendsen is needed.

Berendsen thermostat

The Berendsen thermostat influences the velocity directly, and not its derivative to keep the temperature constant. Thus, the friction coefficient χ and the velocity v are:

$$\chi = \sqrt{1 + \frac{\Delta t}{\tau_T}\left(\frac{T_0}{T} - 1\right)}$$

$$V(t + \frac{1}{2}\Delta t) = \chi\left(v(t - \frac{1}{2}\Delta t) + \Delta t \frac{f(t)}{m}\right) \tag{IV-5}$$

A similar procedure is used in the Berendsen barostat, which can run parallel to the thermostat. To control the pressure, the cell volume is multiplied by friction coefficient η:

$$\eta = 1 - \frac{\beta \Delta t}{\tau_p}(p_0 - p) \tag{IV-6}$$

and the coordinates and cell vectors by $\eta^{1/3}$. Here, β is the isothermal compressibility of the system, which is normally taken to be equal to that of liquid water. The exact value is not very important, because it is divided by the input parameter τ_p.

Appendix V

Radial distribution function

The radial distribution function $g(r)$ gives the relative number density of particles around another particle as a function of the distance from this particle. In practice, it is calculated by counting the number of particles in a spherical shell with radius r and thickness dr around a particle and dividing this by the average density times the volume of this shell:

$$g(r) = \frac{\rho_{local}}{\rho_{\infty}} = \frac{n_{r,r+dr}}{4\pi r^2 dr \rho_{\infty}} \qquad \text{(V-1)}$$

To make sure that each particle pair is taken into account only once, the distance r should not be more than half a box length. With $g(r)$, it is possible to distinguish between for example a liquid (Figure 2-VA) and a crystal (Figure 2-VB). Note that a glass will have a *g(r)* similar to that of a liquid, while it also has a number of solid-like properties. The radial distribution functions for liquid and solid (crystallized) argon were calculated using DL-POLY molecular dynamics simulation package presented in paragraph 2.2 of this chapter.

When different types of particles, for example A and B, are present within one box, several distribution functions can be calculated. In this case that would be the distribution of A around A, B around B and A around B (which is the same as B around A). By multiplying the radial distribution function by $4\pi r^2 \rho_{\infty}$, the number of particles at a certain distance within a shell dr can be counted. Upon integration, the (cumulative) number of particles in a sphere centered at a particle is given as a function of r, see Figure 2-V C. This graph shows that every particle has 12 nearest neighbours, 6 second-nearest neighbours etc. In this way, the structure of the crystal can be deduced from its coordination numbers.

When the temperature of a solid is raised, the peaks in the radial distribution function will broaden due to thermal motion of the particles around their equilibrium position. The broadening can be so large, that it is difficult to see whether one is dealing with a solid or a liquid. In this case, it might be helpful to lower the temperature to 10 K (or another very low value) at once and leave it there for a while. If the substance was a solid at the higher temperature, the peaks will become much narrower at 10 K. If it was a liquid, the sudden temperature change will turn it into a glass, so the peak widths will hardly change.

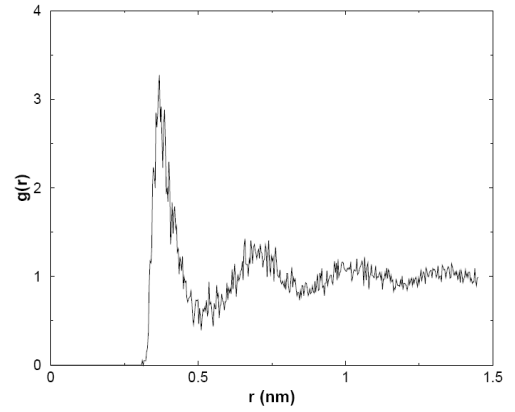

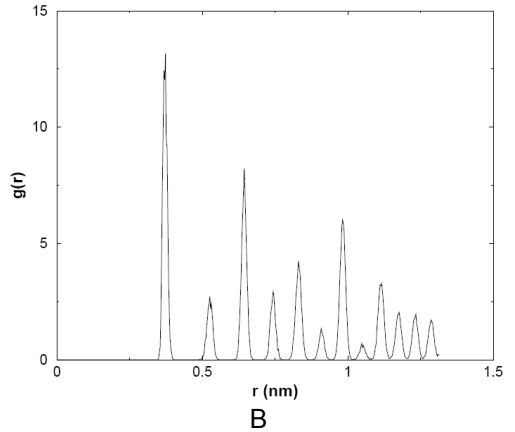

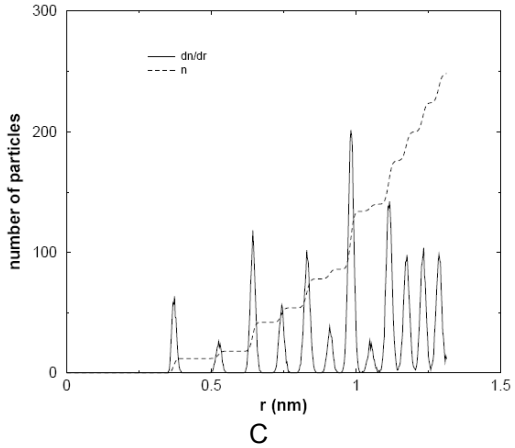

Figure 2-V. A) Radial distribution function of liquid argon. B) Radial distribution function of solid argon, a crystal with an FCC structure. C) Crystallized argon at 12 K. The dotted line shows the cumulative number of particles around one sphere. The y-axis corresponds to this line.

Appendix VI

Mean square displacement

The mean square displacement (msd) is what it says: the squared displacement of each particle in a certain time interval is taken and averaged over all particles. Note that one particle can make several contributions to this sum, because a time interval of for example 1 nanosecond can occur several times during a simulation time of 10 nanoseconds. If the particles are in a liquid state, the msd is linear with time (Figure 2-VI A). If it is a solid, the msd is constant and close to zero, because in a crystal or glass the particles move only a little around their equilibrium position (Figure 2-VI B).

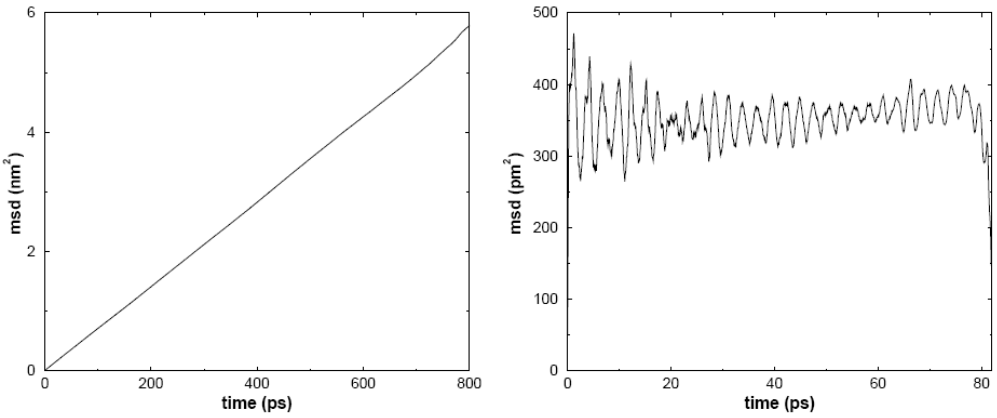

A B

Figure 2-VI. A) Mean square displacement of liquid argon. B) Mean square displacement of solid argon. Note the scale difference with Figure 2-VI A.

References

[1] K. M. Ho, C. T. Chan, C. M. Soukoulis, *Phys. Rev. Lett.* **1990**, *65*, 3152.
[2] P. N. Pusey, W. van Megen, *Nature* **1986**, *320*, 340.
[3] Z. Cheng, W. B. Russel, P. M. Chaikin, *Nature* **1999**, *401*, 893.
[4] P. Bartlett, R. H. Ottewill, P. N. Pusey, *Phys. Rev. Lett.* **1992**, *68*, 3801.
[5] E. B. Sirota, H. D. Ou-Yang, S. K. Sinha, P. M. Chaikin, J. D. Axe, Y. Fujii, *Phys. Rev. Lett.* **1989**, *62*, 1524.
[6] M. E. Leunissen, C. G. Christova, A.-P. Hynninen, C. P. Royall, A. I. Campbell, A. Imhof, M. Dijkstra, R. van Roij, A. van Blaaderen, *Nature* **2005**, *437*, 235.
[7] A. P. Gast, W. B. Russel, *Physics Today* **1998**, *51*, 24.
[8] Review: M. Dijkstra, *Curr. Opin. Coll. Int. Sci.* **2001**, *6*, 372.
[9] M. O. Robbins, K. Kremer, G. S. Grest, *J. Chem. Phys.* **1988**, *88*, 3286.
[10] E. J. Meijer, F. E. Azhar, *J. Chem. Phys.* **1997**, *106*, 4678.
[11] E. Trizac, M. D. Eldridge, P. A. Madden, *Mol. Phys.* **1997**, *90*, 675.
[12] M. D. Eldridge, P. A. Madden, D. Frenkel, *Nature* **1993**, *365*, 35.
[13] K. Kremer, M. O. Robbins, G. S. Grest, *Phys. Rev. Lett.* **1986**, *57*, 2694.
[14] F. El-Azhar, M. Baus, J. P. Ryckaert, E. J. Meijer, *J. Chem. Phys.* **2000**, *112*, 5121.
[15] C. Kittel, *Introduction to Solid State Physics*, 5th ed., Wiley, NY, **1976**.
[16] A. A. Louis, E. Allahyarov, H. Löwen, R. Roth, *Phys. Rev. E* **2002**, *65*, 61407.
[17] J. Z. Wu, D. Bratko, H. W. Blanch, J. M. Prausnitz, *Phys. Rev. E* **2000**, *62*, 5273.
[18] H. Löwen, *Physica B* **1996,** *228*, 78.
[19] P. C. Hiemenz, R. Rajagopalan, *Principles of Colloid and Surface Chemistry*, 3d ed., Marcel Dekker, Inc., NY, **1997**.
[20] H. L. Tepper, Ph.D. thesis, University of Twente, Enschede, **2001**.
[21] D. J. Shaw, *Colloid & Surface Chemistry*, 4th ed., Butterworth-Heinemann, Oxford, **1998**.
[22] R. J. Hunter, *Foundations of Colloid Science,* v.1, Oxford University press, Oxford, **1987**.
[23] R. M. Fitch, *Polymer Colloids: A Comprehensive Introduction,* Academic press, San Diego, **1997**.
[24] D. M. Adams, *Inorganic Solids: An Introduction to Concepts in Solid-State Structural Chemistry*, Wiley, London, **1974**.
[25] S. Auer, D. Frenkel, *J. Phys. Condens. Matter* **2002**, *14*, 7667.
[26] D. Frenkel, B. Smit, *Understanding Molecular Simulation: From Algorithms to Applications,* Academic Press, San Diego, **1996**.
[27] M. P. Allen, D. J. Tildesley, *Computer Simulation of Liquids*, 7th ed., Oxford science publications, NY, **1993**.
[28] H. C. Andersen, *J. Chem. Phys.* **1980**, *72*, 2384.

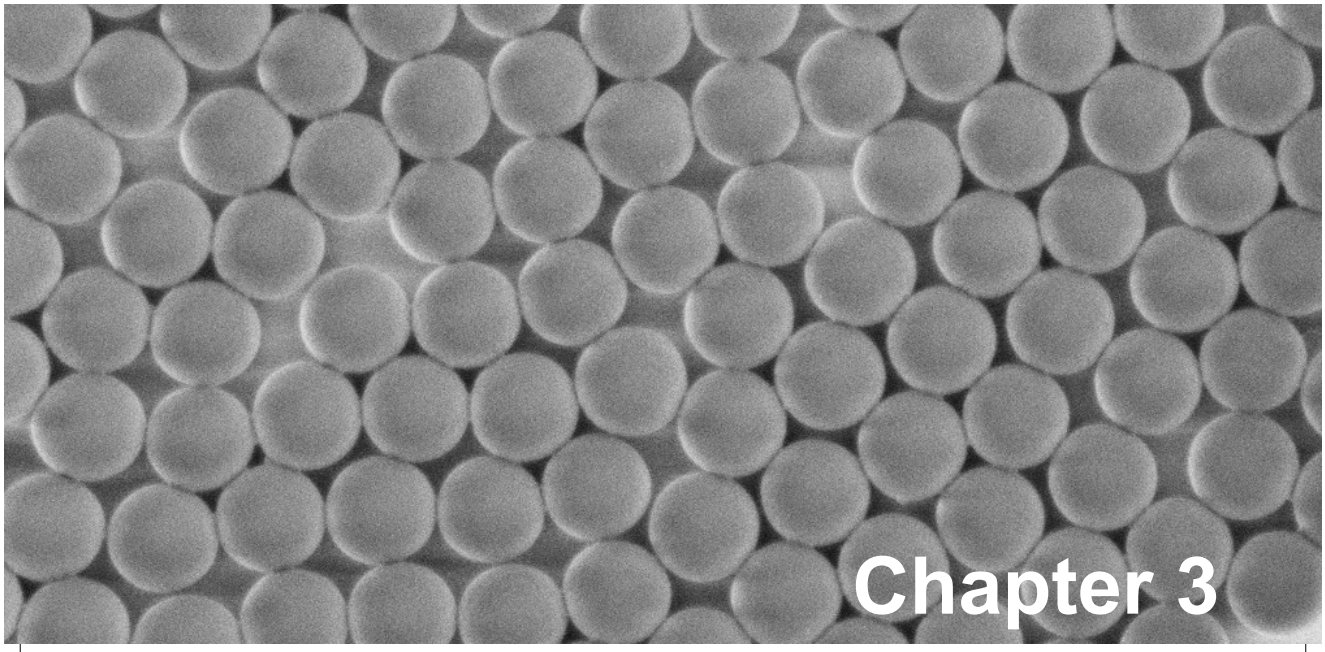

Chapter 3

Synthesis and Characterization of Monodispersed Anionic Colloidal Particles

Monodispersed polystyrene core-shell colloidal particles were synthesized using surfactant-free seeded emulsion polymerization. The size of colloidal core particles could be tuned between 200 nm and 500 nm by varying monomer concentrations. Anionic shells were introduced by co-polymerizing styrene with the anionic monomer sodium styrenesulfonate (NaSS). Surface charge densities of the colloidal particles were controlled by varying the concentrations of co-monomer NaSS between 0.8 mol% and 2.5 mol% in styrene. Colloidal particles were characterized using High-Resolution SEM, conductometric titration and zeta potential measurements.

Introduction

Various polymerization methods[1] such as emulsion, dispersion, precipitation and suspension polymerizations are used to synthesize polymer colloidal particles. In order to obtain high quality colloidal crystals (see also Chapter 2), monodisperse colloidal particles with controlled surface characteristics are required. For the preparation of charge-stabilized polymer colloids, emulsion or emulsifier-free emulsion polymerizations are used. Charge-stabilized "soft" colloidal particles open up many possibilities to control colloidal crystallization. Charged colloidal particles undergo a fluid-crystal transition and reveal various crystalline phases at volume fractions much lower than observed for hard colloidal spheres.[2] Charged colloidal particles can also be deposited onto chemically patterned surfaces covered with oppositely charged molecules[3] and can interact with direct[4,5] and alternating[6] electric fields. Finally, if bimodal colloidal particles possess opposite surface charges, then one can try to fabricate colloidal crystals with different A_xB_y crystal symmetries that mimic ionic crystals and possess low crystal symmetry.[7] If the refractive index contrast between the constituents is high enough, these structures could be promising candidates for photonics applications. Successful fabrication of such structures requires full control of size and surface charge of the polymer microparticles. In this contribution we describe the synthesis and characterization of core-shell negatively charged colloidal particles.

Emulsion polymerization[1,8] comprises emulsification of a water-immiscible monomer in a continuous water medium and polymerization using a water-soluble or oil-soluble initiator, to give a colloidal dispersion of polymer particles in water. In conventional emulsion polymerization, (oil-in-water) colloidal particles are stabilized by the presence of surfactant molecules (emulsifier) and the size of colloidal particles obtained is usually between 0.05 and 0.3 μm. In emulsifier-free emulsion polymerization, colloidal particles are stabilized by ionic initiator residues covalently bound to the polymer particles[9] and the particle size can be varied between 0.1 and 1 μm. Emulsifier-free emulsion polymerization belongs to a group of free radical polymerizations where initiator radicals react with monomer molecules, initiating polymer chain growth that continues until the supply of monomer or free radicals is exhausted. Formed surface-active oligomers grow, associate, nucleate and form particles. However, these primary particles are not stable in emulsion until enough charged groups are formed at the particle surface to give a particle an adequate electrostatic surface potential. Therefore, small particles coagulate and form larger particles until the potential energy of

electrostatic repulsion between the particles is adequate to ensure colloid stability in the ionic environment in which the colloidal particles are formed.

Potassium persulfate (KPS) was intensively used as anionic initiator in single stage[9] as well as in multistage seeded polymerizations of micrometer-size particles.[10] In these processes, surface charge originating from initiator fragments and the ionic initiator itself changes the ionic strength of an emulsion, thus changing particle size,[9] and, therefore, surface charge density and particle size cannot be controlled independently. Surface charge density can be influenced by incorporation of functional monomer.[11] In this direct copolymerization of structural monomers with ionic comonomers such as sodium styrenesulfonate (NaSS)[12] or sodium 1-allyloxy-2-hydroxypropane sulfonate (AHSS),[13] particle size strongly depends on the ionic monomer concentration and drastically decreases with an increase in comonomer concentration. This method leads to the formation of colloids of sizes up to 300 nm. Seeded polymerizations allow one to vary particle size in a wide range but generally provide limited control over surface charge density.[14]

Two-stage shot growth emulsion polymerization[14,15] enables one to introduce high surface charge densities on colloid particles and provides independent control over particle size up to 300 nm. In the first stage, e.g. styrene is copolymerized with a small quantity of ionic monomer. In this stage the size of the seed particles is regulated. When a high conversion (> 90%) is reached, a second stage monomer mixture is added. The ratio of structural monomer to ionic monomer in this mixture determines the final surface charge density. Colloidal particles with surface charge densities between 21 $\mu C/cm^2$ and 72 $\mu C/cm^2$ have been reported.

In our research, we have been interested mainly in tailoring colloidal sizes and surface charge densities, so seeded surfactant-free emulsion polymerization was therefore chosen, as in the first stage colloidal particle size can be controlled while surface charge density can be varied in the second polymerization stage. We describe the synthesis and characterization of cross-linked core-shell anionic latex particles using a two-stage process composed of emulsifier-free emulsion polymerization of styrene and the subsequent formation of a shell around the polystyrene seeds by co-polymerization of styrene with anionic comonomers. An anionic monomer, sodium styrene sulfonate (NaSS), was used with the aim of synthesizing well-defined anionic latex particles of which the size and surface charge density can be controlled independently.

High-resolution scanning electron microscopy (HR-SEM) was used in this study for the visualization of the colloidal particles.

3.1. Core preparation

Polystyrene colloidal particles were prepared by surfactant-free emulsion polymerization of styrene in the presence of a cross-linker (1,3-diisopropenylbenzene (DI), 2 mol% with respect to styrene), using an anionic initiator (potassium persulfate, KPS). Various polymerizations were carried out at different styrene concentrations. Corresponding particle diameter values with standard deviations and latex yield are summarized in Table 3.1 and Figure 3.2A. Figure 3.2B shows a logarithmic plot of the number average particle diameter against monomer concentration. The dependence of the particle diameter D on styrene concentration for colloids in the range from 200 nm to 500 nm at constant initiator concentration, ionic strength[16] and temperature, using monomer concentrations between 0.1 and 1 mol/L is given by the equation:

$$\log (D) = 0.36 \cdot \log [St^I] + 2.67.$$

The particle diameter varied as the 0.36 power of the initial monomer concentration. Similar results were found in other emulsifier-free emulsion polymerization systems. At styrene concentrations above 1 mol/L no further increase in size of colloidal particles was detected. Colloidal particles with a number average diameter of 300 nm and large amounts of homopolymer residues were obtained (see also Table 3.1 and Figure 3.2). A subsequent increase in size of colloidal particles (above 500 nm) can be achieved by increasing the ionic strength of the dispersion medium and by lowering the reaction temperature. The core synthesis was found to be highly reproducible. A typical SEM image of colloidal particles presented in Table 3.1 is shown in Figure 3.1. SEM images confirmed the formation of highly monodispersed,[17] well-defined colloidal particles possessing a low surface roughness.

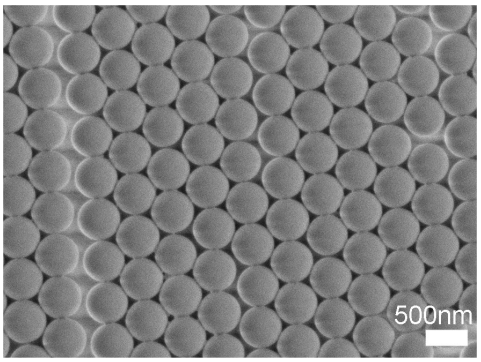

Figure 3.1. SEM image of polystyrene colloidal particles obtained by surfactant-free emulsion polymerization in this study.

Table 3.1
Influence of styrene concentration on particle size[a]

Sample	$[St^I]$ (mol/L)	Number average diameter (nm)[b]	Standard deviation (nm)	Variation on the mean (%)	Latex yield (%)
173	0.11	219.6 (220)	4.1	1.9	75
169	0.17	252.2 (252)	4.3	1.7	68
167	0.33	306.8 (307)	5.5	1.8	73
166	0.56	353.1 (353)	5.9	1.7	65
165	0.78	420.3 (420)	4.4	1.0	82
130	1	503.2 (503)	8.0	1.6	98
174	1.18	295.1 (295)	7.3	2.5	19
172	1.33	315.4 (315)	10.8	3.5	25

[a] [KPS] = 2 mmol/L, [NaCl] = 2.57 mmol/L, DI content = 2 mol% of the styrene amount (mol) used in the core (St^I), ionic strength = 8.57 x 10^{-3} mol/kg. Polymerization temperature: 70 °C
[b] Determined using high-resolution SEM.

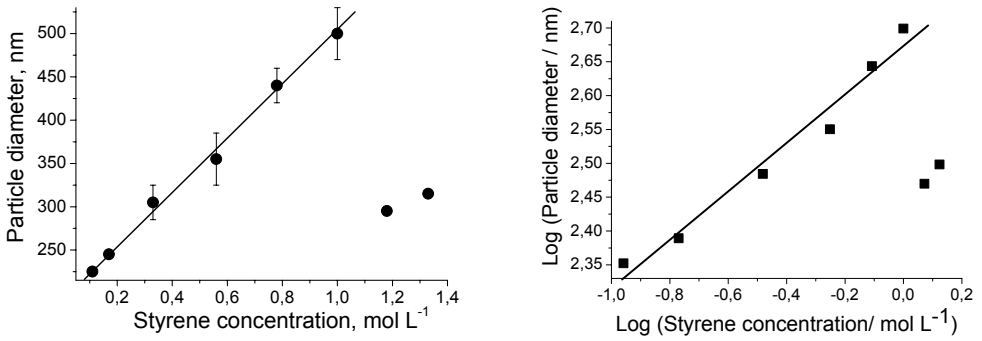

A B

Figure 3.2. A) Number average particle diameter versus initial monomer concentration (see also Table 3.1), D = 190.8 + 315.4$[St^I]$; B) Logarithmic plot of number average particle diameter versus initial monomer concentration, $\log(D) = 2.67 + 0.36 \log[St^I]$.

3.2. Shell preparation

The size of colloidal particles was controlled in the first stage (core) of the polymerization, while the surface charge density was controlled in the second stage (shell). Surface charge was introduced on the colloidal particles via co-polymerization of styrene with an anionic co-monomer. In addition to the surface charge density, final tuning of colloidal particle size can be achieved by varying the amount of St in the second stage. Precise control of the final colloidal particle size becomes important in the growth of binary colloidal crystals and colloidal crystals on patterned surfaces. The amount of styrene for co-polymerization in the second stage (St^{II}) was adjusted with respect to the amount of styrene used in the first stage (St^I), Table 3.2 and Figure 3.3. The ratio of styrene added in the second stage to the first stage (St^{II}:St^I) was varied as 1:2, 1:3 and 1:5, respectively. In a seeded polymerization

mechanism, stable colloidal particles are formed during the coagulation of primary and seed particles.[18] After polymerization, the average number diameter of colloidal particles increased indicating shell formation. The shell thickness for different sizes of colloidal particles is shown in Figure 3.3. The relative shell thickness was varied between 1 % and 5 %, Figure 3.3B. A linear relation between shell thickness and particle size was determined. For small colloidal particles, a larger amount of styrene needed to be added in the second stage compared to large colloidal particles in order to obtain the same increase in shell thickness. Such a linear increase in shell thickness can be related to the surface area of core particles, which increases with a decrease in particle size.

Table 3.2
Influence of monomer concentration on particle size in stage II [a]

Sample	$[St^{I}]$ (mol/L)	Number average $diameter^{I}$ (nm)	$[St^{II-1}]$ (mol/L) **1:5**	Number average $diameter^{II-1}$ (nm)	$[St^{II-2}]$ (mol/L) **1:3**	Number average $diameter^{II-2}$ (nm)	$[St^{II-3}]$ (mol/L) **1:2**	Number average $diameter^{II-3}$ (nm)
173	0.11	**220**			0.023	**222**	0.031	**225**
169	0.17	**252**			0.035	**256**	0.053	**262**
167	0.33	**307**			0.07	**315**	0.083	**324**
166	0.56	**353**	0.07	**361**	0.12	**367**		
130	1	**503**	0.125	**516**	0.208	**527**		

[a] KPS content = 1 wt% based on the total monomer amount (g), St + NaSS + DI; NaSS content = 1.64 wt% based on styrene used in the shell (St^{II}); [NaCl] = 1.7 mmol/L. Polymerization temperature: 70 °C.

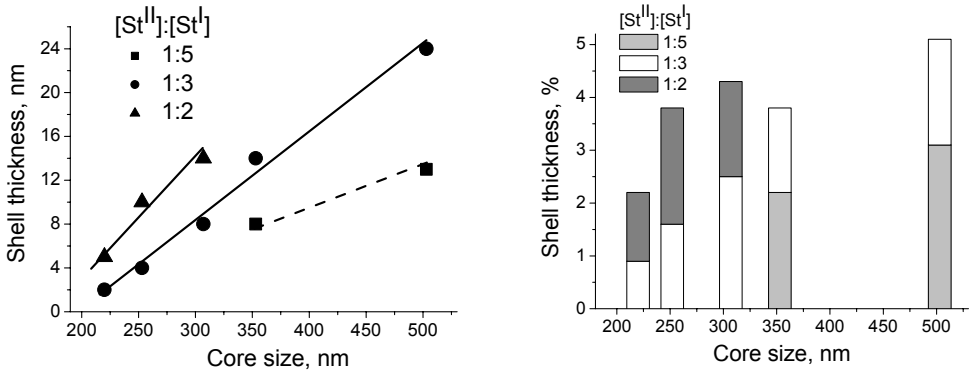

Figure 3.3 A) Shell thickness versus monomer concentration in stage II for colloidal particles (cores) of different sizes (see also Table 3.2); B) Graph 3.3A represents the percentage of the shell thickness of the size of a core-shell particle.

Sodium styrene sulfonate (NaSS) was used as an anionic monomer in the second stage of polymerization. NaSS is widely used as a co-monomer in polyelectrolyte synthesis and for

charge control of colloidal particles. By varying the NaSS amount, surface charge density on the colloidal particles can be controlled. At the same time, the amount of co-monomer (NaSS) affects the secondary particle generation. An increased tendency to form secondary particles at high concentrations of NaSS is expected because of the high surface charge of growing particles, which creates a noticeable electrostatic repulsion and reduced coagulation rate.[15] The concentration of NaSS monomer was varied between 0.8, 1.64 and 2.5 mol%, Table 3.3. At these NaSS concentrations, secondary colloidal particles were not observed. All copolymerization reactions were performed in the presence of 7.5 mol% cross-linking agent (DI). Salt concentration was not changed in the suspension during polymerization, therefore, variations in ionic strength are caused by the different amounts of initiator and co-monomer (NaSS). Surface charge densities (σ) were measured by conductometric titration of the colloidal suspension. The surface charge densities increased with increasing anionic monomer concentrations, Table 3.3.

Zeta potential measurements were carried out to characterize the stability of the colloidal core-shell particles. The magnitude of the zeta potential gives an indication of the stability of colloidal systems. If particles in a suspension have a large negative zeta potential, particles repel each other and the suspension is stable. At low values of the zeta potential, the colloidal particles may aggregate due to the attractive forces. Absolute zeta potential values above 30 mV are commonly associated with stable colloidal suspensions, while values below 30 mV indicate susceptibility to agglomeration.[19] Zeta potential measurements, presented in Table 3.3 are just above the absolute zeta potential value of 30 mV. Indeed, from our experience, colloidal suspensions presented in Table 3.3 showed an excellent stability upon storage for almost 3 years, during which no particle coagulation was observed.

Table 3.3
Influence of NaSS concentration on shell formation[a]

Sample[b]	[St^{II}] (mol/L)[c]	[KPS], mol% (wt%)[d]	[NaSS] mol% (wt%)[e]	Ionic strength (mmol/kg)	Number average diameter[II], nm[f]	Zeta potential (mV)	σ ($\mu C/cm^2$)[g]
84	0.1	0.46 (1.0)	0.80 (1.64)	3.82	328	-31.4	16.2
86	0.1	0.46 (1.0)	1.64 (3.28)	4.68	322	-33.8	21.3
87	0.1	0.46 (1.0)	2.50 (4.92)	5.58	325	-34.1	25.5

[a] DI = 7.5 mol % with respect to mol St^{II}+NaSS. [NaCl] = 1.7 mM, polymerization temperature 70° C.
[c] [St^{I}] = 0.5 mol/L; ratio of styrene in the shell and styrene in the core: St^{II} : St^{I} = 1:3.
[d] Based on mol St^{II}+DI+NaSS.
[e] With respect to mol St^{II}.
[f] Number average diameter of initial colloidal particles (core) = 310 nm.
[g] Obtained by conductometric titration.

3.3. Conclusions

Emulsifier-free emulsion polymerization was successfully applied to synthesize monodisperse core-shell polystyrene colloidal particles. This establishes one of the building blocks for assembling bimodal colloidal crystals in correspondence with inorganic structures. The size of colloidal core particles was controlled by the amount of monomer. Upon raising the monomer concentration from 0.11 mol/L to 1 mol/L, the size of colloidal core particles increased from 220 nm to 500 nm at a constant ionic strength of the colloidal emulsion of 8.57×10^{-3} mol/kg. Anionic shells were introduced by co-polymerization of styrene with the anionic monomer NaSS. Shell thickness and, therefore, the final size of core-shell colloidal particles were fine-tuned by the amount of styrene monomer added in the second stage of polymerization. By tuning the amount of monomer in the second stage, the shell thickness was varied between 1 % and 5 % of the final size of core-shell colloidal particles. It was found that for small colloidal particles of 220 nm, more monomer had to be added for shell preparation in order to obtain the same thickness increase as for large particles of 500 nm, which required a much lower monomer concentration. Monomer concentrations for shell preparation were adjusted such that a linear relation between shell thickness and colloidal particle was achieved. Surface charge density of the colloidal particles was adjusted by varying the concentration of anionic monomer in styrene.

Experimental part

Materials

Styrene (St), (Merck) was distilled under reduced pressure and stored at 4 °C. Sodium styrenesulfonate (NaSS) (Scheme 3.1), potassium persulfate (KPS) (>99 %) and 1,3-diisopropenylbenzene (DI) (>97 %), were purchased from Aldrich and were used without further purification. Sodium chloride (NaCl) (>99.5 %, Fluka) was used as received. Ion-exchange resin Amberlite IR-120 (H^+ form) was thoroughly washed with Milli-Q water before use. Milli-Q water (Millipore, 18.2 MΩ cm) was used in all experiments.

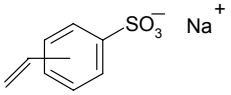

Scheme 3.1. Chemical structure of NaSS.

Synthesis of polystyrene core particles

All polymerisation reactions were carried out in a 250 cm^3 three-necked round-bottomed flask equipped with a reflux condenser, septum and magnetic stirring bar. A total reaction volume of 200 cm^3 was normally used.

An emulsifier-free emulsion polymerisation recipe as described by Ottewill was employed for the preparation of the polystyrene colloids. Representative recipes are shown in Table 3.1. A typical preparation of latex particles was carried our in the following manner. A flask was charged with Milli-Q water (180 mL) and NaCl (2.57 mM). Oxygen was removed by passing a slow stream of nitrogen through the solution for 30 min while stirring at 450 rpm. The gas flow rate was kept low in order to minimize evaporation. After 30 min, a mixture of styrene and cross-linker (DI) was added at once to the three-necked flask. Initiator (KPS) (2 mM) was

dissolved in Milli-Q water (20 mL) in a separate conical flask and was degassed. The three-necked flask was them immersed in a preheated oil bath (70 °C) and left for 1 hour to attain thermal equilibrium. Finally, KPS was added in one portion. Concentrations of initiator and NaCl were identical for all reactions. Therefore, the ionic strength was constant for experiments ($8.57 \cdot 10^{-3}$ mol/kg). Stirring was continued for 24 hours. Then, the vessel was removed from the oil bath and left to cool. The latex dispersion was decanted through a filter packed with glass wool in order to remove any homopolymer film and coagulum formed during the synthesis. The colloidal particles were used as seeds for the growth of the shell layer.

Synthesis of core-shell colloidal particles

In a typical experiment (sample 84, Table 3.3) the set-up described above was charged with seed suspension (80 mL) which was degassed and heated to 70 ºC while stirring at 450 rpm. In separate flasks, two solutions were prepared: one containing styrene (1.44 mL) and a cross-linker (DI) (0.16 mL) and the other with the KPS initiator (0.015 g) and anionic co-monomer NaSS (0.021 g) dissolved in Milli-Q water (20 mL). The solutions were degassed using nitrogen and added simultaneously within 30 min to the seed dispersion. After 24 hours, the flask was removed from the oil bath and allowed to cool. The latex was decanted through a filter packed with glass wool.

Particle size determination

A small amount of colloidal suspension was diluted with Milli-Q water until the solution was almost transparent. A drop of suspension was placed on a cleaned silicon substrate and left to dry. Dried colloids were examined with a High Resolution LEO 1550 FEG scanning electron microscope (SEM) at low acceleration voltages (0.5 kV), allowing us to image the latex samples without applying a metal coating. The colloidal particle number average diameter and standard deviation were calculated from SEM images[20] based on 30-50 particles per sample, using the image processing program Scion Image, version Beta 4.0.2.

Yield determination

The yield of the colloidal particles formation was determined gravimetrically at the end of the polymerization. A measured amount of latex dispersion was centrifuged at 15000 rpm for 15 min and dried at room temperature in a vacuum oven. The yield was calculated according to the following equation:[21]

$$C(\%) = \frac{W_1 / W_2}{m_1 / (m_1 + m_2)} \times 100\%$$

where $C(\%)$ is the total conversion to polymer; W_1 is the weight of dried polymer; W_2 is the weight of the sample withdrawn from the reaction solution; m_1 is the weight of monomer added; m_2 is the weight of the medium.

Zeta potential measurements

Zeta potential values were determined by laser Doppler electrophoresis using a Zetasizer 2000 (Malvern Instruments Ltd., Malvern, UK). For the measurements, a small amount of a latex dispersion was diluted with Milli-Q water until the solution was almost transparent.

Determination of surface charge densities

Surface charge densities were analyzed by conductometric titration of colloidal suspensions using 0.01 N NaOH. Conductometric titration was performed under nitrogen atmosphere. Before titration, the latex suspension was placed in polycarbonate tubes and centrifuged several times at 17000 rpm for half an hour to remove possibly formed polyelectrolyte species. After each centrifugation step, the colloidal particles were re-dispersed in Milli-Q water using an ultrasound bath. Then, the colloid suspension was passed through an ion-exchange column filled with Amberlite IR-120 (H^+) several times and finally dialyzed for several days using a Spectra/Por membrane, (cutoff molar mass 12-14000 g mol^{-1}, Spectrum Laboratories) until the conductivity of the water used became constant.
The values of surface charge densities (σ) were calculated according to the following equation:[22]

$$\sigma = \frac{Fn\rho R}{3W}$$

where F is the Faraday constant; n is the number of moles of NaOH required to neutralize the surface functional groups of colloidal particles; ρ is the density of colloidal particles (1.05 g/cm^3); R is the radius of the latex sphere, and W is the fraction solid content of the latex.

References and Notes

[1] R. Arshady, *Coll. Polym. Sci.* **1992**, *270*, 717.
[2] P. N. Pusey, W. van Megen, *Nature* **1986,** *320*, 340.
[3] I. Lee, H. Zheng, M. F. Rubner, P. T. Hammond, *Adv. Mater.* **2002**, *14*, 572.
[4] S.-R. Yeh, M. Seul, B. I. Shraiman, *Nature* **1997**, *386*, 57.
[5] M. Trau, D. A. Saville, I. A. Aksay, *Langmuir* **1997**, *13*, 6375.
[6] K.-Q. Zhang, X. Y. Liu, *Nature* **2004**, *429*, 739.
[7] M. E. Leunissen, C. G. Christova, A.-P. Hynninen, C. P. Royall, A. I. Campbell, A. Imhof, M. Dijkstra, R. van Roij, A. van Blaaderen, *Nature* **2005**, *437*, 235.
[8] J. W. Vanderhoff, *Chem. Eng. Sci.* **1993**, *48*, 203.
[9] J. W. Goodwin, J. Hearn, C. C. Ho, R. H. Ottewill, *Coll. Polym. Sci.* **1974**, *252*, 464.
[10] S.-E. Shim, Y.-J. Cha, J.-M. Byun, S. Choe, *J. Appl. Polym. Sci.* **1999**, *71*, 2259.
[11] R. Arshady, *J. Macromol. Sci., Rev. Macromol. Chem. Phys.* **1992**, *32*, 101.
[12] M. S. Juang, I. M. Krieger, *J. Polym. Sci. Polym. Chem.* **1976**, *14*, 2089.
[13] C. E. Reese, C. D. Guerrero, J. M. Weissman, K. Lee, S. A. Asher, *J. Coll. Int. Sci.* **2000**, *232*, 76.
[14] J. H. Kim, M. Chainey, M. S. El-Aasser, J. W. Vanderhoff, *J. Polym. Sci., Polym. Chem.* **1989**, *27*, 3187.
[15] J. H. Kim, M. Chainey, M. S. El-Aasser, J. W. Vanderhoff, *J. Polym. Sci., Polym. Chem.* **1992**, *30*, 171.
[16] Ionic strength was calculated based on the total volume of the aqueous phase. The initiator was treated as a 2:1 electrolyte and its concentration was taken as the initial value in the aqueous phase before decomposition had occurred.
[17] Colloidal particles were considered being monodisperse when the variation on the mean was less than 4%.
[18] L. J. Liu, I. M. Krieger, *J. Polym. Sci. Polym. Chem. Ed.* **1981**, *19*, 3013.
[19] N. Spanos, P. G. Klepetsanis, P. G. Koutsoukos. *Encyclopedia of Surface and Colloid Science*, ed. A. T. Hubbard, NY, Marcel Dekker, Inc. **2002**, *1*, 829.
[20] *Emulsion Polymerization and Emulsion Polymers,* ed. P. A. Lovell, M. S. El-Aasser*,* Chichester: John Wiley & Sons Ltd; **1997**, ch. 12, 391.
[21] Y.-M. Wang, C. Y. Pan, *Coll. Polym. Sci.* **1998**, *277*, 658.
[22] H. B. Sunkara, J. M. Jethmalani, W. T. Ford *J. Polym. Sci*., *Part A* **1994**, *32*, 1431.

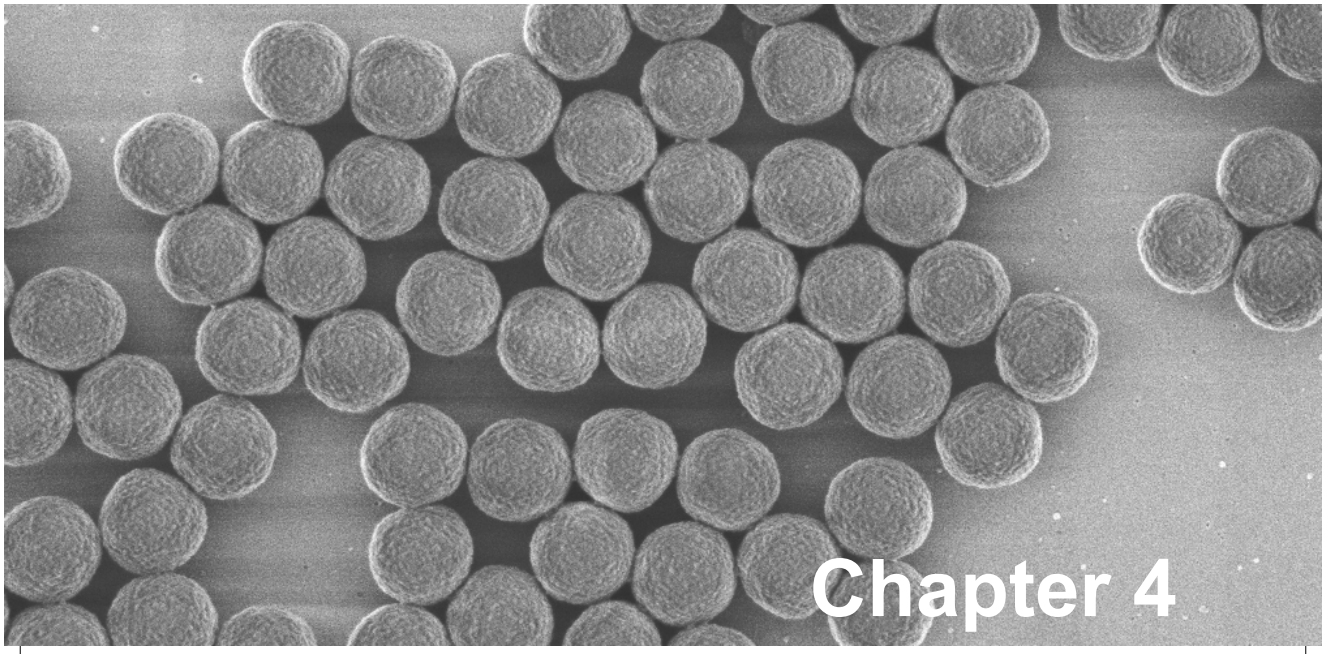

Chapter 4

Synthesis and Characterization of Monodispersed Cationic Colloidal Particles[*]

Surfactant-free seeded (core-shell) polymerization of monodispersed cationic polymer colloids is presented. Polystyrene core particles with sizes between 200 nm and 500 nm were synthesised. Cationic shells were introduced by copolymerizing styrene with the cationic monomers (vinylbenzyl)trimethylammonium chloride (VBTMAC), [(2-methacryloyloxy)ethyl] trimethylammonium chloride (METMAC) and [(2-acryloyloxy)ethyl] trimethylammonium chloride (AETMAC) onto the polystyrene cores. The cationic monomer AETMAC, undocumented to our knowledge in colloid synthesis, produced the best cationic shells and could be incorporated at much higher concentrations in the shell compared to the commonly used VBTMAC and METMAC, which yielded undesired polyelectrolyte side products already at relatively low cationic monomer concentrations. In shell formation, feed concentrations of AETMAC between 1.3 mol % (2.4 wt %) and 10.7 mol % (20 wt %) in styrene could be employed, allowing us to control colloid surface charge density over a wide range. The influence of various polymerization parameters (initiator concentration, crosslinking agent, and ionic strength) on the copolymerization process with AETMAC is discussed. Core-shell particles were characterized using HR-SEM, potentiometric titration and zeta potential measurements.

[*] Parts of this chapter have been published in: N. V. Dziomkina, M. A. Hempenius, G. J. Vancso, *European Polymer Journal* **2006**, *42*, 81.

Introduction

In recent years there has been an increasing interest in studying the crystallization mechanism of monodisperse charged colloidal particles and the corresponding packing and particle interaction mechanisms.[1] Control over the size, polydispersity and surface charge density of polymer colloidal particles opens up a way towards controlled colloidal crystallization. For successful colloidal crystal packing and crystal engineering, near-monodisperse particles are needed. Packing within colloidal crystals can in principle be controlled by the size and surface charge density of the building blocks (colloidal particles). If particles exhibiting bimodal distributions are used, one may, in principle, obtain stable structures of A_xB_y types, which would exhibit lower degrees of symmetry as compared with the bcc lattice. Crystallization of bimodal colloidal particles of the same surface sign leads to the formation of AB_2 or AB_{13} crystal structures.[2,3] If bimodal colloidal particles possess opposite surface charge, then one can try to fabricate colloidal crystals with different crystal symmetries that mimic ionic crystals.[4] If the refractive index contrast between the constituents is high enough, these structures could be promising candidates for photonics applications. Prerequisite for successful fabrication of such structures is full control of size and surface charge of the polymer microparticles. In this chapter we describe the synthesis and characterization of relatively unexplored core-shell positively charged colloidal particles.

Emulsifier-free emulsion polymerization[5,6] has found widespread use due to the possibility of colloid stabilization via ionic initiator residues covalently bound to the polymer particles and has been successfully applied to both the preparation of anionic and cationic[6] monodisperse colloidal particles with sizes up to 1 μm. In this process, surface charge originates from initiator fragments and as initiator concentration influences particle size, surface charge density cannot be varied independently.

In the direct copolymerization of structural monomers with ionic monomers,[7,8,9,10,11,12] surface charge density and particle size can not be controlled independently since particle size strongly depends on the ionic monomer concentration.[13,14] This method leads to the formation of colloids of sizes up to 300 nm with a high surface charge density. Chemical modification of preformed functional colloid surfaces via, for example, quaternization of latexes containing benzyl chloride moieties using tertiary amines,[9,10,15] or by aminolysis of epoxy groups[12,16] has been used as an alternative approach to increase surface charge density.

Two-stage shot growth emulsion polymerization[11,15,17] enables one to introduce high surface charge densities on colloid particles and provides independent control over particle size up to 400 nm. In the first stage, e.g. styrene is copolymerized with a small quantity of ionic monomer. In this stage the size of the seed particles is regulated. When a high conversion (> 90%) is reached, a second stage monomer mixture is added. The ratio of structural monomer to ionic monomer in this mixture determines the final surface charge density. Finally, seeded polymerizations allow one to vary particle size in a wide range but generally provide limited control over surface charge density due to the formation of free, water-soluble polyelectrolyte at high ionic monomer concentrations.[17,18] Seeded polymerization constitutes a versatile approach if polyelectrolyte formation can be avoided.

Here we describe the synthesis and characterization of cross-linked core-shell cationic latexes using a two-stage process composed of emulsifier-free emulsion polymerization of styrene and the subsequent formation of a shell around the polystyrene seeds by co-polymerization of styrene with cationic comonomers. A novel cationic monomer, [(2-acryloyloxy)ethyl] trimethylammonium chloride (AETMAC) is employed and compared with [(2-methacryloyloxy)ethyl] trimethylammonium chloride (METMAC) and (vinylbenzyl)trimetylammonium chloride (VBTMAC) (for the chemical structures, see Scheme 4.1 in the Experimental Section), with the aim of synthesizing well-defined cationic latex particles of which the size and surface charge density can be controlled independently.

High-resolution scanning electron microscopy (HR-SEM) was used in this study for the visualization of the colloidal particles. HR-SEM allows one to study polymer samples without coating them with a conducting metal layer, as low electron acceleration voltages are used during measurements. Using HR-SEM, not only the size distribution of the colloidal particles but also their surface topology and possible side products such as small particles or polyelectrolyte formed during the shell formation step can be characterized.

4.1. Core preparation

Polystyrene latex particles were prepared by emulsifier-free emulsion polymerization of styrene in the presence of a crosslinker (DI, 5 mol % with respect to styrene), using a cationic initiator. The size of the particles was established by means of HR-SEM measurements. Various polymerizations were carried out at different styrene (St) concentrations. The corresponding particle diameter values with standard deviations and latex yield are summarized in Table 4.1. Figure 4.1 shows a logarithmic plot of the number average particle diameter against monomer concentration. The dependence of the particle diameter *D* on styrene concentration for colloids in the range from 200 nm to 500 nm at constant initiator concentration, ionic strength and temperature, using monomer concentrations between 0.1 and 0.8 mol/L is given by the equation:

$$\log (D) = 0.343 \cdot \log [St^I] + 2.701$$

Thus, the particle diameter varied as the 0.34 power of the initial monomer concentration. Similar results were found in other emulsifier-free emulsion polymerization systems.[5,6,14] The core syntheses were found to be highly reproducible. SEM images of the colloidal microparticles specified in Table 4.1 are shown in Figure 4.2.

The SEM images in Figure 4.2 clearly show the influence of changes in relative initiator and styrene concentrations on the particle morphology. At low styrene concentrations (Figure 4.2A) and, therefore, relatively high initiator concentrations, colloid microparticles with a small particle size and a high surface roughness were obtained. Upon increasing the monomer concentration, less rough and more rounded particles (Figure 4.2B) were formed, until finally, smooth and well-defined colloids (Figure 4.2C and 4.2D) were obtained. In all experiments, almost a full conversion of monomer to latex particles was achieved.

Table 4.1. Influence of styrene concentration on particle size[a]

Sample	$[St^I]$ (mol/L)	Number average diameter (nm)[b]	Standard deviation (nm)	% Variation on the mean	Latex yield (%)[c]
43	0.11	241	7	3.0	99
79	0.30	321	5	1.5	99
66	0.50	388	5	1.3	99
24	0.60	417	8	1.9	99
88	0.67	435	8	1.8	98
183	0.80	487	11	2.3	99

[a] [AIBA] = 4.42 mmol/L, [NaCl] = 2.57 mmol/L, DI = 5 mol % of the styrene amount (mol) used in the core (St^I), ionic strength = $15.8 \cdot 10^{-3}$ mol/kg, polymerization temperature: 70 °C.
[b] Determined using high-resolution SEM.
[c] Determined gravimetrically.

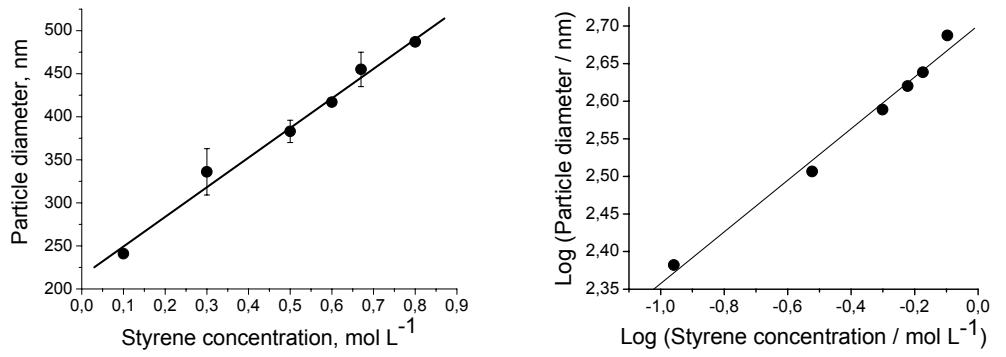

A B

Figure 4.1. A) Final particle diameter plotted versus monomer concentration. There is a linear relationship between the number average particle size and styrene concentration: $D = 244 \cdot [St] + 215$. B) Logarithmic plot of number average particle diameter against initial monomer concentration (see also Table 4.1).

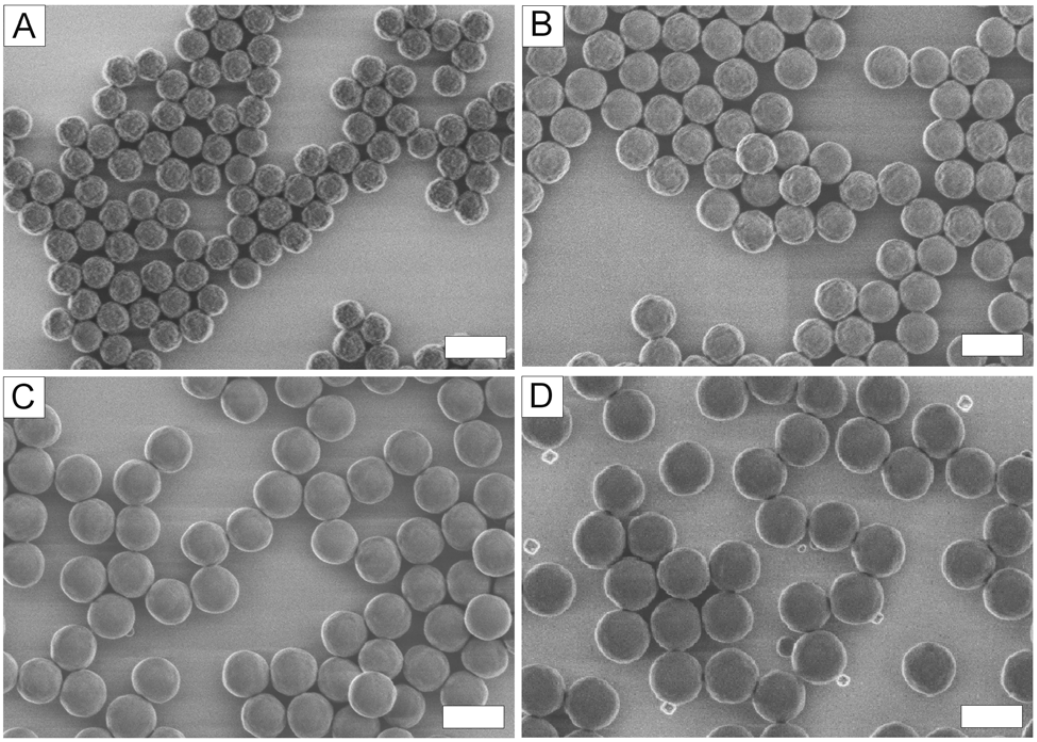

Figure 4.2. SEM images of selected samples shown in Table 4.1 with diameters of: A) ∅ 241 nm (43); B) ∅ 321 nm (79); C) ∅ 388 nm (66); D) ∅ 435 nm (88, the rectangles in Figure 4.2D are defects at the silicon surface). The scale bars are 500 nm.

4.2. Shell preparation

Colloidal particle size was controlled in the first stage (seed) of the polymerization, while the surface charge density was controlled in the second stage (shell). Surface charges were introduced on the latex particles via copolymerization of styrene with a cationic comonomer. The amount of styrene for copolymerization in the second stage was adjusted with respect to the amount of styrene used in the first stage. Comonomer concentrations were varied in the range between 1.3 mol % (2.4 wt %) and 10.7 mol % (20 wt %) based on the styrene charged in the second stage. A crosslinker, divinylbenzene (DVB), was added to ensure colloidal particle stability and minimize the chance of particle coagulation.

4.2.1. Cationic comonomers

Three functional monomers (VBTMAC, METMAC and AETMAC) were compared for their efficiency in forming cationic shells, initially at low comonomer content, see Table 4.2 and Figure 4.3. At low ionic comonomer concentrations, undesired side reactions, such as homopolymerization of ionic monomer or its copolymerization with styrene, forming water-soluble polyelectrolytes, are less likely to occur. Thus, the major part of the ionic monomers can be expected to be incorporated in the colloid particle shell. After copolymerization, the number average diameter of the colloidal particles increased by almost 30 nm, indicating shell formation. The formed core-shell particles were very stable and, as it is clearly seen in Figure 4.3, and possessed a low surface roughness. Despite the low concentration of VBTMAC, polyelectrolyte homopolymer or VBTMAC/St copolymer was observed near the edges of the dried sample (Figure 4.3A). This SEM image also shows that colloidal particles with the VBTMAC shells coagulate to some extent in the dry film. Using AETMAC, well-defined non-coagulating cationic core-shell particles were obtained (Figure 4.3B, right).

Table 4.2. Influence of cationic comonomer type on shell formation[a]

Sample	Comonomer	Comonomer mol % (wt %)[b]	Ionic strength x10^3 (mol/kg)	Number average final diameter (nm)
80	VBTMAC	1.3 (2.6)	5.56	348
81	AETMAC	1.3 (2.4)	5.57	348

[a] Core particles with a number average diameter of 321 nm (Table 4.1, entry 79) were used.
[b] AIBA content = 1.5 mol % based on the total monomer amount (mol) St^{II}+CoM+DVB.
$[St^{II}]$ = 0.067 mol/L, St^{II} : St^{I} = 1 : 3. DVB = 7.7 mol % based on the amount (mol) of St^{II}+CoM. [NaCl] = 1.7 mmol/L. Polymerization temperature: 70 °C. St^{I} = styrene used in the core, St^{II} = styrene used in the shell.

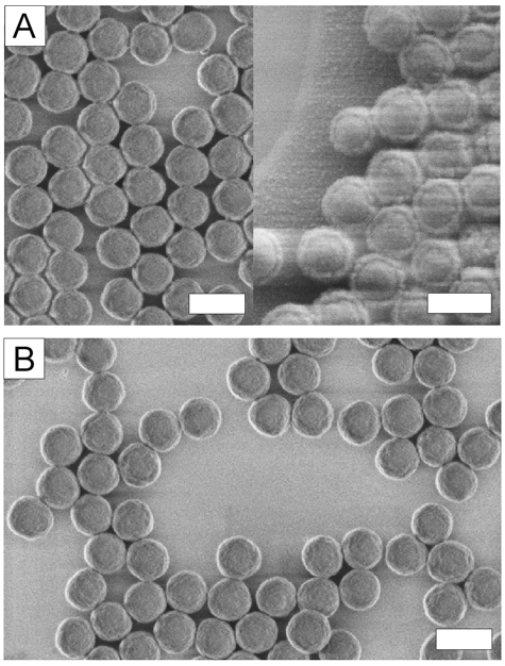

Figure 4.3. SEM images corresponding to core-shell microparticles with cationic shell comonomer A) VBTMAC; B) AETMAC, presented in Table 4.2. The scale bars are 500 nm.

Then, a much higher concentration of the cationic monomers was employed in shell formation (Table 4.3). The resulting core-shell particles are shown in Figure 4.4. In the case of VBTMAC and METMAC, the amount of undesired polyelectrolyte formed had increased. Colloid particles in the bulk featuring these monomers (Figure 4.4A, 4.4B, respectively) possessed a low surface roughness, but did show some coagulation, likely due to bridging by water-soluble polyelectrolyte.[19] With AETMAC the formation of polyelectrolyte was insignificant (Figure 4.4C). In addition, colloids with AETMAC comonomer were very stable (> 1 year) and demonstrated a low surface roughness, therefore this monomer was chosen for further shell-forming experiments.

Table 4.3. Influence of cationic comonomer type on shell formation[a]

Sample	Comonomer	Comonomer wt % (mol %)[b]	Ionic strength x10^3 (mol/kg)	Number average final diameter (nm)
70	VBTMAC	15 (7.3)	15.6	423
71	AETMAC	15 (8.0)	16.5	418
72	METMAC	15 (7.5)	15.7	420

[a] Core particles with a number average diameter of 388 nm (Table 4.1, entry 66) were used.
[b] AIBA content = 4 mol % based on the total monomer amount (mol) St^{II}+CoM+DVB.
$[St^{II}]$ = 0.067 mol/L, St^{II} : St^{I} = 1 : 5. DI = 5 mol % based on mol St^{II}+CoM. [NaCl] = 1.7 mmol/L.
Polymerization temperature: 70 °C.

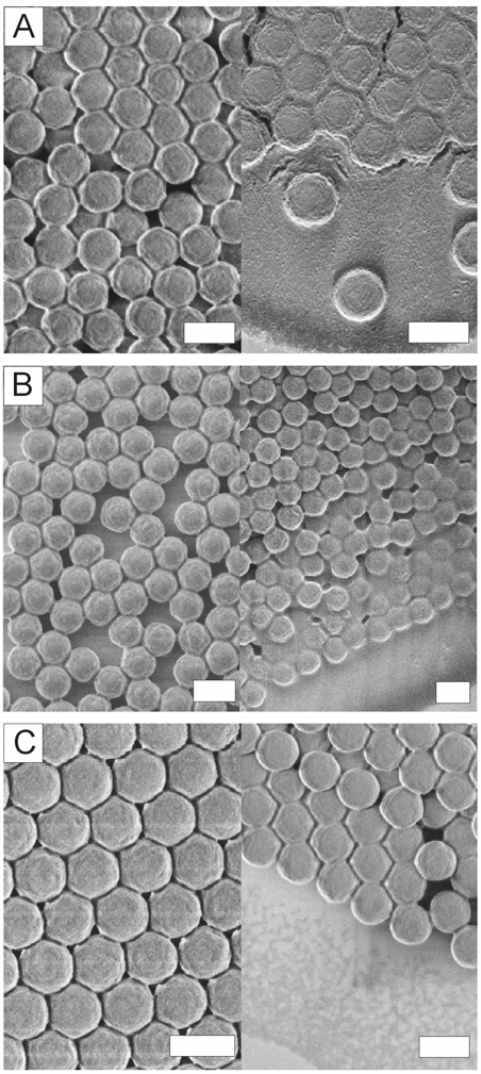

Figure 4.4. SEM images corresponding to core-shell microparticles with cationic shell comonomer A) VBTMAC; B) METMAC; C) AETMAC, see Table 4.3. The images on the right were taken near the sample edge. The scale bars are 500 nm.

4.2.2. Influence of cross-linker on shell formation

The stability of the shell in the cationic core-shell particles may be enhanced using crosslinkers. In order to gauge the influence of crosslinking, shells were formed in the presence and absence of a crosslinking agent. Addition of crosslinker led to the formation of core-shell particles with a more dense shell structure. In the presence of crosslinker, the final colloidal size was about 25 nm smaller than for colloids without crosslinker (Table 4.4). Also, colloidal particles with crosslinked shells possessed a much lower surface roughness

compared to particles with uncrosslinked shells. Shell crosslinking did not influence the amount of undesired polyelectrolyte formed, very little was found near the edges of both samples. Crosslinking does reduce particle coagulation (Figure 4.5).

Table 4.4. Influence of cross-linker on shell formation using AETMAC[a]

Sample	$[St^{II}]$ (mol/L)[b]	DI (mol %)[c]	Ionic strength x10^3 (mol/kg)	Number average final diameter (nm)
77	0.064 (1:5)[d]	-	16	442
71	0.064 (1:5)[d]	5	16	418

[a] Core particles with a number average diameter of 388 nm (Table 4.1, entry 66) were used.
[b] AIBA content = 3 mol % based on the total monomer amount (mol) St^{II}+AETMAC+DVB. $[St^{II}]$ = 0.064 mol/L, St^{II} : St^{I} = 1 : 5. AETMAC content = 8 mol % (15 wt %) based on mol styrene used in the shell (St^{II}). [NaCl] = 1.7 mmol/L. Polymerization temperature: 70 °C.
[c] Based on mol St^{II}.
[d] Ratio of styrene in the shell and styrene in the core: St^{II} : St^{I}.

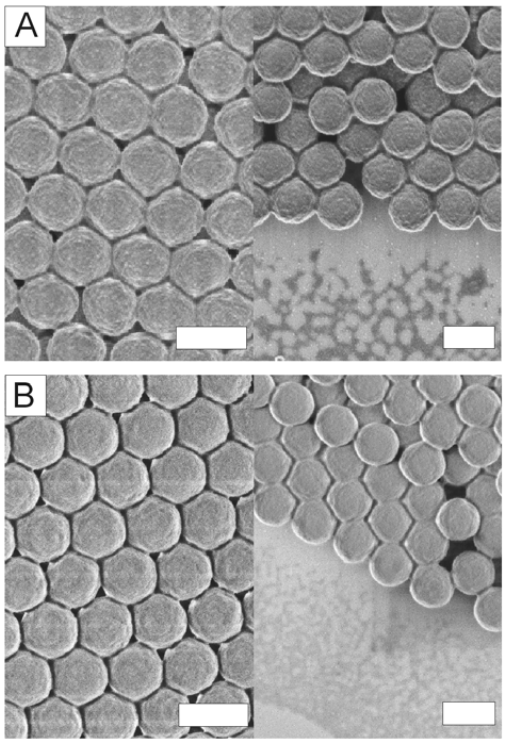

Figure 4.5. SEM images of core-shell microparticles featuring AETMAC cationic shells. Sample A) without crosslinker; B) with 5 mol % crosslinker, see Table 4.4. The images on the right were taken near the sample edge. The scale bars are 500 nm.

Table 4.5. Influence of initiator concentration on shell formation using AETMAC[a]

Sample	[St^{II}] (mol/L)[b]	AIBA (mol %)[c]	Ionic strength x10^3 (mol/kg)	Number average diameter core (nm)	No. av. diameter core+shell (nm)
84	0.067 (1:3)[d]	1.5	6.11	338 (Table 1, recipe 79)	353
90	0.156 (1:3)[d]	0.61	7.66	435 (Table 1, recipe 88)	480
96	0.093 (1:5)[d]	0.2	4	475 (Table 1, recipe 88)	510

[a] AETMAC content = 1.75 mol % (3.3 wt %) based on mol St^{II}. DVB content = 7 mol % based on mol St^{II}+AETMAC. [NaCl] = 1.7 mmol/L. Polymerization temperature: 70 °C.
[b] St^{II} = styrene used in the shell preparation (stage II).
[c] Based on mol St^{II}+DVB+AETMAC.
[d] Ratio of styrene in the shell and styrene in the core: St^{II} : St^{I}.

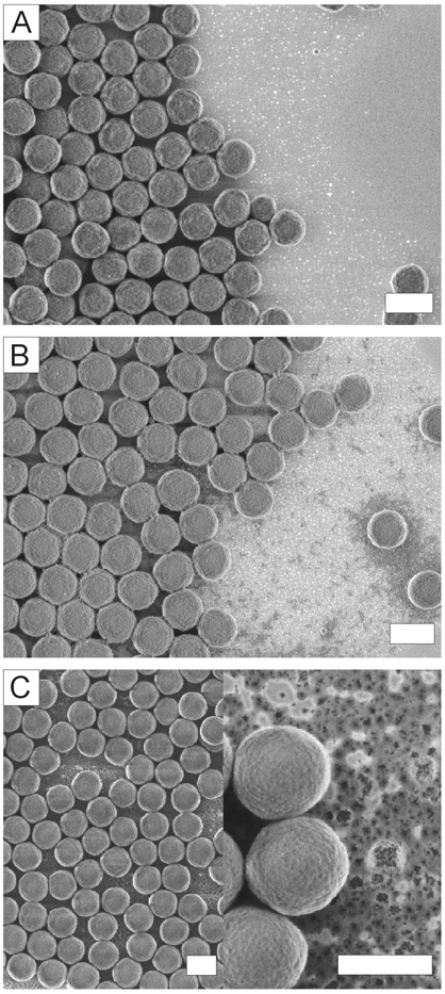

Figure 4.6. SEM images of core-shell microparticles featuring AETMAC cationic shells with initiator concentrations in shell formation of A) 1.5 mol %; B) 0.6 mol %; C) 0.2 mol %, see Table 4.5. The scale bars are 500 nm.

4.2.3. Influence of initiator concentration on shell formation

Table 4.5 summarizes the results of the core-shell particle formation with various initiator concentrations. In all reactions, 1.75 mol % of AETMAC monomer was used. The shell was cross-linked with 7 mol % of DVB. The amount of initiator was calculated in relation to the amount of monomers used in the second stage and was taken as 1.5, 0.6 and 0.2 mol % of the total, respectively. SEM images of these particles are presented in Figure 4.6. As a result of copolymerization, number average particle diameter values increased by 15-45 nm. When the initiator amount was 1.5 mol %, a small number of particles exhibiting diameters of 5-10 nm was found near the edge of the dried sample (Figure 4.6A). The surface roughness of the colloidal microparticles was found to be low by visual inspection of the SEM images. As the initiator level was decreased to 0.6 mol %, the surface roughness increased, and an increased number of small particles was observed (Figure 4.6B). With a further decrease in the amount of initiator, a large quantity of polyelectrolyte appeared (Figure 4.6C). On the basis of these observations, 1.5 mol % of initiator was taken as the optimal concentration.

4.2.4. Cationic core-shell latex particles with controlled surface charge densities

In the previous paragraphs, several comonomers were compared. By using AETMAC in the shell-forming step, well-defined cationic colloidal particles were obtained while only a small amount of polyelectrolyte, even at a relatively high comonomer concentration of 8.1 mol % (15 wt %), and no polyelectrolyte at 1.3 mol % (2.4 wt %) of comonomer was observed. In Table 4.6, the results of copolymerization of styrene with AETMAC at different concentrations are presented. All copolymerization reactions were performed in the presence of 7.5 mol % cross-linking agent (DVB). Salt concentration was not changed in the emulsion during polymerization, therefore, variations in ionic strength are caused by the different amounts of initiator and comonomer. The size of the colloids increased by 15-45 nm, indicating shell formation. Particles formed after the core-shell polymerization were well-defined and possessed a low surface roughness, see Figure 4.7.

Based on this more extensive range of employed AETMAC concentrations, we can conclude that below 5.3 mol % (10 wt %), no polyelectrolyte was detected, while at high comonomer concentrations (above 5.3 mol %) a small amount of free polyelectrolyte (not incorporated in the shell) was detected. The amount of free polyelectrolyte did not increase when the AETMAC concentration was increased further from 5.3 mol % to 10.7 mol %.

Table 4.6. Influence of AETMAC concentration on shell formation[a]

Sample	[St^{II}] (mol/L)	AIBA (mol %)[b]	AETMAC, mol % (wt %)[c]	Ionic strength x10^3 (mol/kg)	Number average diameter core (nm)	No. av. diameter core+shell (nm)	Zeta potential (mV)	σ, ($\mu C/cm^2$)[d]
81	0.067 (1:3)[e]	1.5	1.3 (2.4)	5.57	325	348	51.8	11.6
84	0.067 (1:3)[e]	1.5	1.72 (3.3)	6.11	338	360	52.3	14.0
85	0.067 (1:3)[e]	1.5	2.7 (4.95)	6.80	338	370	55.6	17.5
155	0.067 (1:3)[e]	1.3	5.3 (10)	6.6	365	380	51.8	-
71	0.064 (1:5)[e]	4	8.1 (15)	16.5	388	418	50.9	36.6
156	0.04 (1:5)[e]	2.4	10.7 (20)	9.87	365	380	56.4	44.6

[a] DVB content = 7.5 mol % based on mol St^{II}+AETMAC. [NaCl] = 1.7 mmol/L. Polymerization temperature: 70 °C.
[b] Based on mol St^{II}+DVB+AETMAC.
[c] With respect to mol St^{II}.
[d] Obtained by potentiometric titration.
[e] Ratio of styrene in the shell and styrene in the core: St^{II} : St^{I}.

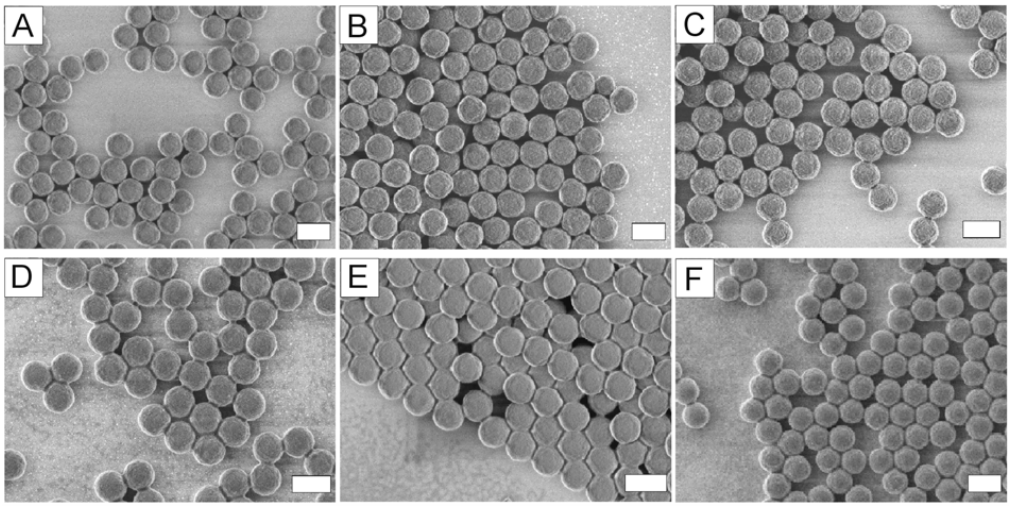

Figure 4.7. SEM images of core-shell microparticles featuring cationic shells, formed using AETMAC concentrations of A) 1.3 mol %; B) 1.72 mol %; C) 2.7 mol %; D) 5.3 mol %; E) 8.1 mol %; F) 10.7 mol %, see Table 4.6. The scale bars are 500 nm.

Zeta potential measurements were carried out to characterize the stability of the colloidal core-shell particles. According to the DLVO (Deryaguin-Landau-Verwey-Overbeek) theory, stability of colloidal systems is governed by a balance between attractive Van der Waals forces and the electrical repulsion due to colloid particle surface charge. The magnitude of the zeta potential gives an indication of the stability of colloidal systems. If particles in a dispersion have a large negative or positive zeta potential, they repel each other and the dispersion is stable. At low values of the zeta potential, the colloidal particles may

aggregate due to the attractive forces. Absolute zeta potential values above 30 mV are commonly associated with stable colloids while values below 30 mV indicate susceptibility to agglomeration.[20] Zeta potential measurements, presented in Table 4.6, show that the core-shell particles formed are highly stable in the dispersion. Indeed, no coagulation was observed in the colloidal dispersion upon storage for more than a year.

Surface charge densities (σ) were measured by potentiometric titration of the latex dispersions. The surface charge densities increased with increasing cationic monomer concentration, but deviated slightly from a linear dependence at higher AETMAC concentrations. At these high concentrations, monomer incorporation in the shell was accompanied by some polyelectrolyte formation outside the shell. This polyelectrolyte homopolymer was removed in the purification of the core-shell particles, leading to a slightly lower surface charge density than anticipated. Figure 4.8 demonstrates that surface charge density can be controlled by varying the cationic comonomer concentration.

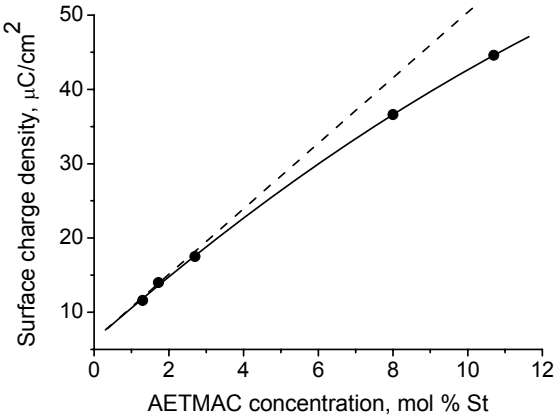

Figure 4.8. Surface charge density versus AETMAC concentration expressed in mol % of St used in the shell formation. The dashed line represents the expected surface charge density at full ionic monomer incorporation.

The stability of surfactant-free colloidal systems is not only determined by surface charge density but also depends on the ionic strength of the aqueous medium, as electrostatic repulsion is reduced due to charge screening by counterions in the colloidal dispersion.[21] Ionic strength is known to have a marked influence on particle size (cores) in emulsifier-free emulsion polymerization processes. Upon increasing ionic strength, the final diameter of both anionic[5] and cationic polystyrene colloidal particles increased. The lowest utilizable ionic strength is determined by the initiator concentration, the highest ionic strength by the onset of polydispersity or coagulation.[5,6] To establish whether ionic strength had an influence on shell

formation, the ionic strength in the colloidal core dispersion was adjusted by adding NaCl, see Table 4.7. Shell formation was performed in the presence of DVB at an AETMAC concentration of 8 mol % (15 wt %). An increase in NaCl concentration from 1.7 to 2.2 mM led to the formation of new colloids of small size (Figure 4.9) and to large quantities of free polyelectrolyte. At ionic strengths of up to $16 \cdot 10^{-3}$ mol/kg, the formation of such undesired side products is prevented.

Table 4.7. Influence of ionic strength on AETMAC shell formation[a]

Sample	$[St^{II}]$ (mol/L)[b]	NaCl (mM)	Ionic strength $x10^3$ (mol/kg)	Number average diameter core+shell (nm)
71	0.064 (1:5)[c]	1.7	16	418
76	0.064 (1:5)[c]	2.2	21.1	410

[a] Core particles with a number average diameter of 388 nm (Table 4.1, entry 66) were used.
[b] AIBA content = 4 mol % based on the total monomer amount (mol) St^{II}+AETMAC+DVB. AETMAC content = 8 mol % (15 wt %) based on mol St^{II}. DVB = 7.5 mol % based on mol St^{II}+AETMAC. Polymerization temperature: 70 °C.
[c] Ratio of styrene in the shell and styrene in the core: St^{II} : St^{I}.

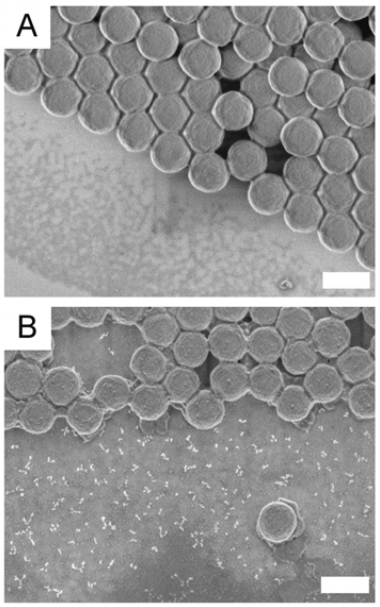

Figure 4.9. SEM images correspond to the samples with A) 1.7 mM NaCl; B) 2.2 mM NaCl presented in Table 4.7. The scale bars are 500 nm.

Conclusion

Polystyrene colloids with number average diameter values between 200 and 500 nm exhibiting narrow size distributions were prepared in a two stage polymerization process. The number average diameter of the core colloids increased with increasing styrene concentration in the employed concentration range. Three monomers were explored for their efficiency in forming cationic shells around the polystyrene cores. The monomer AETMAC, to our knowledge not reported in the literature for the preparation of cationic colloidal core-shell particles, formed smooth cationic shells and could be incorporated in higher concentrations than proved possible with the commonly used VBTMAC and METMAC monomers, which gave undersired polyelectrolyte side products already at low cationic monomer concentrations. Thus, colloid surface charge densities could be controlled over a wider range than was possible with VBTMAC and METMAC. Crosslinking of the shell was found to enhance shell stability. Optimal initiator concentration and ionic strength values for shell formation were identified.

Experimental part

Materials

Styrene (St) (for synthesis, Merck) and divinylbenzene (DVB) (50 % in ethyl vinyl benzene, Fluka) were distilled under reduced pressure and stored at 4 °C. [2-(acryloyloxy)ethyl]trimethylammonium chloride (AETMAC) (80 wt % in water, Aldrich) and [2-(metacryloyloxy)ethyl]trimethylammonium chloride (METMAC) (75 wt % in water, Aldrich) were precipitated in acetone, washed several times with acetone and finally washed with ethyl ether. (Vinylbenzyl)trimethylammonium chloride (VBTMAC) (Aldrich, 99 %) was dissolved in ethanol, precipitated in acetone, washed with acetone followed by ethyl ether and dried under reduced pressure.[6] Purified VBTMAC, METMAC and AETMAC were stored at 4 °C. Milli-Q water (Millipore, 18.2 MΩ·cm) was used in all experiments. 2,2'-Azobis(2-methylpropionamidine) dihydrochloride (AIBA, or V-50) (97 %, Aldrich) and 1,3-diisopropenylbenzene (DI) (Aldrich) were used without further purification. Sodium chloride (>99.5 %, Fluka) and all solvents (analytical grade) were purchased from Merck and used as received.

Synthesis of polystyrene core particles

All polymerization reactions were carried out in a 250 mL three-necked round-bottomed flask equipped with a reflux condenser, septum and magnetic stirring bar. A total reaction volume of 200 mL was normally used. Emulsifier-free emulsion polymerization recipes described by Ottewill[5] and Pelton[6] were employed for the preparation of the polystyrene colloids. Representative recipes are shown in Table 4.1. Briefly, the flask was charged with Milli-Q water (180 mL) and NaCl (2.57 mM). Oxygen was removed by passing a slow stream of nitrogen through the solution for 30 min while stirring at 450 rpm. The gas flow rate was kept low in order to minimize evaporation. After 30 min, a mixture of styrene and crosslinker (DI) was added at once to the three-necked flask. AIBA (4.42 mM) was dissolved in Milli-Q (20 mL) in a separate conical flask and was degassed. The three-necked flask was then immersed in a preheated oil bath (70 °C) and left for 1 h to attain thermal equilibrium. Finally AIBA was added in one portion. Concentrations of initiator and NaCl were identical for all reactions, therefore the ionic strength was constant for all experiments ($15.8 \cdot 10^{-3}$ mol/kg). Stirring was continued for 24 h. Finally, the vessel was removed from the oil bath and left to cool. The latex dispersion was decanted through a filter packed with glass wool in order to remove any homopolymer film and coagulum formed during the synthesis. The latex particles were used as seeds for the growth of the shell layer.

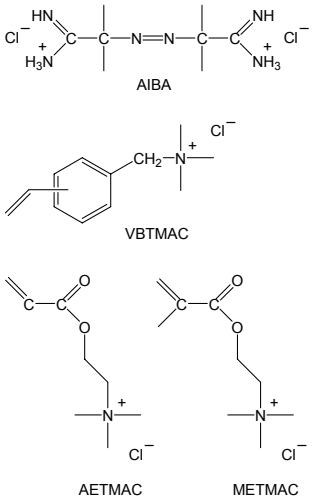

Scheme 4.1. Structures of AIBA, VBTMAC, AETMAC and METMAC.

Synthesis of core-shell latex particles

In a typical experiment (sample 84, Table 4.6), the setup described above was charged with a seed dispersion, which was degassed and heated to 70 °C while stirring at 450 rpm. In separate flasks, two solutions were prepared: one containing styrene and a crosslinker (DVB, 0.055 g), the other the AIBA initiator (0.026 g) and cationic comonomer (0.023 g) dissolved in Milli-Q water (10 mL). The solutions were degassed using nitrogen and added simultaneously within 30 min to the seed dispersion. After 24 hours, the flask was removed from the oil bath and allowed to cool. The latex was decanted through a filter packed with glass wool.

Particle size determination

A small amount of a latex dispersion was diluted with Milli-Q water until the solution was almost transparent. A drop of dispersion was placed on a cleaned silicon substrate and left to dry. Dried colloids were examined with a High Resolution LEO 1550 FEG scanning electron microscope (SEM) at low acceleration voltages (0.5 kV), allowing us to image the latex samples without applying a metal coating. The colloidal particle number average diameter and standard deviation were calculated from the SEM images[22] based on 30-50 particles per latex sample, using the image processing program Scion Image Beta 4.0.2.

Yield determination

The yield of the colloidal particles formation was determined gravimetrically at the end of the polymerization. A measured amount of latex dispersion was centrifuged at 15000 rpm for 15 min and dried at room temperature in a vacuum oven. The yield was calculated according to the following equation:[23]

$$C(\%) = \frac{W_1 / W_2}{m_1 / (m_1 + m_2)} \times 100\%$$

where C(%) is the total conversion of polymer; W_1 is the weight of dried polymer; W_2 is the weight of the sample withdrawn from the reaction solution; m_1 is the weight of monomer added; m_2 is the weight of the medium.

Zeta potential measurements

Zeta potential values were determined by laser Doppler electrophoresis using a Zetasizer 2000 (Malvern Instruments Ltd., Malvern, UK). For the measurements, a small amount of a latex dispersion was diluted with Milli-Q water until the solution was almost transparent.

Determination of surface charge densities

Surface charge densities were analysed by potentiometric titration of latex dispersions using 0.01 N $AgNO_3$. Before titration, the latex dispersion was placed in polycarbonate tubes and centrifuged three times at 17000 rpm for half an hour to remove possibly formed polyelectrolyte species. After each centrifugation step, the latex microparticles obtained were re-dispersed in Milli-Q water using an ultrasonic bath. The values of surface charge densities (σ) were calculated according to the following equation:[24]

$$\sigma = \frac{Fn\rho R}{3W}$$

where F is the Faraday constant, n is the number of moles of $AgNO_3$ required to neutralize the surface functional groups of latex particles, ρ is the density of colloids (1.05 g/cm^3), R is the radius of latex spheres, and W is the fraction solid content of the latex.

References

[1] See for example Y. Xia, B. Gates, Y. Yin, Y. Lu, *Adv. Mater.* **2000**, *12*, 693.
[2] P. Bartlett, R. H. Ottewill, P. N. Pusey, *Phys. Rev. Lett.* **1992**, *68*, 3801.
[3] K. P. Velikov, C. G. Christova, R. P. A. Dullens, A. van Blaaderen, *Science* **2002**, *296*, 106.
[4] M. E. Leunissen, C. G. Christova, A.-P. Hynninen, C. P. Royall, A. I. Campbell, A. Imhof, M. Dijkstra, R. van Roij, A. van Blaaderen, *Nature* **2005**, *437*, 235.
[5] J. W. Goodwin, J. Hearn, C. C. Ho, R. H. Ottewill, *Coll. Polym. Sci.* **1974**, *252*, 464.
[6] J. W. Goodwin, R. H. Ottewill, R. Pelton. *Coll. Polym. Sci.* **1979**, *257*, 61.
[7] R. Arshady, *J. Macromol. Sci., Rev. Macromol. Chem. Phys.* **1992**, *32*, 101.
[8] Z. Liu, H. Xiao, N. Wiseman, *J. Appl. Polym. Sci.* **2000**, *76*, 1129.
[9] Y. Deng, Z. Yan, N. Yang, *Coll. Polym. Sci.* **1999**, *277*, 227.
[10] S. A. F. Bon, H. van Beek, P. Piet, A. L. German, *J. Appl. Polym. Sci.* **1995**, *58*, 19.
[11] K. H. van Streun, W. J. Belt, P. Piet, A. L. German, *Eur. Polym. J.* **1991**, *27*, 931.
[12] D. J. Voorn, W. Ming, A. M. van Herk, *Macromolecules* **2005**, *38*, 3653.
[13] M. S. Juang, I. M. Krieger, *J. Polym. Sci., Polym. Chem.* **1976**, *14*, 2089.
[14] L. J. Liu, I. M. Krieger, *J. Polym. Sci. Polym. Chem.* **1981**, *19*, 3013.
[15] W. T. Ford, H. Yu, J. J. Lee, H. El-Hamshary, *Langmuir* **1993**, *9*, 1698.
[16] For other functional latexes see A. Oláh, M. A. Hempenius, G. J. Vancso, *Eur. Polym. J.* **2004**, *40*, 763.
[17] J. H. Kim, M. Chainey, M. S. El-Aasser, J. W. Vanderhoff, *J. Polym. Sci., Polym. Chem.* **1989**, *27*, 3187.
[18] Z. Liu, H. Xiao, *Polymer* **2000**, *41*, 7023.
[19] J. L. Guillaume, C. Pichot, J. Guillot, *J. Polym. Sci., Polym. Chem.* **1988**, *26*, 1937.
[20] N. Spanos, P. G. Klepetsanis, P. G. Koutsoukos, *Encyclopedia of Surface and Colloid Science*, ed. A. T. Hubbard, NY, Marcel Dekker, Inc. **2002**, vol. 1, 829.
[21] S. Peach, *Macromolecules*, **1998**, *31*, 3372.
[22] E. A. Collins, *Emulsion Polymerization and Emulsion Polymers*, ed. P. A. Lovell, M. S. El-Aasser, Chichester, John Wiley & Sons Ltd, **1997**, ch. 12, 391.
[23] Y.-M. Wang, C. Y. Pan, *Coll. Polym. Sci.* **1998**, *277*, 658.
[24] H. B. Sunkara, J. M. Jethmalani, W. T. Ford, *J. Polym. Sci., Polym. Chem.* **1994**, *32*, 1431.

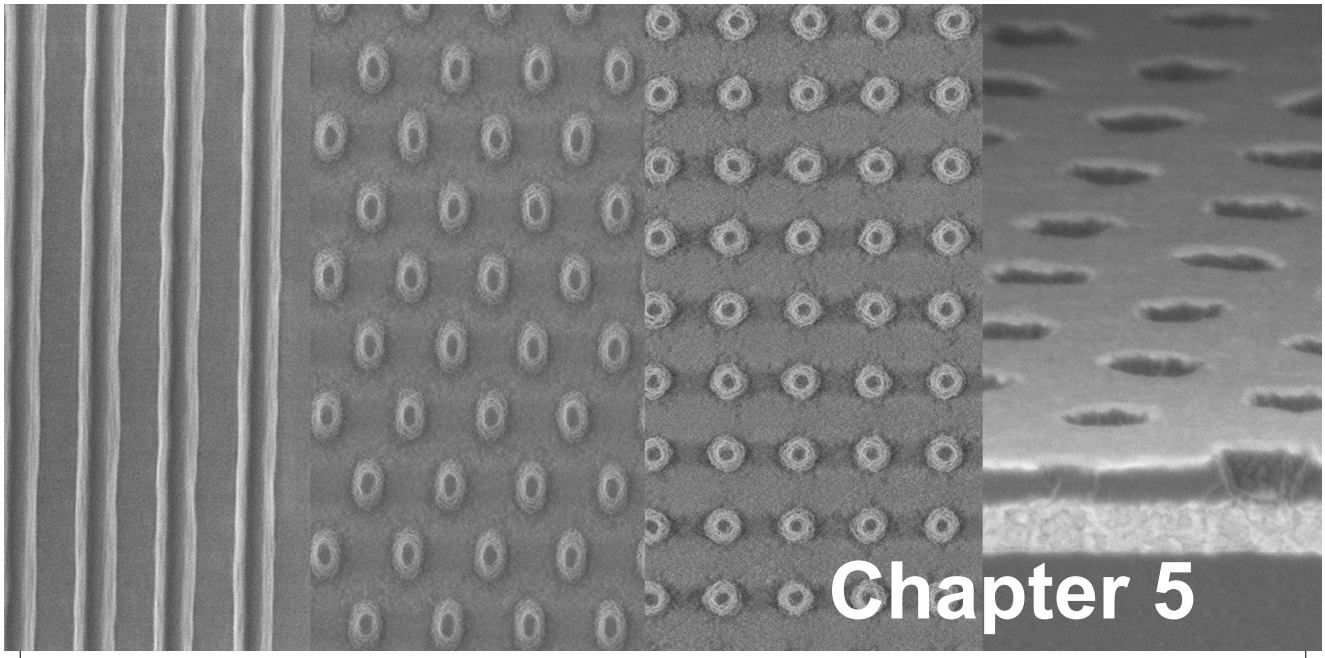

Chapter 5

Electrode Surface Patterning[*]

A procedure for the topological patterning of electrode surfaces was developed. Electrodes composed of a glass disk and a conductive ITO layer were topologically structured using a combination of laser interference lithography (LIL)[†] and a lift-off method. Lines, hexagonal, square and rectangular patterns were generated by LIL in a suitable positive photoresist. The patterns covered the electrode surface over an area of 1.5 x 1.5 cm. Pattern periodicities were tuned between 0.3 μm and 1 μm by changing the angle between the sample holder and incoming laser beam. Photoresist patterns were translated in the form of depressions into a dielectric SiO_2 layer using a lift-off process. Lithographic process parameters as exposure dose, development time and etching conditions are discussed. Electrode patterns were characterized by HR-SEM.

[*] Parts of this chapter have been published in: N. V. Dziomkina, M. A. Hempenius, G. J. Vancso, *Advanced Materials* **2005**, *17*, 237.

[†] The LIL set-up was property of the groups "Integrated Optical MicroSystems", "Systems and Materials for Information Storage" and "Transducers Science and Technology" (University of Twente) and access was kindly provided for our research.

Introduction

To enable the study of colloidal crystallization in confined geometries, various lithographic techniques have been applied for surface patterning such as conventional optical lithography,[1,2,3,4] soft lithography,[5,6,7,8] imprint lithography,[9] holographic lithography,[10,11,12,13] electron beam[14,15] and focused ion beam[16] techniques. In our project, the generation of periodic patterns with sub-micrometer periodicities and various pattern symmetries was necessary to direct template-assisted growth. Conventional optical lithography requires use of a photomask[17] and as a consequence a resolution limit of 1.5 μm (system specific)[18] can be achieved. In soft[19,20] and imprint[21] lithography, patterned structures with sub-micrometer resolution can be easily obtained, but these techniques require corresponding masters. Electron and ion beam techniques allow one to create the extremely fine patterns in the desired region of periodicities, but these techniques are slow and expensive.[17] Holographic lithography[22,23,24] is a maskless technique that allows generating 2D periodic structures over large areas (on the order of cm^2) with sub-micrometer resolution.[25,26] It is also fast (periodic patterns are generated in tens of seconds) and cost-effective (it does not require a complicated set-up). Consequently, holographic lithography was chosen as a suitable technique for surface patterning that corresponds to our requirements. Holographic lithography has been already successfully applied in the fabrication of 3D photonic crystals,[27] photonic crystal slabs,[28] microsieves,[26,29] high-density data storage devices,[30] grating filters[31] and beam splitters.[32]

5.1. Laser Interference Lithography

Laser interference lithography (LIL)[25,26,33,34] is a holographic technique, where an interference pattern of two obliquely incident beams of laser light is generated in a suitable photoresist. There are two basic LIL set-up configurations: Lloyd's mirror configuration[26,33,34,35] and a set-up comprising a beam splitter.[22,25,26] A LIL set-up with Lloyd's mirror configuration was used in this project, see Figure 5.1. In Lloyd's mirror configuration a mirror[‡] is placed perpendicular to a sample holder, allowing one to obtain two incident beams from one light source: one part of the light reaches the substrate directly and another is first reflected by a mirror and then hits the substrate surface. The sample holder is positioned at a distance L (L = 2 m) from a special filter, featuring a pinhole and a lens, in such a way that a divergent laser beam completely covers the mirror/sample holder.

[‡] Dielectric UV-MAXBRlte mirror (with 007 coating) with an average reflectance of > 98 % for a wavelength range of 245 – 390 nm.

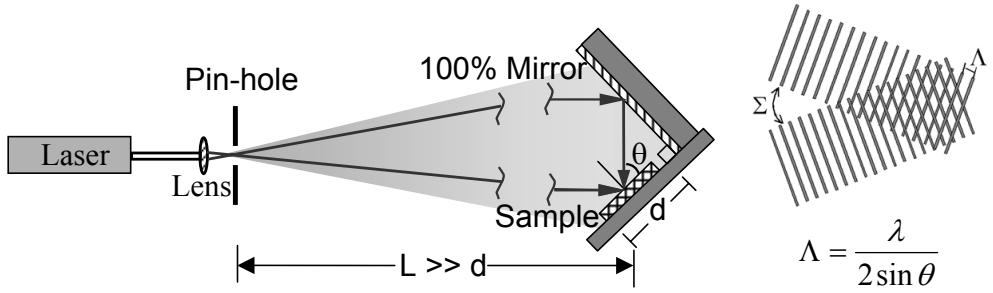

Figure 5.1. Schematic representation of the laser interference lithography (LIL) set-up (left) and double exposure pattern, where Σ is the rotation angle of the sample holder that can be varied between 0º, 60º and 90º (right), θ is angle of incidence, λ is wavelength of the light and Λ is the pattern periodicity. The distance (L) between pinhole and sample holder is much larger than the sample size (d) to ensure good beam uniformity over the sample surface and full sample surface coverage.

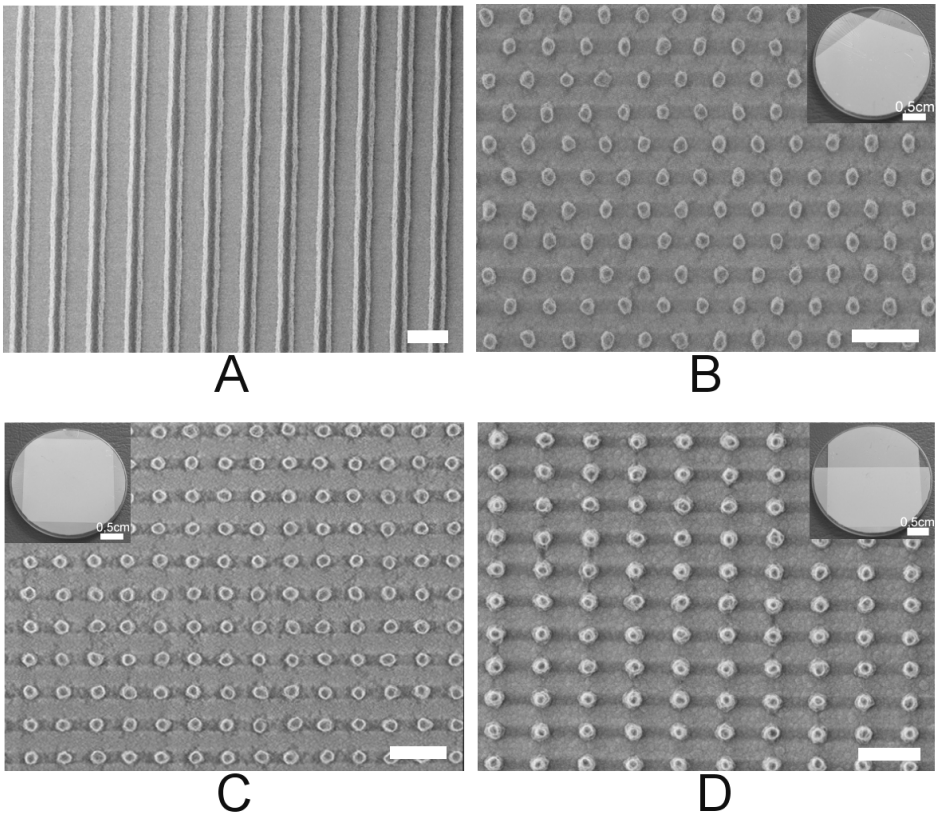

Figure 5.2. SEM images of photoresist patterns: A) lines, B) hexagonal, C) square and D) rectangular. In the corner of the images B, C and D, pictures of actual electrodes are shown. Scale bar is 0.5 μm.

This distance is large enough to obtain such a diameter for the spherical Gaussian beam on the mirror/sample holder that the incoming wave front can be approximated as a plane wave over the exposed area. A special filter allows also high frequency noise to be removed from the beam to provide a clean Gaussian profile. Lloyd's mirror set-up configuration has some advantages over other interferometers like:

- The fixed position of the mirror perpendicular to the substrate guarantees, using simple trigonometry, that the light reflected from the mirror is always incident on the substrate at the same angle as the original beam;
- The fixed mirror/substrate system is less sensitive to vibrations, beam motions, etc;
- The set-up is simple in alignment and adjustment;

Besides set-up advantages there are also some disadvantages like:

- Roughness of the mirror directly influences the grating quality;
- Sensitivity to dust particles and a damaged mirror surface.

As a consequence of interference, a line pattern in the photoresist layer is obtained, see Figure 5.2A. By rotating the sample holder by 60 or 90 degrees and performing a second light exposure on the same sample (double exposure), hexagonal and square types of pattern can be created, respectively. If a positive photoresist is used in double exposure, then the illuminated areas of the photoresist become soluble, revealing a pillar photoresist structure after development. In the case of a negative photoresist, exposed parts of the photoresist cross-link, revealing a pit (hole) photoresist structure after development.[36] Examples of patterned hexagonal and square structures in positive photoresist are shown in Figure 5.2, B, C. Pattern periodicity Λ relates to the incident angle θ and can be determined from the following formula:

$$\Lambda = \frac{\lambda}{2\sin\theta}$$

where λ is the wavelength of the laser light which in our case is 266 nm. The smallest period that can be theoretically obtained equals to $\lambda/2$, corresponding to $\theta = 90°$. Practically, in this case the laser light slides along the sample surface and no interference in the photoresist layer occurs. By performing multiple exposures in the same photoresist layers, varying pattern periodicities and rotation angle, patterns of various complex structures can be obtained. As an example, the combination of two different pattern periodicities at a rotation angle of the sample holder $\Sigma = 90°$ leads to the formation of the rectangular type of pattern, Figure 5.2D.

The profile of structures generated in a photoresist depends on several factors: light exposure pattern, photoresist sensitization and photoresist development. The grating profile for a single photoresist exposure is shown in Figure 5.3A. In fabricating gratings, control over the initial resist thickness is important in order to minimize losses that are due to absorption of the incident wave in the film and to ensure that the pattern extends completely down to the substrate surface. The photoresist thickness can be adjusted by using a companion thinner and by the spin-coating speed. In addition, wet development is an isotropic process that introduces stronger nonlinearities to a photoresist profile than those arising from photosensitization processes. This phenomenon generally is called loss in resolution, and occurs because of several effects such as chemical diffusion of photoactive and developer species, dependence of the development rate on surface curvature, the size of the smallest particles of photoresist that are removed by the developer etc. Depending on the combination of exposure time, light intensity and development time, the grating profile can be optimized.

When a photoresist is exposed twice to UV light, then the photoresist contour plot of

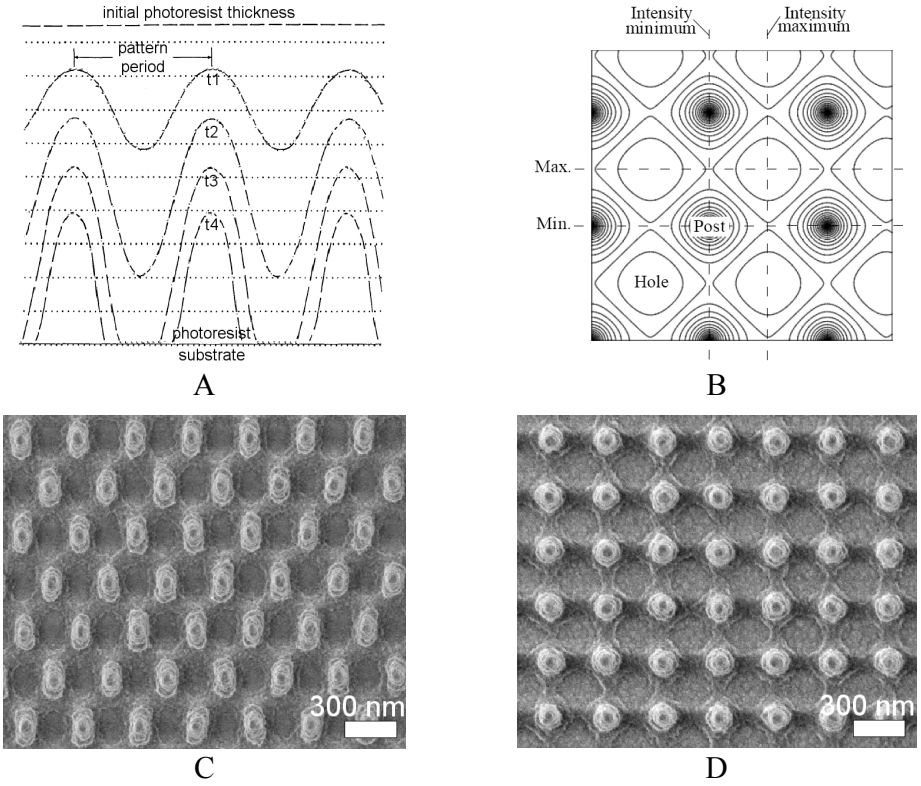

Figure 5.3. A) Photoresist profile dependence on development time from t1 to t4; B) Contour plot of the received dose of UV light in photoresist exposed twice to UV light with an intermediate rotation over 90° (logarithmic scale of intensity);[26] C) Hexagonal and D) square types of photoresist structures, where photoresist was exposed to UV with an exposure dose of 43.6 mJ/cm^2 and 40.54 mJ/cm^2, respectively and a development time of 10 s, these were rather low in order to clean up the substrate surface between neighboring photoresist pillars.

the received dose is represented by holes (areas of crossed maximum intensities or exposed photoresist) and posts (areas of crossed minimum intensities or unexposed photoresist), shown in Figure 5.3B. The received dose or exposure dose *ED* is determined by multiplying the total absorbed intensity in the layer of material I_{abs} by the exposure time τ. The reflectance from the SiO_2 and ITO layers was not included in absorbed intensity calculations. The total absorbed intensity by the materials:

$$I_{abs} = I_{\max} - I_{trans} = I_{\max} T(1 - e^{-\frac{4\pi}{\lambda}\varepsilon L})$$

where I_{trans} is the intensity of light after the passage of radiation through a layer of material of thickness L (here – photoresist); $T = (1 - R)$ – transmittance, R is the reflectance for the case of s-polarized light determined from Fresnel's equations, ε is an extinction coefficient. The reflectance from underlying layers was neglected, because of the low refractive index contrast.

The intensity in interference maxima I_{max} can be calculated from the so called interference equation:[37]

$$I_{\max} = I_1 + I_2 + 2(I_1 I_2)^{1/2} \cos\varphi$$

where I_1 and I_2 are intensities of constituent waves, assumed to be equal, and assuming that the light intensity reflected from the mirror had the same value as a direct beam, $\varphi = \varphi_2 - \varphi_1$ is the phase difference. In the case when $\varphi = 0$ and $I_1 = I_2 = I_0$, the intensity of the total wave is $I_{max} = 4I_0$. The initial wave intensity I_0 was determined experimentally as:

$$I_0 = \frac{P}{\pi R^2}$$

where P is the continuous wave power (μW), measured by an Ultima LabMaster™ power meter placed in front of the sample/mirror holder and R = 3 mm is the radius of the detector active area[§].

SEM examples of hexagonal and square types of photoresist structures obtained in this work are shown in Figure 5.3C and Figure 5.3D. Photoresist was exposed to UV light, using a sufficient exposure dose (it will be shown later) but development time was rather short to open up the substrate surface between photoresist pillars (post areas). A subsequent increase in development time (see Figure 5.3A) cleared up substrate surface between neighboring post regions. The same type of images was obtained when photoresist was exposed to UV light with an insufficient exposure dose (see Figure 5.3B). A value of the exposure dose and

[§] LM-2 UV-enhanced silicon sensor for a wavelength of 250 - 400 nm (Coherent Inc.).

development time can be optimized in such a way that photoresist post areas can be separated from each other. During the exposure, the laser light is partially reflected by the substrate and interferes with the incoming beam, creating an interference pattern in the vertical direction (vertical standing wave patterns). As a result of vertical interference, the sidewall shape of a developed photoresist reveals a rippled structure. For high reflectivity substrates, the multiple reflections can be suppressed by covering the substrate with an antireflective material (thickness, refractive index and incident angle dependent). The effect of multiple reflections can be completely neglected for materials whose refractive index is close to the photoresist refractive index.[23] The existence of a vertical pattern has a positive effect in the preparation of shadow masks for lift-off processes due to easier solvent penetration into photoresist covered areas during the photoresist removal step.[23]

The actual surface covered by patterned areas is shown in insets in the corners of the SEM images, Figure 5.2. The insets correspond to samples presented in the SEM images. A surface coverage by patterned areas of 1.5 x 1.5 cm is typical for samples with the smallest periodicity used in this project, which equals to 330 nm, Figure 5.2. Increase in pattern periodicity leads to a decrease in surface coverage by patterned area.

5.2. Electrode patterning

The procedure of surface patterning, called "lift-off" process[38] is schematically depicted in Figure 5.4. There are four fabrication steps in this process, see Figure 5.4. In the first step an approximately 50 nm (for 330 and 350 nm pattern periodicity) or 100 nm (for 380 nm pattern periodicity and higher) thick SiO_2 layer was evaporated on top of the ITO coated glass disk (electrode) using an e-gun evaporator. The SiO_2 layer in our experiments acts as a dielectric layer for the conducting substrate. SiO_2 is an often-used material for many applications such as protective coating against ambient, insulation material, capacitor dielectric, antireflective coating, etc.[36] The thickness of the dielectric layer was chosen such that colloidal particles, fitted in its holes, were able to contact the conductive ITO layer. In the second step a double LIL exposure was performed to pattern a positive photoresist film of a thickness of 200 nm, which was previously spin-coated onto the SiO_2 covered substrate, see Figure 5.4A. Illuminated areas of the photoresist were removed from the substrate after development. The remaining photoresist pattern is thus the mimic of the intensity minima of

the interference pattern, Figure 5.4B. An example of a hexagonal pattern obtained is presented in Figure 5.4, B1.

In the lift-off process, a photoresist pattern is transferred into a SiO_2 layer using a suitable hard mask. Therefore, in the third step a thin layer of aluminum (Al) (18 – 20 nm) was evaporated onto the substrates with the photoresist patterns. During this Al deposition step the photoresist "columns" were partially covered with an Al layer. Partial Al coverage allows an easy removal of photoresist pillars by immersing the substrates in a photoresist stripper,[**] leaving behind a pattern consisting of holes in the Al layer, as shown in Figure 5.4 by the step between C and D. An Al thickness of 18 nm to 20 nm was found to be optimal. Thicknesses above 20 nm lead to difficulties in photoresist pattern removal.

In the fourth step, reactive ion etching (RIE)[39] of the SiO_2 layer was performed through the depressions (holes) of the Al "mask". Any fluorine-containing gas can be used as a SiO_2 etchant such as CF_4, SF_6 or CHF_3 (the latter used specifically where selectivity against silicon is required). In this project, CHF_3 gas was used for SiO_2 etching.[40] It provides fluorine and carbon for etching (SiF_4 and CO_2 etch products) and CF_2* radicals, which are polymer precursors. Polymerization takes place on silicon surfaces, whereas on oxide surfaces $(CF_2)_n$ polymerisation does not occur due to oxygen supply: the reaction on oxide surface results in CO_2 formation. An Al layer with native Al_2O_3 oxide acts as a hard mask - it is very difficult to etch using oxygen and fluorine-containing gases.[41] Al can be etched in chlorine (Cl_2) and chlorine-containing gases, forming $AlCl_3$ as the main etch product. Etching conditions for the SiO_2 layer were chosen such that anisotropic SiO_2 etching was achieved and that the surface of the ITO layer became exposed at the bottom of the holes. An Al cathode was used in RIE in order to suppress the formation of oxygen bearing species which occurs when an SiO_2 electrode is used, decreasing the etch rate. Finally, the remaining Al layer was removed in a wet etching step using a commercially available Al etchant.[††] Al removal is based on the oxidation of Al by HNO_3 and the simultaneous removal of the oxide by the acid constituents.[42] The final electrode is depicted schematically in Figure 5.4D. Examples of patterned SiO_2 layers (cross section) are shown in the SEM images, depicted in Figure 5.4, D1. The SEM images of the patterns in Figure 5.4 show highly ordered and defect-free structures on the electrode surfaces.

[**] Photoresist stripper Baker PRS 2000 (mixture of various organic compounds) is a commercial product that provides a versatile cleaning of bulk photoresist. This photoresist stripper is suitable for application on aluminum and silicon dioxide layers.

[††] This commercially available Al-etchant consists of a mixture of acids H_3PO_4 : CH_3COOH : HNO_3 : H_2O with the relative composition 73:11:2:14 (weight %).

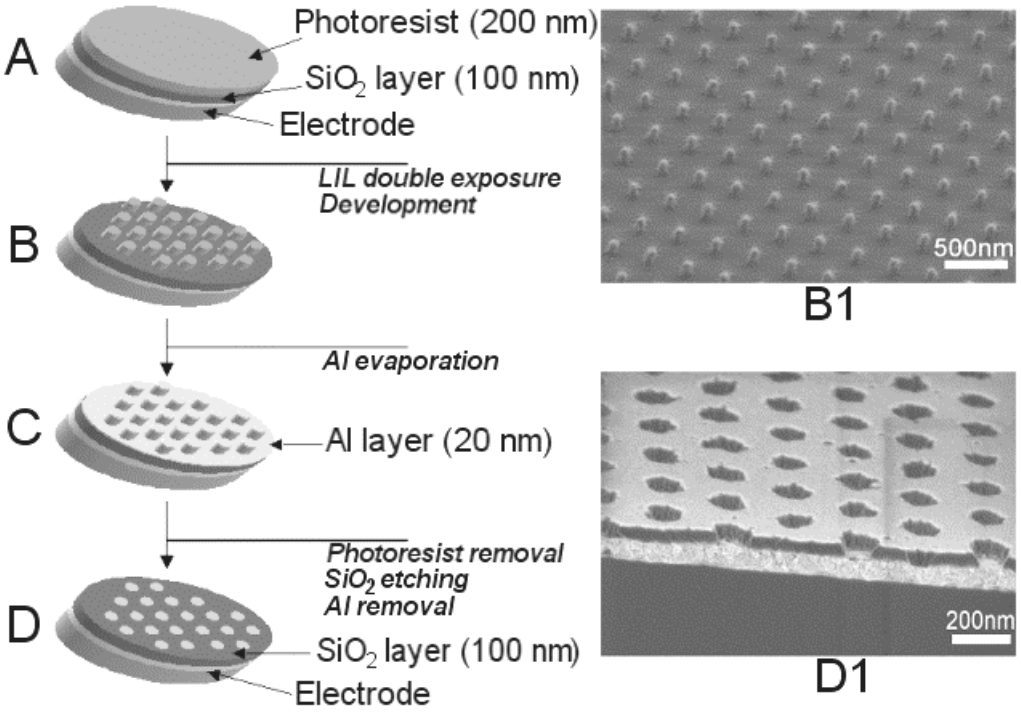

Figure 5.4. A-D Schematic representation of the template patterning process. A) Dielectric layer (SiO_2) and a photoresist deposited on the electrode surface consisting of a glass plate and a conducting ITO layer on top. B) Developed photoresist after LIL exposures. B1) SEM image of a hexagonally patterned photoresist (side view). C) Thin metal layer deposited on top of the patterned photoresist. D) Etched dielectric layer after Al mask removal (final structure). D1) SEM image of an etched dielectric layer (side view).

5.3. Laser interference lithography results

Examples of photoresist pattering using laser interference lithography are presented in Figure 5.5 and 5.6. Double exposures were performed in the photoresist at 60° or 90° rotation angles to produce either hexagonal or square types of pattern, respectively. Exposure parameters were defined experimentally for each particular periodicity. The influence of an increase in exposure dose on pattern structure is presented for a periodicity of 530 nm in Figure 5.5. The exposure dose (E) was determined by multiplying the total absorbed intensity of the photoresist layer (I_{abs}) by the exposure time (τ). Therefore, an exposure dose can be varied either by the light intensity or by exposure time. An optimal development time, as was also determined experimentally, was 35 - 40 sec. A slight increase in exposure dose from 27.26 to 30.38 mJ/cm^2 led to the formation of separately formed photoresist pillars, Figure 5.5 A-C. A rippled sidewall structure indicated the presence of vertical standing waves. We observed changes in the photoresist profile with a decrease in the SiO_2 thickness twice. Walls of photoresist pillars became more straight, but the diameter of the pillars did not decrease even at further increased exposure doses, Figure 5.5D. That is due to the presence of destructive interference with reflected light, when the thickness of the 2nd layer equals $\lambda/4$. In the course of our experiments ("lift-off process"), we did not aim to improve the photoresist profile, because a conical shape of the photoresist pillars was preferred, allowing one to obtain depressions with a larger diameter in the dielectric layer after "lift-off". The thickness of the SiO_2 layer was chosen specifically with respect to the diameter of the colloidal particle used.

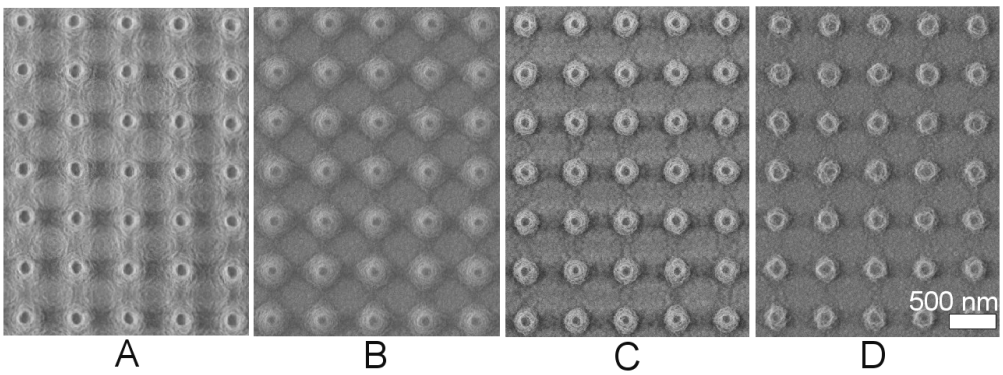

Figure 5.5. SEM images of patterned photoresist layers (Λ= 530 nm) exposed to UV light with **exposure doses** (E): A) **27.26** mJ/cm^2 (I = 410.7 μW/cm^2, t = 34 sec, SiO_2 thickness = 100 nm); B) **29.65** mJ/cm^2 (I = 446.4 μW/cm^2, t = 34 sec, SiO_2 thickness = 100 nm); C) **30.38** mJ/cm^2 (I = 432.1 μW/cm^2, t = 36 sec, SiO_2 thickness = 100 nm); and D) **31.9** mJ/cm^2 (I = 453.6 μW/cm^2, t = 36 sec, SiO_2 thickness = 50 nm).

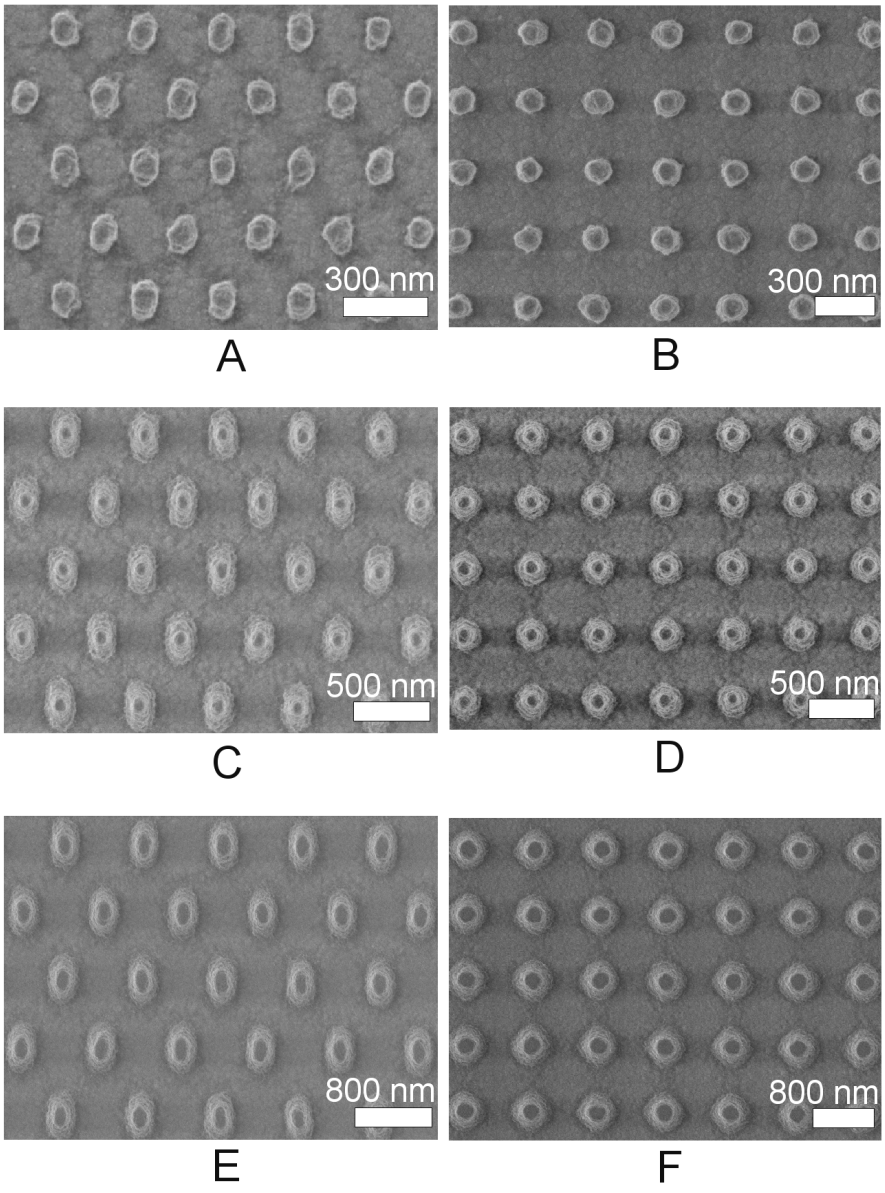

Figure 5.6. Hexagonal and square types of photoresist patterns with various periodicities (SiO_2 thickness = 100 nm): A) 350 nm (E = **45.16** mJ/cm^2, I = 428.6 μW/cm^2, t = 38 sec); B) 350 nm (E = **41.34** mJ/cm^2, I = 428.6 μW/cm^2, t = 38 sec); C) 530 nm (E = **34.03** mJ/cm^2, I = 432.1 μW/cm^2, t = 36 sec); D) 530 nm (E = **30.43** mJ/cm^2, I = 432.1 μW/cm^2, t = 36 sec); E) 850 nm (E = **22.92** mJ/cm^2, I = 439.3 μW/cm^2, t = 34 sec); F) 850 nm (E = **21.00** mJ/cm^2, I = 439.3 μW/cm^2, t = 34 sec). The ratio of average pillar diameters at the substrate surface (for the hexagonal patterns it is the smallest pillar dimension) to the pattern periodicity (R_{PP}): for hexagonal patterns: A) 0.32; C) 0.37; E) 0.38; for square patterns: B) 0.4; D) 0.47; F) 0.55.

For patterns with larger pattern periodicity, the exposure dose was decreased, in order to keep the pillar diameter as large as possible, Figure 5.6. The photoresist profile for all periodicities is determined by the angle of incidence, because the thickness of the SiO_2 layer of 100 nm was the same. The ratio of average pillar diameters at the substrate surface (for the hexagonal patterns it is the smallest dimensions) to the pattern periodicity (R_{PP}) was varied between 0.3 and 0.4 for hexagonal patterns and between 0.4 and 0.55 for square patterns for a given range of periodicities.

5.4. Etching results

Cross-sections of patterned electrodes with dielectric layers etched with different etching parameters are shown in Figure 5.7. The procedure for photoresist layer patterning was the same for all samples: for hexagonal patterns with a periodicity of 530 nm, E = 65.7 mJ/cm^2, t_{dev} = 35 sec. SiO_2 layer thickness was 100 nm. The deposited aluminum layer had a thickness of 20 nm. The choice of etching parameters was based on the article by K. Frick *et al*.[40] These authors advised to use a combination of low pressure and pure CHF_3 in order to promote anisotropic etching of the SiO_2 layer. The etching rate of the SiO_2 layer was 20 nm/min, using the following RIE parameters: gas flow rate (FR) = 30 sccm CHF_3, chamber pressure (P) = 20 - 30 mTorr, RF power (FP) = 75 W.

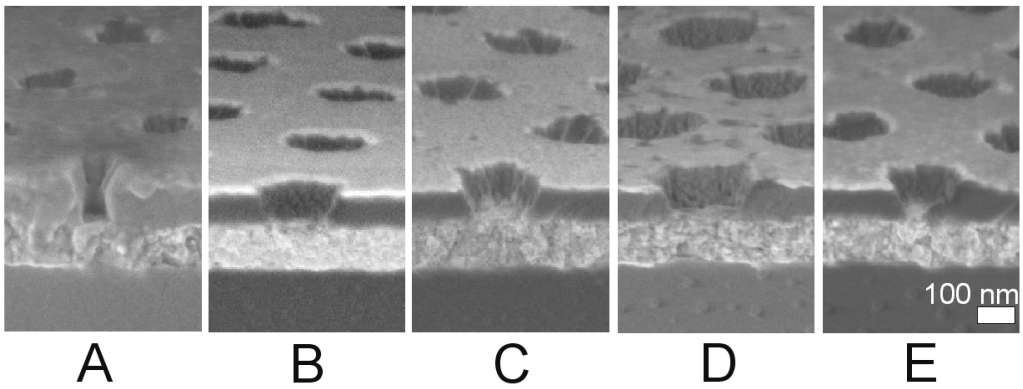

Figure 5.7. SiO_2 layer profile dependence on RIE parameters: A) gas flow rate (FR) = 25 sccm CHF_3 and **2 sccm O_2**, chamber pressure (P) = 30 mTorr, RF power (FP) = 75 W, t_{etch} = 4 min, Al cathode; B) FR = **20 sccm CHF_3**, P = 30 mTorr, FP = 75 W, t_{etch} = 10 min, Al cathode; C) FR = 20 sccm CHF_3, P = 30 mTorr, FP = 75 W, t_{etch} = 10 min, **Quartz cathode**; D) FR = **10 sccm CHF_3**, P = 30 mTorr, FP = 75 W, t_{etch} = 10 min, Al cathode; E) FR = 20 sccm CHF_3, P = **20 mTorr**, FP = 75 W, t_{etch} = 10 min, Al cathode. In all SEM pictures, the top layer is a 20 nm thick Al layer.

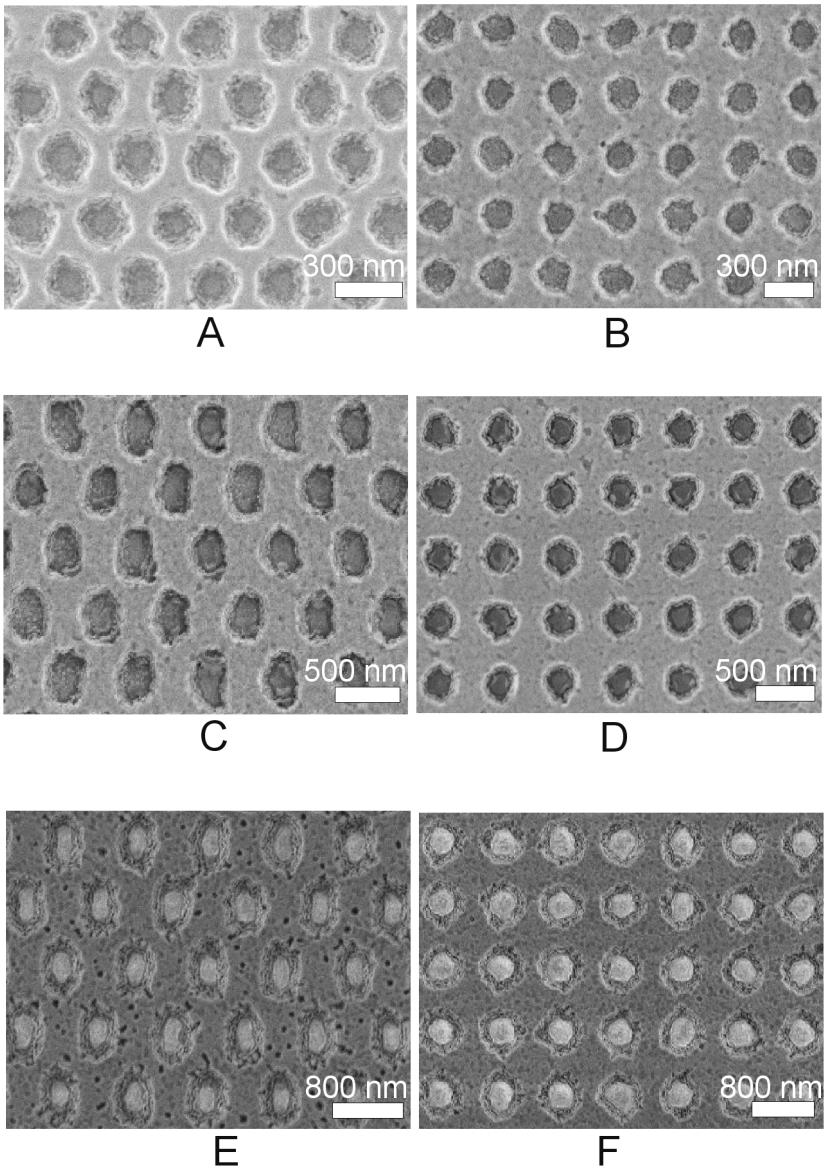

Figure 5.8. Hexagonal and square patterns in a SiO_2 layer with various periodicities: A) and B) 350 nm; C) and D) 530 nm; E) and F) 840 nm. RIE parameters: *FR* = 20 sccm CHF_3, *P* = 20 mTorr, *FP* = 75 W. Ratio of the average hole diameters at the substrate surface (for hexagonal patterns it is the smallest dimension) to the pattern periodicity (R_{HP}): for hexagonal patterns: A) 0.72 (Al thickness = 18 nm, t_{etch} = 13 min); C) 0.54 (Al thickness = 20 nm, t_{etch} = 13 min); E) 0.55 (Al thickness = 18 nm, t_{etch} = 15 min); for square patterns: B) 0.6 (Al thickness = 20 nm, t_{etch} = 13 min); D) 0.56 (Al thickness = 20 nm, t_{etch} = 13 min); F) 0.65 (Al thickness = 18 nm, t_{etch} = 15 min). All SEM pictures presented were taken with the Al layer still in place.

The maximum CHF_3 flow rate in the employed RIE apparatus was 25 sccm. Etching a SiO_2 layer using *FR* = 20 sccm CHF_3, *P* = **20** or **30 mTorr** and *FP* = 75 W for 10 min (see Figure 5.7, B and E) gave similar results as were obtained by Frick at even lower gas flow rates. An identical etching profile was obtained for different values of chamber pressure. Addition of O_2 led to a slightly overetched profile already after 4 minutes, see Figure 5.7A, lower half of the SiO_2 layer. Oxygen reacts with gas fragments and keeps the fluorine concentration high by preventing fluorine recombination with the gas fragments. The use of a quartz cathode instead of an Al cathode in the chamber, where O_2 was not used in the gas mixture, led to inhomogeneous etching. Overetching was observed at the sample edges, while overetching did not occur in the middle part of the samples, see Figure 5.7C. The width of the overetched areas increased towards the middle of the sample with an increase in etching time, indicating that oxygen was introduced into the plasma by etching of the electrode. Therefore, in order to obtain a homogeneous etching over the whole substrate, an Al cathode was used. Upon decreasing the gas flow rate from 20 to 10 sccm CHF_3, an strong increase in the diameter of the depressions was observed, see Figure 5.7D. Therefore, optimal parameters such as *FR* = 20 sccm CHF_3, *P* = 20 mTorr, *FP* = 75 W for SiO_2 layer etching using Al as cathode material were used in following experiments. Examples of etched SiO_2 layers for patterns with different periodicities are presented in Figure 5.8. An Al layer of 18 to 20 nm in height was found to have the optimal thickness. It was observed, that if the thickness of the Al layer was higher than 20 nm, it was difficult to completely remove photoresist pillars, therefore, leading to defects in the periodic patterned structures. In the case of an Al layer thickness of 20 nm (see Figure 5.8 B, C and D), an anisotropically etched SiO_2 profile was obtained. In the case of an 18 nm thick Al layer, the Al layer was rather thin and was partially removed together with SiO_2 due to physical sputtering, leading to a positive taper profile. The diameter of the depressions increased during the RIE etching by 15 - 30 %, compared with the diameter of photoresist pillars. The high roughness of the depressions is basically determined by the photoresist pillar profile.

Conclusions

A procedure of electrode surface patterning was developed on the basis of a “lift-off” technique. A photoresist pattern was translated into a dielectric SiO_2 layer via a thin Al mask. Photoresist patterns in the form of periodic gratings with hexagonal, square and rectangular types of structures were obtained via a double UV light exposure in the photoresist while

rotating the sample holder by 60° or 90°. Grating periodicity was varied by adjusting the incident angle of the light in correspondence to the substrate surface. Exposure dose and development time of the photoresist after the exposure were optimized specifically for each periodicity. These two parameters were found to significantly influence the profile and diameter of the photoresist pillars. A thickness of the Al layer between 18 nm and 20 nm was found to be optimal. Above 20 nm, it was rather difficult to completely remove the photoresist. Below 18 nm, isotropic etching of the dielectric layer was observed. Optimal etching parameters such as *FR* = 20 sccm CHF_3, *P* = 20 mTorr, *FP* = 75 W were found by comparison of profiles of etched dielectric layers for different etching conditions. The use of an Al cathode was found to be essential. The diameter of the depressions was increased during the RIE etching by 15 – 30 %, compared with the diameter of the photoresist pillars. The diameter of the depressions in the dielectric layer can be varied by adjusting the etching parameters.

Experimental

Template preparation

Electrodes consisting of 1 inch float glass disks, covered with 100 nm conductive ITO layers were supplied by Ssens bv, The Netherlands and were used as received. Before deposition of the SiO_2 layer, electrodes were sonicated for 5 min in isopropanol (Merck, VLSI Selectipur) and Milli-Q water (Millipore, 18.2 MΩ·cm) and kept on a hot plate (120 °C) equipped with a lid for 30 min. The positive resist Olin 907/12 (ARCH) with an initial thickness of 1.2 μm (at standard spin-coating parameters) was thinned with a mixture of ethyl-3-ethoxypropionate (EEP) (Aldrich, 99 %) and methyl-3-methoxypropionate (MMP) (Fluka, > 99 %) with a composition Resist:EEP:MMP = 5:2:3 and filtrated through a filter with a pore size of 0.2 μm (PALL, Acrodisc CR). EEP and MMP are immediate constituents of Olin 907/12 photoresist, therefore, were compatible with the diluent mixture. Photoresist was spin-coated in a two-step process (first 10 sec at 500 rpm and continuing for another 30 sec at 4000 rpm) in order to form a layer with a thickness of 200 nm. Electrodes with photoresist on top were baked for 90 sec at 95 ºC (soft baking). Prior to photoresist coating, adhesive promoter hexamethyldisilazane (HMDS) was spin-coated at 4000 rpm for 20 sec. LIL exposures were performed with an Azure™ solid-state laser[‡‡] at a wavelength of 266 nm. After LIL exposures, electrodes were baked for 90 sec at 120 ºC (post baking) and then developed in developer solution OPD 4262 (ARCH) for 30 - 40 sec. Finally, electrodes with patterned photoresist were left on a hot plate for 10 min (hard baking).

Thin SiO_2 (50 and 100 nm) and Al layers (18 nm) were deposited on the ITO electrodes or on the electrode covered with a patterned photoresist in an e-gun evaporator "Balzers BAK 600". RIE of the SiO_2 was performed in a CHF_3 plasma (20 sccm CHF_3, at a chamber pressure of 20 mTorr and a forward power of 75 W, 10 ºC) for 11 - 15 min (pattern dimension dependent) in an Elektrotech Twin system PF 340. The etch rate was 11 - 15 nm/min. An Al thin plate was used as a cathode. Before RIE of samples, the chamber was exposed to oxygen plasma (standard chamber cleaning routine) for 10 min (20 sccm O_2, at a chamber pressure of 50 mTorr and a forward power of 150 W, 10 ºC) followed by CHF_3 plasma "cleaning" for 5 min with the same parameters as for sample etching. Photoresist was removed in the standard photoresist stripper solution PRS 2000 (J. T. Baker) set at 50 °C in an ultrasonic bath for 1 hour. The aluminum mask was removed using a commercial Al-etch solution (Merck) at 55 °C for several minutes.

[‡‡] The Azure™ uses the field-proven Verdi™ laser (solid-state, diode-pumped, frequency-doubled Nd:YVO_4 laser) that provides single-frequency green output at 532 nm, which is then frequency-doubled to 266 nm in a resonant enhancement cavity.

Measurements

All SEM images were captured by a high-resolution LEO 1550 FEG scanning electron microscope.

References and Notes

[1] S. H. Park, D. Qin, Y. Xia, *Adv. Mater.* **1998**, *10*, 1028.
[2] Y. Yin, Y. Xia, *Adv. Mater.* **2001**, *13*, 267.
[3] Y. Xia, Y. Yin, Y. Lu, J. McLellan, *Adv. Funct. Mater.* **2003**, *13*, 907.
[4] R. E. Schaak, R. E. Cable, B. M. Leonard, B. C. Norris, *Langmuir* **2004**, *20*, 7293.
[5] S. M. Yang, G. A. Ozin, *Chem. Commun.* **2000**, 2507.
[6] G. A. Ozin, S. M. Yang, *Adv. Funct. Mater.* **2001**, *11*, 95.
[7] S. M. Yang, H. Miguez, G. A. Ozin, *Adv. Funct. Mater.* **2002**, *12*, 425.
[8] E. Kumacheva, P. Garstecki, H. Wu, G. M. Whitesides, *Phys. Rev. Lett.* **2003**, *91*, 128301.
[9] K.-H. Lin, J. C. Crocker, V. Prasad, A. Schofield, D. A. Weitz, T. C. Lubensky, A. G. Yodh, *Phys. Rev. Lett.* **2000**, *85*, 1770.
[10] Y.-H. Ye, S. Badilescu, Vo-Van Truong, P. Rochon, A. Natansohn, *Appl. Phys. Lett.* **2001**, *79*, 872.
[11] D. K. Yi, E.-M. Seo, D.-Y. Kim, *Appl. Phys. Lett.* **2002**, *80*, 225.
[12] D. K. Yi, M. J. Kim, D.-Y. Kim, *Langmuir* **2002**, *18*, 2019.
[13] R. G. Golding, P. C. Lewis, M. Allard, E. H. Sargent, E. Kumacheva, *Langmuir* **2004**, *20*, 1414.
[14] A. van Blaaderen, R. Ruel, P. Wiltzius, *Nature* **1997**, *385*, 321.
[15] J. P. Hoogenboom, C. Rétif, E. de Bres, M. van de Boer, A. K. van Langenuurling, J. Romijn, A. van Blaaderen, *Nano Letters* **2004**, *4*, 205.
[16] W. Lee, A. Chan, M. A. Bevan, J. A. Lewis, P. V. Braun, *Langmuir* **2004**, *20*, 5262.
[17] *Handbook of Microlithography, Micromachining, and Microfabrication*, ed. P. Rai-Choudhury, vol. 1, Microlithography, SPIE Press, Washington, **1997**.
[18] Resolution limit corresponds to Mask alignment machines that are available at Mesa^{+} cleanroom facilities, University of Twente, The Netherlands.
[19] Y. Xia, G. M. Whitesides, *Angew. Chem. Int. Ed.* **1998**, *37*, 550.
[20] E. Delamarche, H. Schmid, A. Bietsch, N. B. Larsen, H. Rothuizen, B. Michel, H. Biebuyck, *J. Phys. Chem. B* **1998**, *102*, 3324.
[21] *Alternative Lithography: Unleashing the Potentials of Nanotechnology*, ed. C. M. Sotomayor Torres, Kluwer Academic, NY, **2003**.
[22] S. Austin, F. T. Stone, *Appl. Opt.* **1976**, *15*, 2126.
[23] B. A. de Mello, I. F. da Costa, C. R. A. Lima, L. Cescato, *Appl. Opt.* **1995**, *34*, 597.
[24] V. Berger, O. Gauthier-Lafayer, E. Costard, *Elect. Lett.* **1997**, *33,* 425.
[25] C. O. Boltzer, C. T. Harris, S. Rabe, D. Rathman, M. A. Hollis, H. J. Smith, *J. Vac. Sci. Technol. B* **1994**, *12*, 629.
[26] S. Kuiper, H. A. G. M. van Wolferen, C. van Rijn, W. Nijdam, G. Krijnen, M. Elwenspoek, *J. Micromech. Microeng.* **2001**, *11*, 33.
[27] M. Campbell, D. N. Sharp, M. T. Harrison, R. G. Denning, A. J. Turberfield, *Nature* **2000**, *404*, 53.
[28] L. Vogelaar, W. Nijdam, H. A. G. M. van Wolferen, R. M. de Ridder, F. B. Segerink, E. Flück, L. Kuipers, N. F. van Hulst, *Adv. Mater.* **2001**, *13*, 1551.
[29] C. J. M. van Rijn, G. J. Veldhuis, S. Kuipers, *Nanotechnology* **1998**, *9*, 343.
[30] A. Fernandez, P. J. Bedrossian, S. L. Baker, S. P. Vernon, D. R. Kania, *IEEE Trans. Mag.* **1996**, *32*, 4472.
[31] D. C. Flanders, H. Kogelnik, R. V. Schmidt, C. V. Shank, *Appl. Phys. Lett.* **1974**, *24*, 194.
[32] K. S. Pennington, L. Kuhn, *Opt. Commun.* **1971**, *3*, 357.
[33] X. Mai, R. Moshrefzadeh, U. J. Gibson, G. I. Stegeman, C.T. Seaton, *Appl. Opt.* **1985**, *24*, 3155.
[34] S. H. Zaidi, S. R. J. Brueck, *J. Vac. Sci. Technol. B* **1993**, *11*, 658.
[35] E. Hecht, *Optics*, 2nd ed., Addison-Wesley, **1987**, p. 343.
[36] See for example, S. Franssila, *Introduction to Microfabrication,* Wiley, Chichester, **2004**, p. 109.
[37] B. E. A. Saleh, M. C. Teich, *Fundamentals of Photonics,* Wiley, NY, **1991**, p. 64.
[38] M. Hatzakis, B. J. Canavello, J. M. Shaw, *IBM J. Res. Develop.* **1980**, *24*, 452.
[39] RIE, also known as ion-assisted etching, is a combination of chemical (reactive: isotropic but highly selective) and physical (bombardment: anisotropic but low selectivity) processes. The bombardments create reactive sites on the surface and then the target-oriented chemical reaction takes place. By taking advantages of both processes, straight wall profiles in etched materials can be achieved.
[40] C. Steinbrochel, H. W. Lehmann, K. Frick, *J. Elctrochem. Soc.: Solid State Sci. Techol.* **1985**, *132*, 180.
[41] M. Zhang, J. Z. Li, I. Adesida, E. D. Wolf, *J. Vac. Sci. Technol. B* **1983**, *1*, 1037.
[42] D. Westberg, O. Paul, G. I. Andersson, H. Baltes, *J. Micromech. Microeng.* **1996**, *6*, 376.

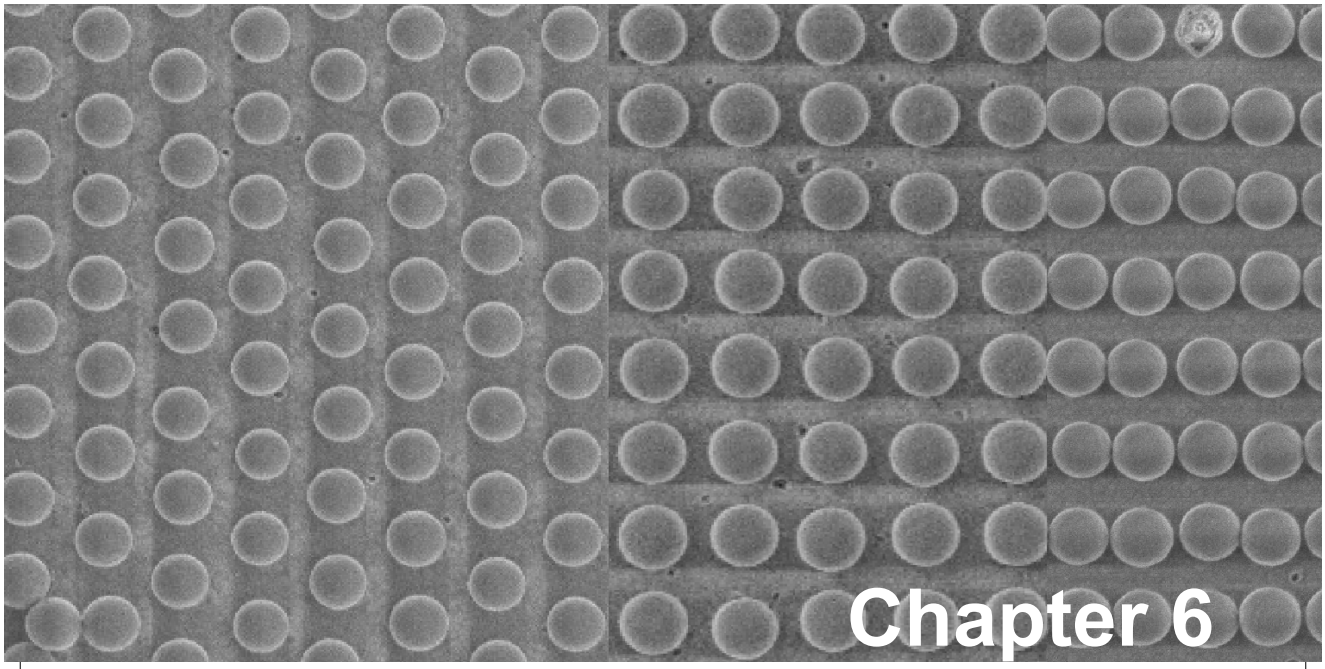

Chapter 6

Deposition of Colloidal Particles and Controlled Formation of Colloidal Monolayers

Electrophoretic deposition of charged polymer colloidal particles on patterned substrates is discussed. The emphasis in this chapter is placed on the formation of colloidal monolayers. Colloidal depositions on hexagonal, square and rectangular surface patterns with different periodicities were performed. Deposition parameters such as applied voltage, concentration of colloidal particles, colloid surface charge density, withdrawal speed of the electrodes and distance between electrodes were examined and optimized for colloidal monolayer growth. Threshold voltages for electrodes with various periodicities were found, beyond which a significant increase in the thickness of colloidal crystals was observed. Threshold voltages decreased at larger pattern periodicities and this decrease in threshold voltage had a non-linear character. A homogeneous surface coverage by colloidal particles for the various electrode periodicities was found at a withdrawal speed of 0.1 mm/s at applied voltages above the threshold voltage.

Introduction

Current intensive efforts to control the ordering and position of colloidal particles on surfaces have been stimulated by a growing number of potential applications in different fields. Colloidal crystals formed by a stack of colloidal layers of one or different particle sizes are of increasing interest for photonic crystal applications.[1] In addition to colloidal crystals, two-dimensional colloidal assemblies have found applications as microlenses in imaging[2] and as physical masks in nanosphere lithography.[3] Colloidal particles placed individually on a surface provide an opportunity to locally study reactions that take place in hollow (nano)capsules used as delivery vehicles for a controlled release of substances such as drugs, cosmetics, dyes and inks.[4]

On flat substrates, control of colloidal crystallization becomes more effective when capillary forces are exploited to drive the colloidal assembly. In practice, this is usually realized by controlled solvent evaporation. This method was applied, in one case, to a substrate immersed vertically in a colloidal suspension[5,6] and left to dry. In another case, a drop of colloidal suspension was spread within a thin rubber ring located on the horizontally placed substrate, forming a concave surface in its center.[7] Finally, control of colloidal crystallization was realized by tuning the withdrawal speed of the sample from the colloidal suspension.[8] In the experiments described above, for control of ordering, domain size and thickness of colloidal crystals, various parameters must be simultaneously considered including the choice of substrate, tilt angle of the substrate with respect to the colloidal suspension (change in the meniscus shape), choice of solvent, evaporation rate, temperature, concentration of colloidal particles and relative humidity. Despite all efforts to date, colloidal monolayers formed on bare substrates without topological or chemical patterns by these methods possess a close packed hexagonal structure.

Surface topology exerts a large influence on the ordering of colloidal particles.[9,10,11,12,13,14,15] For example, Whitesides *et al*.[9] demonstrated the formation of close-packed hexagonal, rhombic, and disordered structures of colloidal monolayers, depending on the ratio of the width of rectangular shaped grooves (1D grating) to the particle diameter. Ozin *et al*. showed that colloidal multilayer orientation depends on the groove shape. Xia *et al*.[13] demonstrated the influence of a variety of surface patterns on colloidal aggregation. Using surface patterns of different geometries like triangular, line or circular, Xia could achieve the ordering of colloidal particles into various structures that simply mimic the surface pattern. Dimensions of surface pattern features (especially width and depth) strongly influence the

colloidal aggregate structure. The depth of the pattern should be on the order of the colloidal particle size. Formation of non-close packed colloidal multilayer structures was realized by a precise control of the periodicity of a 2D surface grating.[14,15]

The response of colloidal particles to an applied electric field and the ordering (or aggregation) phenomena in 2D crystalline structures on electrode surfaces were extensively studied.[16,17] It was shown that an increase in electric field strength from 25 Vcm^{-1} to 75 Vcm^{-1} leads to migration of the colloidal particles across the electrode surface and to the formation of stable 2D colloidal crystals induced by the presence of electro-hydrodynamic flow. Finally, particles were coagulated and firmly attached to the electrode when a strong electric field (electric field strength higher than 100 Vcm^{-1}) was applied.[17] The application of an electric field to the colloidal suspension promotes also the growth of 3D colloidal crystals on planar electrode surfaces.[18] Careful adjustment of colloidal concentration and electric field strength allows one to selectively form various crystal structures on the electrode surface.[19,20] Colloidal crystal structures in solution were studied using a confocal microscope. As a disadvantage of this method, once electrodes are withdrawn from the colloidal suspension at the applied electric field, formed structures of colloidal crystals tend to rearrange into a close-packed or disordered structure. The ordering and orientation of 2D close-packed colloidal structures (colloidal monolayers) and colloidal crystals could be simultaneously realized when colloidal particles were electrophoretically deposited on a topologically patterned electrode.[21,22,23] It was shown that dimensions of the topological pattern play a crucial role in the formation of 2D colloidal structures.

In this chapter, we present a study on the *direct* formation of colloidal monolayers of various structures using a combination of electrophoretic deposition of colloidal particles onto patterned electrodes and controlled withdrawal of the electrodes after the deposition. In addition, the influence of different deposition parameters such as deposition voltage, deposition time, concentration and surface charge density of colloidal particles, pattern periodicity and withdrawal speed of the electrode on colloidal crystal growth were investigated.

6.1. Colloidal particles in an electric field

Electrophoresis was discovered in 1808 by F. F. Ruess[24], who noticed particle migration toward an anode upon passing an electric current through a suspension of clay in water. Later it was also discovered that charged particles move with a constant speed under an applied electric field. This speed increases at increased applied potential and dielectric constant of the medium, and decreases with an increase in medium viscosity.[25]

The charge on colloidal particles, that became apparent during the electrophoresis, is caused by the existence of a double electrical layer of ions at the colloidal surface (see Section 2.1.3). The double electric layer originates from either selective adsorption of one of the electrolyte ions present in the solution (in the case of inorganic particles) or from the ionization of surface-active molecules (in the case of organic particles such as polymer colloids).

Under the applied electric field, a negatively charged colloidal particle moves towards the anode and positively charged counter ions – towards the cathode, forming a dipole. Counter ions that form a second layer around the colloidal particle move towards the cathode, and counter ions that are close to the colloid surface move together with the colloidal particle, due to the relatively high electrical forces acting on them, Figure 6.1. If a colloidal particle is charged positively then the particle movement is in the opposite direction. The electrophoretic mobility of colloidal particles u versus the gradient of the applied external potential H can be expressed via the Helmholz-Smoluchovski equation:

$$u = \frac{f\varepsilon\zeta H}{\pi\eta}$$

where f is a function of the quantity χa introduced later by Henry, where a is the radius of spherical particle and χ is a quantity that equals the inverse of the double layer thickness; f = 1/6 for spherical particles and small values of the quantity χa and f = 1/4 for any particle shape and large values of the quantity χa; ε is the dielectric permittivity and η is a viscosity coefficient of the medium, ζ is the electrokinetic potential (ζ - potential) and $H = E/L$ is the gradient of the external field potential which equals the potential of the external field E

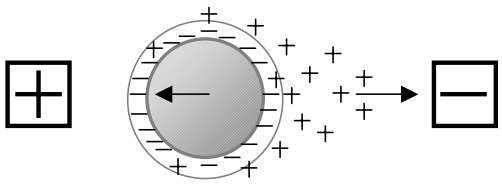

Figure 6.1 Schematic representation of the movement of a colloidal particle and counter ions during electrophoresis.

applied between electrodes separated at a distance *L*. The ζ- potential can be influenced by various factors such as electrolyte type and concentration, concentration of the colloids in the suspension, pH and temperature or polarity of the dispersion medium. For example, an increase in concentration of counter ions leads to a thinner double layer and, therefore, to a decrease in the value of the ζ- potential.

In case of a colloidal suspension under the influence of an electric field, the movement of colloidal particles is accompanied by a continuous interaction of colloidal particles via constant interchange of counter ions. It was found that in polar dielectric media under an applied electric field, an attraction occurs between particles, which becomes more pronounced at distances 2-3 times larger than the particle size. As a result, colloidal strings between electrodes were observed when an electric field was applied. Therefore, the reason of string formation is a disbalance of surface forces, caused by deformation and polarization of the double electric layer, that induce the process of orientated aggregation. Removal of the electric field after the oriented aggregates were formed in the second potential minimum leads to a break-up of aggregates (reversed coagulation), while in the case when aggregates were formed in the first potential minimum, aggregates do not break up (non-reversible coagulation) (see Section 2.1.4).[25] The same processes were experimentally demonstrated when interactions of colloidal particles with electrode surfaces were studied using an optical microscope.

6.2. Electrophoretic deposition of polymer colloidal particles

For the deposition of colloidal particles, an electrophoretic cell was constructed which is schematically illustrated in Figure 6.2A. Two glass/ITO electrodes were separated from each other with a 1 mm thick Teflon spacer. One of the electrodes was patterned in the way described in Chapter 5. The cell was immersed into a colloidal suspension, perpendicular to the suspension surface. The colloidal suspension consisted of polymer colloidal particles with volume fractions of 0.2 vol.% or 0.5 vol.% redistributed in a mixture of ethanol and water (80:20 vol/vol). Negatively charged polystyrene colloidal particles with a diameter of 330 nm, polydispersity index of less than 3% and surface charge densities of 16.2 $\mu C/cm^2$ and 26.5 $\mu C/cm^2$ were used. When a d.c. electric field was applied, the charged polymer colloidal particles moved to the oppositely charged patterned electrode and were deposited on its surface. After a preset deposition time the cell was withdrawn at a preset speed from the

colloidal suspension using a speed control device. Electrodes were withdrawn from colloidal suspensions as presented in Figure 6.2B. The patterned electrode was left for several minutes to dry completely under a continuously applied voltage. Electrophoretic depositions were performed in a glove box under a nitrogen atmosphere in order to maintain constant humidity conditions. Patterned electrodes with deposited colloidal particles were marked in three regions starting from the drying edge, Figure 6.2B. Effective surface coverage as an equivalent value of the average number of colloidal layers was calculated from SEM images over three regions. In region 1, the surface coverage never exceeded 2 colloidal layers (independent on deposition parameters) likely due to the variable speed in the initial phase of withdrawal. Surface coverage in this region 1 was inhomogeneous and contained areas of colloidal layers that did not correspond to the electrode surface pattern. Homogeneous surface coverage was observed in regions 2 and 3, where the withdrawal speed of the electrodes had stabilized. Below region 3, colloidal crystals were thick, polycrystalline and did not correspond to the electrode pattern. Colloidal crystals in this region were formed upon drying of a droplet of colloidal suspension left at the electrode surface when the electrode broke contact with the colloidal suspension. Therefore, regions below region 3 were not taken into account during the analysis of the surface coverage of grown colloidal crystals. Transitions from one region to another were not sharp and varied from one sample to another depending on deposition parameters. In this study of colloidal crystal growth, the width of each region was taken as 3 mm.

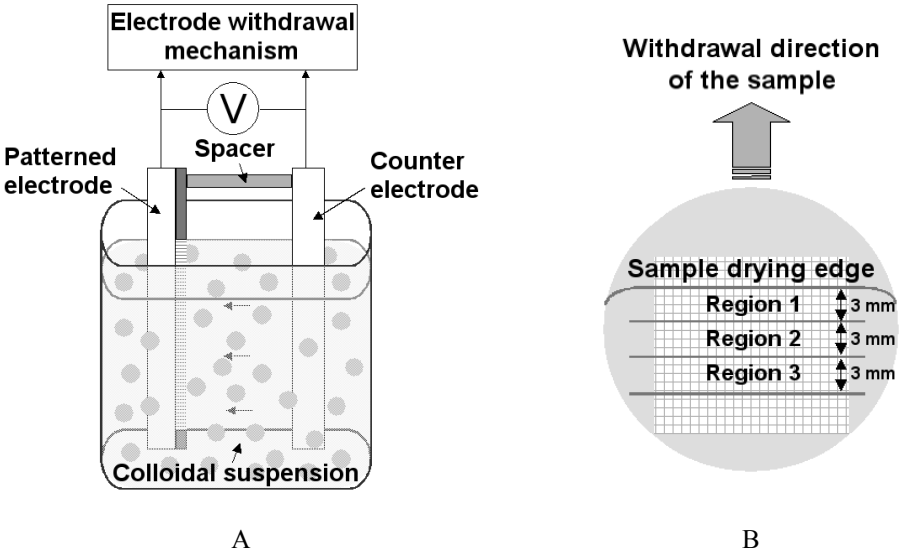

A B

Figure 6.2. A) Schematic illustration of the electrophoretic deposition set-up; B) Schematic representation of the patterned electrode showing the various regions used in subsequent analyses.

6.3. Deposition of colloidal particles on flat (non-patterned) electrode surfaces

During electrophoretic deposition of colloidal particles on electrode surfaces, the formation of a "gaseous" structure is usually observed when a weak field is applied (below 25 Vcm^{-1}), Figure 6.3A. Colloidal particles with a diameter of 330 nm and a surface charge density of 16.2 $\mu C/cm^2$ were deposited on the electrode surface at applied voltages of 2.5, 3.0 and 3.5 V during 1 min, Figure 6.3. These deposition conditions were also applied in electrophoretic colloidal depositions on patterned surfaces discussed in following paragraphs of this chapter. An increase in applied voltage led to an increase in colloidal concentration on the electrode surface and the formation of colloidal crystals with a glassy structure, Figure 6.3 B, C. In principle, colloidal crystal ordering on non-patterned electrode surfaces can be improved by adjusting a set of deposition parameters, such as electric field strength, colloidal size and concentration, etc. A consequence of such adjustments is that hexagonally close-packed colloidal monolayers and colloidal crystals possessing the close-packed FCC crystal structure are formed.[17,18] In order to induce a non close-packed colloidal crystal structure on the electrode surface, structuring of the electrode surfaces is necessary.[21]

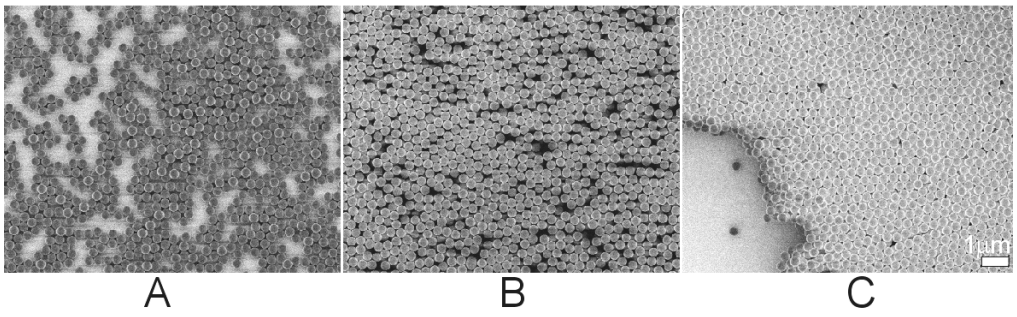

Figure 6.3. Colloidal deposition on un-patterned electrode surfaces at the applied voltage of A) 2.5 V; B) 3.0 V and C) 3.5 V. Negatively charged colloidal particles (surface charge density 16.2 $\mu C/cm^2$) with a diameter of 330 nm were used. Deposition parameters such as a deposition time of 1 min, colloid concentration of 0.5 vol.% and electrode withdrawal speed of 0.04 mm/s were constant for all three depositions.

6.4. Deposition control of colloidal particles on patterned surfaces

Ordering of colloidal particles on patterned electrodes can be accomplished by controlling a set of deposition parameters. These include deposition voltage, concentration and surface charge density of polymer colloidal particles, withdrawal speed of electrodes from the suspension, pattern periodicity and the distance between separated electrodes. In the section below, as a representative case study we show the influence of some selected processing and structural parameters on the deposition process and the packing characteristics of the resulting colloidal layers.

First, we discuss effective surface coverage and its dependence on the deposition parameters. Effective surface coverage is defined as an average equivalent value of the number of deposited colloidal layers over three regions marked in Figure 6.2B.

Surface coverage results for a template periodicity of 350 nm are shown as a function of applied voltage and deposition time in Figure 6.4A. The other deposition parameters such as colloidal concentration (0.5 vol.%), withdrawal speed of the electrodes (0.04 mm/s) and colloid surface charge density of 16.2 $\mu C/cm^2$ were kept constant. The surface coverage is presented for region 2 of the sample as shown in Figure 6.2B. The three data sets depicted (filled circles, triangles and squares) show the influence of increasing cell voltage, which increases the surface coverage at a given deposition time. In Figure 6.4B, surface coverage data obtained at a deposition time of 60 sec are shown for four different electrode pattern periodicities (330, 350, 380 and 450 nm). It is obvious from this figure that for a given pattern periodicity and deposition time, surface coverage begins to dramatically increase if the cell voltage is larger than a given threshold value, indicated by arrows in Figure 6.4B. The value of the threshold voltage decreases with increasing pattern periodicity, see Figure 6.4C. Eventually the value of the threshold voltage drops to zero for the pattern periodicity of 450 nm. The decrease in threshold voltage is determined by the electrode geometry, where pattern quality and colloidal particle polydispersity play an important role. For a pattern periodicity higher than 330 nm (equal to the colloid size), deposited colloidal layers became less sensitive to the particle polydispersity, and therefore more colloidal particles were detected at low applied voltages and a decrease in the threshold voltage was found.

In subsequent experiments, applied (deposition) voltages of 3.5 V and 3.9 V were chosen, that are above the threshold voltage for all pattern periodicities. At applied voltages above 3.9 V, control over the colloidal crystallization in colloidal crystals predetermined by the electrode pattern becomes difficult.

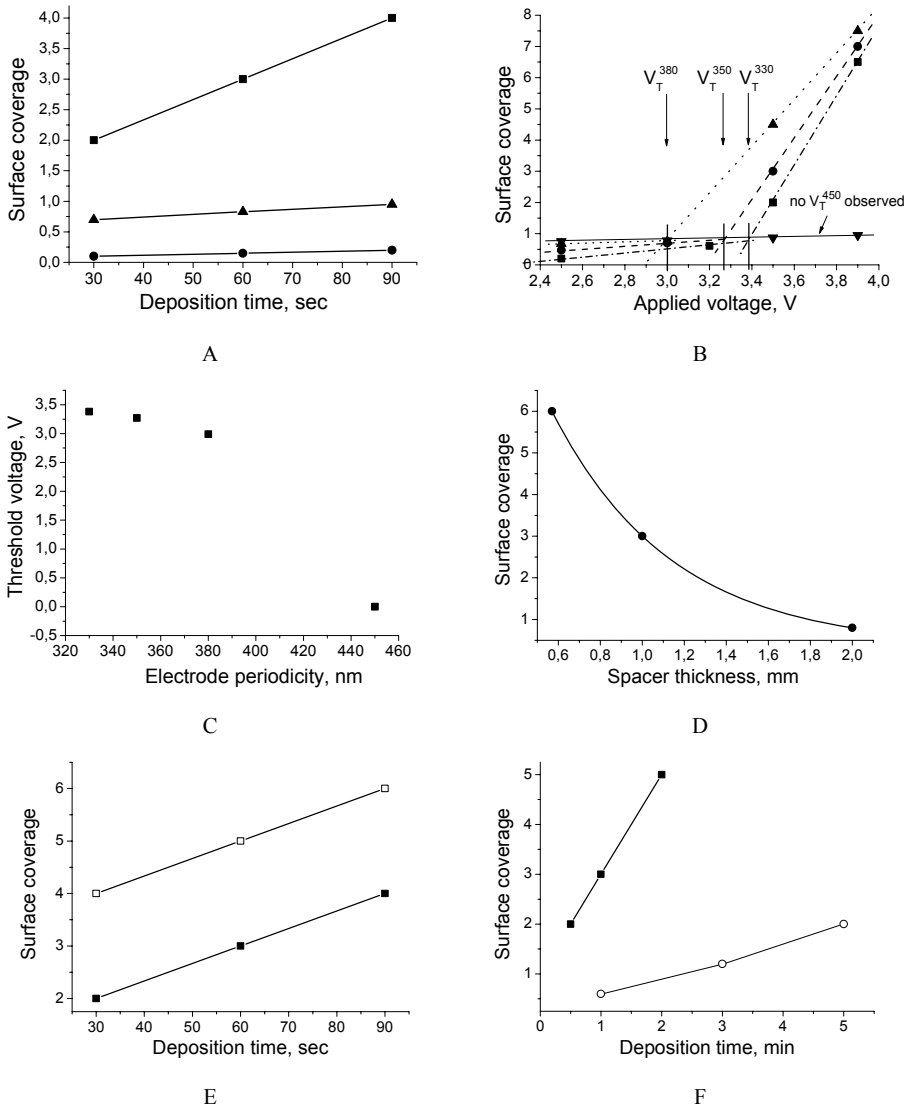

Figure 6.4. Graphs representing the dependence of the number of colloidal layers deposited at various deposition times on different parameters (constant parameters for all graphs are the size of the colloids (330 nm) and electrode withdrawal speed (0.04 mm/s): *Applied voltage dependence: A) time dependence* (—●— 2 V; —▲— 3 V; —■— 3.5 V)*; B) applied voltage dependence for the deposition time 60 sec and various periodicities* (V_T is the threshold voltage*)* (Pattern periodicities: —■— 330 nm; —◆— 350 nm; —▲— 380 nm; —▼— 450 nm); *C) threshold voltage versus pattern periodicity*: additional constant parameters are colloid concentration (0.5 vol%) and surface charge density of colloids = 16.2 μC/cm^2; D) *Spacer thickness dependence* ($y = 11.88 - 12.22x + 3.34x^2$): additional constant parameters are applied voltage (3.5 V), colloid concentration (0.5 vol%) and surface charge density of colloids (16.2 μC/cm^2), deposition time is 60 sec; E) *Surface charge density dependence*: additional constant parameters are applied voltage (3.5 V) and colloid concentration (0.5 vol%) (—■— Colloid diameter = 330 nm and surface charge density = 16.2 μC/cm^2; —□— Colloid diameter = 320 nm and surface charge density = 26.5 μC/cm^2); F) *Concentration dependence*: additional constant parameters are applied voltage (3.5 V), colloid concentration (0.5 vol%) and surface charge density of colloids (16.2 μC/cm^2) (—■— Colloid concentration = 0.5 vol%; —○— Colloid concentration = 0.2 vol%).

The surface coverage versus the distance between electrodes is presented in Figure 6.4D for region 2. Colloidal particles were deposited on the electrode surface with a pattern periodicity of 350 nm. A deposition voltage of 3.5 V was applied to the colloidal suspension of 0.5 vol. % and the electrode withdrawal speed was 0.04 mm/s. The non-linear dependence of colloidal thickness observed was due to a decrease in electric field strength. During the deposition, a decrease in electric field strength leads to a decrease in particle mobility and, therefore, to a lower number of deposited layers. In addition, when electrodes were placed in close proximity to each other (0.57 mm) and immersed in the colloidal suspension, then capillary pressure raised the level of the colloidal suspension between the electrodes over the colloidal suspension surrounding the electrodes, see Figure 6.2A. At this small spacing, colloid suspensions remained longer between the electrodes during electrode withdrawal, prolonging the deposition time. A large distances between electrodes (2 mm), the part of the colloidal suspension between electrodes during the deposition was on the same level as the outside suspension, therefore, electrodes were withdrawn from the suspension without trapping the colloidal solution between the electrodes.

Surface charge densities of colloidal particles play an important role in colloidal deposition. Deposition results for colloids with two different surface charges are presented in Figure 6.4E. Colloidal particles were deposited on an electrode surface with a pattern periodicity of 350 nm at an applied voltage of 3.5 V. The colloidal concentration was 0.5 vol. % and the electrode withdrawal speed was 0.04 mm/s. An increase in the surface charge density increased the surface coverage. For both surface charge densities, an increase in deposition time increased the number of layers. We found by SEM observation that good-quality colloidal monolayers were obtained from lower charge density colloids. Increase in surface charge density increases the mobility of colloidal particles and, therefore, colloidal particles arriving at the electrode surface do not have sufficient time to rearrange according to the electrode surface pattern.

Variations in the colloidal volume fraction have a pronounced influence on the colloidal surface coverage, Figure 6.4F. Here we depicted surface coverage versus deposition time for two volume fractions - 0.5 vol. % (filled squares) and 0.2 vol. % (empty squares). Pattern periodicity (350 nm), applied voltage (3.5 V) and withdrawal speed (0.04 mm/s) were kept constant. As expected, with increasing concentration the coverage dramatically increased (for a given deposition time). However, we also observed a deterioration of the packing quality of the crystals for high concentrations.

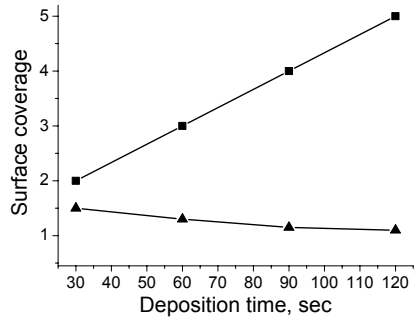

A

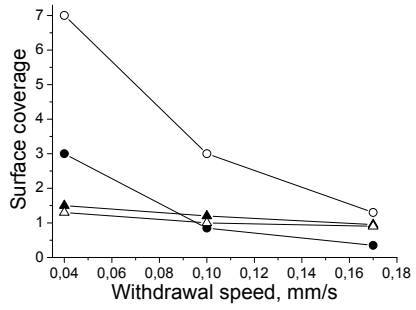

B

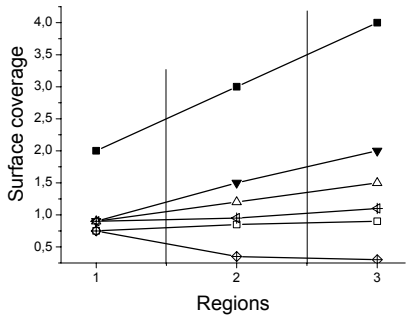

C

Figure 6.5. Graphs representing a comparison of colloidal deposition on patterns with different periodicities (constant parameters for all graphs are colloid size (330 nm), colloid concentration (0.5 vol%) and colloid surface charge density (16.2 μC/cm^2): A) *Pattern periodicity dependence*: additional constant parameters are applied voltage = 3.5 V, withdrawal speed of electrodes = 0.04 mm/s (Pattern periodicity: —■— 350 nm; —▲— 450 nm); B) *Applied voltage and withdrawal speed dependence*: additional constant parameter is deposition time = 1 min (Pattern periodicity of 350 nm: —●— 3.5 V; —○— 3.9 V; Pattern periodicity of 450 nm: —▲— 3.5 V; —△— 3.9 V); C) *Withdrawal speed and region on the sample (see Fig. 6.2B) dependence*: additional constant parameters are applied voltage = 3.5 V and deposition time = 1 min (Pattern periodicity of 350 nm: —■— 0.04 mm/s; —□— 0.1 mm/s; —⊠— 0.17 mm/s; Pattern periodicity of 450 nm: —▼— 0.04 mm/s; —△— 0.1 mm/s; —⊠— 0.17 mm/s).

Colloidal depositions for template electrodes with pattern periodicities of 350 nm and 450 nm and deposition voltages of 3.5 V and 3.9 V are presented in Figure 6.5. Colloidal particles with a diameter of 330 nm and surface charge density of 16.2 $\mu C/cm^2$ were used. The colloidal concentration was 0.5 vol. %. Surface coverage results for two periodicities and an electrode withdrawal speed of 0.04 mm/s are shown as a function of deposition time in Figure 6.5A. For small packing distances (350 nm), the surface coverage linearly increased with deposition time. However, for a pattern periodicity of 450 nm, the surface coverage was close to one layer even for long deposition times.

Colloidal crystal growth with controlled structure and orientation is highly dependent of the withdrawal speed of electrodes from the colloidal suspension and dependent on the angle at which electrodes are withdrawn. In our first experiments, we did not use a controlled withdrawal of electrodes.[26] Prior to electrode withdrawal from the colloidal suspension, the applied electric voltage was increased to above 10 V, in order to get "permanent" adhesion of colloidal particles to the electrode surface. At this relatively high voltage, thick colloidal crystals were formed. In order to get colloidal monolayers, the upper layers were washed away in ethanol without turning off the electric field. In this method, it was difficult to predict when washing had to be stopped. The thickness of colloidal crystals could not be controlled by simply increasing the deposition time. Therefore, in order to control the thickness of colloidal crystals, the influence of the withdrawal speed of electrodes from colloidal suspensions needed to be determined. The relationship between surface coverage and withdrawal speed of electrodes from the colloidal suspension is shown in Figure 6.5B. Results for applied voltages of 3.5 V and 3.9 V and sample regions 2 and 3 (Figure 6.2B) are presented. The surface coverage dramatically decreased with increasing the withdrawal speed of the electrodes with a pattern periodicity of 350 nm. The thickness "gradient" was established over two sample regions. However, there is almost no influence of the withdrawal speed on crystal thickness detected over two sample regions for a pattern periodicity of 450 nm. The difference between depositions on electrode surfaces with different periodicities is related to the surface topology of the deposited colloidal layers. For the pattern periodicity of 450 nm, it was possible to grow colloidal crystals only with a thickness of maximum two colloidal layers at any applied voltage used. This is probably due to smoothening of the surface topology of two deposited layers, where the top layer approximates a flat surface. We speculate that colloids deposited on top of these two layers glide back into the bulk colloidal suspension during electrode withdrawal.

In Figure 6.5C, surface coverage data for the three electrode regions are shown, that were obtained for withdrawal speeds of 0.04, 0.1 and 0.17 mm/s. The deposition voltage of 3.5 V, deposition time of 1 min and colloidal concentration of 0.5 vol% were kept constant. For the pattern periodicity of 350 nm and at withdrawal speeds of 0.04 mm/s, the surface coverage was not homogeneous and increased from the top to the bottom of the sample. Upon increasing the withdrawal speed (0.1 mm/s), the surface coverage became homogeneous over the whole sample area. Above this value, the number of layers decreased from the top to the bottom of the sample. However, for periodicities of 450 nm, a slight increase in the number of layers was detected at all withdrawal speeds, but the difference between three depositions at different withdrawal speeds is small. For the two template periodicities (350 and 450 nm) at a withdrawal speed of 0.17 mm/s, different trends in the surface coverage were observed. For the periodicity of 450 nm, the surface coverage was homogeneous over the sample and for the periodicity of 350 nm, a decrease in surface coverage was detected. We postulate that for the periodicity of 450 nm, deposited colloids interact less with each other via electrostatic forces due to their large separation, and strong electrostatic forces between colloids and electrodes keep the particles on the surface. On the contrary, at the periodicity of 350 nm, colloids are in close proximity to each other and they are not close packed (colloid size is 330 nm), therefore, there is a strong competition between electrostatic forces that act between electrode and colloids and capillary forces acting between colloids. Therefore, for the periodicity of 350 nm, at high withdrawal speeds (0.17 mm/s) colloidal particles were likely driven back to the colloidal suspension.

In separate experiments, the effect of capillary forces on colloidal crystal growth was examined. Colloidal particles were first deposited on a patterned electrode surface with a periodicity of 350 nm by applying an electric field, followed by electrode withdrawal without an applied electric field. In the second experiment, electrodes were kept in colloidal suspension for a certain time without any applied electric field and then pulled out of the colloidal suspension. Deposition parameters used were a colloidal concentration of 0.5 vol.%, applied voltage of 3.5 V for 1 min and a withdrawal speed of 0.04 mm/s. In the two cases, practically no colloidal deposition was observed. Therefore, we conclude that capillary forces at withdrawal speeds used in this study did not have any significant effect on the crystal build-up as shown by control experiments. This finding also shows the importance of leaving the voltage “on” to hold the crystals on the electrodes during withdrawal.

6.5. Formation of colloidal monolayers

Electrophoretic deposition of colloidal particles on a flat electrode surface does not allow structural control of colloidal layers on the electrode substrate with a desired symmetry and periodicity. Upon increasing the deposition time, randomly located colloidal particles on the electrode surface developed into colloidal crystals with a "glassy" structure, Figure 6.3. Colloidal deposition on patterned electrode surfaces allows one to control the symmetry of colloidal monolayers and crystals. Examples of the colloidal deposition of a single colloidal layer on electrodes with hexagonal, square and rectangular surface patterns are presented in Figure 6.6. The electrode pattern periodicity is on the order of the colloid particle diameter. Electrode pattern structures correspond to the FCC (111), (100) and (110) crystal planes. The controlled growth of colloidal crystals with FCC structures exposing different crystal planes parallel to the electrode surface is discussed in Chapter 7.

In the subsequent sections, we focus our attention on the formation of colloidal monolayers using template driven electrophoretic deposition. Surface coverage and surface structure of colloidal monolayers on the electrode surfaces with a periodicity on the order of the colloid particle diameter are presented in Figure 6.6. The hexagonal structure is the most closely packed structure and, therefore, is the most favourable for colloids to be formed on flat electrodes. The formation of almost fully covered colloidal monolayers with a hexagonal structure was easily realized. In this case the electrode pattern influences only the orientation of hexagonal colloid monolayers on the electrode surface, as it is shown in Figure 6.6A. Colloidal layers with square and rectangular structures cannot be fabricated without using patterned electrodes exhibiting the required packing. The growth of colloidal monolayers with square and rectangular structures confirms the influence of a patterned surface on colloidal crystallization. Such colloidal monolayers with square and rectangular symmetry are

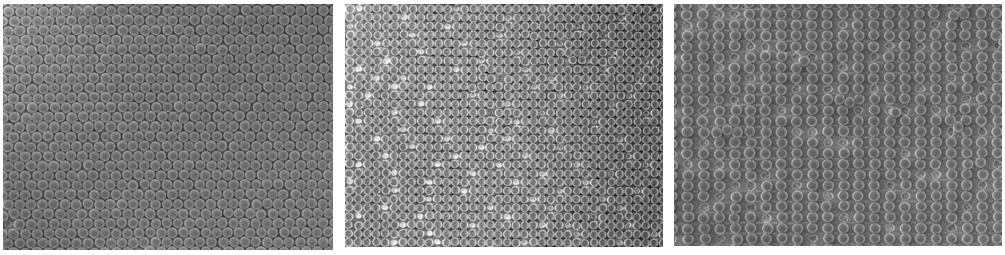

A **B** **C**

Figure 6.6. Colloidal deposition on electrodes with different surface patterns; A) hexagonal, B) square and C) rectangular patterns.

presented in Figure 6.6B and 6.6C, respectively. Growth of colloidal crystals with a thickness of more than two colloidal layers (see Appendix I-I) on a rectangular surface pattern that corresponds to the FCC (110) plane, was difficult to perform. The structure of this crystal plane is close packed in one direction within the plane, but has a large periodicity in the perpendicular direction. Thick colloidal crystals grown at this surface reveal mixed hexagonal and square types of upper layers parallel to the electrode surface. During electrode withdrawal, the colloidal particles tend to rearrange into close packed structures by occupying positions between vertical rows and pushing colloids apart from the predetermined positions dictated by the topological pattern, thus forming polycrystalline layers with hexagonal and square types of structures.

Colloidal monolayers with hexagonal and square types of patterns and various periodicities are presented in Figure 6.7. Pattern periodicities were 350 nm, 380 nm, 450 nm and 500 nm, respectively, excluding examples with a pattern periodicity of 330 nm as shown in Figure 6.6. Again, the colloidal particles used here had a diameter of 330 nm. Increase in the pattern periodicity from one electrode sample to another improved the surface coverage of colloidal monolayers as it was explained earlier. The examples exhibiting two layers, shown in Figure 6.7C could be obtained by increasing e.g. the applied voltage or deposition time, as was demonstrated earlier. In general, the lower the colloidal concentration (here: 0.2 vol. %) and surface charge density (here: 16.2 $\mu C/cm^2$), the slower the deposition process and therefore, the better the quality of deposited colloidal layers. Increase in the applied voltage from 3.5 V to 3.9 V led to a subsequent increase in the number of layers, but the deposited colloidal layers did not correspond to the colloidal crystals that were expected according to the employed surface pattern. Colloidal multilayers (crystals) formed at an applied voltage of 3.9 V were polycrystalline with a mixed crystal orientation and orientation with respect to the electrode pattern orientation. This result was likely caused by the large number of particles arriving simultaneously at the patterned substrate, therefore, the particles lacked the time required to arrange themselves according to the surface pattern. At an applied voltage of 3.5 V, the quality of deposited colloidal layers depended on the withdrawal speed of the electrodes. We found that withdrawal speeds must be tuned to the pattern periodicity. For a pattern periodicity in the order of the colloid size, a low speed (in our case 0.04 mm/s) was preferred, since this enhanced the surface coverage as well as the quality of deposited layers. An increase in surface pattern dimensions should be accompanied by an increase in withdrawal speed. From our experience, for pattern periodicities of 350 nm and 380 nm, a withdrawal speed of 0.07 mm/s was found to be optimal and for periodicities of 450 nm and

500 nm, withdrawal speeds of 0.1 mm/s and 0.17 mm/s were preferred. By adjusting these deposition parameters, we were able to control the quality and thickness of deposited colloidal layers on the electrode surfaces with various (non-closed packed) periodicities over large electrode surface areas (several square millimeters). All these results show that the electrophoretic colloidal deposition on patterned electrodes is a versatile method that allows a good control of the location of deposited colloidal particles and orientation and quality of colloidal layers.

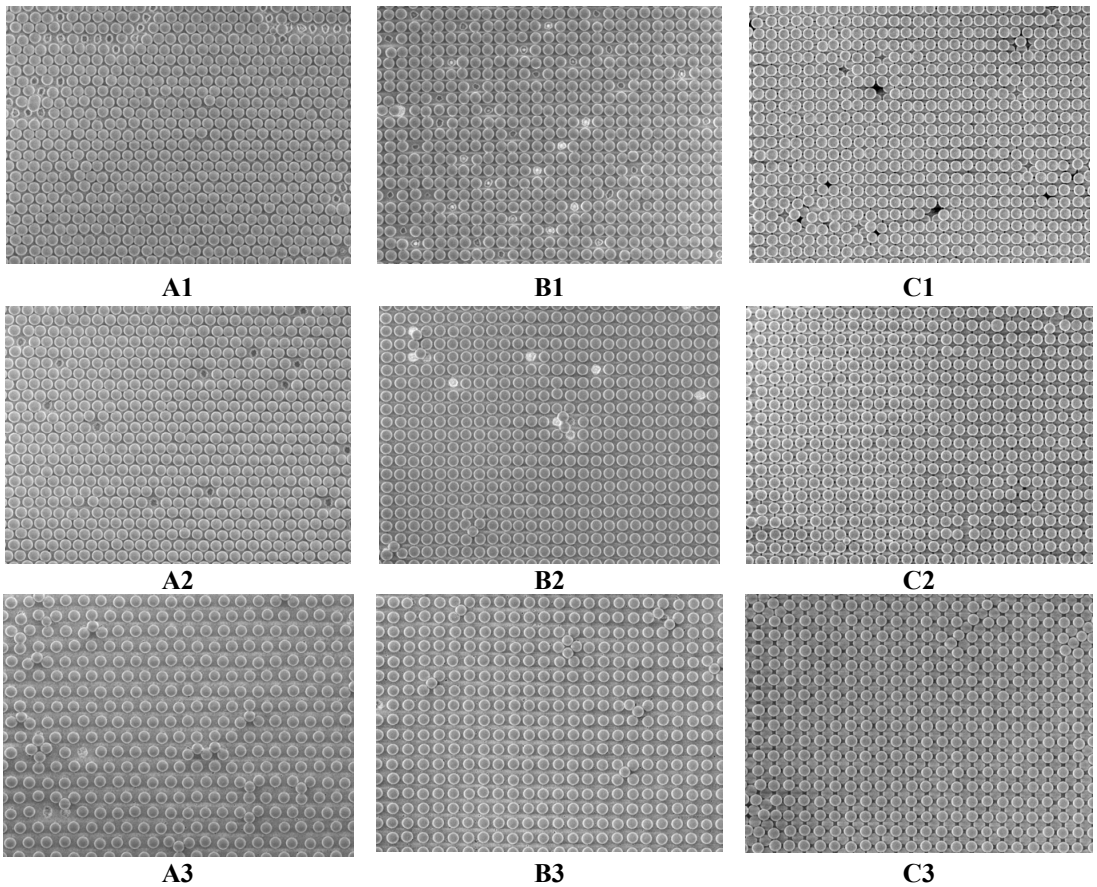

Figure 6.7. Colloidal deposition on electrodes of different periodicities; A) hexagonal pattern with periodicities of A1) 350 nm, A2) 400 nm and A3) 500 nm (see also Appendix I-III); B) and C) square pattern of one and two layers with periodicities of B1) and C1) 350 nm (see also Appendix I-II), B2) (see also Appendix I-IV) and C2) 380 nm (see also Appendix I-V) and B3) and C3) 450 nm (see also Appendix I-VI).

6.6. Defects in colloidal aggregates on patterned substrates

Defects in a structured dielectric layer of an electrode cause the formation of defects in colloidal monolayers and crystals, Figure 6.8. Defects in the patterned layer can be formed during electrode patterning steps or during electrode handling. During electrode patterning most of the defects are introduced in the photoresist patterning step. Large defect structures (on the order of micrometers) are caused usually by the presence of dust particles, swollen photoresist particles or by an inhomogeneous photoresist layer thickness etc, Figure 6.8, A and C. Small defects (in the sub-micrometer range), such as missing pits in a patterned layer or a high roughness of the pit's edges, usually appear during a lift-off step, when photoresist pillars are removed. Mechanical defects are usually caused during electrode handling by scratching a thin patterned dielectric layer with tweezers or any other sharp object, Figure 6.8B. Any defect structure in the patterned layer leads to bare areas of the conductive electrode surface. In these regions, formation of close-packed colloidal aggregates occurs during electrophoretic deposition of colloidal particles, therefore, breaking the colloidal crystal order predetermined by the electrode patterning, see Figure 6.8. Thus, electrode surface defects play a crucial role in directed colloidal crystal growth.

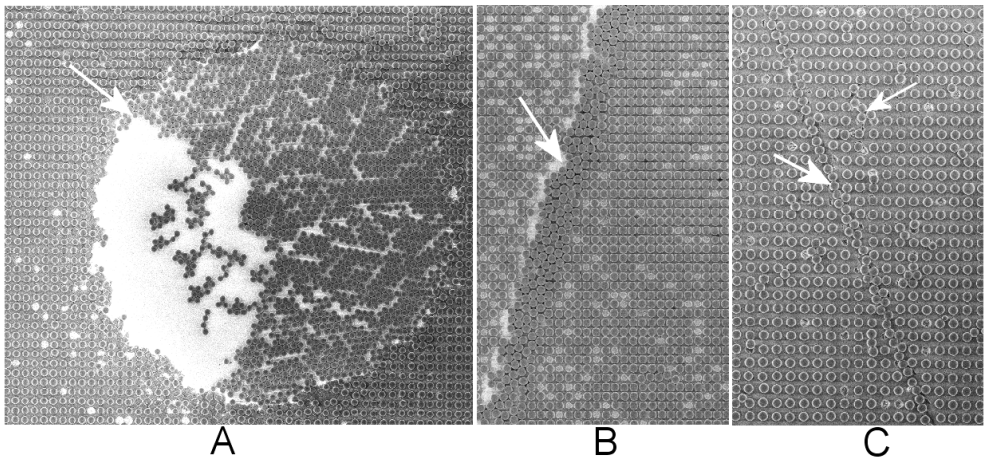

Figure 6.8. Substrate defects: A) circular; B) and C) lines.

Conclusions

The method of electrophoretic deposition of charged polymer colloids onto patterned substrates is a powerful technique to control the structure and orientation of colloidal monolayers. Colloidal deposition on hexagonal, square and rectangular types of electrode patterns with different pattern periodicities in the sub-micrometer range was successfully demonstrated. Increasing the ratio between closest "pit" distance at the patterned electrodes versus colloidal diameter (by increasing the repeat length of the patterns, i.e. pattern periodicity) led to an improved coverage of colloidal monolayer. Electrode surfaces with pattern periodicities on the order of the colloid particle diameter were not covered completely. Various deposition parameters such as applied voltage, distance between electrodes, colloid concentration, surface charge of colloidal particles and withdrawal speed influence the colloidal deposition process and the quality of the resulting layers. The existence of a "threshold voltage" has been established. If the deposition voltage exceeded the value of the threshold voltage, a substantial increase in the number of layers with the applied voltage was detected. The threshold voltage was found to depend on the ratio between particle size and pattern periodicity. The value of the threshold voltage decreased with an increase in pattern periodicity in a non-linear fashion. Optimal deposition parameters were determined for a successful formation of colloidal monolayers over large areas for the given systems (colloidal particles and patterned electrodes) studied. The withdrawal speed plays an essential role in the colloidal crystallization process. A withdrawal speed of 0.1 mm/s for the applied voltages above the threshold voltage was found optimal for homogeneous monolayer formation over large electrode areas.

Appendix I

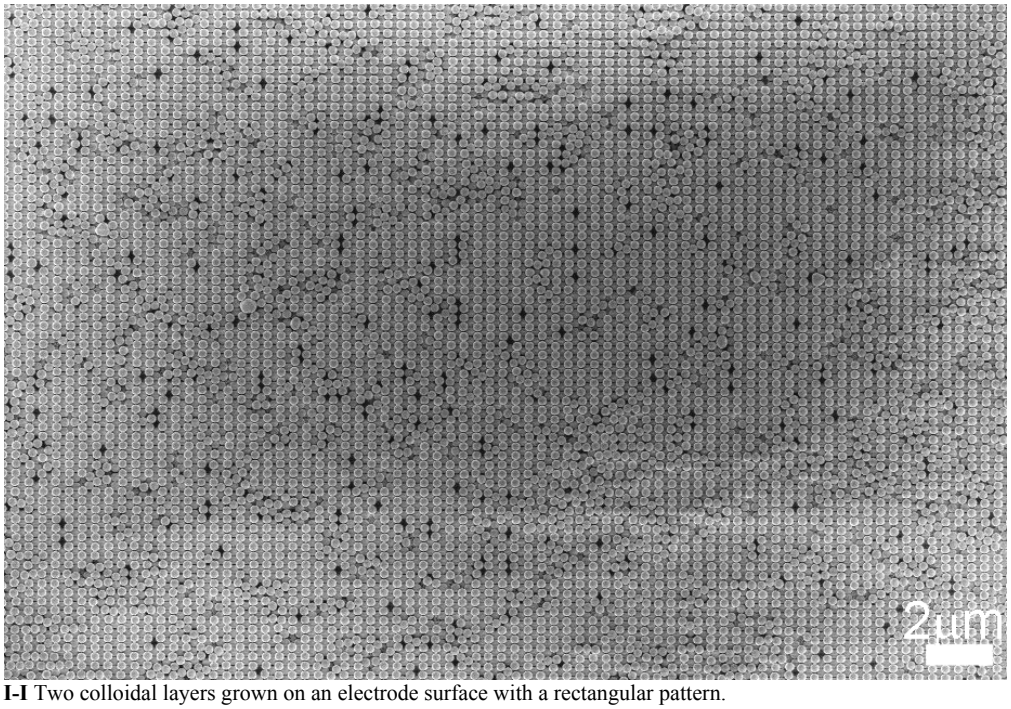

I-I Two colloidal layers grown on an electrode surface with a rectangular pattern.

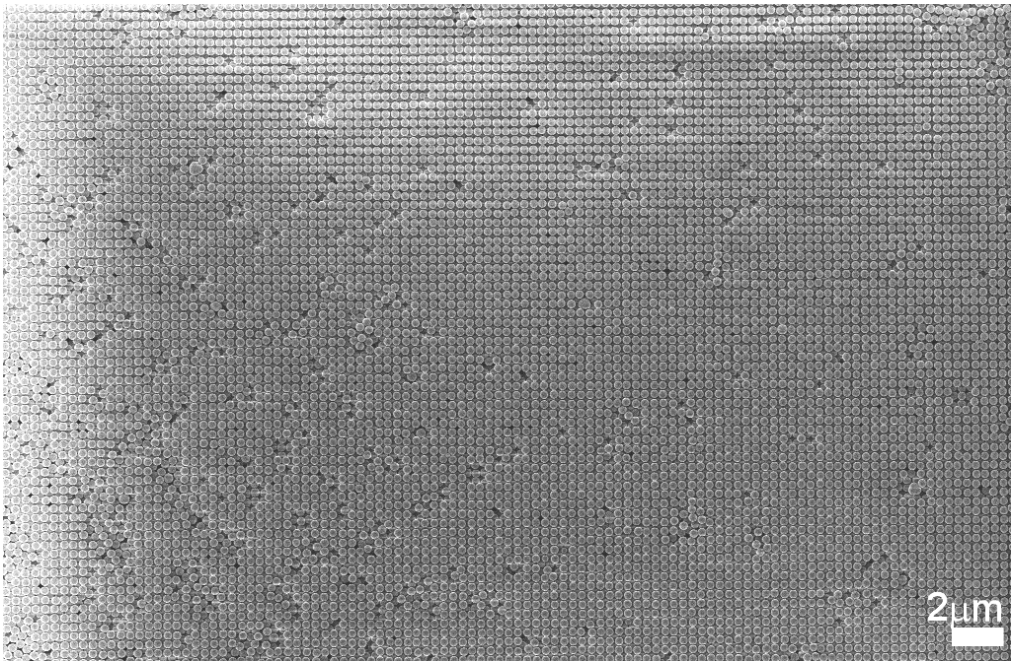

I-II Three colloidal layers with a square structure and a pattern periodicity of 350 nm.

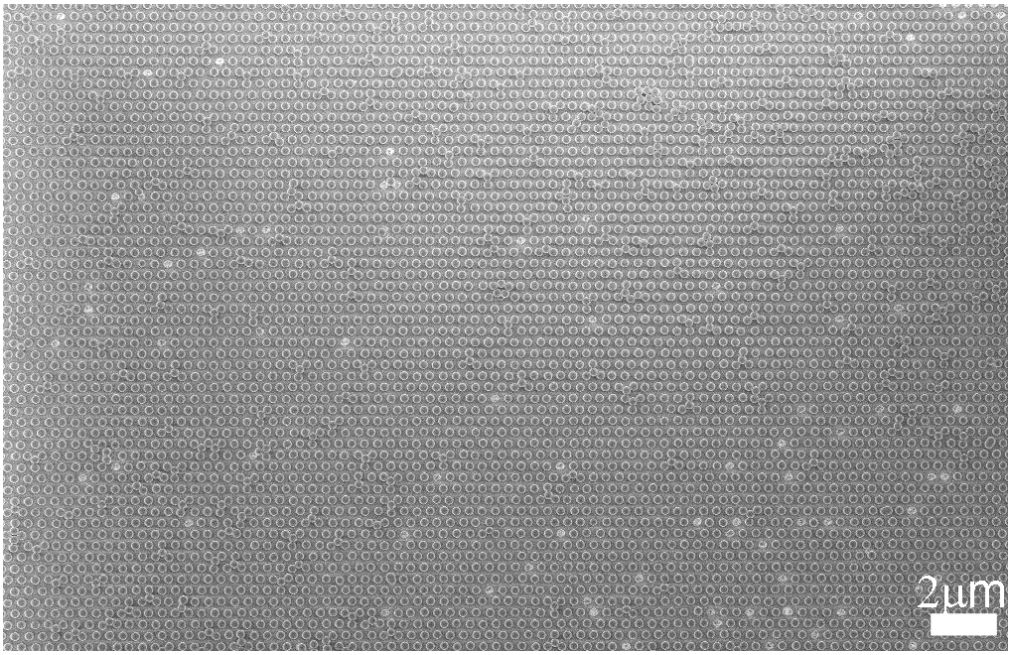

I-III Colloidal monolayer grown on a hexagonally patterned substrate with a pattern periodicity of 500 nm.

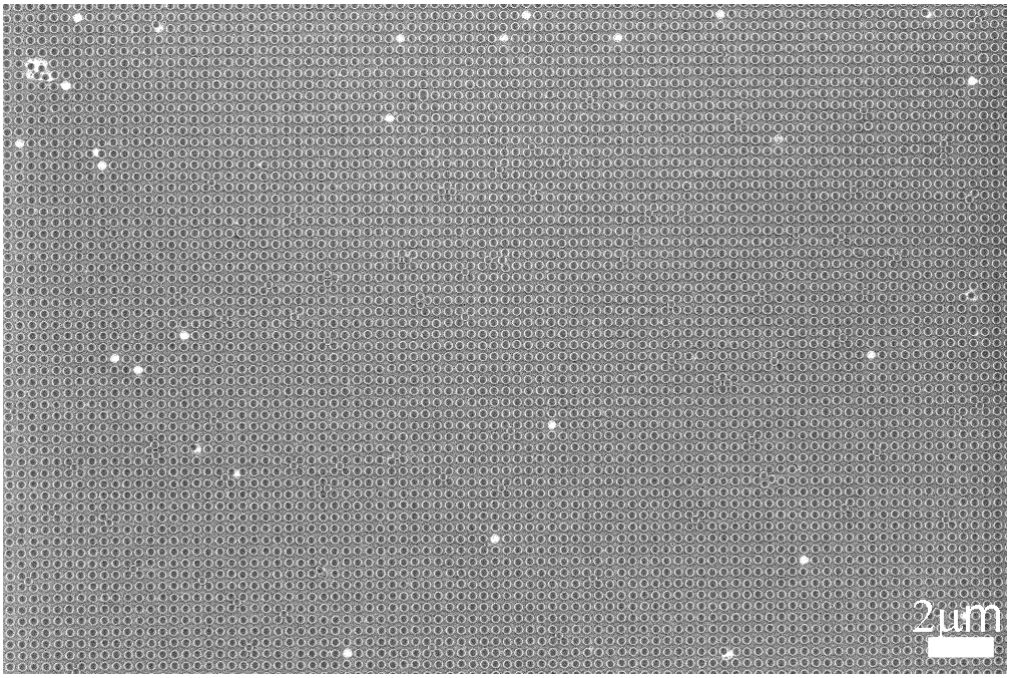

I-IV Colloidal monolayer grown on an electrode surface with a square pattern and a pattern periodicity of 450 nm.

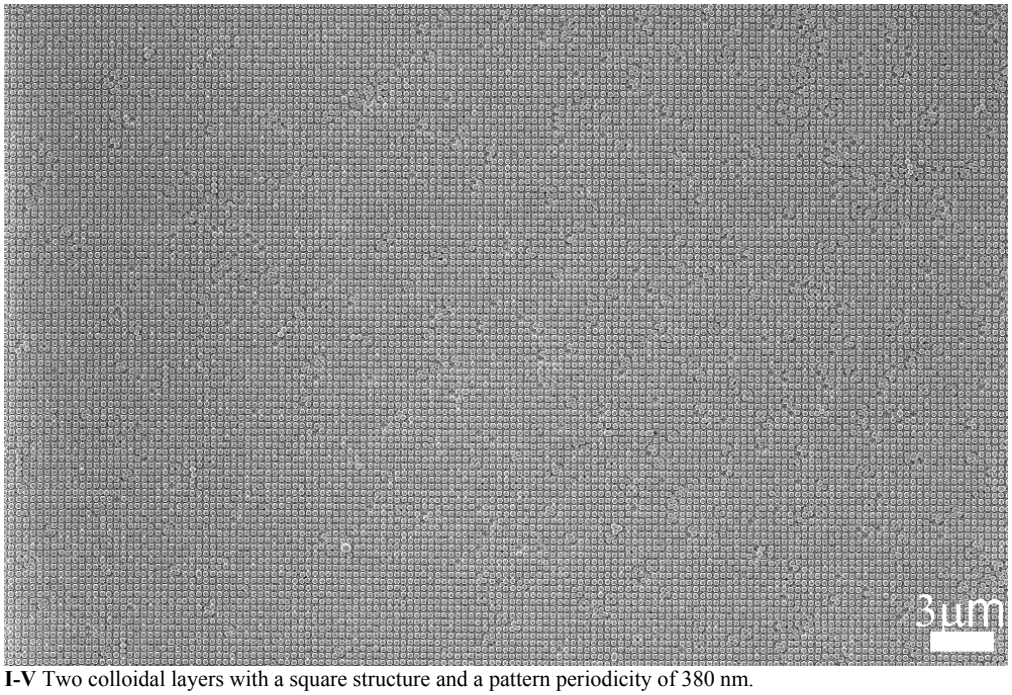

I-V Two colloidal layers with a square structure and a pattern periodicity of 380 nm.

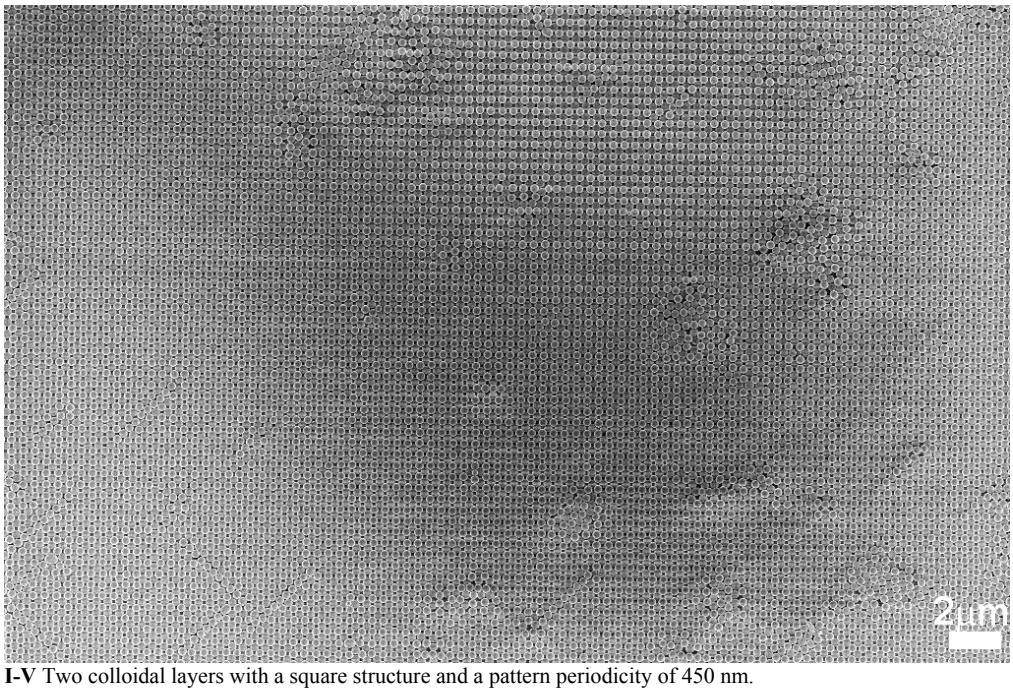

I-V Two colloidal layers with a square structure and a pattern periodicity of 450 nm.

References

[1] J. D. Joannopoulos, R. D. Meade, J. N. Winn, *Photonic Crystals: Molding the Flow of Light*, Princeton University Press, Princeton, NJ **1995**.
[2] S. Hayashi, M. Kobayashi, Y. Kumamoto, K. Suzuki, T. Suzuki, T. Hirai, *J. Coll. Int. Sci.* **1992**, *153*, 509.
[3] J. C. Hulteen, R. P. Van Duyne, *J. Vac. Sci. Technol. Part A* **1995**, *13*, 1553.
[4] F. Caruso, *Chem. Eur. J.* **2000**, *6*, 413.
[5] P. Jiang, J. F. Bertone, K. S. Hwang, V. L. Colvin, *Chem. Mater.* **1999**, *11*, 2132.
[6] S. H. Im, M. H. Kim, O. O. Park, *Chem. Mater.* **2003**, *15*, 1797.
[7] N. D. Denkov, O. D. Velev, P. A. Kralchevsky, I. B. Ivanov, H. Yoshimura, K. Nagayama, *Nature* **1993**, *361*, 26.
[8] A. S. Dimitrov, K. Nagayama, *Langmuir* **1996**, *12*, 1303.
[9] E. Kumacheva, P. Garstecki, H. Wu, G. M. Whitesides, *Phys. Rev. Lett.* **2003**, *91*, 128301.
[10] K.-H. Lin, J. C. Crocker, V. Prasad, A. Schofield, D. A. Weitz, T. C. Lubensky, A. G. Yodh, *Phys. Rev. Lett.* **2000**, *85*, 1770.
[11] Y.-H. Ye, S. Badilescu, Vo-Van Truong, P. Rochon, A. Natansohn, *Appl. Phys. Lett*. **2001**, *79*, 872.
[12] G. A. Ozin, S. M. Yang, *Adv. Funct. Mater.* **2001**, *11*, 95.
[13] Y. Xia, Y. Yin, Y. Lu, J. McLellan, *Adv. Funct. Mater.* **2003**, *13*, 907.
[14] D. K. Yi, E.-M. Seo, D.-Y. Kim, *Appl. Phys. Lett.* **2002**, *80*, 225.
[15] J. P. Hoogenboom, C. Rétif, E. de Bres, M. van de Boer, A. K. van Langen-Suurling, J. Romijn, A. van Blaaderen, *Nano Lett.* **2004**, *4*, 205.
[16] S.-R. Yeh, M. Seul, B. I. Shraiman, *Nature* **1997**, *386*, 57.
[17] M. Trau, D. A. Saville, I. A. Aksay, *Langmuir* **1997**, *13*, 6375.
[18] M. Holgado, F. Garcia-Santamaria, A. Blanco, M. Ibisate, A. Cintas, H. Miguiz, C. J. Serna, C. Molpeceres, J. Requena, A. Mifsud, F. Meseguer, C. Lopez, *Langmuir* **1999**, *15*, 4701.
[19] M. E. Leunissen, C. G. Christova, A.-P. Hynninen, C. P. Royall, A. I. Campbell, A. Imhof, M. Dijkstra, R. van Roij, A. van Blaaderen, *Nature* **2005**, *437*, 235.
[20] A. Yethiraj, A. van Blaaderen, *Nature* **2003**, *421*, 513.
[21] E. Kumacheva, R. K. Golding, M. Allard, E. H. Sargent, *Adv. Mater*. **2002**, *14*, 221.
[22] R. G. Golding, P. C. Lewis, E. Kumacheva, *Langmuir* **2004**, *20*, 1414.
[23] M. Allard, E. H. Sargent, P. C. Lewis, E. Kumacheva, *Adv. Mater*. **2004**, *16*, 1360.
[24] F. F. Ruess, *Mem. Soc. Imp. Natur. Moscou*, **1809**, *2*, 327.
[25] S. S. Vouckii, *A Course of Colloidal Chemistry,* 2nd ed., "Chemistry", Moscow, **1976**.
[26] N. V. Dziomkina, M. A. Hempenius, G. J. Vancso, *Adv. Mater.* **2005**, *17*, 237.

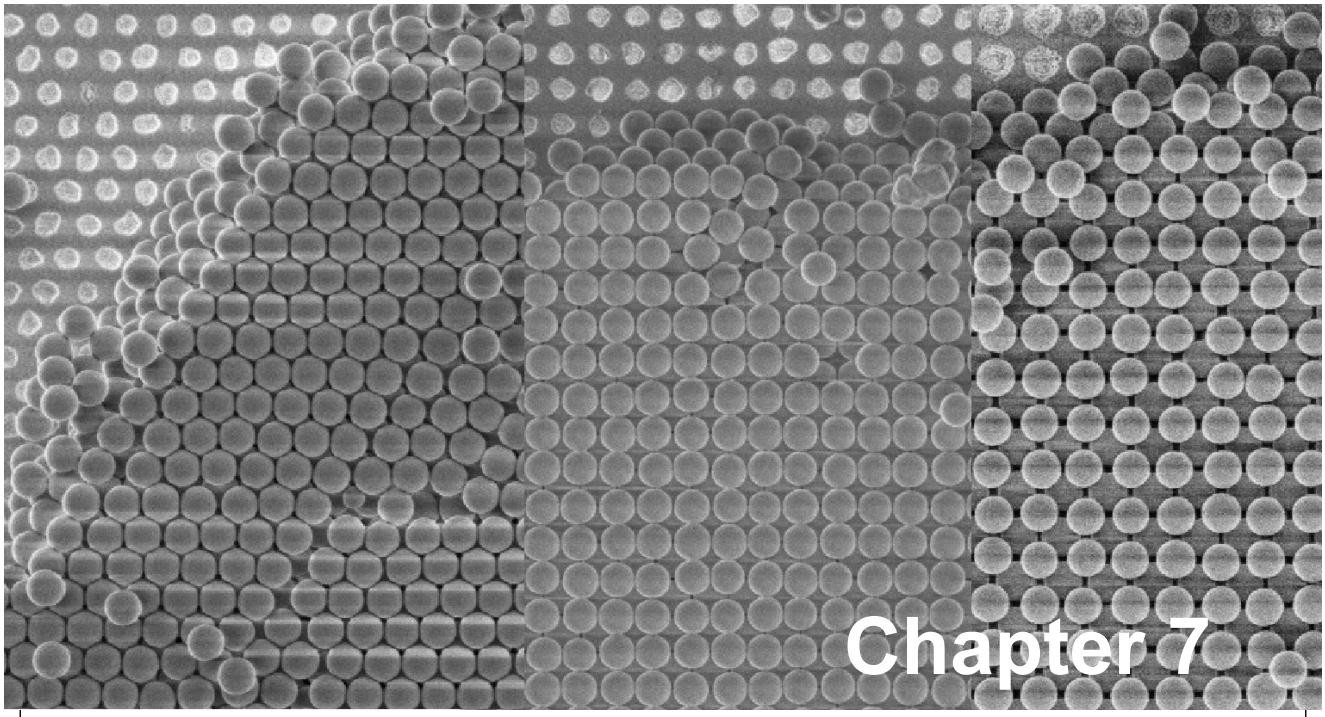

Chapter 7

Growth of FCC and BCC Colloidal Crystals with Controlled Structure and Orientation[*]

The controlled growth of colloidal crystals with FCC and BCC crystal structures is discussed. Colloidal particles were deposited on patterned electrode surfaces under an applied electric field. Crystal growth was influenced by varying the surface topology of patterned electrodes. FCC colloidal crystals with (111), (100) and (110) crystal planes and BCC crystals with (100) crystal planes parallel to the electrode surface are presented. The growth of FCC (111) and (100) was easily controlled, while the growth of the (110) plane in the [110] direction was difficult since this plane is non-close packed. BCC (100) colloidal crystals were successfully grown with a homogeneous surface coverage over several millimeters and with a crystal thickness of up to seven layers. The quality and thickness of the colloidal crystals were optimized by adjusting various deposition parameters such as deposition voltage, colloidal volume fraction and surface charge density, and withdrawal speed of the electrode out of the colloidal suspension after deposition.

[*] Parts of this chapter have been published in: N. V. Dziomkina, M. A. Hempenius, G. J. Vancso, *Proceedings SPIE* **2005**, *5931*, 59310Z.

Introduction

The direction of light propagation in photonic crystals is highly dependent on the photonic crystal structure.[1] It was predicted that colloidal crystals with a diamond structure are able to block the light in all directions,[2] therefore, opening many possibilities to guide light propagation by defect structure control. Fabrication of colloidal crystals with the diamond structure by self-assembly of colloidal particles has not been achieved so far due to the low packing fraction of 0.34.

The structure that is usually obtained by self-assembly of colloidal particles on a flat substrate is a close-packed structure such as face - centred cubic (FCC) with a packing density of 0.74, stacked in the direction of the close - packed (111) plane.[3,4] Photonic crystals with an FCC structure possess a photonic band gap (PBG) only in the second Brillouin zone at a refractive index contrast higher than 2.8, and not in the first zone.[5,6,7] Working in the range of frequencies of the first zone, we deal actually with stop bands that are opened in certain crystal directions. Therefore, if we want to integrate such crystals for example into optical chips, control of the crystal orientation on the substrate is important.

The body-centred cubic (BCC) structure possesses a packing density of 0.68, only slightly lower than that of the FCC, but it is already a problem to fabricate such a structure in a controlled way. Realization of the controlled growth of a BCC colloidal crystal structure will allow one to make a step towards the non-close-packed structures.

Control over colloidal crystal orientation, crystal symmetry, location on the substrate, and defect structure can be realized by the use of topologically patterned substrates, see Chapter 2. The method of template - directed colloidal crystallization has already been demonstrated to influence colloidal crystal orientation of close packed crystals,[8,9] the size of colloidal crystals[10,11] and to tailor to a certain degree the crystal structure.[12,13] Furthermore, the pattern of the surface pre-determines the location of the colloidal crystal on the surface, which is an important aspect for planar integration technology. Van Blaaderen *et al*. showed, for example, that slow sedimentation of colloidal particles into the “holes” of topologically patterned templates direct the formation of FCC colloidal crystals with a crystal orientation of the (100) planes parallel to the patterned surface that is different from the usual (111) plane orientation with respect to the surface. Ozin *et al*.[14,15] who pioneered the fabrication of planarized microphotonic structures based on colloidal crystals, successfully integrated confinement driven colloidal self-assembly, two-dimensional (2D) template growth (the method is called “micromolding in capillaries”). Yodh *et al*.[16] and Xia *et al*.[17] later showed

the use of 2D grating templates with a square pattern to drive the growth of three-dimensional (3D) colloidal crystals with (100) orientation parallel to the substrate by a controlled solvent evaporation process. In the slow evaporation process, a full control of thickness, ordering and domain size of colloidal crystals could be realized by simultaneous consideration of several processing parameters. These parameters include the choice of substrate, tilt angle of the substrate with respect to the free surface of the colloidal suspension (when the substrate is immersed across the suspension-air interface), choice of solvent, evaporation rate, ambient temperature and relative humidity, concentration of colloids,[3,4,18] etc. Unfortunately, the process of controlled evaporation and sedimentation is rather slow and successful fabrication of high-quality colloidal crystals can take from several hours to several months (in the case of colloidal sedimentation).[19,20]

The application of an electric field accelerates the growth of the 3D colloidal crystals on flat electrode surfaces.[21] Careful adjustment of colloidal concentration and electric field strength even leads to the formation of various crystal structures on a flat electrode surface.[22] Several crystal structures were observed using a confocal microscope directly in the colloidal suspension. Solid crystals ("free-standing colloidal crystals") were not obtained. Capillary forces, acting between colloidal particles, simply destroy non-close-packed colloidal crystals when a sample is withdrawn from the colloidal suspension.

In this chapter, we present a study on the *direct* formation of 3D FCC and BCC colloidal crystals with controlled thickness and orientation. The method of electrophoretic deposition of charged colloidal particles onto patterned electrode substrates, presented in Chapter 6, was applied. The influence of various deposition parameters on the quality and thickness of grown colloidal crystals was investigated. Deposition parameters such as deposition voltage, deposition time, concentration of colloidal particles in suspension and withdrawal speed of the electrodes out of the colloidal suspension after the colloidal deposition are discussed.

7.1 Colloidal crystals with FCC crystal structure

Colloidal deposition was performed on patterned electrode surfaces with hexagonal, square and rectangular types of structures, Figure 7.1. These patterned structures correspond to FCC (111), (100) and (110) crystal planes. Pattern periodicity was on the order of the colloidal particle size for close-packed planes. Negatively charged polystyrene colloidal particles with a diameter of 330 nm, polydispersity index of 1.03 and surface charge densities of 16.2 μC/cm^2 and 26.5 μC/cm^2 were used. In the colloidal suspension, polymer colloidal particles with volume fractions of 0.2 vol.% or 0.5 vol.% were redistributed in a mixture of ethanol and water (80:20 vol/vol). Applied voltages were varied between 2.5, 3.0, 3.5 and 3.9 V. Withdrawal speeds of the electrodes from the colloidal suspension were 0.04, 0.08 and 0.1 mm/s.

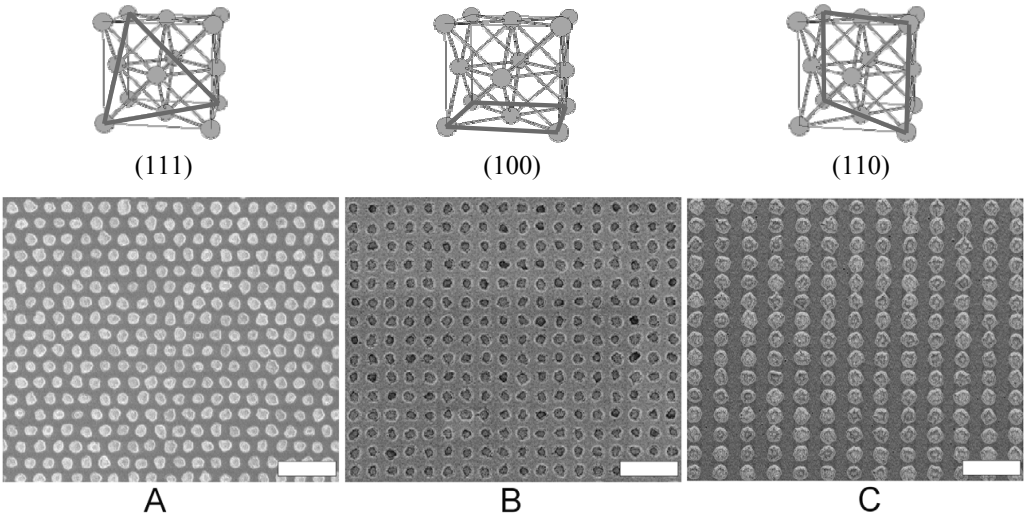

Figure 7.1 SEM images of electrode surfaces with A) hexagonal, B) square, and C) the rectangular patterns. Pattern structures correspond to FCC (111), (100) and (110) crystal planes, shown above the SEM images. The scale bar represents 1 μm.

7.1.1. Deposition of colloidal particles

Results of colloidal depositions are presented as colloidal surface coverage (defined earlier in Chapter 6) versus various deposition parameters in Figure 7.2. Deposition results at different applied voltages are presented in Figure 7.2A. Other parameters such as deposition time (1 min), colloidal concentration (0.5 vol.%) and withdrawing speed of the electrodes (0.04 mm/s) were the same for all samples. The surface coverage for region 2 (Figure 6.2B) is

presented. Upon increasing the applied voltage from 2.5 V to 3 V, a slight increase in surface coverage was detected, but at 3.5 V and 3.9 V a significant amount of layers was grown. From these results, a threshold voltage of ~ 3.4 V could be determined. Therefore, from these experiments we chose 3.5 V and 3.9 V as the applied (deposition) voltage for the following experiments.

The influence of the deposition time on surface coverage at 3.5 V, using a colloidal concentration of 0.5 vol.% and a withdrawal speed of 0.04 mm/s is presented in Figure 7.2B.

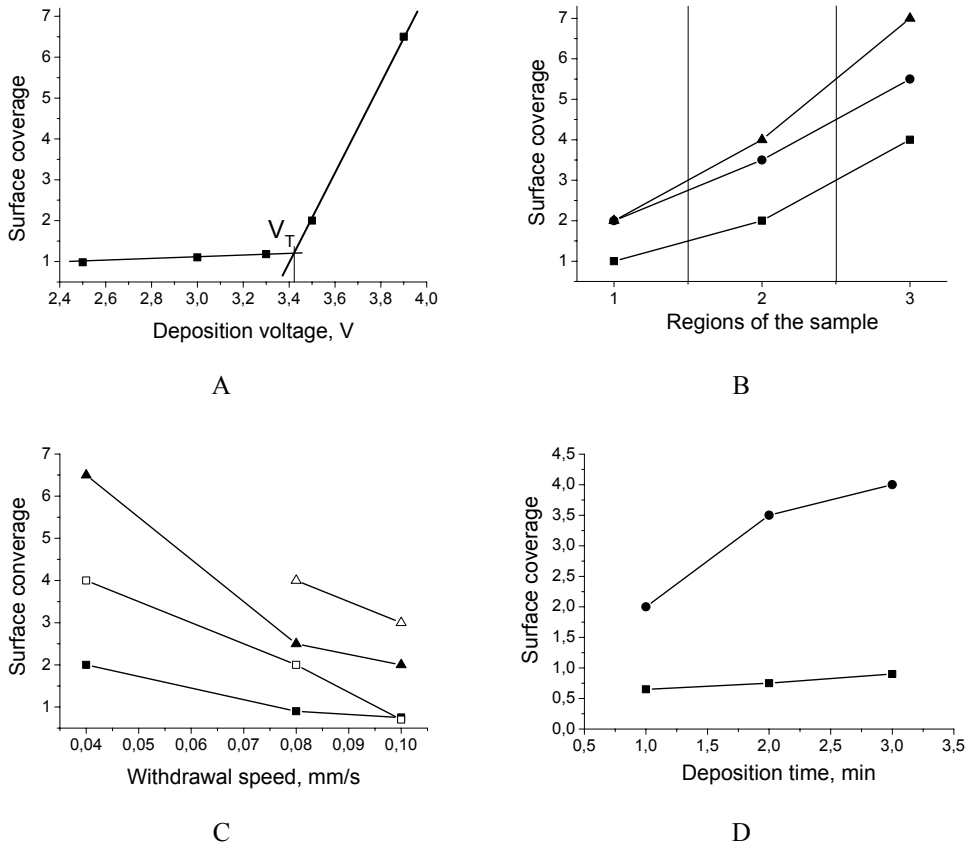

Figure 7.2 Surface coverage versus various deposition parameters (constant parameters for all graphs are the size of the colloids (330 nm) and surface charge density of colloids (16.2 μC/cm^2)): A) *Applied voltage* (deposition time = 1 min, colloidal concentration = 0.5 vol.%, withdrawal speed of electrodes from the colloidal suspension = 0.04 mm/s). Surface coverage was calculated in region 2 (Figure 6.2B). The threshold voltage V_T is ~ 3.4 V; B) *Deposition time* —■— 1 min; —●— 2 min; —▲— 3 min (deposition voltage = 3.5 V, colloidal concentration = 0.5 vol.% and withdrawal speed of electrodes = 0.04 mm/s); C) *Withdrawal speed of electrodes* at a deposition voltage of 3.5 V: —■— region 2; —□— region 3 and deposition voltage of 3.9 V: —▲— region 2; —△— region 3 (colloidal concentration = 0.5 vol.%); D) *Concentrations of colloidal particles* —■— 0.2 vol.%; —●— 0.5 vol.% (deposition voltage = 3.5 V and withdrawal speed of electrodes = 0.04 mm/s).

The surface coverage is shown for the different sample regions as defined in Figure 6.2B. The surface coverage of the whole sample increased substantially from the top to the bottom part of the sample. Already after 3 min of deposition, the number of layers at the bottom part (region 3) reached seven layers on average. From our experience, the surface coverage can be made uniform over the whole surface by increasing the withdrawal speed to above 0.08 mm/s, see Figure 7.2C. The higher the withdrawal speed, the more uniform is the surface coverage, but the longer the deposition time that is needed to increase the number of layers. Surface coverage decreased significantly with increasing withdrawal speed. Corresponding results for region 2 and region 3, shown in Figure 6.2B, are presented in Figure 7.2C. Colloids were deposited at 3.5 V and 3.9 V electrode voltages, respectively, at 1 min deposition time. The colloidal concentration in the suspension was 0.5 vol.%. At all withdrawal speeds, an increase in voltage led to an increase in the surface coverage in all regions. As it is seen in Figure 7.2C, the difference in surface coverage between region 2 and region 3 became smaller at increased withdrawal speeds. The increase in surface coverage with a decrease in withdrawal speed was attributed to the additional deposition of colloidal particles during the withdrawal of the electrodes out of the colloidal suspension.

The results of the deposition of colloidal particles at different colloidal concentrations are shown in Figure 7.2D. An applied voltage of 3.5 V and a withdrawal speed of 0.04 mm/s were used. Results are presented for region 2 (Figure 6.2B). As it was expected, the decrease in colloidal concentration led to a decrease in surface coverage. The surface coverage for a colloidal concentration of 0.2 vol.% did not even reach 1 layer after 3 min of deposition. A decrease in colloid particle concentration slows down deposition, but allows one to better control the quality of the crystals. The quality of the deposited colloidal crystals also depends on the applied voltage. The higher the voltage for the same concentration of the colloidal particles, the worse the quality of the deposited colloidal crystals, as became apparent from the SEM images in the form of polycrystalline domains with different crystal orientations with respect to the patterned substrate. At a voltage higher than 4 V, the deposited crystals were entirely disordered. Arriving in large quantities at the surface, colloidal particles did not have enough time to order according to the pattern of the electrode.

7.1.2. Colloidal crystallization on electrode surfaces with a pattern “gradient”

The influence of a pattern gradient on colloidal crystallization was investigated on a sample that was prepared in such a way that it contained three regions as it is shown in Figure 7.3A, essentially exhibiting a pattern “gradient”. Such patterning became possible by the slight shifting of the sample from the middle position of the sample holder in the LIL set-up during photoresist exposure, so that the double exposure area (region 1) also shifted from the middle to the side of the sample, revealing differently patterned areas. Colloidal particles were deposited at 3.9 V for 2 min and withdrawn from the colloidal suspension at a speed of 0.8 mm/s. Electrodes were withdrawn in the direction perpendicular to the line direction (in the same way as it is shown in Figure 7.3A). After the electrophoretic deposition of colloidal

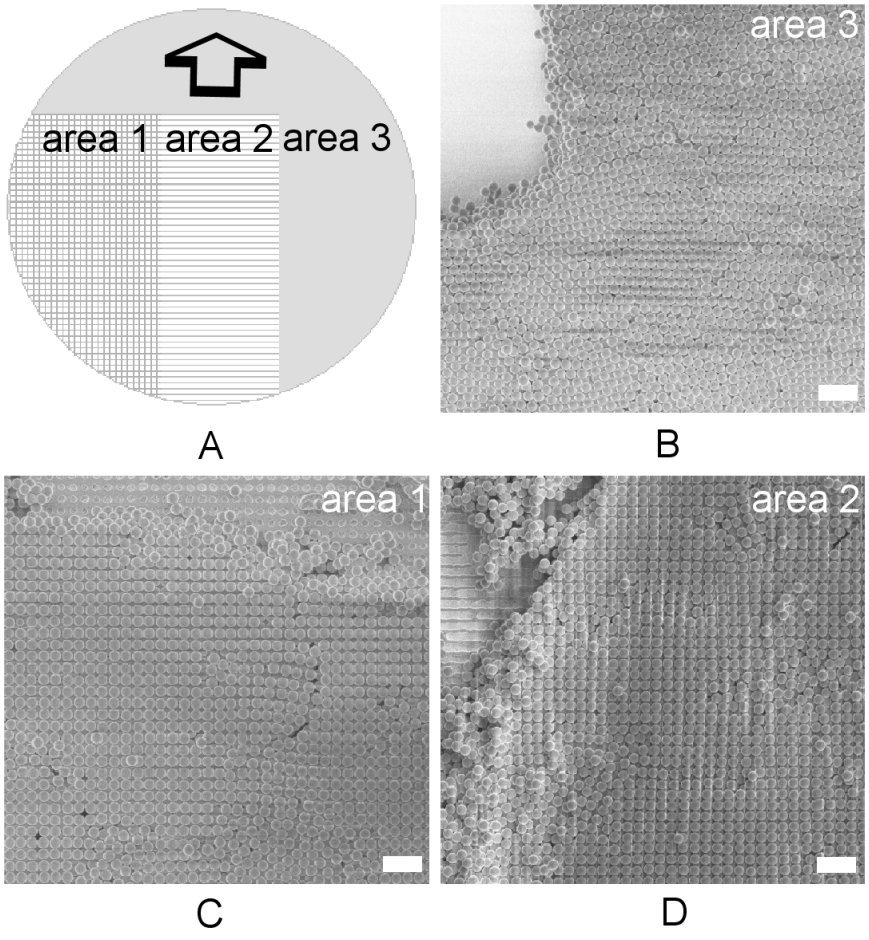

Figure 7.3 Colloidal crystallization on an electrode with different patterned areas; A) schematic representation of the patterned electrode; B) square; C) lines; and D) bare electrode regions. The scale bars represent 1 μm.

particles, the different regions of the sample were studied. Examples of the colloidal deposition are presented in Figure 7.3 B-D. The thickness of colloidal crystals in the different regions was almost the same: approximately five layers.

In the area without any pattern (area 3 in Figure 7.3, A and B), formed colloidal crystals were polycrystalline with mixed small domains of different orientations. Going across this region (from the top to the bottom of the sample), mixed domains were observed and either the (100) or the (111) plane orientation parallel to the electrode surface dominated the pattern.

For the line pattern (area 2 in Figure 7.3A) with a periodicity of 330 nm (the same as the colloidal size), the dominant plane orientation was (100), as it is shown in Figure 7.3D. Going across this region, areas with mixed domains of different crystal orientation such as (100) and (111) were observed, as well. As opposed to the flat electrode surface, all domains were significantly larger and oriented with respect to the line direction. In some locations, small domains with (110) crystal orientation were seen. The origin of the domain orientation in area 2 was difficult to establish. One of the major reasons for this variation could be the non-uniformity of the topologically patterned dielectric layer of the electrode, comprising for instance a variable width of dielectric lines, broken lines or defect areas without lines. The width of the dielectric walls was very thin (less than 100 nm) and therefore it was difficult to control their topology precisely using LIL lithographic techniques. The dominant orientation of colloidal crystal on the line pattern was the (100) plane orientation parallel to the electrode surface, thus, it is fair to say that a line pattern with a periodicity on the order of the colloidal size could be used to generate colloidal crystals with a (100) plane orientation parallel to the electrode surface.

In area 1 (Figure 7.3A) of the electrode, featuring a square pattern and a periodicity of 330 nm (the same as the colloidal size), colloidal crystals with a (100) orientation grew parallel to the electrode pattern. An example of such a crystal structure is presented in Figure 7.3C. Across the patterned area 1, the (100) orientation of the colloidal crystal domains that follows the surface pattern was dominant, and only occasional deviations can be seen. This variation in crystal orientation could be induced by structural non-uniformities of the depressions (holes) in the dielectric layer, the existence of different structural defects such as missing holes or rather big defect areas produced during substrate preparation, see Figure 6.8. From the experimental results, it can be foreseen that the domain size of colloidal crystals grown on the electrode with a square pattern could be increased substantially if the electrode topology could be controlled more precisely.

7.1.3. Thickness and orientation control of FCC colloidal crystals

The orientation of FCC colloidal crystals was induced by the patterning of the electrode surface in relation to the different planes of the FCC crystal. In Figure 7.4, three different patterns are presented: a *hexagonal* pattern (Figure 7.4, A1-A3) that corresponds to the FCC (111) plane (the most close-packed plane of the FCC structure); a *square* pattern (Figure 7.4, B1-B3) that corresponds to the FCC (100) plane (a less close-packed plane than (111)); and a *rectangular* pattern (Figure 7.4, C1-C3) that corresponds to the FCC (110) plane (a non-close-packed plane, for comparison see Figure 7.1). The easiest direction for the colloidal crystals to grow is the direction of the most close-packed plane, the (111). Therefore,

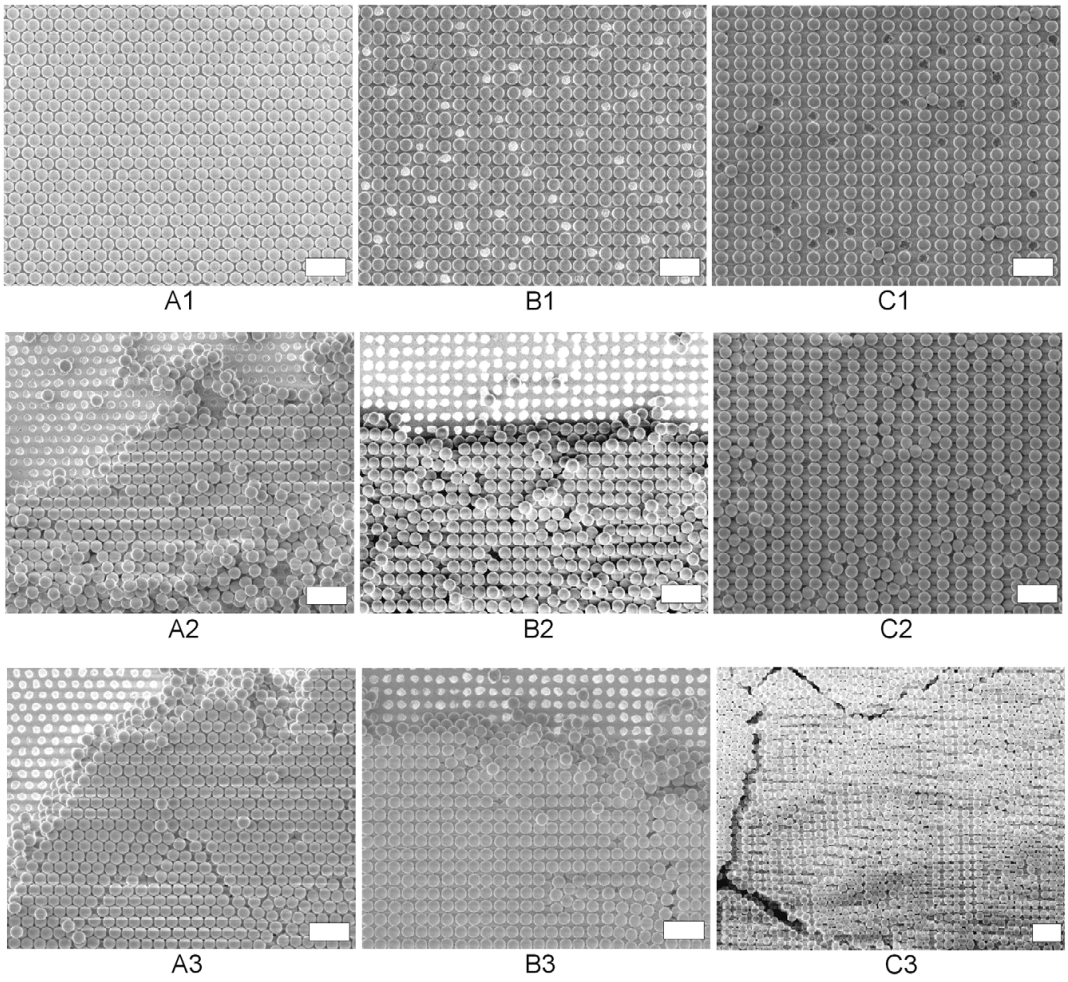

Figure 7.4. FCC crystals grown on different crystal facets: A1) – A3) one, two and five layers of FCC (111); B1) – B2) one, two and four layers of FCC (100); C1) – C2) one, two and seven layers of FCC (110). The scale bars represent 1 μm.

colloidal crystals that are naturally formed onto flat, unpatterned substrates tend to self-assemble into the FCC structure with the (111) plane parallel to the substrate. An FCC (100) crystal could not be formed by self-assembly on flat substrates in a controlled way; therefore, its crystal growth had to be induced by surface structuring. In addition to the electrophoretic deposition method that we present in this chapter, some other methods that induce FCC (100) growth were discussed in the introduction. Growth of an FCC crystal from the non-close-packed plane (110) was rather difficult. We found that one or two layers of FCC (110) structure could be easily formed over large patterned areas at low deposition voltages (3 V or 3.5 V), long deposition times (over 3 min) and high withdrawal speeds (0.1 mm/s), Figure 7.4, C1-C2. Fabrication of thick, homogeneous in thickness FCC (110) crystals was almost impossible. With an increasing number of colloidal layers and due to the tendency of colloidal particles to pack densely, colloidal crystallization on non-close-packed (110) patterns led to the formation of domains with a different orientation (Figure 7.4, C3), but in most of the areas, the formation of colloidal crystals with either the (111) or the (100) crystal orientation was observed.

The thickness of colloidal crystals could be controlled in two ways. Firstly, a thickness gradient could be maintained across the sample at low withdrawal speeds (e.g. 0.04 mm/s) of the electrodes and at applied voltages (3.5 V and 3.9 V) and deposition times tuned to the desired thickness gradient, Figure 7.2B. Secondly, a uniform thickness over the whole sample was achieved by applying a high withdrawal speed (0.08 mm/s or even 0.1 mm/s) by varying the applied voltage (3.5 V or 3.9 V) and by tuning the deposition time, Figure 7.2C. In the last case, the crystal thickness could be increased by increasing the deposition time. Examples of the thickness control of colloidal crystals with different crystal orientations are presented in Figure 7.4, A-B.

A high quality FCC colloidal crystal with a very low defect concentration could be grown if the periodicity of the patterned electrode was precisely controlled in relation to the dimensions of the FCC colloidal crystal. If there is a small mismatch between the substrate periodicity and colloidal size, line defects would grow through the colloidal crystal as it is shown in Figure 7.4, A3 for a hexagonal pattern. Defect structures formed in colloidal crystals resemble those formed during the deposition of inorganic materials.[23] In general, defects in colloidal crystals are formed due to the drying process following colloidal deposition when colloids, while trying to pack densely, destroy the hexagonal packing in some parts of the sample, forming line defects. The monodispersity of colloidal particles plays an important role in determining the quality of formed colloidal crystals.

7.1.4. Conclusions

The influence of the combination of electrophoresis of charged colloids, topologically patterned electrodes and controlled solvent evaporation on the growth of FCC colloidal crystals was discussed. We showed, that the deposition of charged colloids by electrophoresis is very fast and, therefore, in a few minutes thick colloidal crystals can be grown. The effective number of grown layers can be controlled by the adjustment of different process parameters such as deposition voltage and time, colloidal concentration, and withdrawal speed of the electrodes. The surface coverage was found to increase with an increase in the applied voltage. A threshold voltage of 3.4 V was determined for the processing parameter set used, after which a significant increase in the number of colloidal layers was observed. An increase in the colloidal concentration resulted in a decrease in the number of layers, but improved the quality of the crystals. We demonstrated thickness control for colloidal crystals either by forming of a thickness gradient over the sample at low withdrawal speeds or by fabricating a homogeneous film over the whole sample at higher withdrawal speeds. We also showed that electrode surface patterning predetermines the orientation of the crystal growth. First, the growth on patterned and unpatterned electrodes was compared, demonstrating a profound effect of patterned substrates on colloidal crystal growth. Then, growth of FCC crystals with different orientations parallel to the electrode surface such as (111), (100) and (110) was successfully demonstrated on patterned electrode surfaces. The mismatch between pattern periodicity and colloid diameter that determines the colloid crystal lattice constant, plays an important role in defect structure formation in the colloidal crystals grown. The method of electrophoretic deposition of colloidal particles on patterned electrode surfaces provides new opportunities for the control of the orientation and thickness of colloidal crystals on solid substrates.

7.2 Colloidal crystals with BCC crystal structure

Colloidal deposition was performed on a patterned electrode surface with a square type of structure, Figure 7.5 in order to grow corresponding BCC (100) crystal planes. The pattern periodicity was chosen equal to the distance between neighbouring colloids in the (100) plane. Negatively charged polystyrene colloidal particles with a diameter of 330 nm, polydispersity index of 1.03 and surface charge densities of 16.2 μC/cm^2 and 26.5 μC/cm^2 were used. In the colloidal suspension, polymer colloidal particles with volume fractions of 0.2 vol.% or 0.5 vol.% were redistributed in a mixture of ethanol and water (80:20 vol/vol). Applied voltages were varied between 2.5, 3.0, 3.5 and 3.9 V. Withdrawal speeds of the electrodes from the colloidal suspension were 0.04, 0.08 and 0.1 mm/s.

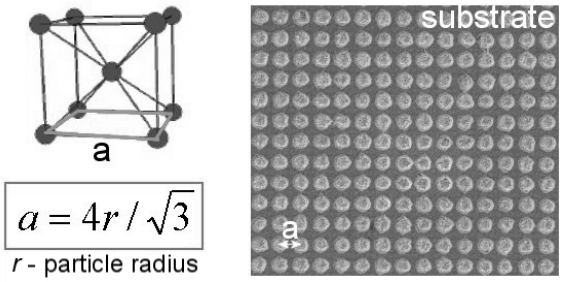

Figure 7.5. Schematic illustration of the BCC structure (left); SEM image of the patterned electrode surface with a periodicity (*a*) equal to the distance between colloids in the (100) plane (right).

7.2.1. Thickness and structure control of BCC colloidal crystals

Deposition results at different applied voltages are presented in Figure 7.6. Colloidal particles with a surface charge density of 16.2 μC/cm^2 were deposited on a patterned electrode surface for 1 min and subsequently withdrawn from the colloidal suspension (colloid concentration = 0.5 vol.%) with a speed of 0.04 mm/s. Surface coverage was calculated for region 2 (Figure 6.2B). An increase in the applied voltage led to an increase in the surface coverage. A significant growth of colloidal crystals was detected above the threshold voltage as described earlier. The value of the threshold voltage for this system was 3.0 V. Therefore, for subsequent colloidal crystal growth, values of applied voltages above the threshold voltage were used. SEM images of colloidal crystals (top view) corresponding to the different values of applied voltage are shown in Figure 7.6.

As it is clearly seen in the SEM images, thick colloidal crystals with polycrystalline domains were obtained, without any visible relationship of their orientation with respect to the electrode pattern. The polycrystalline structure of the colloidal crystals can be a result of high concentration, or be due to a relatively low withdrawal speed, both allowing colloidal particles to rearrange and form close-packed structures rather than follow the electrode pattern. Thus we anticipate that by adjusting colloidal concentration and withdrawal speed of the electrodes, ordering of colloidal particles into a BCC structure may be achieved.

The results of the deposition of colloidal particles at different concentrations such as 0.175, 0.2 and 0.5 vol.% are presented in Figure 7.7. Colloidal particles with a surface charge density of 16.2 μC/cm^2 were deposited for 9 min at 3.5 V and then the electrode was withdrawn from the colloidal suspension with a speed of 0.08 mm/s. Surface coverage was calculated for region 2, Figure 6.2B. SEM images correspond to the values of the colloidal concentrations given in the graph. For the colloidal suspension with a concentration of 0.5

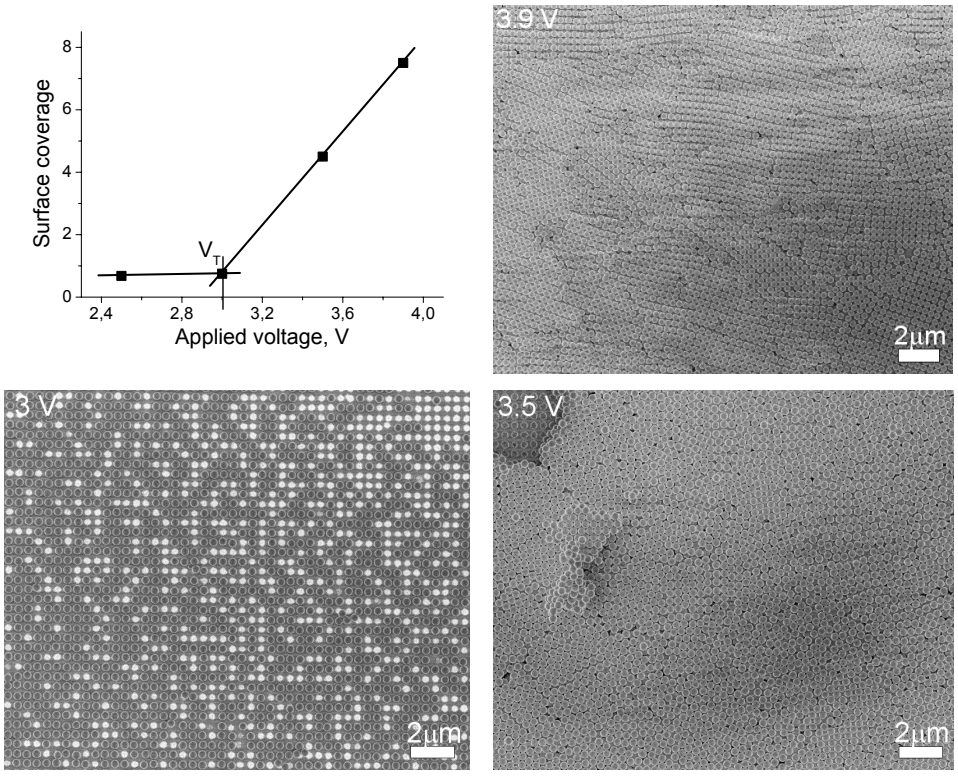

Figure 7.6. Surface coverage of colloidal particles versus deposition voltage: deposited time = 1 min, colloidal concentration = 0.5 vol.%, colloidal surface charge density = 16.2 μC/cm^2, electrode withdrawal speed = 0.04 mm/s. Surface coverage was calculated over region 2, Figure 6.2D. The threshold voltage was 3.0 V. SEM images show a top view of colloidal crystals grown at different applied voltages.

vol.%, an increase in withdrawal speed from 0.04 mm/s (Figure 7.6) to 0.08 mm/s (Figure 7.7) led to a decrease in the number of deposited colloidal layers. In addition, an increase in withdrawal speed led to an improvement in the colloidal particle ordering. Relatively large BCC colloidal crystal domains with a (100) crystal plane parallel to the electrode surface can be easily recognized among hexagonally close packed domains. A decrease in colloidal concentration from 0.5 vol.% to 0.2 vol.% and 0.175 vol.% significantly improved the ordering of colloidal particles, as the top layer of colloidal crystals in SEM images (Figure 7.7) completely replicated the electrode pattern over the full electrode surface area of several millimetres square. The difference in the quality of colloidal layers grown from colloidal suspensions with 0.2 vol.% and 0.175 vol.% was very small, but the difference in the number of deposited colloidal layers was significant. Therefore, colloidal depositions in a colloidal suspension of 0.2 vol.% were preferred.

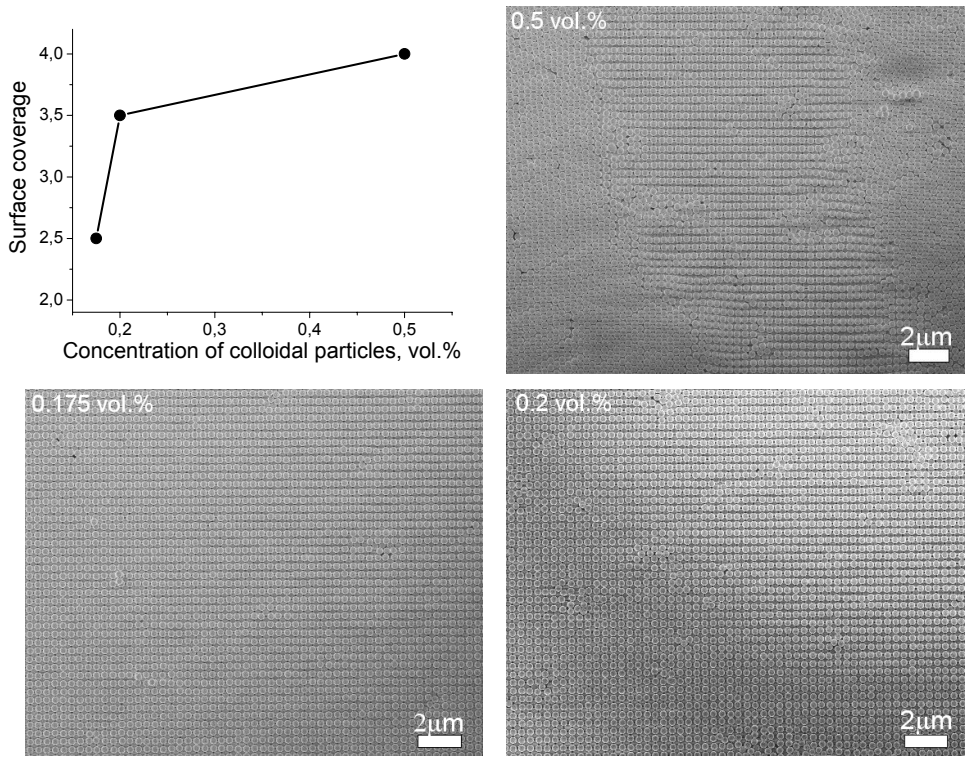

Figure 7.7. Surface coverage versus colloidal particle concentration: deposition voltage = 3.5 V, deposition time = 9 min, colloidal surface charge density = 16.2 μC/cm^2 and withdrawal speed = 0.08 mm/s. Surface coverage was calculated over region 2. SEM images show a top view of colloidal crystals grown at different colloidal concentrations.

The influence of electrode withdrawal speed out of the colloidal suspension on the colloidal crystal ordering is presented in Figure 7.8. Colloidal particles with a surface charge density of 16.2 μC/cm^2 were deposited onto a patterned electrode within 9 min at 3.5 V and withdrawn out of the colloidal suspension with a concentration of 0.2 vol.%. Surface coverage was calculated over region 2, Figure 6.2B. SEM images corresponding to different withdrawal speeds are shown in Figure 7.8.

The influence of withdrawal speed on colloidal ordering was already mentioned when colloidal depositions in colloidal suspension of 0.5 vol.% were discussed. The same effect was observed for a colloidal concentration of 0.2 vol.%. Increase in withdrawal speed decreased the number of deposited colloidal layers. At the same time, the quality of colloidal crystals increased when the withdrawal speed increased from 0.05 mm/s to 0.08 mm/s and 0.1 mm/s. At 0.05 mm/s, relatively large colloidal crystal domains with a BCC crystal structure among hexagonally close-packed domains were observed. The difference in quality of

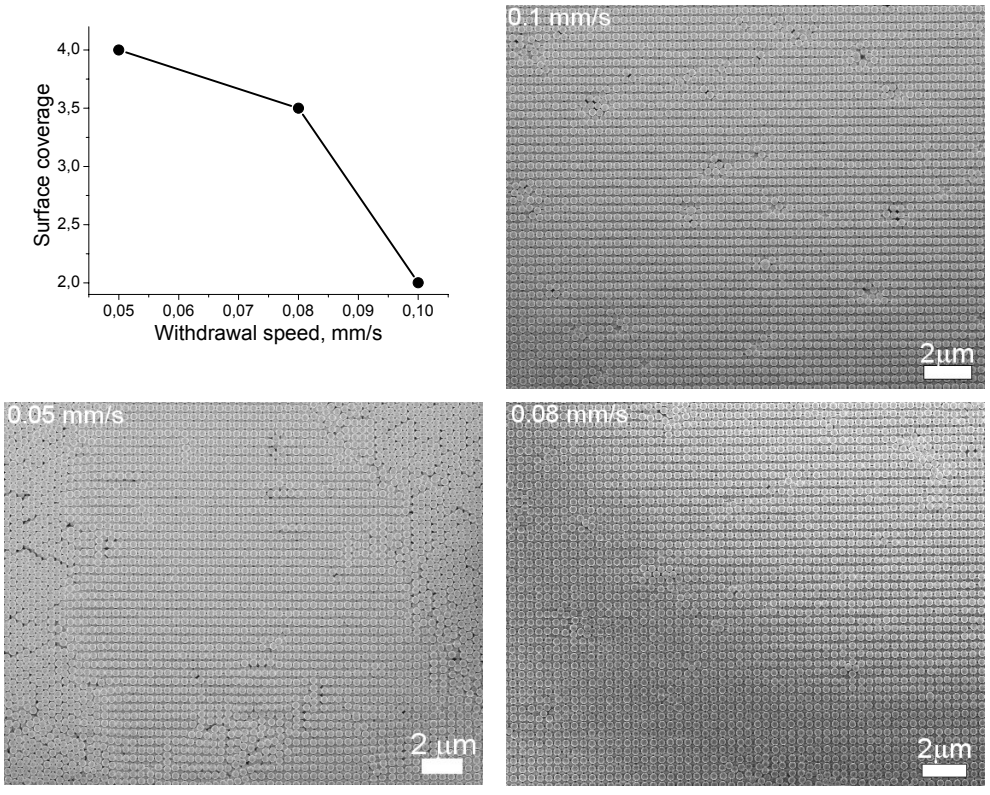

Figure 7.8. Surface coverage versus withdrawal speed of the electrodes from the colloidal suspension: deposition voltage = 3.5 V, deposition time = 9 min, colloidal concentration = 0.2 vol.% and colloidal surface charge density = 16.2 μC/cm^2. Surface coverage was calculated over region 2 (Figure 6.2B). SEM images show top views of colloidal crystals grown at different withdrawal speeds.

colloidal crystals grown, when withdrawal speeds of 0.08 mm/s and 0.1 mm/s were maintained, was very small. On the contrary, the thickness of colloidal crystals differed remarkably (Figure 7.8), therefore, a withdrawal speed of 0.08 mm/s was found to be optimal for BCC colloidal crystal growth with the (100) plane parallel to the electrode surface for the studied system. Homogeneous surface coverage of BCC colloidal crystals was observed on the electrode surface area over several millimetres square.

The surface charge density of colloidal particles influences the colloidal ordering on patterned surfaces. Colloidal particles possessing surface charge densities of 16.2 $\mu C/cm^2$ and 26.5 $\mu C/cm^2$ were deposited for 9 min in a colloidal suspension with a colloid concentration of 0.2 vol.% on a patterned electrode. A deposition voltage of 3.5 V and withdrawal speed of 0.08 mm/s were applied. Increase in surface charge density led to an increase in the number of deposited colloidal layers. As a result, polycrystalline close-packed colloidal crystals with various orientations in plane were obtained that did not correspond to the electrode pattern, Figure 7.9B. On the contrary, for low charge densities of 16.2 $\mu C/cm^2$, significantly lower numbers of colloidal layers were obtained, but colloidal crystal structures grown corresponded very well to the electrode pattern and covered electrode areas over several millimeters square, Figure 7.9A. From our experience, at short deposition times (several minutes), highly charged colloids with a surface charge density of 26.5 $\mu C/cm^2$ could also be arranged according to the electrode surface pattern, forming colloidal crystals possessing a BCC structure with a thickness of several colloidal layers grown over large surface areas. Nevertheless, control over the colloidal deposition was easier when colloidal particles with a

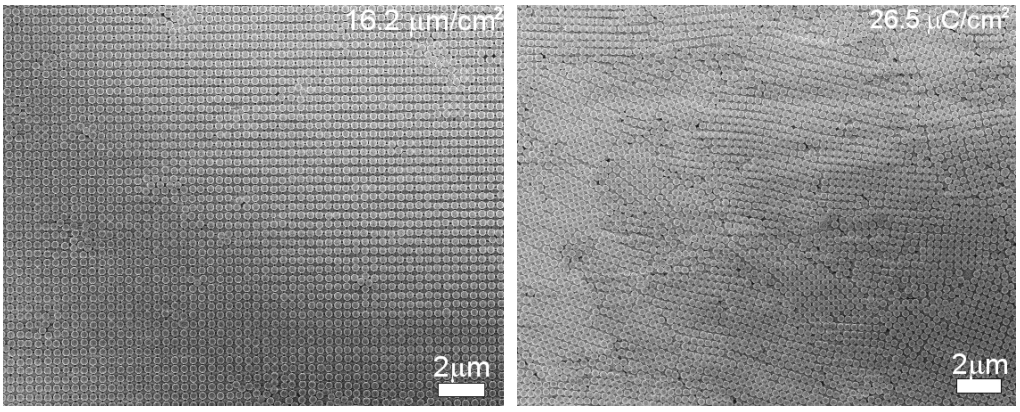

A B

Figure 7.9. SEM images (top view) of colloidal crystals grown from colloidal particles with different surface charge densities A) 16.2 $\mu C/cm^2$ (surface coverage is 3.5 colloidal layers) and B) 26.5 $\mu C/cm^2$ (surface coverage is more than 6 colloidal layers): deposition voltage = 3.5 V, deposition time = 9 min, colloidal concentration = 0.2 vol.% and withdrawal speed = 0.08 mm/s.

low surface charge density were used. Therefore, colloidal particles with a surface charge density of 16.2 μC/cm^2 were preferred for colloidal deposition.

Finally, the growth of colloidal crystals as a function of deposition time was followed, applying the deposition parameters mentioned above. Colloidal particles with a surface charge density of 16.2 μC/cm^2 were deposited at different deposition times in the colloidal suspension with a concentration of 0.2 vol.% at 3.5 V and a withdrawal speed of 0.08 mm/s. An increase in the deposition time resulted in a linear increase in colloidal surface coverage, Figure 7.10. Examples of colloidal crystals with different thicknesses are presented in the

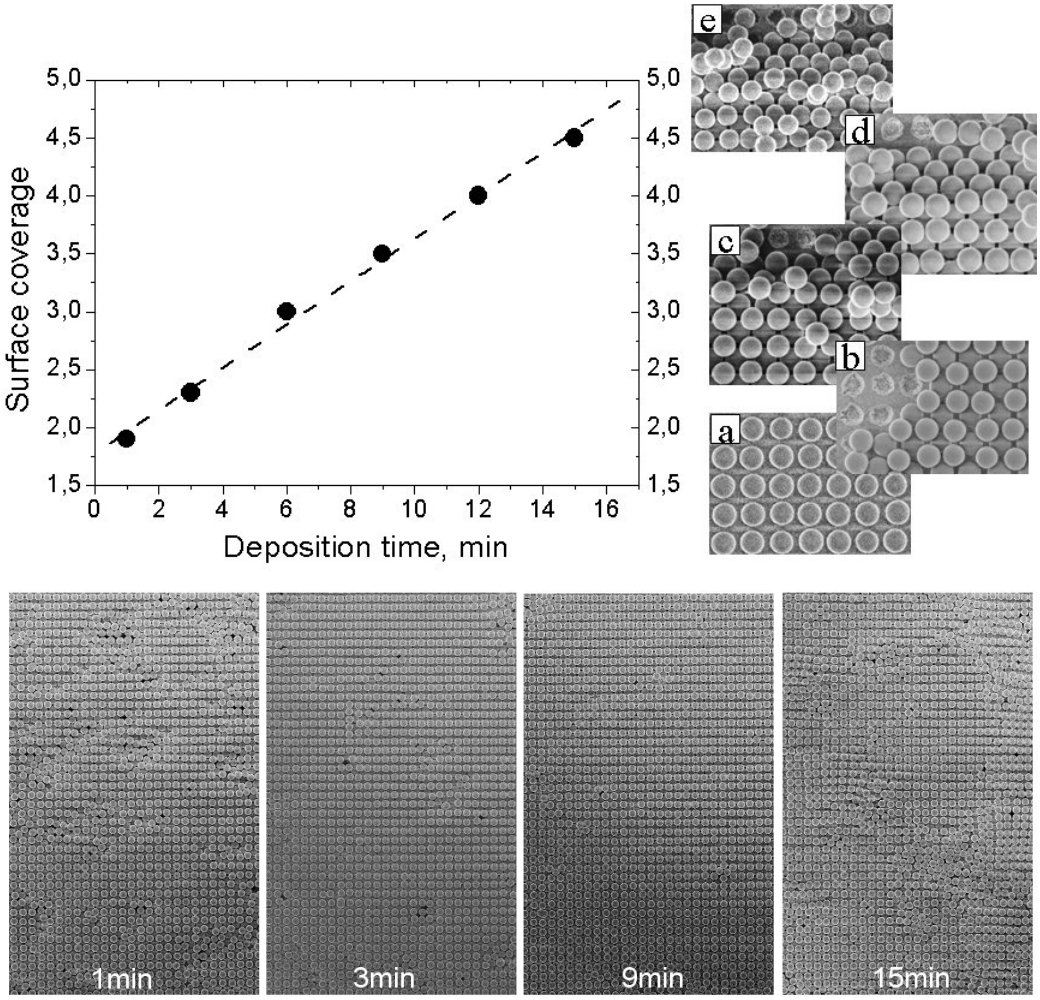

Figure 7.10 Surface coverage versus deposition time calculated over the region 2 (y = 1.78 + 0.19x), (top left corner): deposition voltage = 3.5 V, withdrawal speed = 0.08 mm/s, colloidal concentration = 0.2 vol.% and colloidal surface charge density = 16.2 μC/cm^2; SEM images of crystals with various thicknesses (top right corner): a) 1 layer, b) 2 layers, c) 3 layers, d) 4 layers and e) 5 layers. SEM images at the bottom represent top views of colloidal crystals grown at different deposition times.

SEM images, Figure 7.10a-e. Such colloidal crystals covered large electrode areas of several millimeters square. The thickness of the colloidal crystals could be accurately controlled at fixed deposition parameters and was reproducible. Top layers of colloidal crystals, whose values of surface coverage are presented in the graph, are shown in the SEM images placed at the bottom of Figure 7.10. Large, almost defect free colloidal crystals were grown up to a deposition time of 15 min. At a deposition time of approximately 15 min, crystal defects became significant which eventually destroyed the colloidal crystal homogeneity. Upon increasing the deposition time further to 20 min, polycrystalline close-packed domains and no BCC colloidal crystal domains were observed. Therefore, using this method, colloidal crystals possessing a BCC crystal structure oriented in the direction of the (100) plane could be grown with a thickness of up to five colloidal layers.

In order to increase the number of layers of colloidal crystals further, we varied the meniscus shape of the colloidal suspension between the electrodes, Figure 7.11A. The meniscus can be increased by several methods: 1) by changing the tilt angle of the electrodes with respect to the colloidal suspension by a few degrees or 2) obstacles for the colloidal suspension of different thickness can be introduced. We tried both methods and we obtained the same results. The disadvantage of the second method is that not the whole electrode surface takes part in the colloidal deposition and thickness control of colloidal crystal growth must be realized by the precise level of immersion of electrodes in the colloidal suspension. The first method is much more practical, as only a tilt angle must be fixed during the colloidal

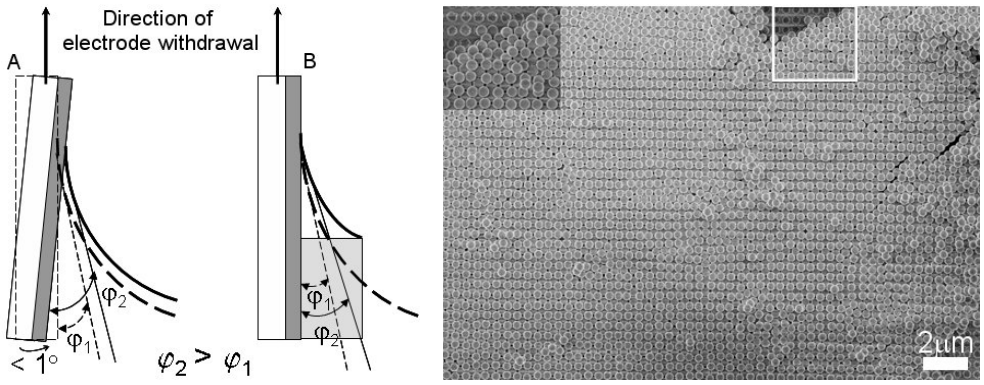

A B

Figure 7.11 A) Two types of meniscus modification: A) by tilting the sample in relation to the colloidal suspension or B) by introducing obstacles of certain thickness. B) SEM image of colloidal crystals with a thickness of six layers grown by electrode tilt shown in Fig. 7.11A. Deposition voltage = 3.5 $V_{,}$ deposition time = 15 min, colloidal concentration = 0.175 vol.%, colloidal surface charge density = 16.2 μC/cm^2 and withdrawal speed = 0.08 mm/s.

deposition. As a result, by changing the tilt angle by approximately 1º, colloidal crystals possessing a BCC crystal structure and a thickness of up to seven colloidal layers were obtained. Colloidal crystals with a BCC crystal structure and with a thickness of six colloidal layers are presented in Figure 7.11B.

7.2.1. Conclusions

The fabrication of colloidal crystals possessing the BCC crystal structure is discussed. BCC colloidal crystals with a thickness of up to seven colloidal layers were grown in the direction of the (100) crystal plane. Defect free colloidal crystals with a homogeneous surface coverage were obtained over a surface area of several square millimeters. This was achieved by electrophoretic deposition of charged polymer colloidal particles on patterned surfaces. A square type of electrode pattern was used corresponding to the (100) plane of a BCC crystal structure. Quality and thickness of grown colloidal crystals were controlled by a set of deposition parameters such as deposition voltage, deposition time, and concentration of colloidal particles in the colloidal suspension, colloid surface charge density and withdrawal speed of electrodes out of the suspension. A threshold voltage of 3.0 V was determined, beyond which a significant crystal growth was observed. Optimal deposition parameters were found such as an applied voltage of 3.5 V, colloidal volume fraction of 0.2 vol.%, colloid surface charge density of 16.2 $\mu C/cm^2$ and a withdrawal speed of 0.08 mm/s for the system studied.

References

[1] J. D. Joannopoulos, R. D. Meade, J. N. Winn, *Photonic Crystals, Molding the Flow of Light*, Princeton University Press, Princeton, NJ, **1996**.
[2] K. M. Ho, C. T. Chan, C. M. Soukoulis, *Phys. Rev. Lett.* **1990**, *65*, 3152.
[3] A. S. Dimitrov, K. Nagayama, *Langmuir* **1996**, *12*, 1303.
[4] P. Jiang, J. F. Bertone, K. S. Hwang, V. L. Colvin, *Chem. Mater.* **1999**, *11*, 2132.
[5] A. Moroz, C. Sommers, *J. Phys. Cond. Matter* **1999**, *11*, 997.
[6] A. Blanco, E. Chomski, S. Grabtchak, M. Ibisate, S. John, S. W. Leonard, C. Lopez, F. Meseguer, H. Miguez, J. P. Mondia, G. A. Ozin, O. Toader, H. M. van Driel, *Nature* **2000**, *405*, 437.
[7] Y. A. Vlasov, X.-Z. Bo, J. C. Sturm, D. J. Norris, *Nature* **2001**, *414*, 289.
[8] A. van Blaaderen, R. Ruel, P. Wiltzius, *Nature* **1997**, *385*, 321.
[9] Y. Yin, Y. Xia, *Adv. Mater.* **2002**, *14*, 605.
[10] S. M. Yang, G. A. Ozin, *Chem. Commun.* **2000**, 2507.
[11] S. H. Park, D. Qin, Y. Xia, *Adv. Mater.* **1998**, *10*, 1028.
[12] J. P. Hoogenboom, C. Retif, E. de Bres, M. van de Boer, A. K. van Langen-Suurling, J. Romijn, A. van Blaaderen, *Nano Lett.* **2004**, *4*, 205.
[13] D.-K. Yi, E.-M. Seo, D.-Y. Kim, *Appl. Phys. Lett.* **2002**, *80*, 225.
[14] G. A. Ozin, S. M. Yang, *Adv. Funct. Mater.* **2001**, *11*, 95.
[15] S. M. Yang, H. Miguez, G. A. Ozin, *Adv. Funct. Mater.* **2002**, *12*, 425.
[16] J. Zhang, A. Alsayed, K. H. Lin, S. Sanyal, F. Zhang, W.-J. Pao, V. S. K. Balagurusamy, P. A. Heiney, A. G. Yodh, *Appl. Phys. Lett.* **2002**, *81*, 3176.
[17] Y. Yin, Z.-Y. Li, Y. Xia, *Langmuir* **2003**, *19*, 622.
[18] S. H. Im, M. H. Kim, O. O. Park, *Chem. Mater.* **2003**, *15*, 1797.
[19] R. Mayoral, J. Requena, J. S. Moya, C. Lopez, A. Cintas, H. Miguez, F. Meseguer, L. Vazquez, M. Holgado, A. Blanco, *Adv. Mater.* **1997**, *9*, 257.
[20] H. Miguez, F. Meseguer, C. Lopez, A. Mifsud, J. S. Moya, L. Vazquez, *Langmuir* **1997**, *13*, 6009.
[21] M. Holgado, F. Garcia-Santamaria, A. Blanco, M. Ibisate, A. Cintas, H. Miguiz, C. J. Serna, C. Molpeceres, J. Requena, A. Mifsud, F. Meseguer, C. Lopez, *Langmuir* **1999**, *15*, 4701.
[22] A. Yethiraj, A. van Blaaderen, *Nature* **2003**, *421*, 513.
[23] See for example: L. B. Freund, S. Suresh, *Thin Film Materials: Stress, Defect Formation and Surface Evolution*, Cambridge University Press, Cambridge, **2004**.

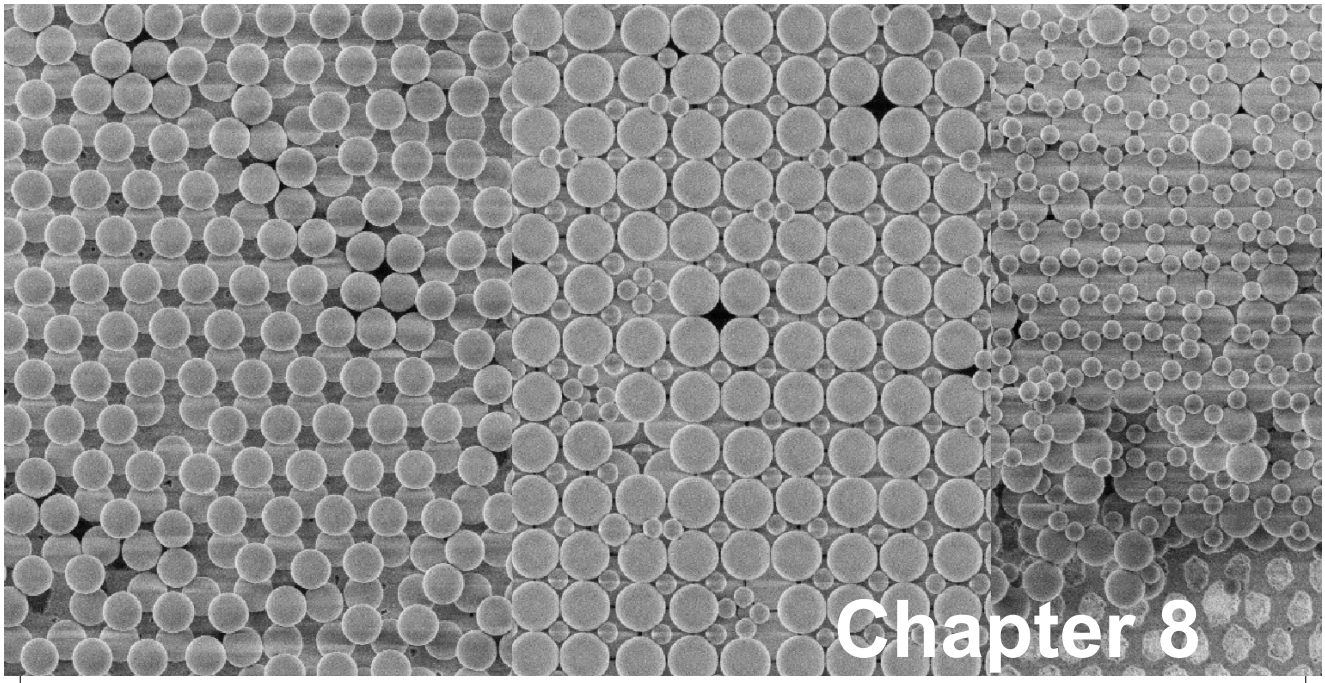

Chapter 8

Layer-by-Layer Colloidal Crystal Growth

Layer-by-layer deposition of colloidal particles on patterned electrode surfaces under an applied electric field is discussed. Colloidal crystals with a low packing density, grown on hexagonally patterned electrode substrates are presented. A nucleation mechanism of colloidal layer formation determined the grain size of colloidal crystals. Alternating deposition of large and small colloidal particles with radii ratios of 0.41 and 0.49 on patterned surfaces with hexagonal and square types of pattern led to the formation of 2D and 3D colloidal crystals with stoichiometries LS, LS_2 and LS_3. Growth of binary colloidal crystals with the same and oppositely charged colloidal particles is presented. Planar defects in form of colloidal monolayers composed of colloidal particles of smaller sizes were easily introduced into colloidal crystals using the layer-by-layer deposition technique.

Introduction

Photonic crystals with a diamond structure possess a photonic band gap in the first Brillouin zone.[1] The diamond structure has a low packing density of 0.34. This structure is difficult to realize by self-assembly of colloidal particles on flat substrates as this leads to formation of close-packed structures. In order to fabricate colloidal crystals with a diamond structure, one can think of mimicking the packing of ionic crystal lattices by scaling up the ions with the corresponding ionic radii and charges to colloidal dimensions. For example, the zinc blende type packing has the structure of the diamond lattice but consists of ions of different sizes and charge signs.

The crystallization of a mixture of large (L) and small (S) colloidal particles can result in 2D and 3D binary colloidal crystals. Binary colloidal crystals with stoichiometries of LS_2 (atomic analog - AlB_2) and LS_{13} (atomic analog – $NaZn_{13}$, UBe_{13}, etc.) have first been discovered in Brazilian opals.[2] Theoretically and experimentally these structures have been intensively studied in hard-sphere colloidal suspensions.[3,4,5,6,7,8,9] Recently, it was demonstrated by means of confocal microscopy, that colloidal particles of different sizes and opposite charges can yield a variety of colloidal structures, such as LS (atomic analog - NaCl and NiAs), LS_2, LS_6, and CsCl ($R_S/R_L \approx 1$).[10] The formation of binary colloidal crystals from nanoparticles of metals, semiconductors and metal oxides has recently received tremendous interest, as well.[11,12,13,14] Structures of binary colloidal crystals are determined by the radii ratios of colloidal particles R_S/R_L, the total packing fraction $\phi = \phi_L + \phi_S$ and the relative numbers of small and large colloidal particles n_S/n_L.[7,8,9] Theoretically, it was calculated that binary colloidal crystals can be obtained for R_S/R_L between 0.15 and 0.5. Below 0.15 the small colloids could freely flow, while above 0.5 (smaller than 0.58) the small colloids would no longer fit inside colloidal crystals formed from large particles.[8,15] In the binary suspensions, the entropic depletion effect induced by the existence of the small spheres forces large spheres

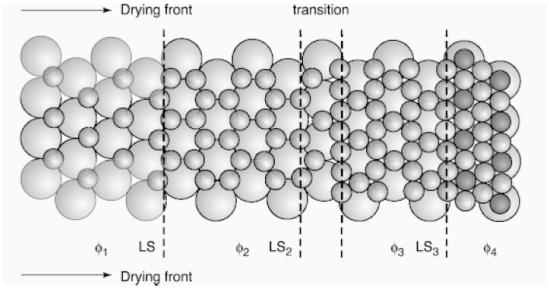

Figure 8.1. Schematic representation of the structure of small colloidal particles "nested" onto a hexagonal layer of large colloidal particles $R_S/R_L = 0.5$ as a function of volume fraction ϕ.[17]

to closely pack into an ordered structure, and then small colloids are spontaneously trapped within voids in the ordered assembly of large colloids.[4,5] Formation of large binary colloidal crystals with large R_S/R_L ratios was recently demonstrated utilizing accelerated solvent evaporation.[16] A combination of "colloidal epitaxy" and controlled drying in a layer-by-layer deposition of colloidal particles with $R_S/R_L = 0.5$ allows one to fabricate 2D colloidal crystals with stoichiometries LS, LS_2 and LS_3, Figure 8.1.[17] The self-assembly of small colloidal particles between hexagonally packed larger colloids is the result of the interplay of the geometrical packing arrangement, minimization of the surface tension of the drying liquid film and capillary forces induced at the curved meniscus. In addition to the controlled drying method, LS_2 and LS_3 colloidal crystals were also formed by a stepwise spin-coating method.[18] A disadvantage of layer-by-layer growth of binary colloidal crystals on flat surfaces is the limited possibility for variation of colloidal crystal structures. The utilization of patterned surfaces for the guided deposition of large colloidal particles will lead to the formation of various structures of such particles and, therefore, allow the formation of more complex binary colloidal crystal structures. Moreover, when such binary colloidal crystals consist of colloidal particles of different nature such as polymers and inorganic material, then a selective removal of one type of colloidal particles can lead to the formation of colloidal crystals of the remaining colloidal particles possessing low crystal symmetry.[19,20] In addition to binary colloidal crystals, layer-by-layer deposition of colloidal particles possessing the same charge sign on patterned surfaces with periodicities larger than the colloidal size could open possibilities to directly grow colloidal crystals with low packing densities. Layer-by-layer deposition of colloidal particles also allows one to introduce planar defects in the form of colloidal layers of different particle size into colloidal crystals.

In this chapter, we present a layer-by-layer electrophoretic method to deposit colloidal particles onto patterned electrodes. Electrophoretic deposition allows one to guide colloidal particles onto patterned electrode surfaces, to control the thickness of deposited colloidal layers by variation of deposition parameters and also to accelerate the colloidal crystal growth (taking only several minutes instead of several days or a month[7,8] as in case of controlled solvent evaporation experiments or crystallization in solution, respectively). Deposition parameters used in this study were based on those discussed in Chapter 6. The formation of binary colloidal crystals with the same and oppositely charged colloidal particles is presented. The influence of the electrode pattern on colloidal crystal structure is discussed. In addition, the formation of planar defects in the form of a colloidal layer of particles with different (smaller) sizes is shown.

8.1. Non-close-packed colloidal crystals

Growth of colloidal crystals on patterned surfaces with pattern periodicities larger than the colloid diameter (Figure 8.2A) or with a pattern with two different periodicities (e.g. the rectangular pattern, Chapter 7.1) (Figure 8.2B) is rather difficult. Colloidal particles tend to pack into close-packed polycrystalline structures of different orientation that do not correspond to the surface pattern. In order to improve colloidal crystallization on such types of patterns, layer-by-layer deposition of colloidal particles was performed. After each colloidal layer deposition, the sample was dried in order to adhere the colloidal particles permanently to their deposition site. Deposition parameters for monolayer formation were defined using data presented in Chapter 6. Negatively charged colloidal particles with a diameter of 545 nm were deposited onto a hexagonally patterned electrode surface (colloid diameter (D) to pattern periodicity (Λ) ratio $D/\Lambda = 0.75$) at an applied voltage of 3.5 V during 90 sec. Electrodes were withdrawn from the colloidal suspension with a colloid volume fraction of 0.2 vol.% with a speed of 0.1 mm/s. After colloidal deposition, electrodes were left to dry for several minutes under the applied voltage. Under these conditions, the first deposited colloidal layer covered an electrode surface over several millimetres, see Figure 8.3A. The first colloidal layer already shows some disorder caused either by defects in the substrate pattern or by a local increase in colloid concentration. Then three more layers were deposited using the same deposition parameters, Figure 8.3 B, C and D.

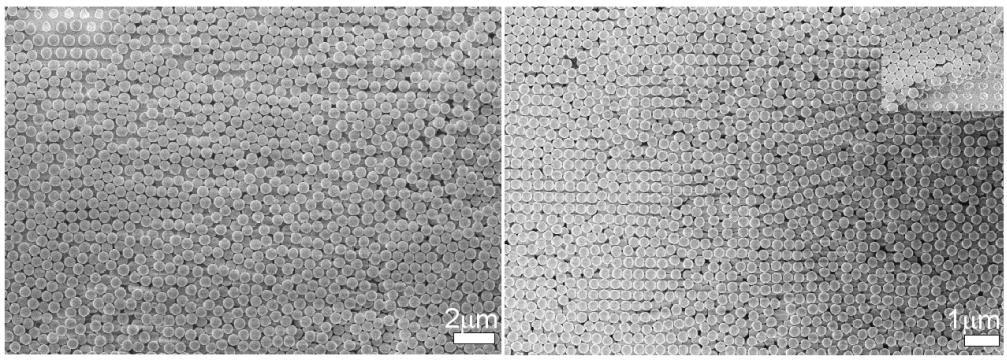

Figure 8.2. Colloidal particles deposited on A) a *hexagonally patterned surface* with a ratio of colloidal diameter to surface periodicity of 0.75 (negatively charged colloidal particles of the diameter 545 nm and surface charge density of 25.3 μC/cm^2, redistributed in ethanol/water (80:20 vol/vol) mixture (colloidal volume fraction of 0.2 vol.%) were deposited for 3 min at an applied voltage of 3.5 V, withdrawal speed = 0.08 mm/s); B) a *rectangular patterned electrode* surface with a pattern periodicity of 330 nm by 450 nm in perpendicular directions (negatively charged colloidal particles with a diameter of 330 nm and a surface charge density of 16.2 μC/cm^2, redistributed in ethanol/water (80:20 vol/vol) mixture (colloidal volume fraction of 0.5 vol.%) were deposited for 2 min at an applied voltage of 3.5 V, withdrawal speed = 0.08 mm/s).

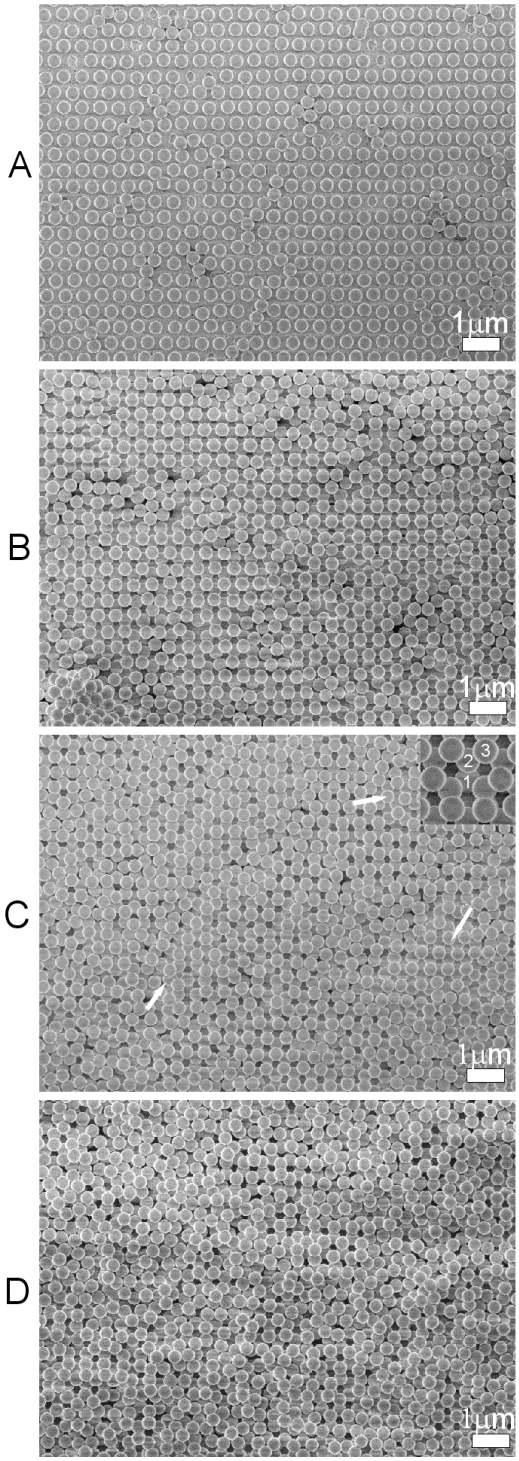

Figure 8.3. Colloidal multilayers grown on hexagonally patterned substrates (colloid diameter was 545 nm and pattern periodicity was 722 nm): A) one layer; B) two, C) three and D) four layers. Arrows indicate areas with A-B-A sequences.

Deposition of colloidal particles resembles atomic layer vacuum deposition of inorganic materials.[21] In both cases a nucleation and growth mechanism operates. Nucleation on a flat surface is usually characterized by a critical nuclear diameter at which, depending on deposition conditions, further crystal growth may continue. Any kind of defect usually acts as a nucleation centre. Electrode surfaces featuring a periodic pit structure in a dielectric layer are ideal candidates for colloidal particle nucleation, Figure 8.3A. The structure of the first colloidal layer is determined by the pattern of the electrode. Then, the deposited colloidal monolayer on the patterned electrode surface acts itself as a nucleation layer (periodic defect structure) for the second colloidal layer. Deposition of the second layer is more complex. When the colloidal diameter is slightly different from the value of the pattern periodicity (D/Λ = 0.75), colloidal particles cannot occupy each site in depressions between neighbouring colloidal particles of the first layer. Nucleation on the surface starts randomly on the first colloidal layer, and further colloidal layer growth around a nucleation centre leads to mismatches between neighbouring colloidal crystal grains, Figure 8.3B. With deposition of third and fourth layers, Figure 8.3, C and D the colloidal grain size decreased. Colloidal crystals with three and four colloidal layers possess predominantly an A-B-A layer sequence as found in the hexagonal close-packed (HCP) crystal structure, while small areas of several micrometers with an A-B-C layer sequence (an FCC analog) were also present, Figure 8.3C. Growth in a dominating A-B-A sequence instead of an A-B-C is induced by a heightened counter ion concentration in the first two deposited layers in interparticle spaces (formed in the "tail" of colloidal particles, when an electric field is applied, see Figure 6.1). Approaching colloidal particles are electrostatically attracted by counter ions of deposited colloidal particles and thus take up their positions on top of preliminary deposited colloidal layers. Therefore, a decrease in grain size of colloidal crystals with three and four colloidal layers is caused only by growing defect structures formed in the first colloidal layer. Colloidal crystals presented in Figure 8.3 possess a low packing density compared to, for example, the close-packed HCP colloidal crystal.

The quality of colloidal crystals with FCC (110) parallel to the electrode surface and a thickness of more than two layers were subsequently improved by layer-by-layer colloidal deposition. During each deposition, an additional two colloidal layers were grown. Colloidal particles with a diameter of 330 nm and a surface charge density of 16.2 $\mu C/cm^2$ were deposited on a rectangular patterned structure with a periodicity of 330 nm by 450 nm at 3V during 6 min. Electrodes were withdrawn from the colloidal suspension with a colloidal volume fraction of 0.5 vol.% with a speed of 0.1 mm/s.

8.2. Binary colloidal monolayers

Binary colloidal monolayers were fabricated on electrode surfaces with hexagonal and square structures under an applied electric field, Figure 8.4. Layer-by-layer deposition of charged colloidal particles was performed electrophoretically by the method discussed in Chapter 6. Optimal deposition parameters were determined separately for each type of colloidal particle and patterned substrate. Large colloidal particles with a diameter of 545 nm and a surface charge density of 25.3 $\mu C/cm^2$ were deposited on a square pattern at 3.9 V during 45 sec and withdrawn from the colloidal suspension with a colloidal volume fraction of 0.2 vol.% at a speed of 0.1 mm/s. On hexagonally patterned surfaces, large colloidal particles were deposited at 3.5 V during 90 sec, followed by withdrawal (speed = 0.1 mm/s). After deposition, electrodes covered with monolayers of colloidal particles were left to dry for several minutes. Then, electrodes with deposited large colloidal particles were immersed in a colloidal suspension of small colloidal particles at a speed of 0.97 mm/s (the highest speed of the speed controlled device used) with a preset applied potential on them. Small colloidal particles with a diameter of 225 nm and a surface charge density of 17.7 $\mu C/cm^2$ were deposited on the square pattern at 3.0 V and 3.5 V during 30 sec and withdrawn from the colloidal suspension (colloidal volume fraction of 0.2 vol.%) at a speed of 0.1 mm/s. On hexagonally patterned surfaces, small colloidal particles with a diameter of 265 nm and a surface charge density of 17.0 $\mu C/cm^2$ were deposited at 3.0 V during 30 and 45 sec and subsequently withdrawn at a speed of 0.1 mm/s. The deposition time was measured from the time electrodes touched the colloidal suspension during electrode immersion. As it was mentioned in the previous paragraph, deposition of colloidal particles is very similar to the deposition of inorganic materials. Similar to inorganic materials, colloidal particles deposited onto an electrode surface tend to first nucleate at surface irregularities (or defects). Surface irregularities can artificially be introduced by periodically patterned surfaces. Small colloidal particles arriving at the electrode surface covered with a periodic structure of large particles take their positions in depressions between large colloidal particles, forming binary colloidal layers. On electrodes with the square pattern, two binary colloidal structures were formed with stoichiometries LS and LS_5* with $D_L/\Lambda = 1$, Figure 8.4 A and B. A LS_5 structure was also found in the bottom parts of the sample with a LS structure (region 3, Figure 6.2B).

* LS_5 stoichiometry was determined for a colloidal monolayer. In the case of colloidal crystals the crystal structure and stoichiometry are not known.

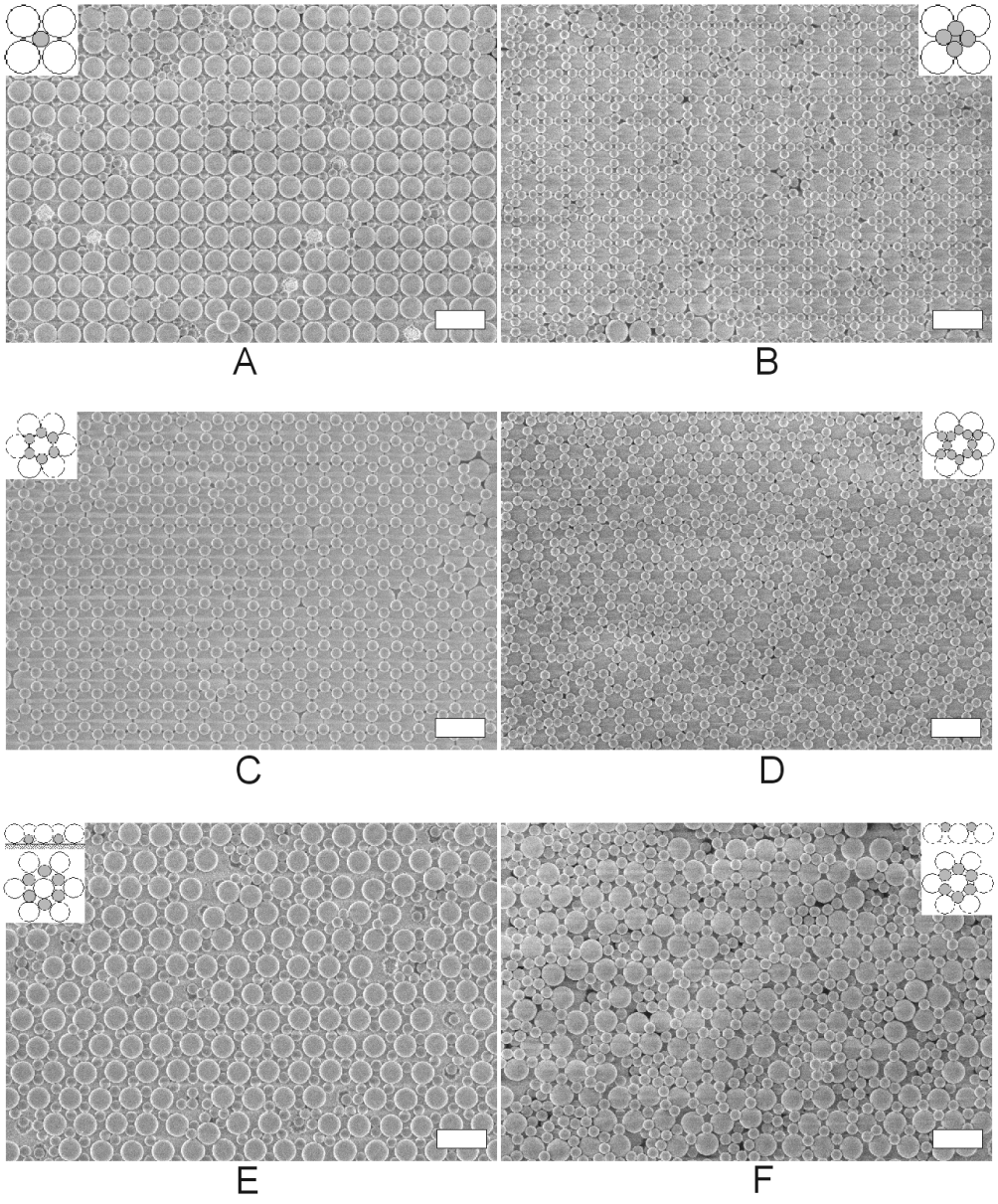

Figure 8.4. Binary colloidal monolayers with *stoichiometries*: A) LS, B) LS_5, C), E) and F) LS_2 and D) LS_4; *Ratios of colloidal radii* R_S/R_L: A), B) and D) 0.41; C), E) and F) 0.49; and *ratios of diameters of large particles to pattern periodicities* D_L/Λ: A), B), C) and D) 1; E) 0.78 and F) 0.83. Large colloidal particles with a diameter of 545 nm were deposited A) and B) at 3.9 V during 45 sec, electrode withdrawal speeds = 0.1 mm/s; C) – F) at 3.5 V during 90 sec, electrode withdrawal speeds = 0.1 mm/s. Small colloidal particles with a diameter of 225 nm were deposited A) at 3.0 V and B) at 3.5 V during 30 sec, electrode withdrawal speeds = 0.1 mm/s. Small colloidal particles with a diameter of 265 nm were deposited at 3.0 V during C) and D) 45 sec, and E) and F) 30 sec, electrode withdrawal speeds = 0.1 mm/s. In the corner of each image, a schematic representation of corresponding monolayer structures is depicted. Scale bar = 1 μm.

The number of small colloidal particles and, therefore, colloidal crystal stoichiometry, was varied by tuning the applied voltages, but it also could be increased by increasing the deposition time. Colloidal crystals grown on the square type of surface pattern with LS stoichiometry have a binary atomic analog i.e. NaCl. Structures of binary colloidal layers on hexagonally patterned surfaces can be varied either by tuning colloidal particle diameter or by changing pattern periodicity. Examples of LS_2 and LS_4 structures formed with colloidal particles of radii ratios R_S/R_L equal to 0.49 and 0.41, respectively, are shown in Figure 8.4 C and D. Deposition parameters for both binary colloidal structures were the same. An atomic analog for LS_2 colloidal crystals was found to be AlB_2. To our knowledge, LS_4 does not have a reported isostructural binary atomic analog. At shorter deposition times (20 - 30 sec), small colloidal particles with $R_S/R_L = 0.41$ order in colloidal layers with LS_2 stoichiometry, as well. In the bottom part of the sample with $R_S/R_L = 0.49$, presented in Figure 8.4C, at higher applied voltages and longer deposition times, binary colloidal layers with LS_3 stoichiometry (see Figure 8.1) as well as mixed areas (transition regions) of LS_2 and LS_3 were observed. Decreasing the ratios of colloidal diameters to pattern periodicities for a hexagonally patterned electrode from $D_L/\Lambda = 1$ to 0.83 and 0.78 allows the formation of non-close-packed binary colloidal monolayers that possess an LS_2 stoichiometry, Figure 8.4 E and F. Deposition parameters were the same in both cases. Although the colloidal monolayers formed possess defect structures, it is clear that small colloidal particles are laying on the electrode surface (Figure 8.4E), and small colloidal particles are located on top of large colloidal particles, forming hexagons around them (Figure 8.4F). The binary colloidal monolayers cover large electrode areas of several square millimeters. An example of the non-close-packed LS_2 structure presented in Figure 8.4E is also shown in Appendix I-1. The ability to form such non-close-packed monolayer structures on electrode areas of several micrometers indicates that with some improvements, formation of large-area, non-close-packed colloidal crystals could be possible.

Electrophoretic deposition of charged colloidal particles on patterned surfaces allows one to realize various complex binary colloidal monolayer structures, including non-close-packed ones, by changing electrode pattern structure and periodicity.

8.3. Formation of planar defects

Control over the formation of defect structures in colloidal crystals is important in their application as photonic crystals. Light propagation in photonic crystals can be guided through artificially created defects. Planar defects in colloidal crystals can be introduced in the form of a colloidal layer or layers formed with colloidal particles of a size different from the main crystal particle size. Electrophoretic deposition of charged colloidal particles, presented in Chapter 6, allows one to control colloidal crystal structure, orientation and thickness. Planar defects can also be introduced in a controlled way by performing a layer-by-layer deposition method and adjusting deposition parameters.

Negatively charged large colloidal particles with a diameter of 545 nm were deposited on a hexagonally patterned electrode surface with $D_L/\Lambda = 1$ at 3.5 V during 3 min and withdrawn from the colloidal suspension with a colloidal volume fraction of 0.2 vol.% at a

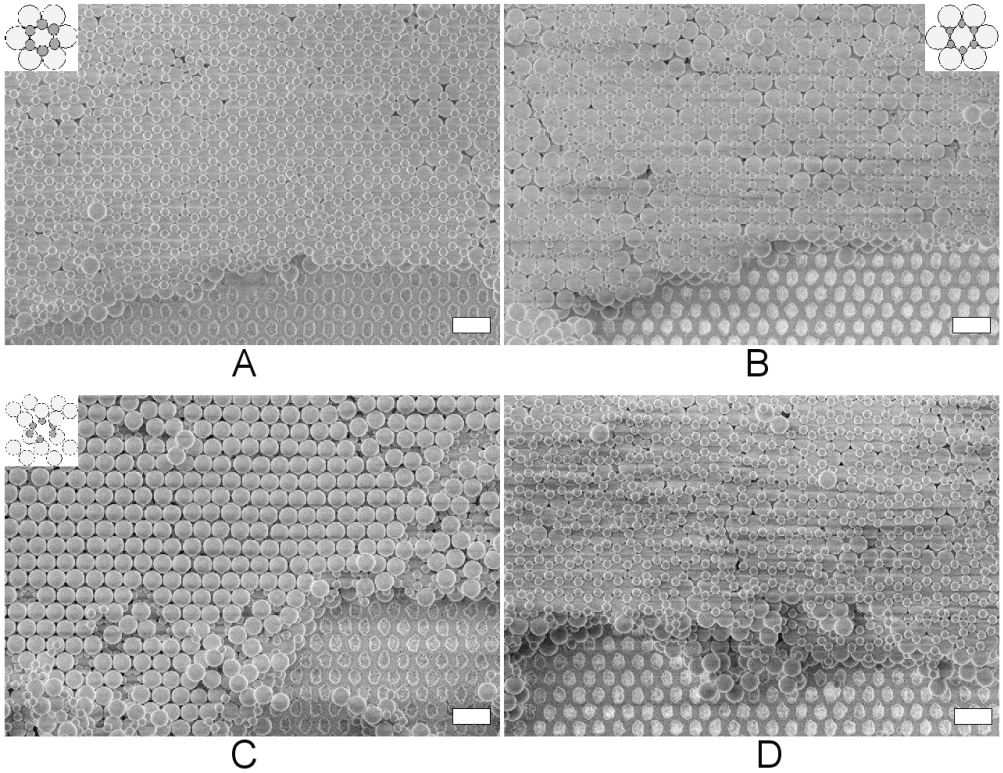

Figure 8.5. Layer-by-layer deposited binary colloidal layers on a hexagonally patterned electrode surface: A) two layers of large colloids (R_L) and one layer of small colloids (R_S), $R_S/R_L = 0.49$ and B) three layers of large colloids (R_L) and one layer of small colloids (R_S), $R_S/R_L = 0.41$; sandwich (alternating) structure of colloidal layers with 2 large, 1 small, 2 large and 1 small colloidal particles, $R_S/R_L = 0.49$; D) sandwich structure of colloidal layers with 2 large, 1 small and 1 large colloidal particles, $R_S/R_L = 0.49$. In the corner of images A, B and C, a schematic representation of corresponding layer structures is shown (for C the view is "in perspective"). Scale bar = 1 μm.

speed of 0.04 mm/s. At this withdrawal speed, a thickness gradient in the colloidal crystal was formed over the electrode surface. The thickness and surface coverage of colloidal crystals formed with large colloidal particles could be easily varied by adjusting deposition parameters such as deposition voltage and time, colloidal concentration and electrode withdrawal speed (for details, see Chapter 6). Then, the sample was left to dry for several minutes and small colloidal particles were deposited on top of the large ones. The structure of small colloidal particles can be adjusted to one with LS, LS_2, LS_3 and LS_4 stoichiometries depending on deposition parameters (see paragraph 8.2) and colloidal radii ratios. Examples of colloidal layers with LS_2 stoichiometry and colloidal radii ratios of R_S/R_L = 0.49 and 0.41 are shown in Figure 8.5 A and B. Negatively charged small colloidal particles were deposited at 3 V during 45 sec (R_S/R_L = 0.49) and 30 sec (R_S/R_L = 0.41), and the electrode was withdrawn at 0.1 mm/s from the colloidal suspension with a colloid volume fraction of 0.2 vol.%. In depositions following the first deposition, electrodes were immersed in colloidal suspension at a speed of 0.97 mm/s and the deposition time was measured from the time electrodes touched the surface of the colloidal suspension. Using the layer-by-layer method, a layer of small colloidal particles can be deposited among layers of large colloidal particles, breaking the usual sequence of a colloidal crystal, as it is schematically presented in the corner of Figure 8.5C. In Figure 8.5C only one top layer of large particles was deposited in order to clearly see the changes induced in layers with large colloidal particles caused by a layer of small particles. Large colloidal particles were deposited at 3.5 V during 6 min and electrodes were withdrawn at speed of 0.1 mm/s. In order to demonstrate the flexibility of this method, a sandwich structure of alternating colloidal layers with small and large colloidal particles was grown on the hexagonally patterned electrode surface shown in Figure 8.5D. Deposition parameters for the first two layers were the same as for those presented in Figure 8.5 A, B, and C. The next layers of large colloidal particles were deposited at 3.5 V during 2 min and using a withdrawal speed of 0.04 mm/s. The top layer of small colloids was deposited at 3 V during 60 sec, the electrode withdrawal speed was 0.1 mm/s.

Planar defect structures can also be introduced in colloidal crystals grown on electrode surfaces with a square pattern. Structures of small colloidal particles in this case can possess LS or LS_5 stoichiometries, as presented earlier in Figure 8.4 A and B. Further growth of large colloidal particles on top of the layer of small particles is more complex. The quality of colloidal layers with large colloidal particles is highly dependent on the homogeneity in surface coverage of underlying small colloidal particles.

8.4. Colloidal crystals with NaCl structure

Colloidal crystals possessing a NaCl structure (LS stoichiometry) can be fabricated by layer-by-layer deposition of large and small colloidal particles on surfaces with a square pattern, where small colloidal particles take their places in between the large ones, as shown in Figure 8.6. Large colloidal particles were deposited on an electrode surface in close-packed fashion ($D_L/\Lambda = 1$). The ratio of colloidal radii was $R_S/R_L = 0.41$, corresponding to the smallest possible value for the NaCl type structure, where colloidal particles are arranged in a close-packed manner. Deposition parameters were determined for each type of colloidal particle according to the approach presented in Chapter 6. Growth of binary colloidal crystals can be started from one or two colloidal layers of large colloidal particles. Starting the growth of such colloidal crystals with two layers of large colloidal particles has an advantage. Small colloidal particles position themselves precisely among the particles, which decreases the ability of large colloidal particles to rearrange themselves during following depositions. Small colloidal particles deposited onto a monolayer of large colloidal particles did not have any influence in our case on subsequent depositions. Negatively charged large colloidal particles with a diameter 545 nm were deposited at 3.9 V during 45 sec and withdrawn from the colloidal suspension with a colloidal volume fraction of 0.2 vol.% at a speed of 0.1 mm/s (in the case of monolayer formation, Figure 8.6A) and at 3.5 V during 3 min and a withdrawal speed of 0.04 mm/s in the case of two colloidal layers (Figure 8.6B). Electrodes were left to dry for several minutes prior to deposition of small colloidal particles. Then, electrodes with deposited large colloidal particles were immersed in a colloidal suspension of small colloidal particles at a speed of 0.97 mm/s under a preset applied potential. Negatively charged small colloidal particles were deposited at 3 V during 30 sec (in the case of one layer of large colloidal particles) and 45 sec (in the case of two layers), and withdrawn with an electrode speed of 0.1 mm/s from the colloidal suspension with a colloid volume fraction of 0.2 vol.%. The next layer of large colloidal particles was deposited at 3.5 V during 2 min and employing a withdrawal speed of 0.04 mm/s, Figure 8.6C. Examples of large area binary colloidal layers are presented in Appendix I-2.

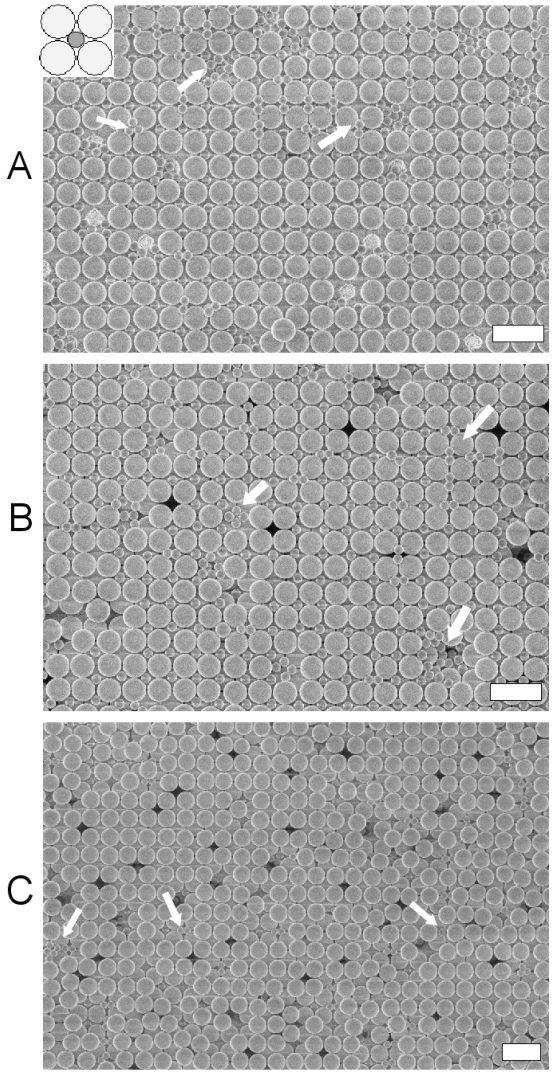

Figure 8.6. Layer-by-layer colloidal deposition on a square patterned substrate with a radii ratio of $R_S/R_L = 0.41$: A) colloidal monolayer, B) and C) two layers. In the corner of the first image, a schematic representation of corresponding layer structures is shown. Scale bar = 1 μm. Arrows indicate defects in colloidal structures.

The growth of good quality binary colloidal crystals using the layer-by-layer deposition method under an applied electric field is very sensitive to the quality of the colloidal monolayers formed in each deposition step. Various defect structures in deposited colloidal layers are indicated by white arrows in Figure 8.6. Defects in initial layers of large colloidal particles are usually introduced by missing colloidal particles. Partial coverage by small colloidal particles of such defects occurs, destroying the ordering of subsequently deposited colloidal layers. The homogeneity of deposited small colloidal particles plays an important role in determining the quality of subsequently deposited colloidal layers. Although the colloidal suspensions used were homogeneous, the local concentration of colloidal particles in suspension may vary. The local colloidal concentration of small colloidal particles close to an electrode surface influences their distribution in the layer of large colloidal particles. In addition to single small colloidal particles occupying vacancies between large colloidal particles, double, triple and quadruple aggregates of small colloidal particles as well as no particles at all were observed on colloidal layers. As a consequence of the existence of such diverse colloidal aggregates, displacement of large colloidal particles from their original positions takes place, Figure 8.6C. When such defect structures are eliminated, large area binary colloidal crystals with a NaCl structure can be grown.

8.5. Deposition of oppositely charged binary colloidal particles

Layer-by-layer electrophoretic deposition of oppositely charged binary colloidal particles on electrode surfaces with a hexagonal and square pattern was also performed. Negatively charged large colloidal particles with a diameter of 545 nm were deposited on the electrode surface with $D_L/\Lambda = 1$ at 3.5 V during 90 sec (hexagonally patterned electrode, Figure 8.7A) and at 3.9 V during 45 sec (square patterned electrode, Figure 8.7B) and withdrawn from the colloidal suspension (colloidal volume fraction 0.2 vol.%) at a speed of 0.1 mm/s. Positively charged small colloidal particles of the size 225 nm ($R_S/R_L = 0.41$) and a surface charge density of 13.2 $\mu C/cm^2$ were deposited at 2.0 V during 30 sec (hexagonally patterned electrode) or at 2.5 V during 25 sec (square patterned electrode) and the corresponding electrodes were withdrawn at 0.1 mm/s from the colloidal suspension which had a colloid volume fraction of 0.2 vol.%. After each deposition, electrodes were dried for several minutes before the next deposition. It was rather difficult to obtain a homogeneous coverage of small colloidal particles. There were always a large number of additional small

colloidal particles present that did not organize themselves according to the template formed by the large colloidal particles, Figure 8.7. It was also observed, that there was no change in the layer structure of large colloidal particles following the deposition of small colloidal particles, when the potential of the electrodes was changed to opposite. Thick colloidal crystals were formed by the deposition of several layers of large colloidal particles at 3.5 V for 3 min and a withdrawal speed of 0.04 mm/s, following by one layer of small colloidal particles at 2.0 V (Figure 8.7C) and 1.5 V (Figure 8.7D) during 30 sec and using an electrode withdrawal speed of 0.1 mm/s. It was observed, that during the withdrawal of thick colloidal crystals after the deposition of small colloidal particles, at the bottom part of the sample, all colloidal layers were driven back into the colloidal suspension, revealing the electrode surface. Electrostatic repulsion between an electrode surface that h as the same charge sign as the lower layers in a colloidal crystal may cause the colloidal crystal to be easily driven back

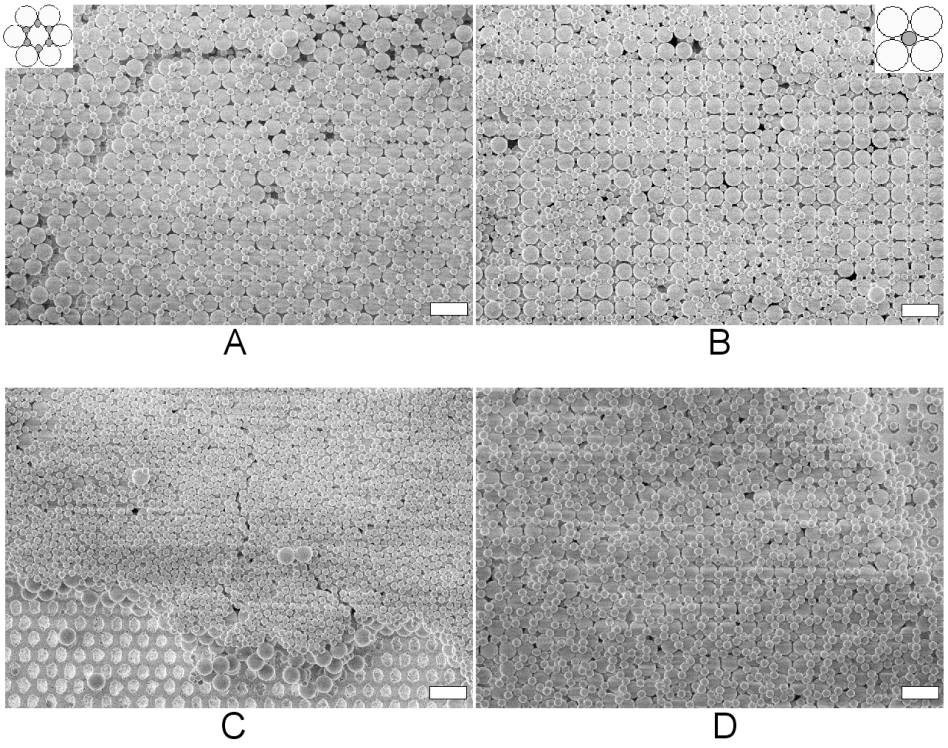

Figure 8.7. Layer-by-layer deposition of binary colloidal layers of oppositely charged particles (large colloids are negatively charged and small colloids – positively charged): on a hexagonally patterned electrode surface: A) R_S/R_L = 0.41 and C) R_S/R_L = 0.49; on a square patterned electrode surface, two layers of large colloids (R_L) and one layer of small colloids (R_S): B) R_S/R_L = 0.41 and D) R_S/R_L = 0.49. Large colloidal particles with a diameter of 545 nm were deposited A) 3.5 V during 90 min and B) at 3.9V during 45 sec and using an electrode withdrawal speed of 0.1 mm/s; C) and D) at 3.5V during 3 min, electrode withdrawal speed = 0.04 mm/s. Small colloidal particles with a diameter of 225 nm were deposited A) at 2.0 V during 30 sec; B) at 2.5 V during 25 sec; C) at 2.0 V during 40 sec and D) 1.5 V during 30 sec, electrode withdrawal speed = 0.1 mm/s. In the corner of images A and B, a schematic representation of corresponding layer structures is shown. Scale bar = 1 μm.

to the colloidal suspension under its own weight, aided by applied capillary forces from the meniscus of the colloidal suspension passing along the electrode surface during electrode withdrawal. The number of small positively charged colloidal particles was always higher than was expected according to the template of large colloidal particles and did not depend on colloidal concentration, applied voltage and decreased deposition time. Attractive electrostatic forces between oppositely charged large and small colloidal particles led to particle coagulation on the colloidal crystal surface, making deposition control of oppositely charged colloidal particles more difficult compared to that of binary colloidal particles possessing the same charge sign.

Conclusions

Layer-by-layer electrophoretic deposition of colloidal particles with monomodal and bimodal distributions on electrode surfaces with periodic patterns was performed. Colloidal binary monolayers with LS, LS_2, LS_3, LS_4 and LS_5 stoichiometries were formed by this method on electrode surfaces with square and hexagonal patterns. A decrease in D/Λ ratio from 1 to 0.75 led to the formation of non-close-packed binary colloidal monolayers. Layer-by-layer deposition of large and small colloidal particles with radii ratios of 0.41 and 0.49 on square and hexagonal patterns, respectively, led to the formation of binary colloidal crystals with atomic analogs as NaCl and AlB_2, respectively. Deposition of binary colloidal particles of the same charge sign (for example, only negatively charged colloidal particles) was easier to control than deposition of oppositely charged colloidal particles. The number of deposited positively charged colloidal particles was always higher than expected based on colloidal concentration, applied voltage and deposition time. Planar defects could be introduced in colloidal crystals in the form of deposited mono- (multi-) layers of colloidal particles with a colloid diameter different from the colloidal particles forming the main crystal. Growth of non-close-packed colloidal crystals formed by colloidal particles of the same size and charge was successfully performed. Formation of non-close-packed colloidal crystals with an A-B-A sequence (analogous to the HCP crystal structure) on hexagonally patterned surfaces with a D/Λ ratio of 0.75 was demonstrated. In addition, the growth of FCC colloidal crystals with the (110) plane parallel to the electrode surface was improved due to a stepwise construction of the crystal. Layer-by-layer electrophoretic deposition of colloidal particles on patterned electrode surfaces is a powerful method for the fabrication of non-close-packed and binary colloidal crystals with various crystal structures.

Appendix I

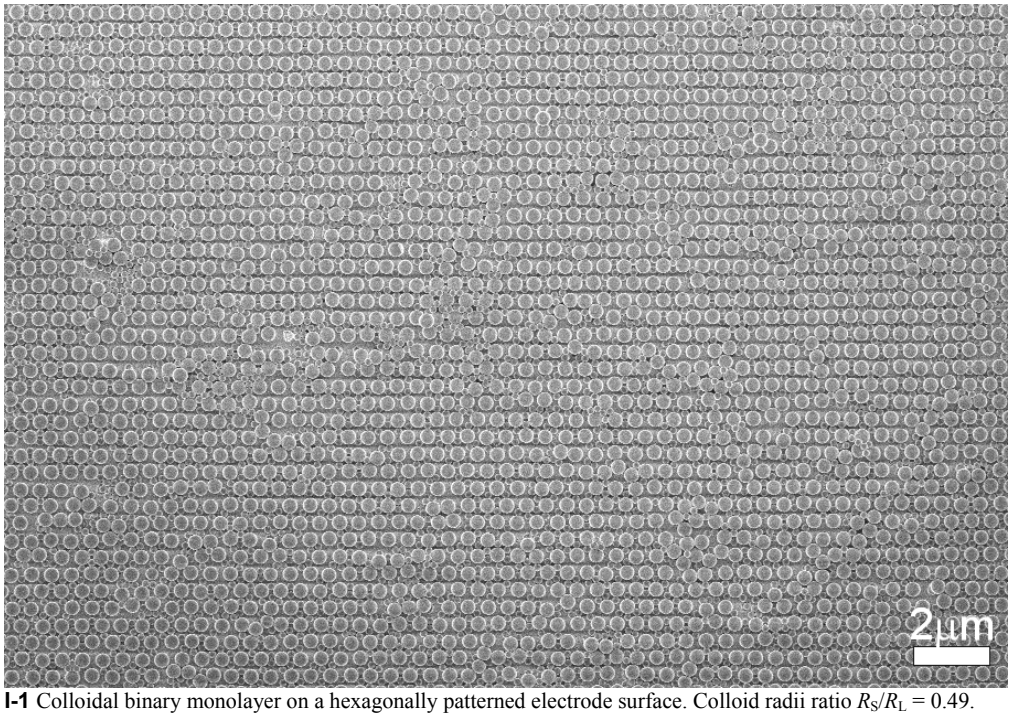

I-1 Colloidal binary monolayer on a hexagonally patterned electrode surface. Colloid radii ratio $R_S/R_L = 0.49$.

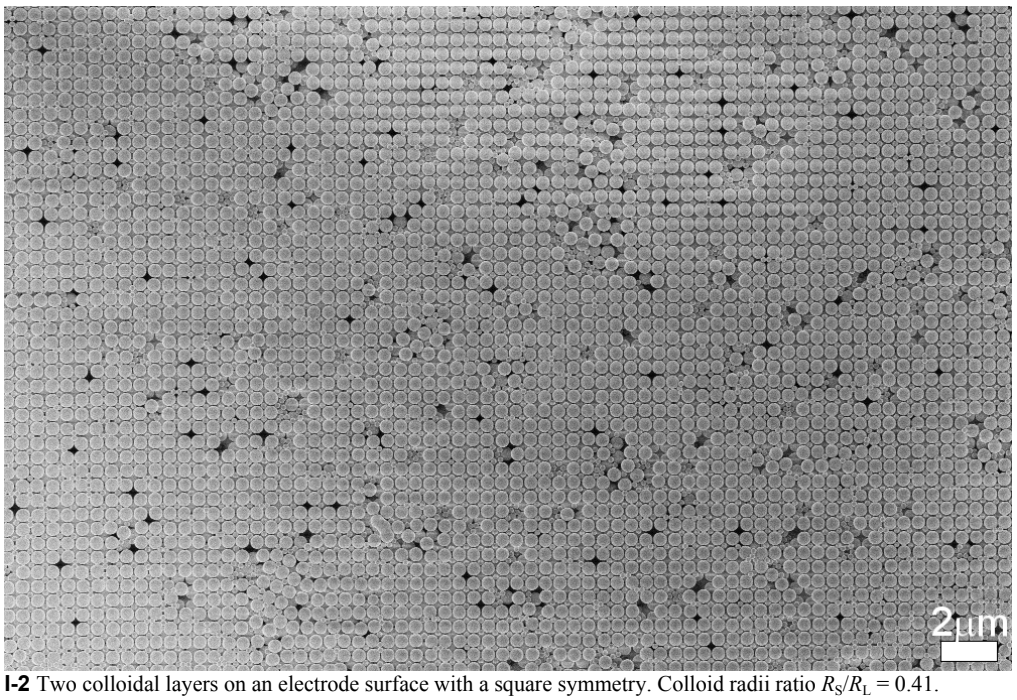

I-2 Two colloidal layers on an electrode surface with a square symmetry. Colloid radii ratio $R_S/R_L = 0.41$.

References

[1] K. M. Ho, C. T. Chan, C. M. Soukoulis, *Phys. Rev. Lett.* **1990**, *65*, 3152.
[2] M. J. Murray, J. V. Sanders, *Nature* **1978**, *275*, 201.
[3] A. D. Dinsmore, A. G. Yodh, D. J. Pine, *Nature* **1996**, *383*, 243.
[4] S. Hachisu, S. Yoshimura, *Nature* **1980**, *283*, 188.
[5] M. D. Eldridge, P. A. Madden, D. Frenkel, *Nature* **1993**, *365*, 35.
[6] A. Imhof, J. K. G. Dhnot, *Phys. Rev. Lett.* **1995**, *75*, 1662.
[7] P. Bartlett, R. H. Ottewill, P. N. Pusey, *Phys. Rev. Lett.* **1992**, *68*, 3801.
[8] P. Bartlett, P. N. Pusey, *Physica A* **1993**, *194*, 415.
[9] N. Hunt, R. Jardine, P. Bartlett, *Phys. Rev. E* **2000**, *62*, 900.
[10] M. E. Leunissen, C. G. Christova, A.-P. Hynninen, C. P. Royall, A. I. Campbell, A. Imhof, M. Dijkstra, R. van Roij, A. van Blaaderen, *Nature* **2005**, *437*, 235.
[11] C. J. Kiely, J. Fink, M. Brust, D. Bethell, D. J. Schiffrin, *Nature* **1998**, *396*, 444.
[12] F. X. Redl, K.-S. Cho, C. B. Murray, S. O'Brien, *Nature* **2003**, *423*, 968.
[13] D. Zanchet, M. S. Moreno, D. Ugarte, *Phys. Rev. Lett.* **1999**, *82*, 5277.
[14] E. V. Shevchenko, D. V. Talapin, A. L. Rogach, A, Kornowski, M. Haase, H. Weller, *J. Am. Chem. Soc.* **2002**, *124*, 11480.
[15] A. D. Dinsmore, A. G. Yodh, D. J. Pine, *Phys. Rev. E* **1995**, *52*, 4045.
[16] V. Kitaev, G. A. Ozin, *Adv. Mater.* **2003**, *15*, 75.
[17] K. P. Velikov, C. G. Christova, R. P. A. Dullens, A. van Blaaderen, *Science* **2002**, *296*, 106.
[18] D. Wang, H. Möhwald, *Adv. Mater.* **2004**, *16*, 244.
[19] F. Garcia-Santamaria, C. Lopez, F. Meseguer, F. Lopez-Tejeira, J. Sanchez-Dehesa, H. T. Miyazaki, *Appl. Phys. Lett.* **2001**, *79*, 2309.
[20] F. Garcia-Santamaria, H. T. Miyazaki, A. Urquia, M. Ibisate, M. Belmonte, M. Shinya, F. Meseguer, C. Lopez, *Adv. Mater.* **2002**, *14*, 1144.
[21] See for example: L. B. Freund, S. Suresh, *Thin Film Materials: Stress, Defect Formation and Surface Evolution*, Cambridge University Press, Cambridge, **2004**.

Outlook

Within this thesis we showed that by combining various colloidal deposition approaches, an independent control of colloidal crystal structure, orientation and thickness was achieved. Moreover, we showed that the electrophoretic deposition technique we used is convenient and does not require a complicated set-up. The results obtained in the course of this work clearly indicate that tuning the interactions between building blocks of the colloidal deposition system allows us to produce other than the usual close-packed colloidal crystal structures. We also showed, that structured (patterned) surfaces play an essential role in the formation of colloidal crystals with desired crystal structures. We demonstrated this on examples of colloidal crystals with BCC and non-close-packed HCP crystal structures. Control over colloidal deposition parameters allows us also to introduce crystal defects and induce binary colloidal crystal growth.

In this part we present an outlook for the continuation of this study. We hope that the demonstrated opportunities to induce growth of non-close-packed colloidal crystals will stimulate researches in this field to find methods of fabricating low-symmetry colloidal crystals by self-assembly of colloidal particles for photonic crystal applications.

The method of electrophoretic deposition of charged colloidal particles on patterned electrode surfaces described in this thesis is very efficient for fabricating a variety of colloidal crystals. Although this method is very successful, there is also room for further improvements and research:

- In Chapter 5 we presented the patterning of electrode surfaces. The patterned topography has a *strong* influence on the homogeneity of the colloidal particle coverage especially in the case of non-close-packed colloidal structures. Therefore, to perfect pattern topography, the choice of the applied patterning procedure and the choice of photoresist and the substrate materials are important;
- The set-up for the electrophoretic deposition could be improved to allow a precise control of electrode positions such as tilt angle and rotation angle of the patterned areas of the electrodes with respect to the colloidal suspension surface, and the distance between electrodes. These parameters play an important role in the growth of colloidal crystals and influence their crystal structure, thickness and the size of the area covered by a certain predetermined structure;
- The deposition of non-close-packed and binary colloidal crystals discussed in Chapter 8 can be recommended for further studies. Our first experiments showed that the layer-by-layer colloidal deposition process has a large potential to fabricate non-close-packed and binary colloidal crystals: the colloidal layer structures are not changed (rearranged or destroyed) after consecutive depositions. This goes for the deposition of similarly as well as oppositely charged colloidal particles. Therefore, the influence of concentration, electric field strength, and withdrawal speed of the electrodes on the colloidal particle coverage needs to be studied first, especially in the case of small colloidal particles because they create defects in a subsequently deposited layers of large colloidal particles;
- Corresponding characterizations of colloidal crystal ordering are recommended. Scattering experiments (small-angle X-ray scattering) determine what type of structure (FCC, HCP or random stacking) of colloidal crystals is preferably formed on the hexagonally patterned electrodes and provide information on the average interparticle spacing.[1] From the diffraction pattern one can also determine the Debye - Waller factor (showing the displacement of the colloidal particles from their original lattice positions), the average domain size, and the correlation length of colloidal crystals.

These parameters can also be calculated for 2D and 3D colloidal crystals of known structures from SEM images, using corresponding computational programs.[2]

Crystals with the diamond-like symmetry are highly desired for PBG materials. Fabrication of such structures has been realized by using a fully directed, one-by-one positioning and colloidal particle assembly by nanorobotic manipulation.[3] However, an inherent problem remains the slow speed related to the serial character of these processes. Parallelization would help, although it is not trivial in practice. "Soft lithography"[4] is another widely used technique for printing organic molecules by an elastomeric stamp on a large variety of substrates. When organic molecules have a good affinity for a substrate material, various patterned structures can be simply realized. Nowadays, surface properties of colloidal particles as well as substrate surface chemistry can be easily controlled and, therefore, the combination of soft lithography with colloidal particles could be an alternative approach to the nanorobotic parallelization technique. Introduction of structural defects is another important issue in the fabrication of photonic crystals, where the colloidal soft lithography can make its contribution. By tuning interactions between colloidal particles and an elastomeric stamp, colloidal particles can either be locally removed from the colloidal crystal surface or colloidal particles of different nature can be deposited on the surface with their subsequent removal after the introduced defect is closed by the rest of the colloidal crystal.

In this work spherical polymer colloidal particles were used, due to the availability of simple synthetic routes for the preparation of well-characterized and highly monodispersed colloidal spheres. However, whether low-symmetry colloidal crystals can be fabricated from spherical colloidal particles by colloidal self-assembly still remains an open question. It was calculated that photonic crystals formed from colloidal particles of ellipsoidal shape possess larger photonic band gaps than those made from spherical colloidal particles.[5] Various ways exist for the controlled fabrication of elliptical colloidal particles.[6,7] Use of the method presented in this thesis could promote controlled colloidal crystal growth also with non-spherical colloidal particles. Firstly, colloidal particles would be oriented along electric field lines, when an electric potential is applied. Secondly, electrode surface patterning would predetermine the colloidal crystal growth, targeting the fabrication of low-symmetry colloidal crystals. In addition to ellipsoidal colloidal particles, some other approaches were proposed to make spherical particles "directional".[8] One of those approaches comprises coating of spherical colloidal particles with anisotropic objects, e.g., lipids, triblock copolymers, or

liquid crystals. In case of a strong coating anisotropy, the formation of a 2D nematic liquid crystal with four strongly repulsive disclination defects on the surface of spherical colloidal particles was predicted. This would make the corresponding colloidal particles exhibit a four-fold valence-like structure similar to an sp^3-hybridized carbon atom.

Significant improvement of colloidal particle ordering with the implementation of surface patterning (or physical confinement) was pointed out subsequently throughout this thesis. One more example we would like to mention here is the fabrication of colloidal crystals packed in cylindrical tubes by the pressure-assisted method.[9] These colloidal cylindrical columns exhibited high structural order over length scales covering several centimeters in cylinder length. In addition, it was shown previously on examples of 2D colloidal structures, that the ratio between the colloidal size and the width of patterned stripes determines the 2D colloidal structure and the colloidal packing density.[10,11,12] Therefore, if such "cylindrical tubes" are placed in a close-packed manner overlapping each other, then a precise adjustment of the diameter ratio between colloidal particles and cylinders will determine whether the colloidal particle's packing in a spiral manner in each cylinder leads to the formation of an overall colloidal crystal possessing a low crystal symmetry (a diamond-like structure).

Colloidal particles were demonstrated to be universal building blocks with a great potential. They can be prepared with well-controlled surface properties from a variety of organic as well as inorganic materials, allowing us to manipulate them easily with applied external forces. Being highly monodisperse, the colloidal particles pack themselves into close-packed periodic structures. Introducing the template structures, the colloidal particle assembly can be guided to non-trivial forms of packing in 3D, while maintaining the effects of templates through the crystals. In this content, the colloidal particles open many challenges for researchers to achieve full control over colloidal crystallization and finally to realize colloidal particle self-assembly into low-symmetry (diamond) colloidal crystal structures.

References

[1] W. L. Vos, M. Megens, C. M. van Kats, P. Bösecke, *Langmuir* **1997**, *13*, 6004.
[2] T. G. Euser, diploma thesis (under direction of W. Vos and L. Kuipers), University of Twente, **2002**.
[3] F. Garcia-Santamaria, H. T. Miyazaki, A. Urquia, M. Ibisate, M. Belmonte, M. Shinya, F. Meseguer, C. Lopez, *Adv. Mater.* **2002**, *14*, 1144.
[4] Y. Xia, G. M. Whitesides, *Angew. Chem. Int. Ed.* **1998**, *37*, 550.
[5] Z.-Y. Li, J. Wang, B.-Y. Gu, *Phys. Rev. B* **1998**, *58*, 3721.
[6] Y. Lu, Y. Yin, Y. Xia, *Adv. Mater.* **2001**, *13*, 271.
[7] T. van Dillen, A. van Blaaderen, A. Polman, *Materials Today* **2004**, *7*, 40.
[8] D. R. Nelson, *NanoLetters* **2002**, *2*, 1125.
[9] U. Kamp, V. Kitaev, G. von Freymann, G. A. Ozin, S. A. Mabury, *Adv. Mater.* **2005**, *17*, 438.
[10] E. Kumacheva, P. Garstecki, H. Wu, G. M. Whitesides, *Phys. Rev. Lett.* **2003**, *91*, 128301.
[11] K.-H. Lin, J. C. Crocker, V. Prasad, A. Schofield, D. A. Weitz, T. C. Lubensky, A. G. Yodh, *Phys. Rev. Lett.* **2000**, *85*, 1770.
[12] R. G. Golding, P. C. Lewis, E. Kumacheva, *Langmuir* **2004**, *20*, 1414.

Summary

The method of “Electrophoretic deposition of charged polymer colloids on patterned substrates” was developed, where patterned surfaces predetermine the location of colloidal particles on the surface and an electric field acts as a driving force in the colloidal crystallization process. This method allows an independent control of colloidal crystal structure, orientation and crystal thickness. The technique was successfully applied to grow single and binary colloidal monolayers, colloidal crystals with FCC crystal structures and (111), (100) and (110) plane orientations, BCC colloidal crystals grown from a (100) crystal plane, non-close-packed colloidal multilayers with a HCP crystal sequence and binary colloidal crystals with NaCl and AlB_2 analogs. Planar defects were easily introduced and controlled by the set of deposition parameters.

A brief introduction to the topics that are relevant for this thesis is presented in **Chapter 1**. Attention was given to various colloidal crystallization methods, such as colloidal crystallization on flat, chemically and lithographically modified substrates as well as under applied external fields. Special emphasis was placed on reviewing the current status in the area of colloidal crystallization on topologically patterned substrates.

Crystallization of oppositely charged colloidal particles was studied using "Molecular Dynamics" computations in **Chapter 2**. The stability of colloidal crystals with various crystal structures was examined. It was found that stable colloidal crystal structures resemble those found among the inorganic materials. The range of sphere size ratios for stable colloidal structures was determined. Colloidal crystals with the zinc blende inorganic analog were found to be stable at size ratio 0.2, with the sodium chloride analog – at size ratio 0.4 and with the cesium chloride analog – at values of size ratios higher than 0.6. The presence of a surface charge was necessary to keep the structure together, but the size of this charge was not important for stable structures, although a large surface charge assists in breaking down unstable crystal structures.

Seeded emulsifier-free emulsion polymerization of styrene monomer allowed the synthesis of monodispersed colloidal particles with controlled surface charge densities and a colloidal size in the sub-micrometer range. **Chapter 3** and **Chapter 4** described the synthesis and characterization of negatively and positively charged colloidal particles, respectively. Colloidal size and size monodispersity were controlled in the first polymerization stage (core particles) and were characterized by HR-SEM measurements. Surface charge densities were controlled via polymerization of styrene monomer and ionic co-monomer around core particles in the second stage (core-shell particles). Surface charge densities were determined by conductometric (for negatively charged particles) and potentiometric (for positively charged particles) titrations. The influence of co-monomer type, initiator and polymerization conditions on colloid size, size monodispersity and surface charge density were discussed. A new co-monomer was found that yields high surface charge densities in a seeded polymerization process without forming polyelectrolyte residues in the colloidal suspension.

In **Chapter 5**, a lithographic method for electrode surface patterning was developed. The method comprised the transfer of a photoresist pattern in a dielectric SiO_2 layer, applying a lift-off process. Hexagonal, square and rectangular types of periodic patterns in photoresist were generated by laser interference lithography (LIL). LIL allowed us to generate periodic patterned surfaces with pattern periodicities between 300 nm and 900 nm. Optimal process parameters for photoresist patterning and SiO_2 layer etching were found.

The method of electrophoretic deposition of colloidal particles onto patterned electrode substrates was introduced in **Chapter 6**. Deposition on flat and patterned electrode surfaces was compared. Deposition on flat electrode surfaces led to the formation of disordered colloidal monolayers and crystals, while patterned surfaces pre-determined the location of colloidal particles on electrode surfaces by physical confinement. Deposition parameters such as electric field strength, colloid concentration, surface charge density, withdrawal speed of electrodes etc. were shown to play an important role in colloidal crystal growth. It was found that colloidal particles with low surface charge densities allowed a better control over colloidal crystallization. An optimal deposition voltage of 3.5 V was found for colloidal crystal growth. At higher deposition voltages, more disorder in colloidal crystals occured and at lower voltages the deposition process was ineffective. The withdrawal speed of electrodes from the colloidal suspension plays an important role in determining the thickness and growth of colloidal crystals with non-close-packed structures. For different crystal structures, the withdrawal speed was optimized for the systems considered. Specifically, the formation of colloidal monolayers (two-dimensional crystals) was discussed in this chapter.

The growth of colloidal crystals with FCC and BCC structures was discussed in **Chapter 7**. The electrophoretic method, presented in Chapter 6, was applied. Colloidal crystals were deposited on electrode surfaces with various symmetries in order to induce colloidal crystal growth from different crystal planes. Colloidal crystals with FCC crystal structure grown in [111], [100] and [110] crystal directions and BCC in the [100] direction were presented. The influence of topologically patterned electrode surfaces on colloidal crystal growth was a main topic of this chapter. It was found, that growth of FCC (111) and (100) could be easily controlled at low withdrawal speeds, while growth of FCC (110) colloidal crystals was limited to two colloidal layers. Thick colloidal crystals grown in the [110] crystal direction finally possessed small polycrystalline regions with (111), (100) and (110) crystal planes. Disorder and polycrystallinity were caused by the geometrical factor of this plane, which is not close-packed in one of the main (perpendicular) directions. Growth of high quality close-packed FCC colloidal crystals was determined by the precise match of crystal lattice constant and electrode pattern periodicity. Fabrication of colloidal crystals with a BCC structure from the (100) crystal plane was also discussed in this chapter. Optimal deposition parameters were found for the systems investigated, allowing us to grow up to seven layers of this crystal structure.

The layer-by-layer electrophoretic deposition method of colloidal particles on patterned electrode surfaces was introduced in **Chapter 8**. Applying this method, binary colloidal monolayers with LS, LS_2, LS_3, LS_4 and LS_5 stoichiometries were formed on hexagonally and square patterned electrode surfaces. Non-close-packed colloidal crystals with A-B-A sequence (an analog of the HCP crystal structure) were successfully fabricated. FCC colloidal crystal growth in the direction perpendicular to the (110) crystal plane was substantially improved. Plane defects using colloidal particles of different size were easily introduced. Finally, bimodal colloidal crystals with NaCl and AlB_2 analogs were fabricated by layer-by-layer deposition of colloidal particles either of the same charge or opposite charge, respectively.

Samenvatting

De methode van “Electrophoretische depositie van geladen polymeercolloïden op gestructureerde substraten” werd ontwikkeld, waarin topografisch gestructureerde substraten de locatie van colloïdale deeltjes bepalen op het oppervlak, en waarin een elektrisch veld als drijvende kracht werkt in het proces van colloïdale kristallisatie. Deze methode maakt het mogelijk om colloïdale kristalstructuur, orientatie en kristaldikte onafhankelijk van elkaar te beïnvloeden. De techniek werd met succes toegepast om verschillende kristallen te vormen, zoals enkelvoudige (één colloïdgrootte) en binaire colloïdale monolagen (twee verschillende deeltjesgroottes), colloïdale kristallen met FCC structuur en (111), (100) en (110) vlakoriëntaties, BCC kristallen gegroeid van een (100) kristalvlak, niet dichtgepakte colloïdale multilagen met een HCP kristalordening en binaire colloïdale kristallen analoog aan NaCl en AlB_2 structuren. Vlakdefecten konden eenvoudig worden geïntroduceerd en beïnvloed door aanpassing van de depositieparameters.

Een korte inleiding in de onderwerpen die relevant zijn voor dit proefschrift wordt gegeven in **Hoofdstuk 1**. Aandacht wordt besteed aan verschillende methoden van colloïdale kristallisatie zoals colloïdale kristallisatie op vlakke, maar ook op chemisch en lithografisch gemodificeerde oppervlakken en onder externe aangelegde velden. Een overzicht wordt gegeven van de huidige stand van zaken op het gebied van colloïdale kristallisatie op lithografisch gemodificeerde substraten.

Kristallisatie van tegengesteld geladen colloïdale deeltjes werd bestudeerd door middel van "Molecular Dynamics" berekeningen in **Hoofdstuk 2**. De stabiliteit van colloïdale kristallen met verschillende structuren werd onderzocht. Er werd gevonden dat stabiele structuren van colloïdale kristallen lijken op die, welke binnen de anorganische materialen worden gevonden. De grootteverhouding van colloïdale deeltjes werd bepaald voor de stabiele structuren. Stabiele colloïdale kristallen met een structuur analoog aan de anorganische zinkblende bleken stabiel te zijn bij een grootteverhouding van 0.2, analoog aan de natriumchloride structuur bij een grootteverhouding van 0.4, en analoog aan de cesiumchloride structuur bij grootteverhoudingen boven 0.6. De aanwezigheid van een oppervlaktelading was noodzakelijk om de structuur bijeen te houden, maar de grootte van deze lading was niet belangrijk voor het verkrijgen van stabiele structuren, hoewel hoge oppervlakteladingsdichtheden bijdroegen aan het uiteenvallen van onstabiele kristalstructuren.

Door middel van seeded emulsifier-free emulsiepolymerisatie van styreen konden monodisperse colloïdale deeltjes met een gedefinieerde oppervlakteladingsdichtheid en colloïdale afmeting in het submicrometergebied worden gesynthetiseerd. **Hoofdstuk 3** en **Hoofdstuk 4** beschrijven de synthese en karakterisering van respectievelijk negatief en positief geladen colloïdale deeltjes. Colloïdale afmetingen en polydispersiteit werden gestuurd in de eerste polymerisatiestap (synthese van de kern) en werden gekarakteriseerd door middel van HR-SEM metingen. Oppervlakteladingsdichtheden werden beïnvloed door polymerisatie van styreen monomeer en ionisch comonomeer rond de kernen in de tweede polymerisatiestap (vorming van core-shell deeltjes). Oppervlakteladingsdichtheden werden bepaald door middel van conductometrische (voor negatief geladen deeltjes) en potentiometrische (voor positief geladen deeltjes) titraties. De invloed van comonomeer type, initiator en polymerisatieomstandigheden op colloïdgrootte, polydispersiteit en oppervlakteladings-dichtheid worden besproken. Een nieuw comonomeer werd gevonden waarmee hoge ladingsdichtheden konden worden gerealiseerd in een seeded polymerisatieproces, zonder vorming van polyelectrolyt in de colloïdale suspensie.

In **Hoofdstuk 5** wordt de ontwikkeling van een lithografische methode om electrodeoppervlakken te structureren beschreven. De methode omvatte de overdracht van een photoresistpatroon in een dielectrische SiO_2 laag, gebruikmakend van een lift-off proces. Hexagonale, vierkante en rechthoekige periodieke patronen werden in de photoresist gegenereerd door middel van Laser Interference Lithography (LIL). Met behulp van LIL konden we periodiek gestructureerde oppervlakken met periodiciteiten tussen 300 nm en 900 nm fabriceren. Optimale procesparameters voor photoresist structurering en het etsen van de SiO_2 laag werden vastgesteld.

De electrophoretische depositiemethode om colloïdale deeltjes op gestructureerde electroden aan te brengen werd geïntroduceerd in **Hoofdstuk 6**. Depositie op vlakke en topografisch gestructureerde electrodeoppervlakken werd vergeleken. Depositie op vlakke electrodeoppervlakken leidde tot de vorming van ongeordende colloïdale monolagen en kristallen, terwijl gestructureerde oppervlakken de locatie van colloïdale deeltjes op electrodeoppervlakken stuurden door ruimtelijke begrenzing. Depositieparameters zoals electrische veldsterkte, colloïdconcentratie, oppervlakteladingsdichtheid en snelheid waarmee de electroden uit de suspensie werden gehaald speelden, zoals werd aangetoond, een belangrijke rol in de colloïdale kristalgroei. Gevonden werd dat colloïdale deeltjes met lage oppervlakteladingsdichtheden een betere controle mogelijk maakten over colloïdale kristallisatie. Een optimaal depositievoltage van 3.5 V werd vastgesteld voor colloïdale groei. Bij hogere depositievoltages onstond meer wanorde in de colloïdale kristallen en bij lagere voltages was het depositieproces niet effectief. De snelheid waarmee electroden uit de colloïdale suspensies werden gehaald had een grote invloed op de groei en de dikte van colloïdale kristallen met niet dichtgepakte structuren. De snelheid werd geoptimaliseerd voor verschillende kristalstructuren. Met name de vorming van colloïdale monolagen (tweedimensionale kristallen) werd besproken in dit hoofdstuk.

De groei van colloïdale kristallen met FCC en BCC structuur werd bediscussieerd in **Hoofdstuk 7**. De electrophoretische methode, gepresenteerd in Hoofdstuk 6, werd toegepast. Depositie van colloïdale kristallen op electrodeoppervlakken met verschillende symmetrieën werd uitgevoerd om colloïdale kristalgroei vanaf verschillende kristalvlakken te induceren. Colloïdale kristallen met FCC kristalstructuur, gegroeid in de [111], [100] en [110] kristalrichtingen, en met BCC kristalstructuur in de [100] richting werden gepresenteerd. De invloed van topografisch gestructureerde electrodeoppervlakken op colloïdale kristalgroei is een belangrijk onderdeel van dit hoofdstuk. Gevonden werd dat de groei van FCC (111) en (100) gemakkelijk kon worden beheersd bij lage terugtrekkingssnelheden wanneer de groei

van FCC (110) colloïdale kristallen beperkt bleef tot twee colloïdale lagen. Dikke colloïdale kristallen gegroeid in de [110] kristalrichting bezaten uiteindelijk kleine polykristallijne gebieden met (111), (100) en (110) kristalvlakken. Wanorde en polykristalliniteit werden veroorzaakt door de geometrische factor van dit vlak, dat niet dichtgepakt is in een van de hoofd (loodrecht) richtingen. De groei van hoge kwaliteit dichtgepakte FCC colloïdale kristallen werd bepaald door de precieze overeenkomst tussen kristalroosterconstante en electrodepatroon periodiciteit. De fabricage van colloïdale kristallen met een BCC structuur vanaf het (100) kristalvlak werd ook besproken in dit hoofdstuk. Optimale depositieparameters werden gevonden voor de onderzochte systemen zodat een kristalstructuur met een dikte tot zeven lagen kon worden opgebouwd.

De laag-op-laag methode van electrophoretische depositie van colloïdale deeltjes op gestructureerde elektrodeoppervlakken werd geïntroduceerd in **Hoofdstuk 8**. Door toepassing van deze methode konden binaire colloïdale monolagen met LS, LS_2, LS_3, LS_4 en LS_5 stoichiometrieën worden gevormd op elektrodeoppervlakken met hexagonale en vierkante patronen. Niet dichtgepakte colloïdkristallen met A-B-A opeenvolging (een analoog van de HCP kristalstructuur) werden succesvol gefabriceerd. FCC colloïdale kristalgroei in de richting loodrecht op het (110) kristalvlak werd aanzienlijk verbeterd. Vlakdefecten gevormd door colloïdale deeltjes met een verschillende grootte konden gemakkelijk worden geïntroduceerd. Tenslotte werden binaire colloïdale kristallen met NaCl en AlB_2 analogie gefabriceerd door middel van laag-op-laag depositie van colloïdale deeltjes met respectievelijk een identieke en tegenovergestelde lading.

Acknowledgements

Four years fly away in a moment. You realize that eventually during your last days when you see that so many things could be done, but you already have to move on and start all over again in a different place. Looking back and analyzing everything, I can truly say that it was one of the most pleasant and successful periods of my life. During this time, I learned and developed myself a lot as professionally as well as socially. For all this, first of all I am very grateful to Prof. Julius Vancso. Julius, thank you that you believed in me from the beginning and let me work in the project I wanted; for your passion at the time when results did not come at the moments you expected them to be; for giving a lot of freedom in thinking and doing; for always being at the moments of "high-level" frustrations and always encouraging and directing in a right way; for an unforgettable time you have always supported to bring the group together – sailing weekends, wadlopen, Christmases and Sinterklaases, all trips to Bath and Mainz and conferences. You have never been just a professor or a supervisor, you have approached everyone personally, always understanding and helping, and never leaving alone – I appreciate it very much.

This project would never be done without a financially support of the MESA$^+$ Institute for Nanotechnology of the University of Twente, in the Strategic Research Orientation "Advanced Photonic Structures" and NanoImpuls, a nanotechnology program of the Ministry of Economic Affairs.

I am very grateful to Mark Hempenius for helping me during these years, specially in my fight with colloids and correcting all my papers and thesis (sometimes several times the same – sorry for that). It does not matter how busy you have been, you always had a minute to

listen to me intently and give wise advice or help solving any problem. You have always created a very relaxed and joyful atmosphere, I have always had a pleasure chatting with you.

I would like to thank Prof. Wim Briels and Wouter den Otter for their interest in my project and for putting a great effort to make computational programs run, and finally, nice results were obtained that became a part of Elske's diploma work and this thesis (Chapter 2).

I am also very grateful to Prof. Laurens (Kobus) Kuipers for very useful discussions: you always gave good advice or a suggestion on what could possibly be done.

During my Ph.D., two students Elske Leenders (colloidal packing simulations) and Harmen Leliveld (literature study) took part in this project. They both did a great job. Specially, I would like to thank Elske. We did not have many contacts: you were in one building, I was in another, and you usually just used to come to ask about some experimental data or to show your simulation results, and the rest we discussed on parties.

I do not know what I would do without Henk van Wolferen – the "LIL master". You were always there when I needed you and had always time to check the set-up, adjust it and explain everything to me. The set-up started working again when you just entered the room, and when you left, it was "jumping" again. I would also like to thank Henry and Rogelio for their help and very useful discussions.

My special thanks to Mark Smithers, the person who knows all gossips about everyone and everything in the university. I enjoyed very much chatting with you during all measurements, and I started missing it already when you let me use the SEM on my own. I am very grateful to you for that: I think I would never finish this work without using that machine almost every evening and weekend. I would like also to thank Albert van den Berg and Enrico Keim for their help. I would never forget, when using the SEM for the first time on my own and Mark was not there, something happened to the SEM. I thought I broke it: it did not do anything, my samples were in, but I did not know what to do. We were sorting this problem together with Enrico and a service engineer from Germany on a phone. When finally, after couple of hours, when the batteries of my telephone had died, and all hopes on sorting this out had disappeared, I discovered that one of the plugs was disconnected. You would not believe what a relief it was.

Some time of my work I spent in the clean-rooms. I want to express my gratitude to all clean-room stuff, who keep this place running for us everyday. Especially, I would like to thank Hans, Huib, Dominique, Gerard, Peter, Marion, Eddy, Samantha and Rene – people with whom I had a direct contact during all these years and who were always ready to help in the clean-room, just dial their phone number. Guys, thank you for everything! Speaking of the

clean-rooms, I would like to thank all people who are working there for all small chats that we had waiting for the machines to pump up or down. I would never recognize them without their clean-room suits. I found that always very funny, meeting people leaving the clean-rooms in the dressing room: “Sorry, is it you with whom I was chatting inside couple of minutes ago?”

Where would I go with all my thousand organization questions without our secretaries Gen, Cindy, Karin, Gerda and Thelma? Specially, I would like to thank Gen and Cindy for being helpful at any time and always smiling and so creating such a lovely atmosphere that charges your batteries with a positive energy for the rest of a day.

I would like also to thank a person without whom everything stops in the group (and possible not only in our group). Clemens, I have never understood, when you have time for all tasks that you have to perform every day. Whatever is asked from you, the answer is the same - smiling and “Ok, no problem, I’ll do that”. Thank you very much for all help during these years. I would like also to thank Zlata for always being very helpful in the chemical lab.

Special thanks to Pascal (SMCT) for helping with nanoimprint (pity, I did not have time to realize my ideas, using it) and Jörg (MT) for helping with the potentiometric titrations.

The time I spent in Twente would not be so enjoyable without you, guys: Holger (always right), Beáta and Douwe-Wiebe (where is a party and who is organizing the next one), Mária (shall we continue at my place?), Attila (still waiting), Igor (which country to choose for next measurements?), Shan (100 data points per day), Joris (hard to follow Shan), Steffi (according to a system), Barbara (smile), Henrik (don’t worry) and Giorgio (Italian), Leon S. (typical Dutch), Elske (red-hair Peppi), Sasha (looking for a BMW), Chuanliang (he?), Jing (a hobby could turn to a job), Dorota (a model), Bela senior and junior (no difference), Iwan (dreaming about Britney), Ramon (knows everything about Ewa’s topic), Yujie and Qi (Chinese is not fun), Lanti (what did she say?), Shuying (who?), Szczepan (perfect), Nikodem (big daddy), Ewa (cakes and tea), Monique (looking for “perfection”), Sandra (assistant professor), Marina (ask Pipi), Edmondo (dangerous driver), Denis (difficult to decide), Joost (one more typical Dutch), In Yee (alien), Oya (relaxed and easy), Anika (everything is planned), Janet (new), Monika (already left), Thomas (girls and parties) and Eugenia (joyful). Apart from working in one group, we were rather close and had a lot of fun together, having parties on all occasions (sometimes without), various sport invents (including bowling), traveling (mostly successful) etc. I think it was the best group I have ever worked in so far. The group is very international, but I am a bit worried at some point mentioning some attempts of learning foreign languages: that was not such a big success, wasn’t it? ☺

Specially, I would like to thank my office mates Ewa and Monique. The girls' office with a scary note on the door for guys – you never miss it. The office, where inside, everyday happiness, sadness, frustrations and craziness came out; where Ewa as a good host always had tea and cakes creating a very nice home atmosphere, while Monique was "working" on her desk after a heavy night ☺. Personally, I am amazed when Monique always finds enough time among activities she performs – running, dancing and organizing next events and certainly involving all her students in that, like Thomas, who could not miss any crazy action where he could be involved and which would be recorded by Monique, hé ☺. All these actions were always supported by many people as Sandra (span.), Siggi (can not work without first attending a beauty salon), Eddy, Francesca (my great tennis partner – we will have still our chance to beat Laura and Priscilla) and others. We had a lot of fun and it was really an unforgettable time. I am very grateful to you guys for such a joyful time.

CT life is never focused inside one group. It starts at the coffee corner and continuous with Triathlon, Sinterklaas, Christmas, girls-nights, beauty evenings, film evenings, restaurants *etc*. This time would not be great without all enthusiastic people from different group like PBM, STEP, RBT, as well as SMCT and MT. Specially, I would like to thank in a random order Francesca, Laurochka, Priscilla, Siggi, Wilco, Ype, Martijn, Edwin, Debbie, Christine, Bas, Kinsuk, Pratip, Mark Bret., Kuno, Vipin, Mukund, Sandra (Port.), Ferry, Boon Hua, Ingrid, Mark Ank., Pipi (Miguel sounds very unusual, don't you think), Marcel, Marek, Wilco, Tony, Alexei, Jacob, Wilma as well as Dana, Laura, Alexei from MT. I would like also add to this list some people from different UT groups as Balaji, Isabel, Arie, Liviu (LT) and Maya, who went with me to Horseback-riding courses at the time when Monique "exchanged" us with karate guys.

As the fates decree, I acquainted with very nice guys from COPS group as WillemV, WillenT, Philip, Tijmen, Alex, Bart, Bernard, Léon, Paolo, Karen Mo. (my sport mate ☺), Lydia, Femius, Boris, Raymond (I hope that "crazy" MTPs did not scare you away ☺), Tom, Ivo, Allard, Karen Mu. and Cock. I enjoyed you company very much. We did pretty well on the Batavierenrace; it is pity you do not take part in it any more. Probably, mountain climbing would be the next step after thorough preparations under the direction of WillemV. In particular, I would like to thank WillemV, Tijmen and Léon for your help and very useful discussions. Special thanks to Philip and Liv for very pleasant evenings we spent together.

Ik wil graag bedanken mijn "privé leraren" Nederlands – Lisette, Steven en Saron. In het begin ging dat ook over het Russisch: jullie wilden naar Rusland gaan studeren en het lukte ook. Eindelijk, werden onze "lessen" in heel gezellige avonden gewijzigd.

Speaking about Dutch, I would like to mention my classmates from “Dutch classes”: Norman, Malin and Tibet. We did not “give up” for a long time, hé ☺, coming each semester to the same teacher. We have also met often outside the classes, listening to Norman’s stories about countries he had visited recently.

I would like to express sincere gratitude to all professors and teachers of Technological Institute in Saint-Petersburg and in particular, Prof. Vladimir Korsakov, Prof. Anatolii Malygin, Victor Zvetov, Yurii Ezhovskyi, Eugenii Smirnov and Galina Ostrovidova for your unlimited support and a hard desire to give us the best education and to form in us good specialists at that rather difficult for all time. Without you, this thesis would not be written.

Coming to Twente, I met a rather large “Russian-speaking community”: Alexei and Natalia, Anton and Nadya, Olya and Artem, Lucia and Vitaly, Yura and Lena, Andrei and Yulya, Natalia and Sergei Uz., Denis M. (my schoolmate), Denis and Katya, Petya and Natalia, “big” Max and “small” Max, Sergei Sh., Sasha, Volodymirs K. and Sch., with whom we spent a lot of time together on various occasions and who became very good friends of mine. Guys, I am very grateful to you all that. I would like to thank all my friends from Germany: Max and Ksenia Sh., Jurgita and Sergei, Marina, Nadya and Boris, Dasha and Mykola, Kuzya, Alex F., Andrei and Ira, Asya and David, Dima and Michael, Rimas and Yurko, who are now spread all over Europe, but still we have a good contact since we first met in Kiel, and time after time we go to visit each other.

My special thanks to my friends from “HOME” since forever – Nadya Il., Mashka Fedot., Zhenya Bol., Tanya Kuz., Tanya Aks., Marinka and Volodya and, of course, Zhora. We do mostly communicate via e-mail or calls, but I promise, I come and visit you soon and all children will finally meet Aunt Nina in person!

Finally, I would like to express my profound gratitude to my family, who gave me a good education and unlimited support in everything I have done. Мама, папа, бабушка и дедушка, спасибо вам большое за всё, что вы для меня сделали, за вашу безграничную помощь и поддержку во всём, за то образование, что вы мне дали; только благодаря вам я достигла своих успехов. Лариса, я очень рада, что у меня есть такая очаровательная сестрёнка, у которой всё тоже обязательно получится.

There are not such words of gratitude that I could express to my sweet husband Ivan, who was always with me in good and bad times, who gave me unlimited support and help during all these years. Ванечка, спасибо тебе большое за твоё терпение, понимание,

чуткость и безграничную помощь во всем чтобы я ни делала. Я бы никогда не справилась с этой работой, если бы ты не был рядом.

Ninochka

Biography

Nina Dziomkina was born on August 8, 1978 in Gomel, Belarus. After graduation from Gomel State Lyceum in 1995, she continued her study at the Faculty of High Technologies at the Saint-Petersburg State Technological Institute (Technical University), where she obtained her bachelor degree in Chemical Technology. She did her diploma work in the group of Prof. V. G. Korsakov *Chemistry and Technology of Materials and Electronic Devices*, where she studied the influence of structure and composition of functional layers of light-emitting diodes on their electro-physical properties. In 1999, she obtained an Erasmus scholarship to continue her education at the Christian-Albrechts University in Kiel, Germany. In 2001 she obtained Master degree in Materials Science and Engineering with the diploma work "Polymer surface treatment by corona discharge", which was done in the *Multicomponent Materials* group led by Prof. F. Faupel. In the same year, to pursue her Ph.D. degree, she joined the *Materials Science and Technology of Polymers* group of Prof. G. J. Vancso at the University of Twente in Enschede, the Netherlands. During her Ph.D. project she was working on fabrication of photonic crystals. The results of her four-year research are described in this thesis. In April, 2006 she will begin to work at ASML in Veldhoven, the Netherlands.